University of Leeds

School of Chemical and Process Engineering

Ab-Initio Studies into Intrinsic Piezoelectric Properties

Author:

Joseph Anthony Hooper

Supervisors:

Dr. Andrew Scott

and Prof. Andrew Bell

Submitted in accordance with the requirements for the degree of Doctoral Training in Advanced Particulate Materials

September 2018

Intellectual Property and Declaration

The candidate confirms that the work submitted is his own and that appropriate credit has been given where reference has been made to the work of others.

"If you feel yourself hitting up against your limit,
remember for what cause you clench your fists.
Remember why you started down this path, and let that
memory carry you beyond your limit."

- All Might

Abstract

We formulate a method of understanding the intrinsic piezoelectric properties of a perovskite system on an atomistic level using a density functional theory (DFT) methodology implemented into the electron density code CASTEP.

First we consider the basic unary perovskites; barium titanate, lead titanate and potassium niobate. Geometry optimisation, elastic compliance, linear response, and simulated strain calculations are performed and the polarisation and piezoelectric coefficients are calculated. We then define the partial piezoelectric coefficient (δ_{ij}^{k}) and demonstrate a way to generate the electron density shift, two novel methods in the understanding of intrinsic piezoelectric properties.

We then study the binary piezoelectric lead titanate, performing the same calculations and analysing the electron density shift and partial piezoelectric coefficient in order to identify new features of binary systems, the equalisation between basic perovskite units and the "sawtooth" bonding asymmetry between the different B-site ions.

Then the feasibility of these calculations is evaluated for bismuth ferrite, a material showing multiferroic properties. The conversion of non-orthonormal lattice axes to a cartesian coordinate system is addressed. We discuss the phonon and electric field calculations, and evaluate what is and is not possible. We find that structural and electron calculations are possible and report the optimised geometry, the elastic compliance, total electron density and spin maps, and the electron density shifts. We identify the symmetry, non-locality, and rotational modes in rhombohedral bismuth ferrite and suggest future research based on these properties.

Acknowledgements

I am incredibly grateful to my supervisors Andy Bell and Andrew Scott for their help and support over many years, for all the discussions, introductions, knowledge, understanding, tears, and laughs. Without them this would never have been possible.

I would also like to thank the other members of the Ferroelectrics and DFT groups for their advice and support. In ferroelectrics; Steven, Laura, Tom, Sam, Tim, Tim, and Anton have been incredibly helpful in finding data and understanding the subject materials. In DFT; the knowledge and expertise of Trevor and Che helped me understand not only how computer modelling works, but why it is essential.

Many thanks to the CASTEP Development Group and the community mailing list for continued assistance and perseverance despite some very silly questions. Many thanks to the ARC help team for their assistance and perseverance despite some catastrophically silly questions.

Mishti Oberoi has provided me with a great drive to improve throughout my research. Thank you, I love you.

My family have supported and loved me unconditionally throughout this time. Their love has made this possible.

And to my friends, too many to name who have helped in small ways, large ways, and all the ways in between. I owe you all. Thank you.

Contents

List of Figures

List of Tables

Nomenclature

DFT	Density Functional Theory
HF	Hartree-Fock
KS	Kohn-Sham
LDA	Local Density Approximation
GGA	Generalised Gradient Approximation
PBE	Perdew-Burke-Ernzerhof
WC	Perdew-Burke-Ernzerhof with Wu-Cohen Exchange
FFT	Fast Fourier Transform
SCF	Self-Consistent Field
MP grid	Monkhorst-Pack grid
FE	Ferroelectric
$BaTiO_3$, BTO	Barium Titanate
$PbTiO_3$, PTO	Lead Titanate
$KNbO_3$, KNO	Potassium Niobate
$PbTi_{1-x}Zr_xO_3$, PZT	Lead Zirconate Titanate
$BiFeO_3$, BFO	Bismuth Ferrite
a, b, c	Lattice Length, given in Angstroms (Å) ($10^{-10}m$)
α, β, γ	Lattice Angle, given in degrees ($^\circ$)
eV	Electron-Volts, a unit of energy (1.602×10^{-19}J)
pm	picometers, a unit of length equal to $10^{-12}m$

Chapter 1

Introduction

1.1 Introduction to Piezoelectrics

1.1.1 What is a Piezoelectric?

A piezoelectric is a material that, through its atomic structure, is able to convert between mechanical and electric energy, and vice versa. The direct piezoelectric effect was discovered by Pierre and Jacques Curie in 1880[1, p. 1] where they found that materials such as quartz and Rochelle salt both developed a current in response to mechanical stress. The inverse piezoelectric effect is the generation of mechanical stress through the application of a voltage or electric field, which was proved to exist thermodynamically by Lippman (1881)[2] and later experimentally observed by the Curies (1881)[3].

During the First World War the potential for piezoelectric devices was realised when Paul Langevin used a quartz crystal between metal plates and a hydrophone to build the first sonar system. The inverse piezoelectric effect was used in order to generate an ultrasonic pulse by applying a voltage to the

plates, and using the echo detected by the hydrophone as the pulse bounced off a solid object, the distance could be ascertained[4].

Since then, the unique properties of piezoelectric materials have led to them being developed in industry, with a drive to develop new materials and technology.

1.1.2 Applications of Piezoelectrics

Piezoelectric materials have become widely used due to their unique properties. Many simple, everyday devices take advantage of the piezoelectric effect by using a cheap piezoelectric element such as quartz. The most common and well known uses are in timekeeping and in lighters.

In a quartz watch time is kept by a crystal oscillator, a piece of quartz crystal attached to a battery that oscillates with a specific frequency due to the inverse piezoelectric effect. Number of vibrations can be counted by an electronic chip, which can then control either a mechanical analogue system or a display for a digital system to ensure that these continue to tick at a stable 1Hz for the lifetime of the battery. These have the advantage that they are much more stable than mechanical timepieces which require springs that must be wound regularly to prevent drift, and they are much cheaper, smaller and have much lower power requirements than other methods that are far more precise than is necessary for day to day use.

The electric or 'hammer' lighter is a common device used by many people in situations where a handy source of fire is useful, for example when someone may wish to light cigarettes, candles, fireworks, or stoves. This device utilises a quartz crystal element and uses the direct piezoelectric effect to create an electric spark that can be used to light the fuel. When the user pushes down

FIGURE 1.1: Examples of common items that use the piezoelectric effect.

on the button force builds in a spring hammer mechanism, until such a point that the mechanical release trips and the hammer is released onto the crystal. This allows a far greater force to impact the crystal than would be possible by a person. As the crystal is struck a mechanical stress is produced that is converted through the piezoelectric effect into an electric charge. This is carried as electric current through a simple wire mechanism to a spark gap, where the spark ignites a stream of fuel in air to create a flame. This is preferable to a flint mechanism, as the crystal is not worn down or damaged easily, and the button mechanism is more comfortable to use.

Although these examples are simple, they demonstrate the piezoelectric and inverse piezoelectric effects in a familiar way. Piezoelectrics are used for many more technical applications that require specific materials to be formed in certain ways. However, these more complex systems work using the same effect that has been described.

The piezoelectric effect is utilised across many fields, with companies such as Morgan Advanced Materials[5] specialising in different components for medical,

FIGURE 1.2: A selection of piezoelectric transducer components available from Morgan Advanced Materials[6].

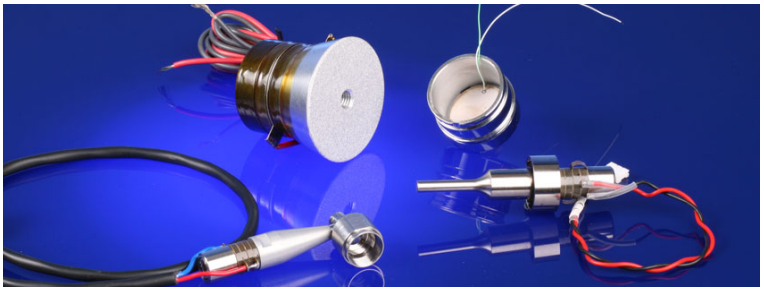

industrial, aerospace, and marine applications, amongst others. Some of the common applications of piezoelectric ceramics are listed below.

- Acoustic transducers can be created over a wide range of frequencies for the detection (using the direct piezoelectric effect) or generation (using the inverse piezoelectric effect) of high frequency vibrations, often at ultrasonic frequencies. These can be utilised to create sonar systems used in a variety of vehicles, from the sonar of a naval submarine to the parking sensors on everyday cars. They can also be used for industrial cleaning by generating ultrasonic waves through liquid that is capable of removing dirt by mechanical force within industrial equipment. Finally they may be used in medical applications for many things, from the massaging of soft tissues to the cutting of bone[6]. Figure 1.2 shows a number of piezoelectric components for transducer use as shown by Morgan Advanced Materials[6].

- Piezoelectrics have also been considered for use as electric generators. Currently most of the focus is on the use of ZnO nanorods on a substrate to create a small amount of power for nanodevices[7]. However, there has been interest in the use of ceramic based materials to harvest energy from walking. In 2014, a proof of concept for an insole that could charge a power bank using the mechanical energy from walking was submitted as

part of the Google Science Fair[8]. Although the design does not output enough power to be commercially viable, it brought wider attention to the possibility of harnessing otherwise wasted energy. Designs have allowed for either an element in the shoes, or by the use of tiles with piezoelectric generators in them that generate energy as they are stepped on such as ones developed by Pavegen Systems[9]. Although this technology shows promise, in order to become more commercially viable materials capable of converting more of the mechanical energy must be developed for a higher power output.

1.1.3 Lead-Free Piezoelectrics

The most widely used piezoelectric ceramic is lead zirconate titanate, otherwise known as PZT or by its chemical formula $Pb(Zr_xTi_{1-x})O_3$. An idealised form of PZT where $x = 0.5$ is shown in figure 1.3. Lead atoms are coloured grey, titanium is silver, zirconium is blue and oxygen is shown as red. In reality the distribution of zirconium and titanium is random throughout the structure leading to Ti and Zr rich areas, therefore for real PZT the repeating unit cell representation cannot be used.

However, PZT is approximately 64% lead by weight. Due to EU directives on the Restriction of Hazardous Substances (RoHS), lead may not be used in electronic equipment due to its toxicity[11]. An exemption is provided for lead used in piezoelectronic devices due to the lack of a low-toxicity replacement, however this exemption must be renewed regularly and there is pressure to find other materials that can be implemented instead.

In order to search for new materials efficiently, it is important to first understand the principles behind the piezoelectric effect. A way to quickly calculate

FIGURE 1.3: Idealised PZT unit cell based on data from Frantti et al. [10]. Grey - Pb, Red - O, Light Grey - Ti, Blue - Zr.

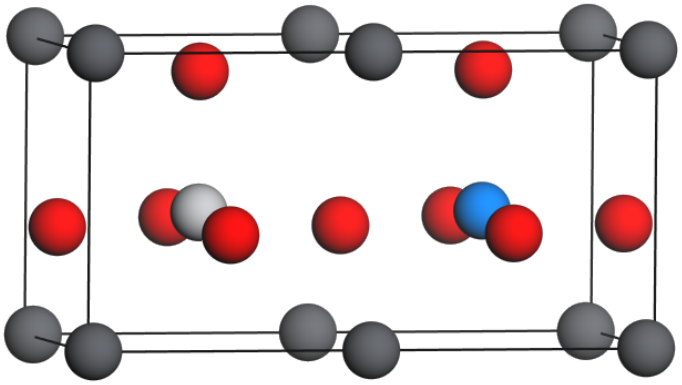

the intrinsic properties of the piezoelectric structure without the need to synthesise it would allow the experiments and material development to be guided in an intelligent and efficient manner.

1.2 Introduction to Computing

1.2.1 Advances in Computational Power

Since the introduction of the first electronic computer Colossus in 1944, computers have been integrated into almost every aspect of life. Laptop and desktop computers are used daily for both work and hobbies, many mundane, everyday items have some form of on board computer to control various functions, and much of a normal daily routine is controlled by servers in secret locations. Smartphones become ever more popular as people want more than simple communication functions while on the move, with predictions that next year a quarter of the world's population will own one[12]. The massive increase in computers is due in part to Moore's law. Although strictly this predicts that

FIGURE 1.4: The progression of Moore's Law since 1971[14].

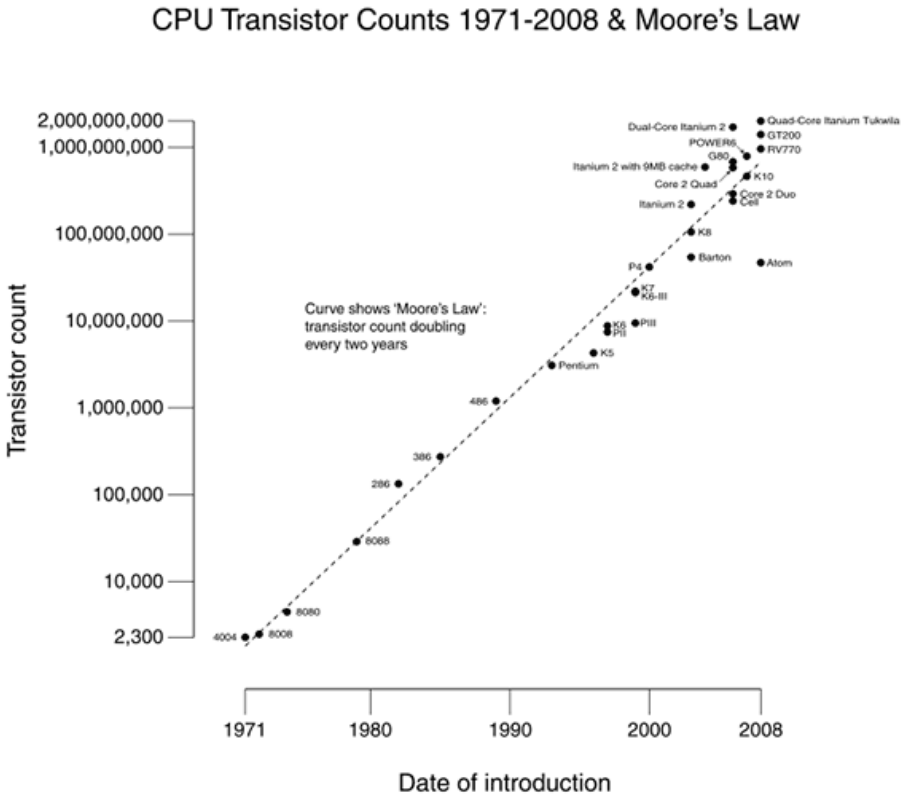

the number of transistors on an integrated circuit doubles approximately every two years, this has a knock on effect to the miniaturisation of general components and the overall affordability of computers for purpose[13]. Figure 1.4 shows the number of transistors on different chips since 1971, with a logarithmic axis used to demonstrate the exponential increase in transistors[14]. Although the validity of the predictions made by this law are often questioned, continued improvements by manufacturers has ensured that processing power has increased while the costs of that power have decreased.

FIGURE 1.5: TITAN Supercomputer at Oak Ridge National Laboratory[15].

1.2.2 Introduction to Scientific Computation

Consumer devices focus on minimising the size of integrated circuits in order to create more powerful devices that are more compact and efficient. For scientific uses however, the increase in processing power and decrease in energy consumption has led to the building of far larger and more powerful machines in order to solve bigger and more complicated equations. A standard consumer device will often have 4 processing cores contained on a single CPU chip, which has become known as quad-core. In contrast, these high-performance computers (HPCs) or supercomputers will have thousands of cores, or in the case of Tianhe-2 several million. Figure 1.5 shows the first of six server racks that house the TITAN supercomputer at Oak Ridge National Laboratory. It is the tier 1 national machine for the USA, and ranks 2nd in the world with almost 300,000 CPU cores and 18,688 GPU accelerators over 4,352 square feet[15].

Although each individual processing core is no more powerful than a consumer device, the combined power of components connected through a high speed network allows programmers to take advantage of far more cores than would ordinarily be available on a standalone computer. By utilising techniques such as Message Passing Interface (MPI) and splitting up a large problem into many

small ones, it is possible that splitting the calculations over a large number of cores will vastly decrease the time taken. In doing so, calculations that would ordinarily take far too long to be of use on a normal computer may be solved much more quickly and efficiently. Most parallel applications will show a marked speed up, however as communication times between all the cores increases it can become less efficient. Depending on the particular program and the calculation task, it may be efficient to use hundreds or even thousands of cores, solving problems in a fraction of the time that would ordinarily be possible.

Scientific computing is used for many purposes in many different fields to compliment experimental work. Over time, experiments become more expensive due to the increased requirements for new materials and equipment, or because it is simply not feasible to perform the desired experiments. Conversely computational power has become cheaper as computers have become more widespread, and there is far less concern for scale or safety of the simulated system than there would be for the equivalent real system.

For instance, Pickard and Needs were able to model the crystalline structure of ammonia under several hundred GPa of pressure, equivalent to the internal pressure of a gas giant[16], predicting a new crystal phase at a given pressure range. Six years later, Ninet et al. (2014) were able to confirm the existence of the predicted phase experimentally using a high-pressure diamond-tipped anvil to generate the required pressures[17]. Figure 1.6 from Pickard and Needs[16] shows predictions for the structures of ammonia at 100, 300 and 450GPa. At the time of publication such pressures were not possible to create in an experimental setting.

This technique has been used to predict the structures of many new and existing materials under a range of conditions from studies of Ni_xInAs for electronic

FIGURE 1.6: High pressure phases of ammonia predicted by computation[16].

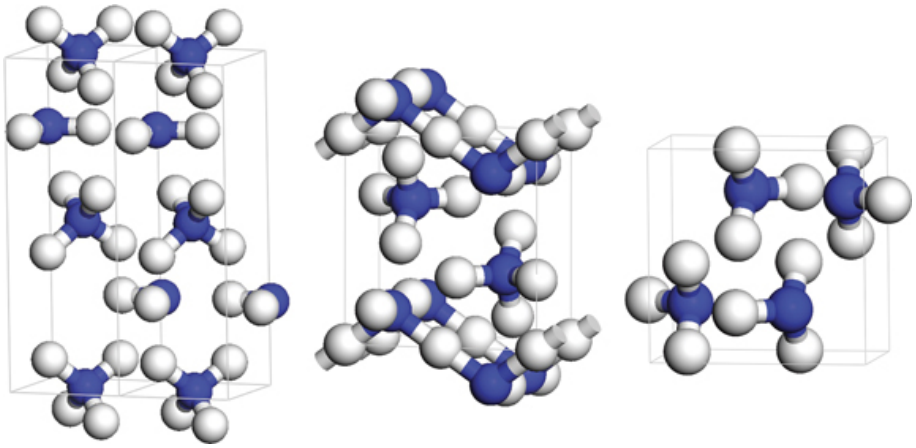

components[18], to modelling of $CaCO_3$ and $MgCO_3$ in the Earth's mantle for geophysical studies[19]. In all of these cases, computation has made predictions to guide experimental studies to their goal.

1.3 Overview of the Project

It is the goal of this project to use computation in order to support the experimental piezoelectrics group. Through the use of Density Functional Theory (DFT) a variety of piezoelectric materials will be modelled in order to calculate and understand the piezoelectric effect on an atomistic level. By understanding and being able to quantify the piezoelectric effect and the industrially relevant quantities associated with the materials in a first principles manner, we will be able to develop a framework for fundamentally understanding how structure and bonding affects the piezoelectric properties.

This understanding can be used in the future to develop new, tailored materials that outperform currently used materials without the downsides of toxicity or environmental damage.

Chapter 2

Scientific Information

2.1 The Science of Piezoelectrics

2.1.1 The Direct and Inverse Piezoelectric Effect

The piezoelectric effect, sometimes referred to as the direct piezoelectric effect, is the ability of certain materials to generate an electric charge as a mechanical stress is applied. The same materials also exhibit the reverse of this process known as the inverse (or converse) piezoelectric effect, whereby an electric charge in the material causes a spontaneous mechanical stress[20]. A schematic view of this is shown in figure 2.1, with P being the direction of the axis of asymmetry, commonly the axis of polarisation.

This effect is caused by a non-centrosymmetric crystal structure which may be formed in 20 of the total 32 crystal classes, however not all of the materials in those classes will exhibit a piezoelectric effect. This effect was first discovered in 1880 by Jacques and Pierre Curie, who discovered that crystals such as quartz, tourmaline, and Rochelle salt gave an observable electrification under

FIGURE 2.1: A schematic illustration of the direct piezoelectric effect due to strain parallel to the axis of polarisation[21].

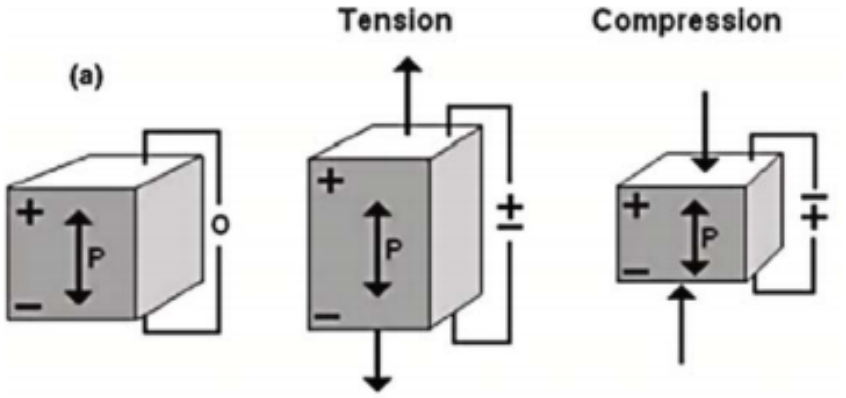

stress[21]. Since then many new bulk piezoelectric materials have been discovered, including perovskite materials such as barium titanate ($BaTiO_3$) and lead titanate ($PbTiO_3$), and recently a piezoelectric effect in nanostructures such as zinc oxide nanorods[7].

Table 2.1 shows the 32 classes and if they are able to exhibit the piezoelectric, pyroelectric, or ferroelectric effect. This was formulated by studying the matrices for equilibrium properties in Nye (1957)[22] and ferroelectric point groups were taken from Mirman (1999)[23].

Figure 2.2 shows the unit cell crystal structure of barium titanate in its low temperature rhombohedral phase. This structure has a clear asymmetry in the [111] direction, producing a piezoelectric response.

Figure 2.3 is an SEM micrograph of a zinc oxide nanorod array produced by Wang and Song for use as a piezoelectric nanogenerator that may be used to produce electricity from ambient vibrations.

TABLE 2.1: The 32 crystallographic point groups, and their electric properties from Nye (1957)[22] and Mirman (1999)[23].

Lattice Type	Point Group	Piezo-	Pyro-	Ferro-
Triclinic	1	•	•	•
	$\overline{1}$			
Monoclinic	2	•	•	•
	m	•	•	•
	$2/m$			
Orthorhombic	222	•		
	$mm2$	•	•	•
	mmm			
Tetragonal	4	•	•	•
	$\overline{4}$	•		
	$4/m$			
	422	•		
	$4mm$	•	•	•
	$\overline{4}2m$	•		
	$\overline{4}/mmm$			
Trigonal	3	•	•	•
	$\overline{3}$			
	32	•		
	$3m$	•	•	•
	$\overline{3}m$			
Hexagonal	6	•	•	•
	$\overline{6}$	•		
	$6/m$			
	$6/mmm$			
	622	•		
	$6mm$	•	•	•
	$\overline{6}m2$	•		
Cubic	23	•		
	$\overline{4}3m$	•		
	$m3$			
	432			
	$m3m$			

FIGURE 2.2: The rhombohedral structure of barium titanate, as observed experimentally below 180K.

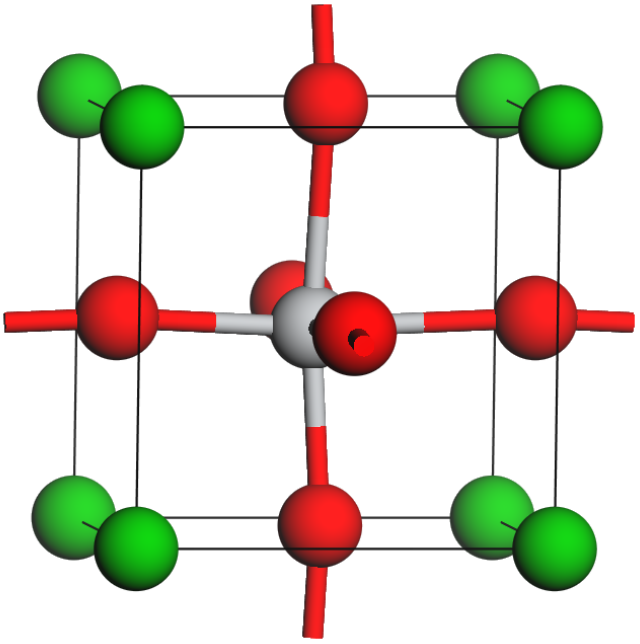

FIGURE 2.3: An SEM image of a piezoelectric ZnO nanorod nanogenerator created by Wang and Song[24].

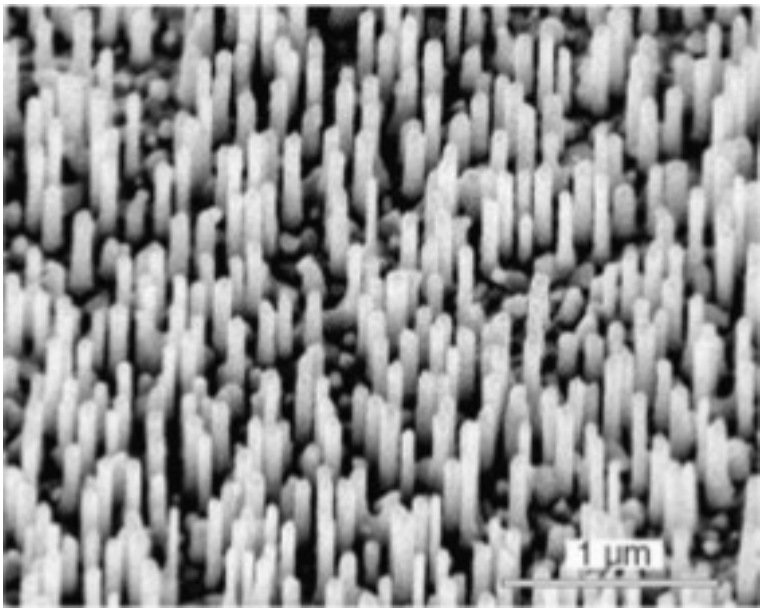

2.1.1.1 Piezoelectric or Ferroelectric?

Though the piezoelectric and ferroelectric effect are separate phenomena, they often appear in materials such as $BaTiO_3$ and PZT. These effects also have the same Curie temperature and ultimately arise from the same asymmetric properties, which leads to further confusion. The definitions for the two effects in relation to ceramics are as follows[25].

- Piezoelectricity – The coupling of elastic and dielectric properties of a solid exhibiting linear dependence of either a mechanical load generating a charge (direct) or an electric field generating a deformation (inverse).
- Ferroelectricity – A non-linear crystal capable of being spontaneously polarised, generally with a high level of permittivity, that exhibits hysteresis in the variation of dielectric polarisation as a function of electric field strength, and has a temperature dependant permittivity.

It is important to distinguish these effects for many materials, as piezoelectricity is supported by 20 crystal classes whereas ferroelectricity is only supported by 10. This means that while many materials may be piezoelectric and ferroelectric, many such as quartz are solely piezoelectric. Overall, discussions on favourable electrical properties are due to the ferroelectric effect, where mechanical properties are due to the piezoelectric effect.

2.1.2 The Perovskite Group

The perovskite group of crystallographic structures is of particular interest to this research. It is named after the mineral perovskite ($CaTiO_3$) and refers

FIGURE 2.4: The idealised perovskite cubic structure, shown as barium titanate as observed above 400K.

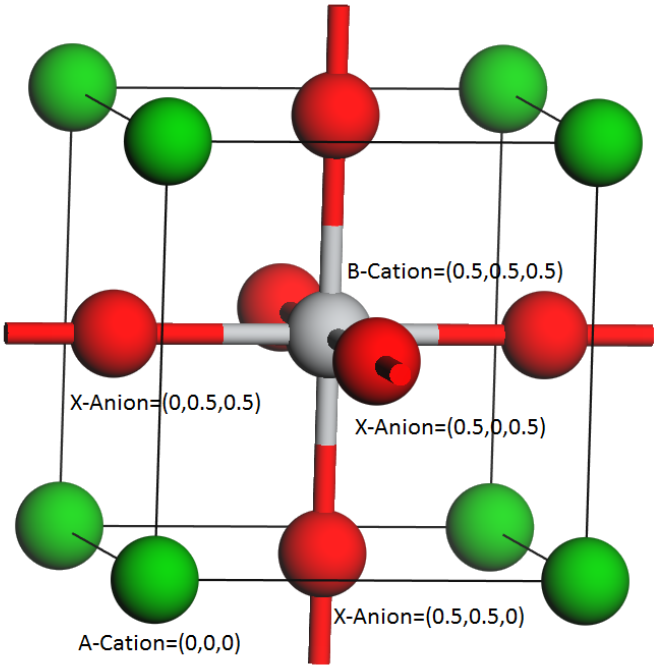

to materials with the similar structures. Although these materials were originally believed to be cubic it was found that most of the structures are in fact only pseudo-cubic, with perovskite itself found to be monoclinic and others discovered to be tetragonal or orthorhombic[26].

In its idealised cubic structure, a perovskite has the generic formula ABX_3 with the A-cation in the $(0, 0, 0)$ position, B-cation in the $(\frac{1}{2}, \frac{1}{2}, \frac{1}{2})$ position and X-anions in the $(\frac{1}{2}, \frac{1}{2}, 0)$, $(\frac{1}{2}, 0, \frac{1}{2})$, and $(0, \frac{1}{2}, \frac{1}{2})$ positions. This idealised structure is shown in figure 2.4.

However, non-cubic phases generally do not have ions on symmetric positions. For instance, in the tetragonal form a piezoelectric such as lead titanate ($PbTiO_3$) the B-cation and all X-anions shift in the z-axis by a small amount, leading to the necessary asymmetry. Similarly in a rhombohedral form such

as barium titanate ($BaTiO_3$) the atoms are shifted along the [111] direction, creating the asymmetry. Convention dictates that the A-cation is always in the (0,0,0) position, with the unit cell and all other atoms relative to this.

2.1.3 Intrinsic Piezoelectric Properties

The strength of the piezoelectric effect is dependent on a mix of intrinsic properties which deal with atomic interactions and bonds, and extrinsic properties that are determined by larger scale effects such as crystal grains and domains. As the extrinsic properties occur on scales far beyond DFT is capable of, the intrinsic properties will be studied.

2.1.3.1 Piezoelectric Charge Constant

The piezoelectric charge constant, known as d_{ij}, is a matrix of elements that determine how the piezoelectric behaves under electric field or stress. It is defined as:

- The polarisation generated per unit of mechanical stress.
- The mechanical strain on the piezoelectric per unit of electric field applied.

These are equivalent, as can be seen by dimensional analysis of the constituent parts in equation 2.1.

$$
\begin{aligned}
Polarisation &= \frac{Coulombs}{Meters^2} = \frac{C}{m^2} \\
Stress &= \frac{Newtons}{Meters^2} = \frac{N}{m^2} \\
Strain &= Dimensionless \\
E - Field &= \frac{Newtons}{Coulomb} = \frac{N}{C}
\end{aligned}
$$

$$
\begin{aligned}
d_{ij} &= \frac{Polarisation}{Stress} \\
d_{ij} &= \frac{\frac{C}{m^2}}{\frac{N}{m^2}} \\
d_{ij} &= \frac{C}{N}
\end{aligned}
\tag{2.1}
$$

$$
\begin{aligned}
d_{ij} &= \frac{Strain}{E - Field} \\
d_{ij} &= \frac{1}{\frac{N}{C}} \\
d_{ij} &= \frac{C}{N}
\end{aligned}
$$

The (i,j) components indicate elements of the matrix, which refer to the direction of polarisation or the applied electric field for the first index, and the direction of the applied stress or induced strain for the second. An index of 1, 2, or 3 denotes an axis direction of x, y, or z, whereas 4, 5, or 6 denote a shear about the respective axis[27]. For a tetragonal material, there are 3 independent quantities in this matrix:

- d_{33} – An electric field in the z-axis giving rise to a displacement in the same direction, or a displacement in the z-axis inducing polarisation in that direction.

TABLE 2.2: Example piezoelectric charge coefficients for barium titanate[28], a PZT variant sold by Morgan Advanced Materials[29], and a proprietary piezoelectric material created by Mide Technology Corporation[30].

	$BaTiO_3$	PZT401	PZT402	CTS-3195HD
$d_{33}(\times 10^{-12} C/N)$	82	315	307	390
$d_{31}(\times 10^{-12} C/N)$	-33	132	125	-190
$d_{15}(\times 10^{-12} C/N)$	150	511	495	585

- d_{31} – An electric field in the z-axis direction gives a strain in the x-axis, or an induced polarisation in the z-axis direction due to a mechanical stress in the x-axis.

- d_{15} - An electric field in the x-axis induces shear strain about the y-axis, or shear stress applied around the y-axis induces a polarisation in the x-axis.

Example values for these quantities are published by companies and are available as datasheets. A few examples are shown in table 2.2. $BaTiO_3$ data is taken from MatWeb[28], PZT data from Morgan Advanced Materials[29], and CTS data is from Mide Technology Corportation[30].

2.1.3.2 Elastic Compliance

The elastic compliance (s_{ij}) of the piezoelectric is the ratio of the strain produced in the material to the mechanical stress applied to it. In the s_{11} and s_{33} directions this is equal to $\frac{1}{Y}$ where Y is the Young's modulus, or modulus of elasticity[27]. The indices (ij) are similar to those of the charge coefficient, with the first being the direction of the induced strain, and the second the direction of the applied stress. Only the (11) and (33) indices are usually listed. There are 2 different types of the compliance:

TABLE 2.3: Example elastic compliance of barium titanate[31], industrial PZT produced by Morgan[29], and an industrial material created by Mide Technology Corporation[30].

	$BaTiO_3$		PZT		
	Crystal	Ceramic	401	402	CTS-3195HD
$s_{11}^E(\times 10^{-12}m^2/N)$	8.05	8.55	12.70	12.30	16.4
$s_{33}^E(\times 10^{-12}m^2/N)$	15.7	8.93	15.60	15.57	18.8
$s_{11}^D(\times 10^{-12}m^2/N)$	7.25	8.18	11.10	10.89	14.4
$s_{33}^D(\times 10^{-12}m^2/N)$	10.8	6.76	7.76	7.94	9.43

- s^E – The compliance under constant electric field.
- s^D - The compliance under constant electric displacement.

Examples of these quantities for the previous ceramics are given in table 2.3. Again, PZT data was taken from Morgan Advanced Materials[29], and CTS data is from Mide Technology Corportation[30]. $BaTiO_3$ data was not given in the original source, so has been taken from Berlincourt and Jaffe (1958)[31].

Berlincourt and Jaffe also give a mathematical expression for the compliance that may be useful in later studies, shown in equation 2.2, where ρ is the density and N_R is the resonance frequency constant.

$$s_{11}^E = 1/(4\rho N_R^2) \tag{2.2}$$

Though this may not be of use in static calculations, it may become useful in connecting ab-initio research with industrially important quantities.

2.1.3.3 Dielectric Permittivity

The dielectric permittivity of the piezoelectric is the dielectric displacement per unit of electric field[27]. This quantity is ultimately a measure of how the material reacts to an electric field and how good the material will be

as a capacitor. As materials like barium titanate are both piezoelectric and ferroelectric the permittivity is expected to be high, as ferroelectric ceramics are commonly used in capacitors. It is represented by ϵ and may be given at either a constant stress or constant strain. This is followed by an index (ij), where the first is the dielectric displacement in the 1, 2, or 3 direction, and the second is the direction of the electric field.

- ϵ_{ij}^{T} - The permittivity for a material under constant stress.
- ϵ_{ij}^{S} - The permittivity for a material under constant strain.

The dielectric permittivity can be related to several other quantities, and which is most suitable may depend on what is being calculated or measured. The relative dielectric constant K is frequently used, which is relative to the permittivity of free space as shown in equation 2.3. This is the quantity usually quoted in publications and data sheets so is most readily available.

$$K = \frac{\epsilon}{\epsilon_0} \tag{2.3}$$

The permittivity of free space is a constant with a value of $\epsilon_0 = 8.85 \times 10^{-12} Fm^{-1}$. This is related to a quantity known as the electric susceptibility χ as $K = 1 + \chi$[32].

The relative dielectric constant of example materials is shown in table 2.4. PZT data was not available from the Morgan data sheet so was taken from Jaffe Piezoelectric Ceramics (1971)[1, p. 146]. CTS data is from Mide Technology Corporation[30]. $BaTiO_3$ data has been taken from Berlincourt and Jaffe (1958)[31].

TABLE 2.4: The relative dielectric constants single crystal and ceramic barium titanate[31], PZT[1, p. 146], and an industrial material from Mide Technology Corporation[30].

	$BaTiO_3$			
	Crystal	Ceramic	PZT	CTS-3195HD
K_{11}^S	2920	1436	612	916
K_{33}^S	168	1680	399	830
K_{11}^T	1970	1123	1180	1730
K_{33}^T	109	1256	730	1700

2.1.3.4 Electromechanical Coupling Coefficient

The electromechanical coupling coefficient (k) is a measure of the piezoelectric efficiency of the material and is described as the best measure of the piezoelectric effect[1, p. 10]. The coupling coefficient is given by equation 2.4 and 2.5 for the direct and inverse piezoelectric effect respectively. As it is effectively a ratio of energies, the overall quantity is dimensionless.

$$k^2 = \frac{\text{Electric Energy Generated}}{\text{Mechanical Energy Inputted}} \tag{2.4}$$

$$k^2 = \frac{\text{Mechanical Energy Generated}}{\text{Electric Energy Inputted}} \tag{2.5}$$

As we are dealing with a physical system, this energy transfer is limited by physics to be incomplete due to energy conservation and thermodynamics and as a result we know that $k^2 < 1 \implies k < 1$. Generally speaking, higher electromechanical coupling coefficients are desired for piezoelectrics. As piezoelectrics tend to have different properties in different directions relative to the axis of polarisation, the coupling factor is split into the same indices as the piezoelectric charge constant in section 2.1.3.1. Table 2.5 shows the piezoelectric coupling coefficient for some sample piezoelectric materials. PZT data was

TABLE 2.5: A table showing the piezoelectric coupling constants of barium titanate[31], PZT from Morgan Advanced Materials[29], and the CTS industrial material produced by Mide Technology Corporation[30].

	$BaTiO_3$		PZT		
	Crystal	Ceramic	401	402	CTS-3195HD
k_{33}	0.560	0.208	0.67	0.70	0.72
k_{31}	0.315	0.494	0.35	0.33	0.36
k_{15}	0.570	0.466	0.70	0.71	0.59

taken from Morgan Advanced Materials[29], and CTS data is from Mide Technology Corporation[30]. $BaTiO_3$ has been taken from Berlincourt and Jaffe (1958)[31].

2.1.4 Relations Between Piezoelectric Constants

Though all of the constants are important in their own right, they can also be used to define a set of equations to quantify the piezoelectric effect. Equations 2.6 and 2.7 are fundamental to the piezoelectric process as they link the strain (x) and dielectric displacement (D) to the applied stress (T) and electric field (E) through the previously described properties[1, p. 9].

$$x = s^E T + dE \tag{2.6}$$

$$D = dT + \epsilon^T E \tag{2.7}$$

We see that in both of these cases that the piezoelectric charge coefficient influences both the mechanical and electric field quantities, which is due to its broad nature discussed in section 2.1.3.1. Additionally we see that the compliance associates with the mechanical quantities while the permittivity is associated with the electric field and dielectric displacement. This gives some insight into the nature of these quantities and how we may be able to

calculate them, as we can isolate mechanical and electric field effects. The electromechanical coupling coefficient can be linked to the other quantities through equation 2.8[33].

$$k^2 = \frac{d^2}{s^E \epsilon^T} \tag{2.8}$$

We see again that like the charge coefficient, the coupling coefficient has both electric field and mechanical components as seen in the denominator, as we would expect due to it being identical for both the direct and inverse piezoelectric effect.

These properties are esential to the macroscale piezoelectric effect, and thus understanding how they work is crucial to our fundamental model of piezoelectricity.

2.1.5 Barium Titanate as a Sample Material

Barium titanate has been selected as the initial material of study due to its industrial, structural, and historical interest. It shows both piezo- and ferroelectricity at room temperature, has a perovskite structure, and in its solid phase has 5 crystal phases that undergo thermal transitions. Figure 2.5 shows a visualisation of the unit cell of the room temperature tetragonal phase.

Characterisation of the tetragonal phase was first performed by Megaw (1945)[35] using copper $K\alpha$ x-rays with a wavelength of 0.15418nm. It was found that the lattice parameters of this phase were $a = 3.9860$Å and $c = 4.0263$Å, however none of the internal features of the cell that give rise to the piezo- and ferroelectric properties were found.

Structural properties of the cubic, tetragonal, and rhombohedral are shown in table 2.6. As not all properties are relevant to a given phase, some quantities

FIGURE 2.5: Visualisation of the tetragonal phase of barium titanate as observed at room temperature[34].

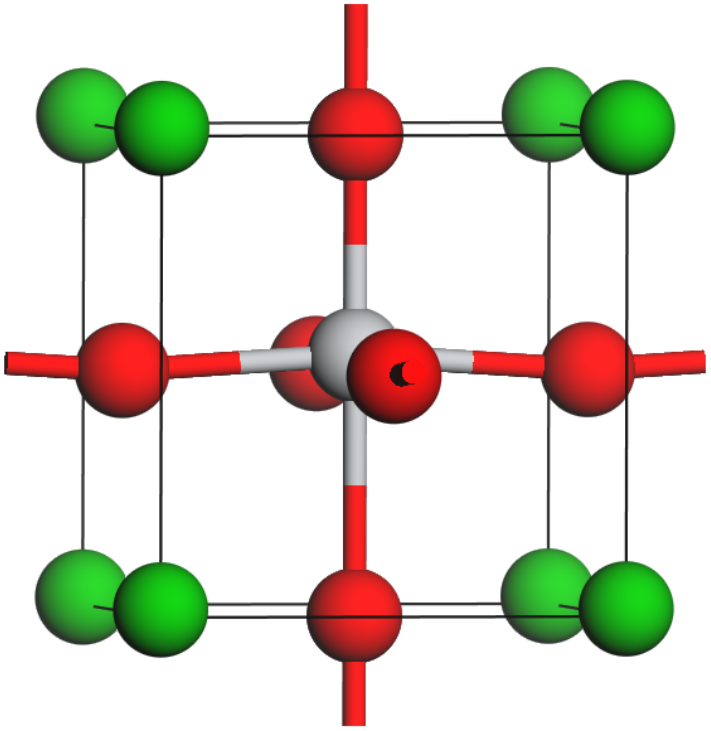

are intentionally omitted. Data for the cubic structure is taken from Edwards, et al. (1951)[36], while data for the other phases is from Kwei, et al. (1993)[34]. The quantities Δa and Δc represent the difference in fractional coordinates from the ideal cubic positions, with $Ti = (\frac{1}{2}, \frac{1}{2}, \frac{1}{2})$, $O_z = (\frac{1}{2}, \frac{1}{2}, 0)$, and $O_a = (\frac{1}{2}, 0, \frac{1}{2})$. By symmetry, the position of O_b is identical to O_a with a rotation about the z-axis in tetragonal and cubic phases, so is not required. In the rhombohedral phase, all of the oxygen atoms are symmetrically identical and therefore only one is required to be defined.

We will begin our research with barium titanate, along with two less common but similar perovskites; lead titanate and potassium niobate.

TABLE 2.6: Structural properties for the cubic, tetragonal, and rhombohedral phases of barium titanate from Edwards, et al.[36] for cubic and Kwei, et al.[34] for the others. Δa and Δc is the difference between the fractional coordinate and the ideal cubic positions in the a- and c-axes.

	Cubic	Tetragonal	Rhombohedral
a (Å)	4.0057	3.9925	4.0036
c (Å)	-	4.0365	-
V (Å^3)	64.274	64.406	64.172
$\alpha(^\circ)$	-	-	89.939
Δa_{Ti}	-	-	-0.0128
Δc_{Ti}	-	0.0203	-
Δa_{Oz}	-	-	0.0109
Δc_{Oz}	-	-0.0258	0.0193
Δc_{Oa}	-	-0.0123	-
Curie Temp. (K)	400	270	-

2.2 Density Functional Theory

2.2.1 Ab-Initio Modelling Using DFT

Ab-initio modelling is a simulation technique based entirely on physical theory, with no direct input from experimental data. It translates as "first principles", or literally "from the beginning". DFT is one such method, using quantum mechanics to determine ground state electronic structures by calculating the electron density. In this way, DFT can be used to calculate the ionic, covalent, and metallic bonding of materials[37, Ch. 6].

In a DFT calculations are based on the electron density function $\vec{n}$, which maps the full 3-dimensional space with the probability of an electron occupying each infinitesimal volume element around the point (x,y,z)[38]. Figure 2.6 shows a 2 dimensional cross section of the electron density for graphene, with red representing a high probability of electron occupancy, and blue representing low probability.

FIGURE 2.6: An electron density plot for graphene, looking down the normal planar axis, calculated using CASTEP. Blue is low electron density, and orange is high.

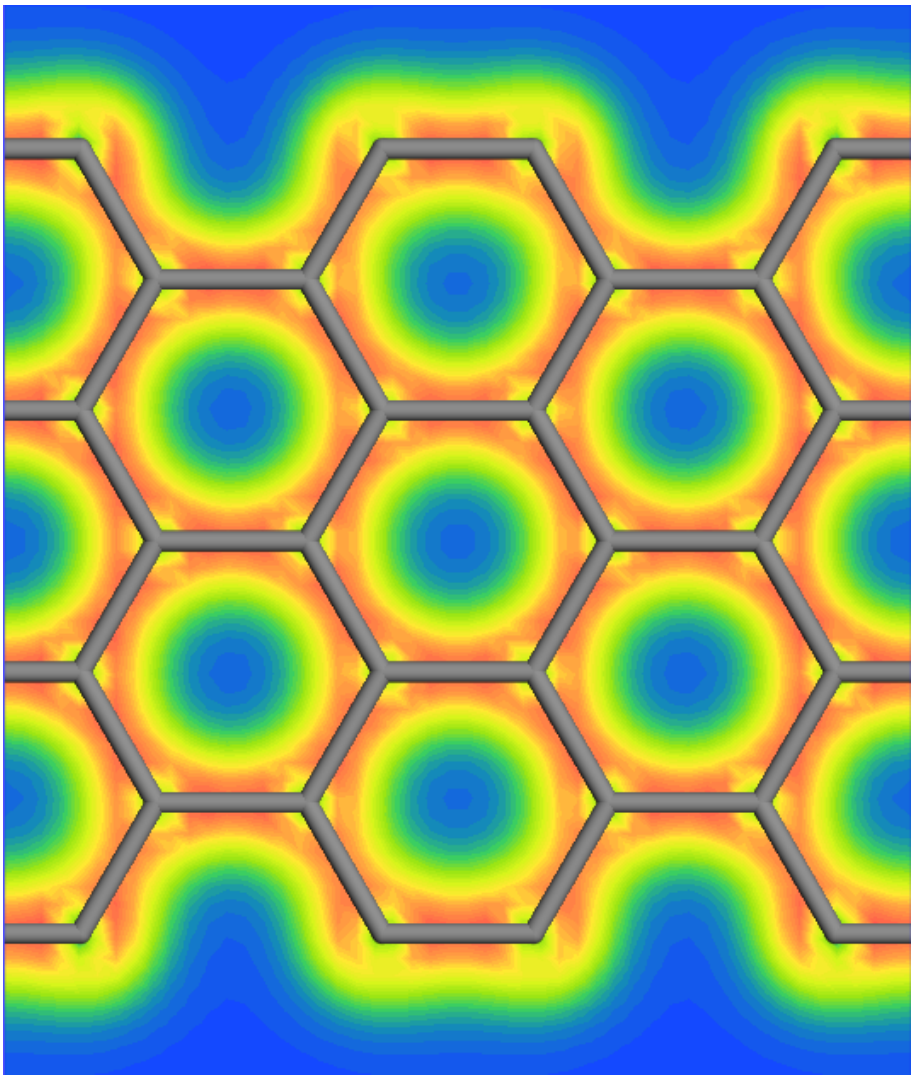

This means that, regardless of the number of electrons in the system, the electron density function is only dependant on 3 variables, such as x, y, and z in a Cartesian coordinate system. In comparison, a Hartree-Fock method is dependent on 3 times the number of electrons in the system (3N)[39, Ch. 3]. Similarly in Schrödinger methods, the wavefunction $\psi(\vec{r_1}, \vec{r_2}, \ldots, \vec{r_N})$ is used, which dependent on 3N variables. This reduction in the variable space can

significantly reduce the computational load of the problem[40].

It is also important to consider the accuracy of DFT in terms of the experimental systems we wish to simulate. As DFT requires a level of numerical convergence in several calculation parameters, a researcher must balance the precision required to represent a real system against the increasing resources and time required for greater precision. This is discussed further in section 2.2.3.5. There is also the question of how accurately a DFT calculation of arbitrary precision is capable of representing the physical system, which is dependant on the exchange-correlation functional. This will be discussed in section 2.2.3.3 and 3.1 as it depends on a number of factors that must be considered, such as the type of system and the calculations that are performed. However, looking at literature for solids[41] and our previous research[42], the PBE-WC functional accurately represents the perovskite system we are studying.

The ab-initio nature of the DFT, the accuracy that can be attained, and the advantage over other quantum methods make this methodology ideal for performing many accurate calculations within a reasonable time in order to study the desired piezoelectric systems.

2.2.2 The Schrödinger Equation and Electron Density

2.2.2.1 Schrödinger Quantum Mechanics

Electrons behave as quantum particles and are therefore governed by the Schrödinger equation (shown in 2.9) where the first term is the kinetic energy of the system, V is the potential, and E is the total energy. In an atomic system the potential V represents coulombic repulsions between each of the

objects, and therefore grows exponentially to the number of objects in the system.

$$-\nabla^2 \frac{\hbar^2}{2m}\psi(\vec{r}) + V(\vec{r})\psi(\vec{r}) = E\psi(\vec{r}) \tag{2.9}$$

Or equivalently,

$$\hat{H}\psi(\vec{r}) = E\psi(\vec{r}) \tag{2.10}$$

In the second formulation the Hamiltonian $\hat{H}$ contains the kinetic and potential energy operators acting on the wavefunction, and may be considered a matrix in certain formulations of quantum physics.

By transforming the Schrödinger equation into radial coordinates it is possible to solve for a hydrogen atom containing a single electron. The probability density of an electron being in the infinitesimal region $r = (\delta x, \delta y, \delta z)$ is given as $\rho(\vec{r}) = \psi^*(\vec{r})\psi(\vec{r}) = |\psi(\vec{r})|^2$ and the probability is the integral of this over the region is given by equation 2.11.

$$P(\vec{r}) = \int\limits_{(\delta x, \delta y, \delta z)} |\psi(\vec{r})|^2 d\vec{r} \tag{2.11}$$

This is normalised so that over all (x,y,z) the probability of finding an electron is given by $P = \int |\psi|^2 d\vec{r} = 1$, i.e. the electron exists with certainty somewhere in space. When a larger number of electrons are included however, the equation becomes unsolvable analytically due to the interactions between electrons. In order to deal with a larger system, a many-body wavefunction Ψ must be introduced to take into account all of the electrons in the Schrödinger equation. However, as electrons are charged fermions they must interact with each other.

These interactions appear in the many body wavefunction as exchange and correlation energy, making the wavefunction more complicated as each new electron is added[37, Ch. 3]. This means that this wavefunction cannot be represented as a combination of wavefunctions, i.e. $\Psi \neq \psi_1\psi_2 \dots \psi_N$. In a many-body wavefunction, the probability of finding an electron in an arbitrary infinitesimal region is given by equation 2.12.

$$P(\vec{r}) = \int\limits_{(\delta x,\delta y,\delta z)} |\Psi(\vec{r})|^2 d\vec{r} \tag{2.12}$$

This equation is virtually identical, due to the fact that electrons are indistinguishable particles. Therefore although this equation gives the probability of finding an electron, it is impossible to discern individual probabilities for each electron from the many-body wavefunction. Note that as electrons are charged fermions it is not possible for more than one electron to occupy this space, therefore the probability would be $0 \leq P \leq 1$ as expected.

While this is not solvable exactly, numerical approximations can be made using high power computing. Though this is accurate, it scales poorly due to the complexity of interacting particles[43]. In order to study systems with many electrons, we require a method that requires fewer variables and is able to be scaled to much larger systems of electrons.

2.2.2.2 Born-Oppenheimer Approximation

Before continuing we must consider an important approximation to be made in the formulation of quantum theories about electronic structure, the Born-Oppenheimer (adiabatic) approximation. This is the approximation that the nucleus of an atom is much heavier and much slower than the electrons. In

the kinetic term of the Schrodinger equation, this makes $\frac{1}{M_{nucleus}}$ negligible, as this will be $10^{-4} - 10^{-5}$ times smaller than the kinetic terms for the electrons. Additionally as the nucleus moves, the electrons keep up with it as they are coupled and it is moving so much more slowly, hence the name adiabatic. This means that instead of treating the movements separately, the nucleus can be effectively ignored as its movement is incorporated into electron paths[37, Ch. 3].

2.2.2.3 What is a functional?

A functional is a relatively simple mathematical object used frequently in applications of variation calculus and perturbation theory. It is a function that acts on a vector space, e.g. the electron density function, to map the space to a real number[44]. It is usually denoted with a capital letter and square brackets around the function it acts on. For example if you were to have a vector space function $t(\vec{r})$ that mapped the thermal energy of each point in a room, then a functional $T[t(\vec{r})]$ would return the temperature of the room as a scalar number.

2.2.2.4 Electron Density, Hohenberg-Kohn Theorems, and Kohn-Sham Equations

The principle of using an alternate form to the wavefunction was originally introduced in 1928 by Fermi[45]. He defined the electron density function, or the number of electrons per unit volume at $\vec{r}$ as shown in equation 2.13, where $p_0(\vec{r})$ is the maximum momentum in phase space.

$$n(\vec{r}) = \frac{8\pi}{3h^3} p_0^3(\vec{r}) \tag{2.13}$$

Defining the electron density in this way gives an obvious connection immediately to the wavefunction. Over an infinitesimal element $(\delta x, \delta y, \delta z)$ the electron density actually gives the probability of finding an indistinguishable electron in the region. Therefore we see that the two quantities can be related through equation 2.14.

$$n(x,y,z) = P(x,y,z) = \int_{\delta x,\delta y,\delta z} |\Psi(\vec{r})|^2 d\vec{r} \tag{2.14}$$

Although the introduction of electron density was an important step in quantum chemistry, Thomas-Fermi theory was fundamentally too inaccurate to be usable as bonds were highly unstable and did not find equilibrium in even basic examples[46]. An overview of Thomas-Fermi theory up to 1957 is provided by March (1957)[47].

The formation of density functional theory began with Hohenberg and Kohn in 1964[48]. In this, the Hamiltonian is broken down into a kinetic, external potential, and coulomb potential term such that $\hat{H} = \hat{T} + \hat{V} + \hat{U}$. Then the ground state electron density is defined in terms of the ground state wavefunction as in equation 2.15, where Ψ is the total ground state wavefunction.

$$n(\vec{r}) = (\Psi, \psi^*(\vec{r})\psi(\vec{r})\Psi) \tag{2.15}$$

The first of the two Hohenberg-Kohn theorems is proved, that the external potential is a unique functional of the electron density function. That is, that each ground state electron density corresponds to exactly one external potential (plus a constant) and vice versa. The second Hohenberg-Kohn theorem is then proved. There is an energy functional dependant solely on $n(\vec{r})$ that gives the ground state energy when minimised, and at this minimum energy

there is a unique ground state density $n_0(\vec{r})$. This allowed the rewriting of the Schrodinger equation shown in 2.9 into a functional based on the electron density function as in equation 2.16.

$$E[n] = \int v(\vec{r})n(\vec{r})d\vec{r} + \frac{1}{2}\int \frac{n(\vec{r})n(\vec{r^*})}{|\vec{r} - \vec{r^*}|}d\vec{r}d\vec{r^*} + G[n] \tag{2.16}$$

This expression can be broken down into its constituent terms. The first integral is the effect of the external (nuclear) potential on the electron density. The second is the coulomb repulsion between a pair of points $\vec{r}$ and $\vec{r^*}$ for all pairs of points, and the final term G[n] is a functional for the final components of the energy, including kinetic terms and the exchange and correlation of the electrons. This gives us an equation for energy based entirely on the electron density function $n(\vec{r})$, two theorems as to the relation between the external potential, the total ground state energy of the system, and the electron density function, and an insight into the exchange-correlation functional.

The equations necessary for density functional theory come from Kohn and Sham (1965)[49]. Beginning with equation 2.16, the G[n] functional is broken down such that it is made up of the kinetic energy of a non-interacting system of electrons with density $n(\vec{r})$ and the exchange-correlation energy as in equation 2.17. It should be noted that due to the Hohenberg-Kohn theorems this kinetic energy is also unique to a density functional, and vice versa. Additionally, due to the Born-Oppenheimer approximation the kinetic energy of the nuclei can be safely ignored, leaving only the electron kinetic energy. In wavefunction terms, the ground state wavefunction of the system of non-interacting particles can now be represented as a product of the one-electron wavefunctions, i.e. $\Psi = \psi_1\psi_2 \ldots \psi_N$.

$$G[n] = T_s[n] + E_{xc}[n] \tag{2.17}$$

There is no exact expression for E_{xc} for an arbitrary $n(\vec{r})$, however if the electron density varies slowly then the exchange-correlation energy can be approximated by equation 2.18.

$$E_{xc}[n] = \int n(\vec{r})\epsilon_{xc}(n(\vec{r})) \tag{2.18}$$

In this equation, ϵ_{xc} represents the exchange-correlation energy of a single electron in a homogeneous electron gas. This is effectively the first exchange-correlation functional in DFT, the Local Density Approximation (LDA). This is shown to be more accurate than the Thomas-Fermi method and better than the Hartree-Fock method, another method of determining electronic structures and energies.

By combining this method with Hartree-Fock, the Kohn-Sham equations are formed, shown as equations 2.19 and 2.20. While based on the Hartree-Fock equations[50], these take into account correlation effects of electrons, whereas previous theories did not. The term μ_{xc} denotes the chemical potential of the homogeneous electron gas.

$$E = \sum_{1}^{N} \epsilon_i - \frac{1}{2}\iint \frac{n(\vec{r})n(\vec{r'})}{|\vec{r} - \vec{r'}|} d\vec{r}d\vec{r'} + \int n(\vec{r})[\epsilon_{xc}(n(\vec{r})) - \mu_{xc}(n(\vec{r}))]d\vec{r} \tag{2.19}$$

$$\begin{aligned} E = \sum_{1}^{N} \epsilon_i - \frac{1}{2}\iint \frac{n(\vec{r})n(\vec{r'})}{|\vec{r} - \vec{r'}|} d\vec{r}d\vec{r'} + \frac{1}{2}\iint \frac{n_1(\vec{r}, \vec{r'})n_1(\vec{r'}, \vec{r})}{|\vec{r} - \vec{r'}|} d\vec{r}d\vec{r'} \\ + \int n(\vec{r})[\epsilon_{xc}(n(\vec{r})) - \mu_{xc}(n(\vec{r}))]d\vec{r} \end{aligned} \tag{2.20}$$

An accurate exchange-correlation functional allows the mapping of a non-interacting system of electrons, which is an easy problem to solve, to a real system of interacting electrons that we wish to study. Although estimating the exchange-correlation energy can never be exact, this simplification allows

much more complicated systems to be studied. Density functional theory has continued to evolve around the principles of the Kohn-Sham equations. As most of the terms in the equations are exactly solvable, most development has gone towards better functionals to calculate the exchange-correlation energy.

2.2.3 Modern DFT and CASTEP

Although it is possible to find solutions to Kohn Sham equations for simple systems, the practicality of doing so for more realistic, more complicated systems has led to the implementation of DFT codes to solve the equations in a self-consistent manner. Many codes are available and have different strengths and weaknesses that must be considered for the purposes of research. A few examples are given below.

- All electron codes such as Wien2k[51] and Elk[52]. All electron codes tend to be the most accurate as they take into account the full electronic structure. However, in order to do so they must perform calculations for every electron, making them expensive.

- Plane wave pseudopotential codes such as VASP[53] and CASTEP[54]. Core electrons have no direct effect on chemical properties, so instead a pseudopotential is used that treats the nucleus and core electron as a single ion acting on the outer electrons. This drastically reduces the number of electrons that must be considered for larger atoms, and can be used to simplify the coulomb potential and wavefunction that must be considered within the atomic radius of the atom. Though much faster, the accuracy of these methods depends on how accurately the pseudopotential models the real potential at the distance required[55].

- Linear scaling code such as ONETEP[56]. Most DFT codes scale such that the time taken per calculation is proportional to the number of electrons cubed, i.e. $T = O(N^3)$. This is not a requirement of the fundamental DFT however, and it is possible for calculations to be performed where the time taken is linearly dependant on the number of electrons. This approach makes large structures, such as bioparticles and nanoparticles feasible to model. However linear scaling is new and codes are generally untested and inefficient for small systems.

In this research the CASTEP code was used for its speed, reliability, and support. This is a plane wave pseudopotential code developed by a team of UK academics and distributed freely to academics in UK and Europe. It is reported that CASTEP is used in hundreds of publications per year, with over 900 in 2013[57].

By using DFT, we can calculate a huge range of material properties such as[58]:

- Energies and enthalpies of electronic systems.
- Structural properties, such as lattice parameters and atomic positions.
- Vibrational and thermodynamic data.
- Polarisability and permittivity.
- Data for comparison with experimental techniques, e.g. SEM, TEM, NMR, AFM, IR, and Raman.

FIGURE 2.7: The .param and .cell files for a single point energy CASTEP calculation of tetragonal barium titanate using the WC functional.

```
comment : CASTEP calculation from Materials Studio
task : SinglePoint
write_bib : false
xc_functional : WC
spin_polarized : false
opt_strategy : Speed
page_wvfns :        0
cut_off_energy :      300.0
grid_scale :        2.000000000000000
fine_grid_scale :         4.000000000000000
finite_basis_corr :         0
elec_energy_tol :   5.000000000000000e-007
max_scf_cycles :      100
fix_occupancy : true
metals_method : dm
mixing_scheme : Pulay
mix_charge_amp :         0.500000000000000
mix_charge_gmax :         1.500000000000000
mix_history_length :       20
nextra_bands : 0
calculate_ELF : false
calculate_stress : false
popn_calculate : false
calculate_hirshfeld : false
calculate_densdiff : false
pdos_calculate_weights : false
num_dump_cycles : 0
```

```
%BLOCK LATTICE_CART
        3.967327115886681       0.000000000000000       0.000000000000000
        0.000000000000000       3.967327115886681       0.000000000000000
        0.000000000000000       0.000000000000000       4.045658089107300
%ENDBLOCK LATTICE_CART

%BLOCK POSITIONS_FRAC
  O   0.500000000000001   0.500000000000001  -0.0107705985204039
  O   0.500000000000001   0.000000000000000   0.4998914429614780
  O   0.000000000000000   0.500000000000001   0.4998914429614780
 Ti   0.500000000000001   0.500000000000001   0.5311314180355140
 Ba   0.000000000000000   0.000000000000000   0.0158562945619357
%ENDBLOCK POSITIONS_FRAC

KPOINTS_MP_GRID 4 4 4

SYMMETRY_GENERATE

FIX_COM : false
%BLOCK IONIC_CONSTRAINTS
%ENDBLOCK IONIC_CONSTRAINTS

%BLOCK EXTERNAL_EFIELD
    0.0000000000     0.0000000000     0.0000000000
%ENDBLOCK EXTERNAL_EFIELD

%BLOCK SPECIES_POT
       O  O_00PBE.usp
      Ti  Ti_00PBE.usp
      Ba  Ba_00PBE.usp
%ENDBLOCK SPECIES_POT
```

2.2.3.1 A CASTEP Calculation

The basic CASTEP calculation requires 2 files to input the necessary data, as shown in figure 2.7. The .cell file contains information about the physical system and includes material information such as atomic positions and symmetry, any constraints or restrictions on the system, and the choice of pseudopotential to be used. The .param file contains the practical information on the calculation such as the type of task to be performed, the numerical limits and convergences, and the algorithms to be used. Although not true for all codes, CASTEP has coded into it a set of default values for almost all of the parameters for the calculation. This means that a calculation can be run with very little input from the user. The only quantities that must be specified are:

- Lattice parameters and atomic coordinates – Essentially the calculation must be told what the material of interest is.
- Task – The type of calculation desired must be specified.

- Exchange-Correlation (XC) Functional – As seen in section 2.2.2.4 the exchange-correlation functional is pivotal to the Kohn-Sham equations, therefore selecting the most suitable one is important as there is generally no correct answer.

Although it can be run with default settings, it is highly recommended that thought and testing is put into the relevant aspects of the calculation to ensure that the results are precise enough to be useful. Although there are specific parameters that must be tailored to individual tasks, in general there are four that are central to the DFT calculation; the exchange-correlation functional, the pseudopotentials, the plane wave energy cut off, and the Monkhorst-Pack grid.

2.2.3.2 Bloch's Theorem

Any measurable quantity of a material will contain a huge number of particles, with just a few grams being made up of $\approx 10^{22}$ atoms. To calculate the properties of the material by considering all the electrons would be impossible. Instead we apply crystallography, and the concept of periodicity. We know that many materials, including the piezoelectrics we are considering such as BTO, can be represented by a small unit cell repeated many times. What Bloch's theorem tells us is that for a periodically repeating system of atoms, the electron density and wavefunction are also repeating with the same periodicity. This allows the calculation to be reduced significantly and makes the computational problem possible to solve. However, it removes any larger scale effects such as grain or domain properties as the system is not large enough to model these.

2.2.3.3 The Exchange-Correlation Functional

As this is fundamental to the Kohn-Sham method, the exchange-correlation (XC) functional must be chosen carefully. Each one has different advantages and disadvantages depending on the type of system to be studied and picking the most suitable is not always obvious. There are categories of XC-functional which depend broadly on the complexity of the functional; LDA, GGA, meta-GGA, and hybrid.

- The local density approximation (LDA) or local spin density approximation was the approximation made by Kohn and Sham in their original paper[49]. Many simple solids can be considered close to a homogeneous electron gas, therefore in the LDA the energy is the integral over the volume for a homogeneous electron gas of the given density[37, Ch. 8]. This is shown in equation 2.21.

$$E_{xc}^{LSDA}[n^{\uparrow}, n^{\downarrow}] = \int n(\vec{r})\epsilon_{xc}^{hom}(n^{\uparrow}(\vec{r}), n^{\downarrow}(\vec{r}))d\vec{r} \tag{2.21}$$

  As the energy is based only on the density position (hence local) this is the simplest. However, this functional is only suitable for simple materials that can be approximated to the homogeneous electron gas. It is not suitable for materials with rapidly varying electron density. It also cannot take into account extra bonding such as hydrogen or van-der-waals. It also tends to overbond materials, predicting lower bond lengths and lattice parameters than expected.

- The generalised gradient approximation (GGA) was first suggested in Kohn and Sham's original paper, and expanded on further by Herman, F. et al. (1969)[59]. In this method the XC-energy is based on both

the electron density at a point and its spatial derivative. This allows for corrections not previously possible, and preserves the desired properties. The most widely used GGA is the Perdew-Burke-Ernzerhof (PBE) functional, often used as it can provide good performance over a wide range of calculations and materials[60]. They give the general equation for a GGA as in equation 2.22, where f is a parametrised, analytic function.

$$E_{XC}^{GGA}[n_\uparrow, n_\downarrow] = \int f(n_\uparrow, n_\downarrow, \nabla n_\uparrow, \nabla n_\downarrow) d\vec{r} \tag{2.22}$$

Many GGAs have been proposed, and at least 5 are supported by the CASTEP code. Although the PBE functional is broadly the most representive across all types of material, each functional has a different specialisation that makes it more suitable for specific types of systems. For instance, the exchange-correlation functional used in this work is the WC functional created by Wu and Cohen (2006)[41], a modification of the PBE functional with more accuracy for solid materials. In this paper they demonstrate that their functional accurately predicts the properties of many simple materials, as well as the tetragonal form of PTO and the rhombohedral form of BTO. In addition to this, in our previous work we have compared the PBE and WC functionals for predicting the phase stability of BTO, with the results shown in figure 2.8. It was found that the WC functional correctly reproduced the themal ordering of all five phases, and was more reliable in finding identical minima for identical structures[42].

GGAs strike an excellent balance between performance and accuracy, and are therefore widely used. However in contrast to LDA they tend to underbind materials, often making the bonds and lattice parameters slightly longer. These GGAs are still localised as they now depend on

FIGURE 2.8: A study on the relative lattice energy for the five phases of barium titanate, using the PBE and WC functionals[42].

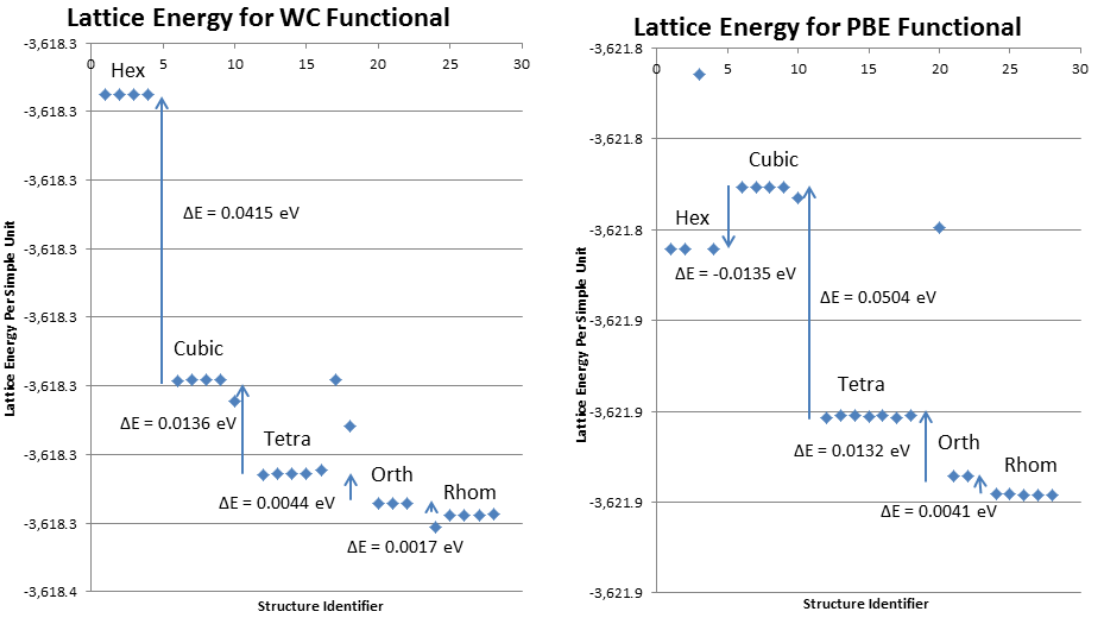

the function and it's gradient at each point. As with most DFT methods, they are unable to calculate the bandgap of materials accurately.

- Meta-GGAs are a class of functional that incorporate the kinetic energy density of occupied Kohn-Sham orbitals into the GGA formulation. The additional complexity of the functional makes it more accurate, with the TPSS functional reported as being uniformly accurate across diverse systems and properties[61].

- The final type of functional is the hybridised functional. These functionals combine the orbital-dependent Hartree-Fock approach with density functional theory to create highly accurate functionals[37, Ch. 8]. These functionals are non-local due to Hartree-Fock contributions and generally require the most computational power. Additionally, they have been criticised for their mixing proportions being chosen to suit experimental

data[58], and that they often excel in only one area making them unfit for general purpose[61].

Clearly then selecting a functional is not a trivial task, and thought and review must be put into this choice. Literature searches and speaking with other researchers in the field are generally the best way to select the most suitable functional for the system.

2.2.3.4 Pseudopotentials

We know that only valence electrons take part in the bonding of molecules and structures; however they are influenced by the potential from both the nucleus and the surrounding core electrons. The core electrons create a wavefunction that does not affect bonding but requires a higher energy cut-off, discussed in section 2.2.3.5, and for DFT to have to consider a larger number of electrons. In the ground state, there are no excited electrons and therefore electrons below the valance level do not need to be considered, except to account for the screening effect from the nuclear potential. Therefore, if the effects of the core electrons and the nucleus can be combined into a form that does not contain the complexity of the core states then the number of electrons that must be calculated is reduced, and the energy cut-off is lowered[55].

For this purpose, Phillips and Kleinman (1959)[62] introduced the concept of a pseudopotential. This method allowed the combination of the simplicity of the previous tight binding approximation within the core electrons with the accuracy of plane waves for valance electrons. Figure 2.9 shows an approximation of the wavefunction and potential for all electrons (AE) and the pseudopotential (PS) as a function of distance from the nucleus to demonstrate the differences[63].

FIGURE 2.9: Illustrative differences between the actual wavefunction and energy potential, and the pseudopotential approach as a function of distance from the centre of the atom. The value of r_{cut} is the core radius of the filled electron bands, and is different for every atom and core electron configuration[63].

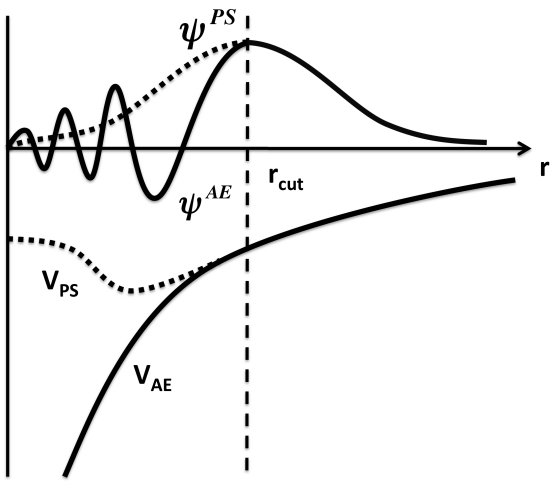

We see that the new potential is less steep and is not asymptotic, and the wavefunction has been greatly simplified. This allows the atom to be described using a much lower plane wave energy cut-off. However, at the core radius the all-electron and pseudopotential converge, generating effectively the same external potential on the valance electrons.

In reality some accuracy is lost in this approximation of the potential and wavefunction. All electron codes, especially WIEN2k, are commonly used as a baseline to test pseudopotentials against. The Center for Molecular Modeling at Ghent University maintains a list of $\Delta-values$ that allows code performance to be approximately compared[64]. Although this does not take many factors into account such as the speed of the calculations, the numerical accuracies and libraries of the system, and the improvements made by specific functionals to certain types of material, this can be used as a rough guide to determine how codes compare. On this list CASTEP has a $\Delta-value$ of 0.5meV/atom against

WIEN2k, an acceptable deviation when the improvements to calculation speed and resources required are considered.

Generally speaking, two types of pseudopotential are used in an ab-initio framework; norm-conserving and ultrasoft. Norm-conserving pseudopotentials were originally formulated by Hamann, et al. (1979)[65]. In this, Hamann stated 4 requirements for the pseudopotential:

1. The real and pseudo eigenvalues of the valance electrons should agree for a given prototype atomic configuration.
2. The real and pseudo wavefunctions agree for a distance r greater than a chosen core radius r_c.
3. The integral from 0 to r of the real and pseudo charge density for each valance electron should agree for any $r > r_c$.
4. The logarithmic derivatives of the real and pseudo wavefunctions and their first derivatives of energy agree for $r > r_c$.

Property 1 and 2 are a basic requirement of any pseudopotential as shown in figure 2.9. Property 3 is the norm-conservation requirement and can be expressed mathematically as equation 2.23, with $\rho(r)$ to represent the charge density.

$$\int_0^r \rho(r)_{AE} dr = \int_0^r \rho(r)_{PS} dr, \forall r > r_c \tag{2.23}$$

Effectively what this means is that if we assume property 2 is held, then the integral of the wavefunction and the pseudowavefunction up to the core radius is equal. When subjected to the normalisation requirement that $\int |\psi|^2 d\vec{r} = 1$ across all space, the normalisation factor will be identical for both forms of the wavefunction. Hence the pseudopotential is norm-conserving. These conditions allow for the creation of pseudopotentials that may be used generically

for a variety of chemical environments. Additionally in the CASTEP code we are using, these pseudopotentials are required for the density functional perturbation theory (DFPT) vibrational calculations. Though this method is limited to specific material types and pseudopotentials, if it can be used it is a much less resource intensive calculation as it does not require the superstructure of an equivalent finite displacement calculation.

The ultrasoft pseudopotential was introduced by Vanderbilt (1990)[66] as a way to further improve the transferability of the pseudopotentials between different chemical environments and further reduce the plane wave cut-off energy required. The hardness of a pseudopotential is a measure of the gradient of the pseudopotential in the core region, which increases the requirement for higher energy cut-offs. Although norm-conserving pseudopotentials do alleviate some of these requirements, the strict norm-conservation means that some orbitals such as O 2p still require a wavefunction similar to the all electron form. If the norm-conservation is discarded, the wavefunction may be simplified significantly while still agreeing with an all electron method for $r > r_c$. This development allowed pseudopotentials to be created for lithium row elements and scandium row transition metals to be developed that required significantly lower plane wave cut offs for a reasonable precision.

The lowering of computational requirements, along with the development of the generalised gradient functions later in the decade, significantly boosted the popularity of DFT in fields such as materials science and quantum chemistry.

There is another type of pseudopotential used in certain studies, the projector augmented-wave pseudopotential (PAW)[67]. In literature these are occasionally referenced, however have not received widespread recognition as they are only used with the VASP code. As they are not relevant to CASTEP, the software we are using, we will not discuss them. However if they are used, they

can be considered to be a different mathematical formulation of the ultrasoft pseudopotential, and have the same advantages and disadvantages.

In cases where either type of pseudopotential may be used, the decrease in plane wave cut-off makes ultrasoft pseudopotentials a better choice as this reduces the calculation time required. CASTEP contains a function to generate new pseudopotentials at the beginning of a calculation, developed by Cocula et al. (2005)[68]. These "on the fly" pseudopotentials are the most up to date and are recommended by the code developers.

2.2.3.5 Plane Wave Energy Cut-Off

The plane wave energy cut-off is one of the two most important numeric aspects to the calculation. Along with the Monkhorst Pack grid, this must be carefully selected to ensure that the computational system resembles the physical system as closely as possible while using the minimum amount of computational power.

As we are dealing with pseudopotentials rather than dealing with an actual wavefunction, the electrons are described instead by a pseudowavefunction based on the wave vectors, and an expansion in a new vector called G-vectors ($\vec{G}$). These G-vectors make up the basis set of the quantum equation. The form of the pseudowavefunction is given in equation 2.24[39, p. 137].

$$\phi_{\vec{k}}^{PS}(\vec{r}) = \frac{1}{\sqrt{\Omega}} \sum_{\vec{G}} c_{\vec{k}+\vec{G}} exp[i(\vec{k}+\vec{G}) \cdot \vec{r}] \tag{2.24}$$

Where $\vec{k}$ is the wave vector, c is the weighting, and Ω is a normalisation. These G-vectors are an infinite basis set, much like the harmonics of a string. Low energy terms dominate with higher energy terms having a decreased weighting. As it would be impossible to calculate the infinite set, we use the fact that low

energies dominate in order to define a plane wave cut off. The energy cut off is defined according to equation 2.25[39, p. 145].

$$E_{cut} = (\frac{\hbar^2}{2m_e})G^2_{max} \tag{2.25}$$

The constant factor at the beginning of this term comes directly from the kinetic energy in the Schrödinger equation, hence the proper name kinetic energy cut-off, and G^2_{max} is the square modulus of the maximum energy G-vector.

This is purely a pseudopotentials requirement, as it determines how accurately the pseudowavefunction fits the real wavefunction of the ions. The smoother a pseudopotential is in its core region, the fewer plane waves are required to describe it. Therefore in general different states of the same material have the same energy cut-off requirement.

In practice this is done by converging to a value of E_{cut} to some quantity known as the figure of merit. This is commonly energy differences between structures, but other simple quantities that can be calculated using a single point energy task would also be suitable such as convergence of forces. When the difference in this figure of merit between successive values of the energy cut-off, corresponding to the addition of higher energy plane waves, is below a predetermined value the system is considered converged. This predetermined value must be decided beforehand depending on the type of calculation. For instance, if the difference in energy between two structures is expected to be a few meV from thermodynamics, experimental data, etc., then the convergence of this energy should be $< 1meV$ to ensure that variations due to the precision of the pseudowavefunction are not greater than the quantity that the user wishes to study.

FIGURE 2.10: The scaling of time against the plane wave cut-off energy for various phases of barium titanate. Each pair of lines for the different phases is marked with the number of k-points and number of processing cores used for each of the calculations.

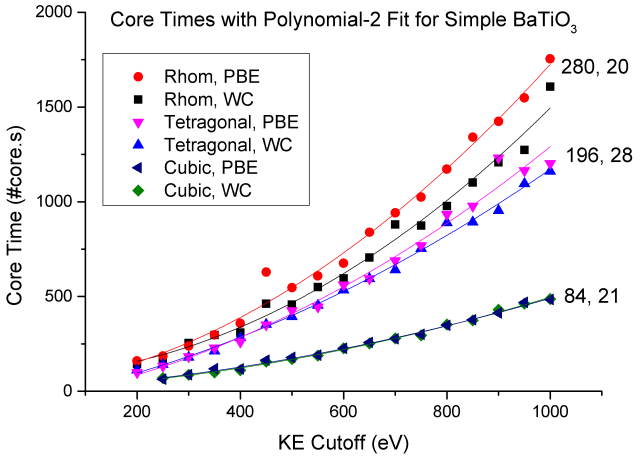

From our previous work[42] we know that the scaling of the time taken for increasing plane wave cut-off is of order $O(E_{cut}^2)$, however communications between cores and other values may interfere with that. Figure 2.10 shows the quadratic relation between the core time and the plane wave cut-off for different phases of barium titanate corresponding to different fixed Monkhorst-Pack grids.

While the cut-off is usually reported in electron-volts, publications may list it in Rydbergs ($13.6eV$) or Hartrees ($27.2eV$) instead.

2.2.3.6 Monkhorst-Pack Grid

While we often consider the atomistic, real structure of materials, DFT calculations generally do not occur on this form. Instead, the structure is transformed into reciprocal space using a fast-Fourier transform method (FFT). This reciprocal space is referred to as the Brillouin Zone (BZ). In general, the larger the

FIGURE 2.11: An image of the 3-dimensional Brillouin Zone for an FCC material, showing the points of high symmetry.

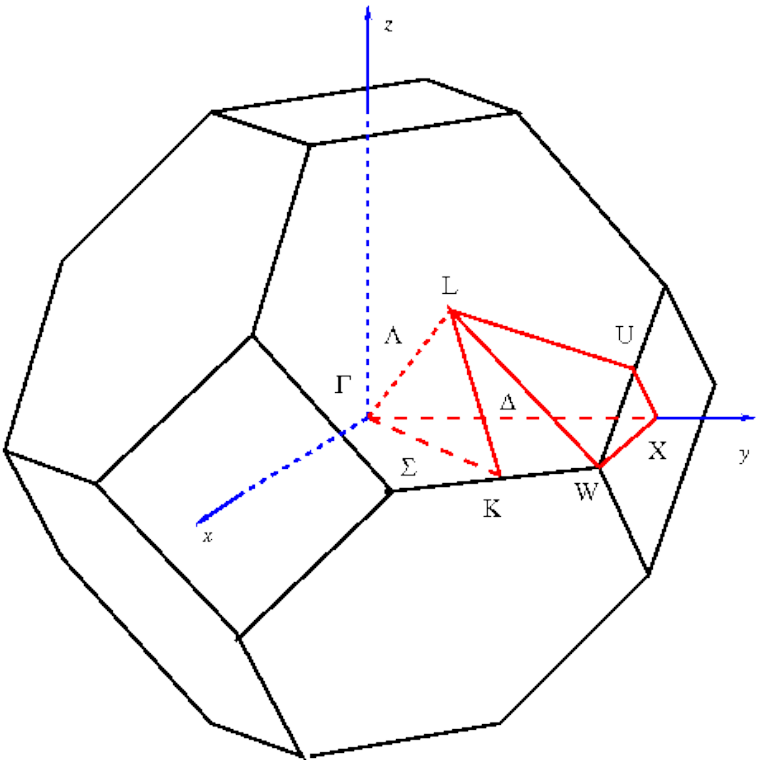

real space cell is the smaller its BZ will be, as for a simple cell without symmetry the lattice vectors are given by $\vec{a^*} = 2\pi/\vec{a}$. The shape of the Brillouin Zone is affected by the symmetry of the structure, with unusual shapes being produced by otherwise regular crystal structures. For instance, figure 2.11 shows the Brillouin zone for a face centred cubic material such as aluminium[69].

We see in the figure that several locations are marked with special designations. These are known as points of high symmetry and those which are present are unique to different lattice types. The centre point however, is the most important. This is known as the gamma point ($\Gamma - Point$) and is located at $\vec{k} = (0, 0, 0)$. This is the point of highest symmetry and allows the symmetry of the structure to be retained. This allows us to draw paths between the other points of high symmetry and construct an irreducible Brillouin Zone,

FIGURE 2.12: The scaling of time against the number of points on an axis of the Monkhorst-Pack sampling grid for different phases of barium titanate.

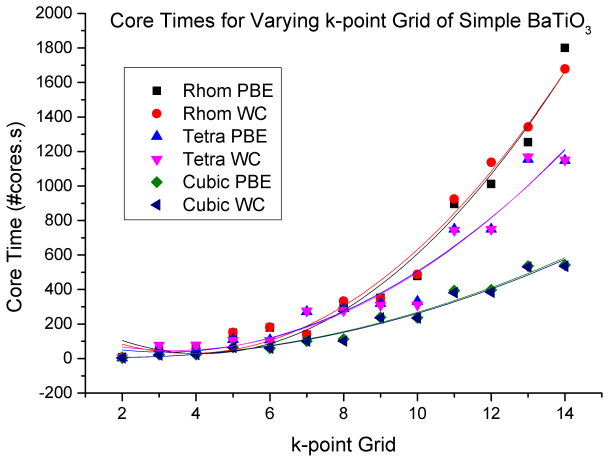

which is smaller and therefore less computationally expensive to calculate. The $\Gamma - Point$ is unique as all optical phonon modes are real and positive.

While to get the 'true' energy of the system requires a continuous function over the Brillouin zone, such a scheme is not possible analytically or numerically. Instead it is sampled by a discrete mesh of points known as the Monkhorst-Pack grid, with each discrete point known as a k-point. The scheme for selecting points for this grid was first published by Monkhorst and Pack (1976)[70]. Using the points of high symmetry to determine the irreducible Brillouin zone leads to a reduction in the number of k-points required, as symmetrically identical k-points are combined into a single k-point with a higher weighting.

The time scaling for these points is of order $O(n_k^2)$, where n_k is the number of points in the irreducible Brillouin zone. This is shown in figure 2.12 from our previous work[42].

We see that while the points are plotted in terms of the total sampling, all structures follow a quadratic, with the high symmetry phases that require a

smaller irreducible BZ having a much shallower gradient than the low symmetry ones. The scaling is less clear for this. This is due to the fact that discrete k-points can be parallelised across for calculations, which allows the calculation speed to be greatly increased. This is often done automatically, depending on the code. However communication time between cores becomes an issue, as between cycles every core will have to wait for the data from all others, which in a highly distributed system can take a long time.

2.2.3.7 Phonons

A phonon is a quantisation of vibrational normal modes in a lattice[71, p. 287]. Phonons are one of the most important quantum mechanical properties of a material. They act as a coupling phase between phonon and photon interaction, such as in IR spectroscopy, couple the electric and vibrational properties in the effective ionic charge, and are a determining factor in the phase change of ferroelectric materials. This is only the basics of how we use phonons in this study, in truth they are a driving force behind many common and esoteric properties of solids, from determining the thermal conductivity to the formation of superconductive states.

Phonon dispersions are a property of any solid material with a periodic structure, as a basic property of the fact that atoms are non-static and vibrate in their positions. These vibrations are considered as a moving wave through the material carrying energy. Of course, due to the periodicity, mass, and bonding of the displaced atoms, there are not a wide spectrum but instead discrete modal frequencies for each lattice. Most important is the scattering capability of these waves. The wide range of modes a lattice is capable of holding allows us to make a distinction between acoustic (low-frequency) and optical (high

frequency) phonon modes. This range of frequencies allows scattering interactions across the spectrum with other phonons, electromagnetic waves, and particles, providing they contain a matching harmonic/anharmonic mode. The phonon dispersions and interactions are far too broad to cover in this work, as we are only using them as a means to an end as a way to calculate other properties. However, they are covered extensively in any solid state physics text, such as Patterson and Bailey[72].

2.2.3.8 Effective Charges

The Born Effective Charge, or Effective Ionic Charge, is defined as the change in polarisation relative to the displacement of an ion[73]. This is a 3×3 rank-2 tensor, as while it is obvious that a displacement in an axis direction will result in a change in polarisation in that direction, it also accounts for a polarisation change in other directions that occur. There is a distinction between the formal charges on an ion, and the effective charge on the same ion. In formal charges we consider electronic occupation of valence states or ionic sites. While this provides a simple set of rules for chemical bonding, it is not possible to clearly determine which electrons in a bond belong to which ion.

This is the nature of the covalent bond, as the valence states of the partner ions overlap to share occupation of electrons. Under displacement, the formal charge does not take into account how many of the valance electrons in bonds change due to the movement of individual ions. The effective charge can be seen as the sum of the formal charge, and the additional electronic charge due to the surrounding electrons which do not formally "belong" to the ion but are perturbed by its displacement regardless.

The formal charge can be seen as a measure of covalency in a compound, which does not provide a good indicator of the piezoelectric property we are studying. By contrast, the Born Effective Charge can be seen as a measure of how the covalency changes under ionic displacement, which is fundamentally what we wish to calculate.

Born Effective Charge is implemented into all phonon capable DFT codes, largely due to how it can be implemented. It can be seen as the coupling coefficient between the electronic perturbation and phononic perturbation modes[74]. When running a DFPT linear response or displacement calculation the electric and phonon perturbations are both calculated. This means that, while we can control the output of the calculation to a file, the full set of properties is calculated, or is at least possible to calculate quickly using the wavefunction and density. Then it is obvious that the effective charge tensor is trivially calculated as the coupling between the two.

As it is defined at $\vec{q} = 0$ it can be calculated purely at the gamma point, allowing for significant memory and CPU time savings in the calculations. Through definition and study we have determined it is invariant of the k-points and inverse path, provided that the gamma point is present.

Now we have discussed the core physics and computation, we must consider how this has been used in the past, to further our understanding of the use, capability, and drawbacks of these methods.

Chapter 3

Literature Review

3.1 The Wu-Cohen Functional

Our functional of choice has been selected as the GGA-PBE with Wu-Cohen exchange, often abbreviated to WC functional. This was introduced in 2006 by Wu and Cohen as a generalised gradient approximation with a focus to improve the performance of DFT for solid structures[41]. Although this makes the functional less suitable for non-crystal systems, such as isolated molecules, when compared to the more generic PBE, for our use this new formulation is advantageous. This work builds on an earlier publication by Wu, Cohen, and Singh[75] in which the LDA, GGA-PBE, and weighted density approximation (WDA) functionals are compared in prediction of crystal structures for several perovskites. Although each has advantages, no functional was able to predict both structural and ferroelectric properties with sufficient accuracy.

In their introduction of the WC functional[41], the authors compare their new functional with the LDA, GGA-PBE, and TPSS meta-GGA functionals along with experimentally obtained structural data. Initial comparisons show that

across 18 simple structures identified in a previous study by Staroverov et al.[76], the WC functional performs well. The mean absolute relative error is calculated as a difference from the experimental values and the WC functional is found to produce an error much lower than the others in lattice constant and bulk modulus, with percentage errors of 0.29 and 3.6 respectively. When calculating the cohesive energy the functional is no worse than the PBE and considerably better than the LDA. Although in the previous paper from Staroverov et al.[76] the methodology for selecting the experimental values for comparison is not given, in Wu and Cohen the use of these values from a single source makes a selection bias in favour of the WC functional difficult.

The mathematical formulation of the functional by modification of the exchange energy in the GGA formulism is clear as it creates a diffuse tail around the exchange-correlation hole which is representative of solids. Conversely in other GGA functionals such as revPBE and RPBE, this tail has been sharpened to give better results for isolated atoms and molecules at the expense of accuracy for solid structures. As electrons are fermions they obey Pauli exclusion, which is responsible for the existence of electron shells. Effectively this means that where an electron is present there is an absence of electron density around it due to this effect, reducing the electron density beyond the classical coulombic repulsion[77]. In isolated atoms and molecules we expect this effect to be sharp, however due to the bonding in solids allowing the effect to be more diffuse greatly improves the accuracy of exchange energy for these systems.

Wu and Cohen also focus on perovskite ferroelectrics in this paper and demonstrate improvements in tetragonal $PbTiO_3$ and rhombohedral $BaTiO_3$ against PBE and LDA calculations. In the prediction of unit cell properties and fractional positions of non-symmetric atoms the WC functional outperforms the

previous functionals. Data for barium titanate has been taken from a the single source provided by Hewat (1974)[78] using neutron powder diffraction. As seen in the previous work by Wu, Cohen, and Singh (2004)[75] the functionals were unable to accurately provide both the lattice parameters and the fractional coordinates responsible for ferroelectric properties, therefore testing the new functional against a single data source shows little selection bias in comparing their theoretical results.

In modern DFT it is possible to use the hybrid functionals, which combine the local GGA functional for the exchange-correlation energy with an amount of the non-local Hartree-Fock approach in order to create a new functional. With these functionals available, we must consider if a hybrid functional is more suitable for our calculations. As hybrid functionals contain both local and non-local components, the computational cost for such calculations is greatly increased from the equivalent GGA. Therefore, even if a hybrid functional is more accurate it may not be worth the extra cost required in either the extra time taken to perform the calculations, or the necessary reduction in precision, in order to perform this type of calculation.

Table 3.1 shows a comparison between three computed values for structural properties of the rhombohedral phase of barium titanate, and their percentage difference from the experimental data. The WC data was taken from Wu and Cohen (2006)[41], the PBE0 data was taken from Mahmoud et al. (2014)[79] and Bandura and Evarstestov (2012)[80], and experimental data is from Kwei et al. (1993)[34]. None of these studies used this source for their experimental comparison, meaning that this data should not favour any of these functionals. Each value is shown with a percentage difference from the experimental data.

It is obvious that the WC outperforms the PBE0 functional in representing the structure accurately, with no greater than 10% deviation from experimental

TABLE 3.1: Comparison of calculated volume, lattice angle, and atomic positions between the WC functional and PBE0 functionals for rhombohedral barium titanate.

	WC	PBE0 2014	PBE0 2012	Expt.
$Vol.(\text{Å}^3)$	64.04 (-0.20)	64.47 (0.47)	62.03 (-3.33)	64.17
$\alpha(^\circ)$	89.86 (+0.02)	89.80 (-0.04)	89.72 (-0.13)	89.84
$\Delta(Ti_z)$	-0.0117 (-8.59)	-0.0132 (3.12)	-0.0151 (+17.97)	-0.0128
$\Delta(O_x)$	0.0116 (+6.42)	0.0232 (+112.84)	0.0129 (+18.35)	0.0109
$\Delta(O_z)$	0.0184 (-4.66)	0.0124 (-35.75)	0.0242 (+25.39)	0.0193

values. This is because of the idea of a universal functional, in which the ideal functional will be accurate regardless of the chemical environment. Whereas the WC functional is tailored towards solid structures at the expense of isolated molecules and atoms, there is a drive now to create functionals which are equally accurate across all systems. This is also true of the GGA-PBE, it is a generic functional that should maintain its accuracy across different chemical environments. This means that there has been no development of a solid-specific hybrid, as theorists designing functionals strive for greater general accuracy. While in theory this is an important goal in the advancement of DFT, in practice we see that for research in specific types of systems a greater accuracy can be achieved with a less complicated and costly functional. Although there may be need to rely on a functional such as PBE0 in the future if certain calculations require it, structural data is best optimised using the WC functional.

Additionally, it is important to note that the study for the WC functional was performed before the PBE0 studies. It is possible that inaccuracy arises due to the available computing power at the time. Due to Moore's Law discussed in chapter 1 we would expect that the computational power available would be 8 times greater in 2012 at the time of the PBE0 study, which may improve the result further due to the additional precision possible.

3.2 Calculating Properties of Piezoelectrics Using DFT

3.2.1 Structural Properties of Piezoelectric Perovskites

We know that the piezoelectric properties are created by asymmetry in the crystal structure, and that in perovskites this is also the cause of the dipole giving rise to the ferroelectric spontaneous polarisation. Therefore it is important to consider the capability of DFT in producing the relevant structural properties.

We would expect that the minimum energy state would correspond to the relaxed position, as a physical system will always attempt to take on its lowest energy state. Therefore by finding the atomic positions and lattice parameters corresponding to the lowest energy state should yield the correct ground state geometry. Most commonly used in DFT is the quasi-Newtonian Broyden–Fletcher–Goldfarb–Shanno (BFGS) algorithm, originally implemented for crystals by Pfrommer et al. (1996)[81]. As a quasi-Newtonian method it utilises a Hessian matrix of forces acting on a vector in order to create a simulated force on both the lattice parameters and the atomic coordinates. By using a gradient descent the force is minimised over many iterations until the system is numerically converged to within the preset parameters of the calculation. This method is able to preserve the symmetry of a system using the construction of the Hessian matrix, so if a symmetry is set or found the calculation will only use allowed symmetric deviations from this. Additionally, this method has been implemented in a low memory form which shows improvements for calculations on large systems.

Structural properties have been calculated for perovskite structures using this method in various papers. The most basic properties calculated are the lattice parameters, which have been well characterised experimentally using x-ray and neutron diffraction methods. These are calculated by allowing the BFGS algorithm to act on both the cell and the atomic positions, which are generally treated as separate quantities in the computation. It is possible to optimise the atomic positions without the lattice parameters, or vice versa, but in doing so there is the risk of poor ground state convergence as such constraints actually serve to make the calculation more difficult.

In order to achieve numerical convergence for the structure, additional convergence parameters must be set that are checked at the end of each BFGS cycle. These parameters can be automatically set by CASTEP, or can be manually entered into the .param file. These variables are as follows:

- Energy Tolerance (eV/atom) – The change in energy per atom of the unit cell.
- Maximum Force Tolerance ($eV/$Å) – The maximum calculated force on the atoms.
- Maximum Stress Tolerance (GPa) – The maximum calculated stress of the unit cell.
- Maximum Displacement (Å) – The maximum displacement of the ions by the optimisation force.

When all four of these criteria are met, i.e. when the code calculates that these quantities are below the set parameters, the calculation is successful and a "Final Geometry" is given. Unlike the plane wave cut-off and Monkhorst-Pack grid, these parameters do not explicitly increase the calculation time,

however generally the smaller these quantities the more cycles are required. Additionally there is a risk that a system will not be able to converge to these parameters, and they must be relaxed slightly in order to achieve the final structure. Although this task is useful in itself for optimised structural properties, it is also a necessary precursor to various other tasks, and it is important to ensure good convergence of the geometry of a cell before undertaking further tasks to ensure good results.

As this type of task is easy to perform, it is widely used and published. We saw in section 3.1 that the structural properties of the optimised cell can be used to compare and evaluate different functionals. Additionally, it is a required step in calculating the elastic and vibrational properties of the structure.

Materials showing piezoelectric and ferroelectric character, such as barium titanate, have a very fine tolerance to lattice parameters. Vanderbilt (1997)[82] states that the ferroelectric instability in $BaTiO_3$ is lost if the lattice parameter is reduced by 2%, thus the inherent error in the LDA functional of around 1% is not acceptable. We expect that our selection of the WC functional performs better, as a difference in volume of -0.20% from the sample experimental value should reflect accuracy in the lattice parameters of the computed system compared to the experimental values. Tinte et al (1998)[83] used the structural property calculations to perform modifications to the PBE functional in order to find a functional that reproduced the experimentally predicted volume. Equation 3.1 shows the form of the exchange energy for the PBE functional originally proposed by Perdew et al (1996)[60].

$$F_x = 1 + \kappa - \frac{\kappa}{(1 + \frac{\mu s^2}{\kappa})} \tag{3.1}$$

Tinte et al (1998) found that by varying the value of κ then the exchange

TABLE 3.2: Functional, plane wave cutoff, Monkhorst-Pack grid, and lattice parameters used in some computational studies on tetragonal barium titanate by Zhao, et al.[84], Long, et al.[85], and Evarestov, et al.[86]. A plane wave cutoff is not present for the Evarestov work due to a slightly different DFT method being used.

Author	Year	Functional	PW Cutoff (eV)	MP Grid	a (Å)	c (Å)
Zhao	2011	PBE	350	6^3	3.99	4.03
Evarestov	2012	PBE	-	12^3	4.01	4.19
		PBE0	-	12^3	3.97	4.14
Long	2013	PBESol	500	7^3	3.98	3.98

correlation hole can be adjusted such that the functional is more suited to the system. However, as the diffuseness of the exchange correlation hole is system dependant, selecting the correct value for κ requires a semi-empiracle approach.

Although this methodology is ultimately flawed from an ab-initio perspective, it demonstrates that the exchange-correlation hole is system dependant and that while the equilibrium structure is dependent on the way the functional handles the hole localisation, the vibrational properties are not dependent on this particular mathematical property. This lead Wu and Cohen (2006)[41] to re-evaluate equation 3.1 from a theoretical standpoint. By leaving κ and modifying the μs^2 term instead the same effect could be reached in a way that is more generic to solids, thus allowing the development of their solid-specific functional in a first principles manner.

Table 3.2 shows the details of the paper published and the lattice parameters computed.

We see that in Zhao et al. (2011)[84] and Long et al. (2013)[85] the stated Monkhorst Pack grid is fairly in line with what would be expected for ultrasoft pseudopotentials. However, as it is not clear what their convergence criteria is these values may not be properly converged. Evarestov et al. (2012)[86] do not

list a plane wave cut off as this calculation was performed with Gaussian basis sets and therefore converged in a different way that is difficult to comment on. However if we can assume that a similar convergence criterion was used for the Monkhorst Pack grid, then we assume that the calculation is strictly converged. As this optimisation is being used as a precursor to a vibrational calculation, tight convergence parameters must be used to ensure the cost of accuracy at the cost of computational power.

There are not a wide variety of sources for computed lattice structures of barium titanate, which would at first indicate a lack of interest in the subject. However for more advanced calculations it is a necessary initial step, therefore although the structures are not explicitly given this type of calculation is widely used and of great interest. We will now look at some of these more advanced calculations.

3.2.2 Band Structure Calculations of Barium Titanate

The band structure of a material is one of the most important things that can be calculated. It gives the energy of the bands in the Brillouin zone (BZ) and can mark the points of high symmetry in the lattice. The Brillouin zone is the reciprocal lattice of the primitive unit cell, and a first BZ can be defined as a Weigner-Seitz cell of the reciprocal unit to be unique. For the simplest example of a simple cubic unit cell with lattice length a, the reciprocal lattice is a cubic cell with reciprocal lattice lengths $\frac{2\pi}{a}$. By integrating over the first BZ, the energy of an electronic structure can be calculated[39, Ch. 4]. The band structure for the cubic phase of barium titanate was published by Piskunov et al (2003)[87] and is shown in figure 3.1.

FIGURE 3.1: The band structure of cubic barium titanate as calculated by Piskunov, et al.[87] using B3PW, and shows the points of high symmetry for the cubic structure.

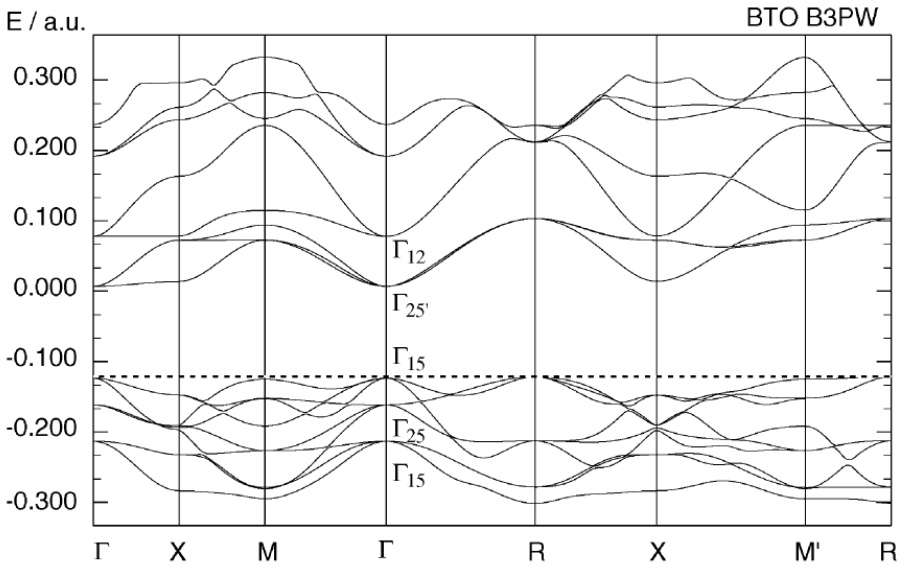

The most important property of the band structure is the band gap, which defines the conductive properties of the material at absolute zero. The band gap is the difference in the band structure between the highest valance band and the lowest conduction band in the material. In a metal there is no band gap, the bands are only partially filed and a current can be induced by the application of an electric field. In an insulator however, the bands are fully filled and there is a large gap in the band structure around the Fermi energy. Filled bands do not generate a current under electric field, and therefore an insulator cannot have an induced current. While this is true for the zero temperature material, in reality thermal excitation occurs. In materials with a small band gap of $< 2eV$ the electrons can be excited from the valance to conduction bands at room temperature and these materials are referred to as semiconductors, such as silicon[39, Ch. 4].

DFT is well known to underestimate the band gap of materials. While it can be said that it should not be possible for DFT as the band gap is an

excited state property, some argue that the band gap is the difference between two ground states and it is well within the purview of DFT to calculate such properties[88]. Currently band gaps are calculated using the hybridised DFT and Hartree-Fock functionals. Where DFT is known to underestimate the property, Hartree-Fock is known to overestimate it. Therefore more accurate band gaps should be achieved by a cancellation of errors. However this presents a definite issue in the ab initio nature of the DFT calculations, as at best this method is an approximation that can only hope to be accurate by a certain amount of luck, and at worst the HF-DFT mixing is created in such a way as to match experimental data on the band gap for already existing structures. Neither of these options fit with our aim to create a broad methodology for both experimentally characterised and unknown systems.

As barium titanate is an insulator its band structure is often not published, however its band gap is calculated and reported by many publications. Table 3.3 shows published band gaps for different phases of barium titanate using a variety of LDA, GGA, and hybridised functionals, with experimental data for comparison. Data is from Evarstov and Bandura (2012)[86], Mahmoud, et al. (2014)[79], Piskunov, et al. (2003)[87], and Wemple, et al. (1968)[89].

We see that the pure DFT functionals massively underestimate the band gap, whereas the hybrid functionals are within 1eV. In particular, the B3LYP hybrid functional calculates closest to the experimental value reported. This is to be expected, as it is a hybrid functional constructed of energy terms from both Hartree-Fock and LDA DFT for the prediction of band gaps.

It is not our intention to directly study the band structure of barium titanate; however it will likely influence many other structural and electronic properties. Therefore it is important to be aware of the issues caused by using DFT for

TABLE 3.3: Published calculated band gaps, structural symmetry, and the functional used in the calculation, for barium titanate from Evarstov, et al.[86], Mahmoud, et al.[79], Piskunov, et al.[87], and Wemple, et al.[89].

Author	Year	Symmetry	Functional	Band Gap (eV)
Evarestov	2012	Cubic	LDA	1.9
			PBE	1.9
			PBE0	4.0
Mahmoud	2014	Cubic	PBE0	4.0
		Tetragonal	PBE0	4.2
		Orthorhombic	PBE0	4.6
		Rhombohedral	PBE0	4.8
Piskunov	2004	Cubic	PBE	2.0
			P3PW	3.6
			B3LYP	3.5
Wemple	1968	Cubic	Expt.	3.2
		Tetragonal	Expt.	3.4

the prediction of this property and, where necessary, use hybridised functionals where our GGA approach is not suitable.

3.2.3 Vibrational Properties of Barium Titanate

The most published properties of barium titanate are the vibrational properties of the lattice. In a solid structure the atomic positions are fixed, however they can be perturbed by vibrational energy in the material. This gives rise to phonons, a quantum mechanical object analogous to photons, though they are made up of discrete packets of kinetic energy rather than electromagnetic. The phonon energy is quantised by the frequency ν and the Planck constant $h = 6.626 \times 10^{-34}$ by equation 3.2[90].

$$E_\nu = h\nu(\nu + \frac{1}{2}) \tag{3.2}$$

FIGURE 3.2: The phonon spectrum for the cubic phase of barium titanate calculated by Ghosez, et al.[92]. The x-axis gives the points of high symmetry in the reciprocal cell.

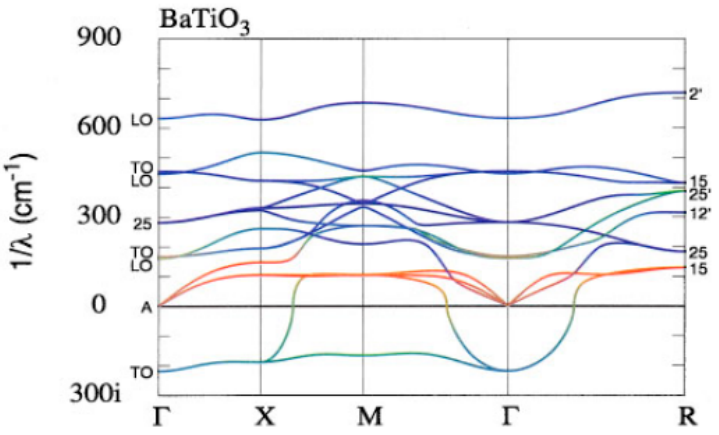

Calculating phonon frequencies is often published as the results can be readily compared to Raman scattering experiments. This uses a monochromatic visible light source, usually a laser, in order to excite phonon frequencies in the sample. Light is scattered from the sample and can be analysed for the change in frequency as photon energy is transferred to phonons. Infra-red spectroscopy can also be used to probe vibrational frequencies, as in semiconductors and insulators it is lattice vibrations that contribute most to the absorption of the incident light. It is due to the Born-Oppenheimer approximation discussed in section 2.2.2.2 that it is possible to decouple the electronic degrees of freedom and the vibrational, making DFT an excellent method of calculating phonons[91]. Figure 3.2 shows a calculated phonon spectrum produced by Ghosez, et al (1999)[92] for the cubic form of $BaTiO_3$.

In CASTEP the vibrational properties can be calculated either by finite displacement or density functional perturbation theory (DFPT). As barium titanate is a polar insulator it is preferable to use the DFPT method in order to model vibrational properties of the system. The only drawbacks to this are

that this method cannot be used with partial occupancy (metallic) systems or ultrasoft pseudopotentials. In calculations requiring either of these a finite displacement supercell must be used, which is computationally less efficient and will be unable to produce Raman or IR spectra if we wish to compare our results to experimental data for publication[93]. It will require study into the differences produced by using norm-conserving or ultrasoft pseudopotentials, and an evaluation into if the two results can be mixed or if a finite displacement supercell must be used to maintain the identical properties of the system already modelled.

Density functional theory is a method that uses the variation principle in perturbation theory to minimize energy. By analogy, density functional perturbation theory uses the vibrational principle to solve equations when the external potential is perturbed. This method defines a Born-Oppenheimer energy surface from the eigenvalues and eigenvectors of the atomic Schrodinger equation, and from that the lattice dynamics can be found as the second derivative of this surface[91].

The finite displacement supercell method is much more straightforward. A supercell is created by repeating several unit cells, and the atoms are displaced from their equilibrium position by a small amount. The forces are calculated on each atom using the standard single point energy calculation and a dynamical matrix is calculated by using numerical differentiation to calculate force constants. Although this method is reliable, easy to understand, and can be used with a wide variety of systems, the necessary symmetry breaking and large supercell mean this type of calculation is very computationally expensive and should be avoided if possible[93].

Most of the published literature on DFT calculations of barium titanate is for vibrational properties. This is due to the use of these calculations for

obtaining dielectric properties of the system, which is of great interest due to BTO's ferroelectric properties. A method for such a calculation is presented by Mahmoud et al (2014)[79], however the CASTEP task 'EFIELD' can be used without modifications providing a phonon calculation has been successfully performed to sufficient precision previously. If we wish to stay strictly within our criteria of structural properties, the phonon calculation will still be used to determine accurate material properties. However, we will need to make approximations on other structural properties such as the fixed-ion polarisation in order to calculate the full range of electric properties.

It is also because of the unstable phonon modes in barium titanate that give rise to the ferroelectric instability in the material, therefore the study of these modes can give information on its ferroelectric state as seen in Bousquet and Ghosez (2006)[94]. These results were also found by Tinte et al (1998, 1999)[83, 95], who published that despite previous claims that functionals (in particular LDA) were not accurate enough to preserve ferroelectric character in the material, the LDA and GGA still show the unstable mode in barium titanate. This is linked to the displacement chain of Ti-O bonds in the [001] direction, which is the cause of piezoelectric properties in the tetragonal system.

Phonon calculations can also be used to determine the thermodynamic properties of the system. This is achieved in CASTEP by taking the results of a phonon calculation and using the task 'THERMODYNAMICS'. While DFT is in itself a zero-temperature method, using the calculated phonon frequencies allows calculations for the temperature dependence of properties such as the free energy and the entropy in the structure. These calculations were performed by Bandura and Evarestov (2012)[80] who were able to calculate the Helmholtz free energy of the system and from that calculate the dependence

on temperature for the physical properties such as thermal expansion coefficients and the bulk modulus. Due to the low temperature required to reach the rhombohedral state, calculating these physical properties experimentally is prohibitively difficult. Therefore, we see that the use of computational techniques is preferable in situations where experiments would not be possible.

Finally we are able to calculate the interatomic force constants from a phonon calculation to determine the forces between pairs of atoms. An example of this was published by Ghosez et al (1999)[92]. We expect the piezoelectric properties of the material to depend on the forces between the displaced ions in the system, where the displacement is in the [001] direction for a tetragonal system.

We see that the vibrational properties of the lattice through DFT are of great interest in publication, and that they provide a large framework for calculating material properties. The issues with this type of study are that it is computationally expensive due to the high precision needed for the calculation. This is further exacerbated if a finite displacement calculation must be performed, as the required supercell will drastically increase the already large computation time. Nevertheless, ensuring well converged phonon calculations are performed early will allow the results to be used throughout the research. By continuing from the binary checkpoint file rather than performing new calculations every time, computational resources will be spared in the future if the initial calculation is performed well.

3.2.4 Piezoelectric Properties of Barium Titanate

We expect that DFT methods should be capable of predicting the piezoelectric constants of materials. Baroni et al (2001)[91] suggests that the full piezoelectric constant tensor $\gamma_{\alpha,\gamma\delta}$ could be formed as the derivative of the electric polarisation with respect to strain as the field tends to zero. It is also possible to define this tensor as the stress induced by a field at zero strain.

There are several issues with these definitions. Firstly is that the macroscopic polarisation can be estimated by DFT using a fixed-ion displacement model. However, the 'true' polarisation is actually obtained by Berry phase integration as shown by Bernardini et al (1997)[96]. Secondly, the equation to create the tensor elements requires the difference between two numerically similar terms, requiring a high degree of both accuracy and precision to distinguish the two that may not be possible due to inherent functional errors. Finally the full piezoelectric tensor is a third order tensor which is usually reduced significantly due to the number of terms that can be disregarded due to the symmetry of the system. For example, in tetragonal barium titanate only three elements are required (d_{13}, d_{33}, and d_{15}). Treating these three quantities as independent objects will be much simpler than having to calculate an entire third rank tensor in order to extract them.

Calculation of piezoelectric components has been performed for III-V nitrides and similar simple structures using a method developed by Vanderbilt (2000)[97] and has been implemented in publications such as Bernardini et al (1997)[96] and Zoroddu et al (2001)[98]. These are relatively simple structures and therefore could be calculated at the time of publication. A more recent study by Furuta and Miura[99] used a similar technique along with in-plane compression to calculate the piezoelectric constant for $SrTiO_3$ and $BaTiO_3$. This in-plane

FIGURE 3.3: The change in tetragonality and polarisation induced by varying the a-axis lattice parameter in barium titanate (blue) and strontium titanate (red) by Furuta and Miura (2010)[99].

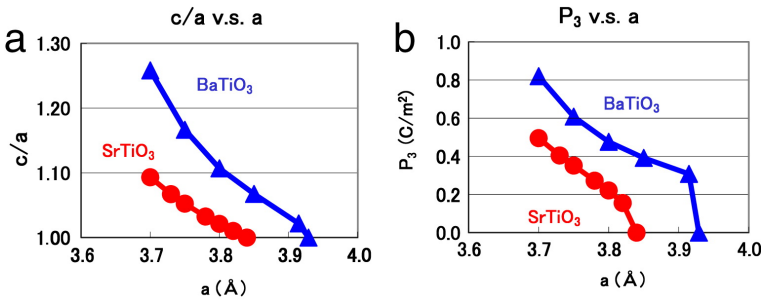

compression method calculates many different properties under immense material strain. We hope to use a method similar, but with more realistic strains in order to determine piezoelectric properties. The results for their calculations by varying lattice constant a are shown in figure 3.3.

We wish to determine if these piezoelectric properties can be calculated from a simple framework with readily available tools. By using already implemented methods in a widely distributed code, we can create an automated framework to study existing piezoelectrics and attempt to find new ones with high coupling factors. This is industrially relevant due to the attempts to find lead-free systems to replace the commonly used lead zirconate titanate (PZT).

3.3 Sample Structures Review

We have discussed barium titanate as it is the starting point for this research, as it is a historic material with a huge number of individual studies devoted to it. However, we will briefly consider the other sample materials we will be studying. These are, generally speaking, not as well published as barium titanate, but are still well known materials in the piezoelectrics community, and are no less important.

3.3.1 Lead Titanate (PTO)

Lead titanate is an essential part of piezoelectric research, however it is rarely considered as a pure material, especially in the case of a single crystal material. It is noted in literature[100] that these crystals are particularly difficult to grow. From speaking to experimentalists, we understand that this is due to the particularly high tetragonality. Normally when a perovskite undergoes a phase transition from the cubic state, the new state is highly pseudocubic, allowing for the crystal to adiabatically change its shape as it cools. Single crystals of lead titanate however, are prone to cracking due to the large internal stress caused by the drastic change in shape. As such, lead titanate is mostly created as a sintered powder ceramic, the macroscale properties of which can be quite different to the single domain, single crystal that our calculations represent.

Table 3.4 shows a comparison of lattice parameters, tetragonality, and volume of four experimental characterisations of tetragonal lead titanate, along with the experimental temperature and the year published. We see that the basic lattice parameters are well agreed upon, with little variation across the years. It is important to ensure that there is good agreement before we begin comparing our calculations, as comparing to a single experimental structure can allow for the practice of cherry picking the closest value to artificially inflate the meaningfulness of results. We also see the high tetragonality of ≈ 1.06, which is sometimes referred to as a ferroelectric strain of 6%. This is significantly higher than the 1% ferroelectric strain in barium titanate, and therefore supports the idea that a single crystal would crack under the radical change of shape associated with the phase transition.

Due to the difficulties inherent in experimental synthesis of a real equivalent to our sample material, it is difficult to give a numerical value for comparison

TABLE 3.4: The structural parameters of lead titanate from experimental studies. We compare the two independent lattice parameters, tetragonality, and cell volume. The temperature at which the material was characterised and the year published is also shown. We see that the lattice parameters are consistent across many decades, demonstrating good consensus on the structure.

	1[101]	2[102]	3[100]	4[103]
a (Å)	3.904	3.902	3.904	3.904
c (Å)	4.135	4.156	4.150	4.160
c/a	1.059	1.065	1.063	1.066
Vol ($Å^3$)	63.022	63.278	63.251	63.403
T (K)	298	298	298	300
Year	2000	1985	1968	2001

of the dielectric permittivity, spontaneous polarisation, or piezoelectric coefficient. However we can estimate the behaviours based on other structures. We expect the lead titanate properties to be similar to those of the barium titanate, but much greater numerically due to its highly exaggerated ferroelectric strain. We expect a numerically large, positive d_{33} component, and a smaller, negative d_{31}. A higher spontaneous polarisation is also expected due to the high ferroelectric strain.

Overall, studies of literature such as those above, along with further studies by Bhide, et al.[104], Pavithra and Madhuri[105], and Yamada, et al.[106], this prediction is well supported, however as these studies are all for composites, multi-crystalline ceramics, and thin-films and are as such not representative of the system we will be studying. In another paper Bhide, et al.[100] have measured a spontaneous polarisation of $66\mu C/cm^2$, greater than that of barium titanate, but acknowledged that their crystals suffered from the same cracking that has been mentioned.

This demonstrates a potential strength of computational models, as limitations that may not be immediately obvious in experimental studies are not a factor

in computation. In order to cover the full range of possible materials in order to gain a fundamental understanding of piezoelectric properties, it is essential that computational and experimental techniques support each other. This allows the weaknesses of each method to be mitigated by other approaches, without dampening the strengths.

3.3.1.1 First Principles Calculations of Lead Titanate

Lead titanate is not often a candidate for calculations. We attribute this to the lack of compatible experimental evidence for the reason noted above, and also to the computational complexity. The electronic structure of lead has historically made accurate pseudopotentials difficult to generate, ultimately making other structures such as barium or strontium titanate more favourable for computational efficiency and experimental comparison.

Lattice parameters of $a = 3.99$Åand $c = 4.03$Åwere calculated using a Hartree-Fock method, which is often considered a precursor to DFT, by Stashans, et al.[107]. We see that these parameters do not compare well to values in table 3.4, as it severely underestimates the tetragonality of the unit cell. This is not surprising, as Hartree-Fock is not at all suitable for this type of material for predicting lattice parameters. DFT studies have been performed which are more suitable. Lebedev[108] calculated lattice parameters of $a = 3.886$Åand $c = 4.115$Å, which are much more representative of the experimental values above. Effective charges and elastic constants are also calculated for many titanates, those relevant to this work are shown in table 3.5.

Lebedev's work considers a total of 10 titanate perovskites, calculating phonon dispersions for each structure. Structural parameters are a necessary part of

TABLE 3.5: Lattice parameters and effective charges calculated by Lebedev[108] for barium and lead titanate. These values are calculated using the ABINIT and the LDA functional. We see the classic overbinding of this functional leading to shorter lattice parameters than expected, but this averages out to give an expected tetragonality.

	$BaTiO_3$	$PbTiO_3$
a (Å)	3.965	3.889
c (Å)	4.007	4.115
c/a	1.011	1.058
Z^*_A	2.738	3.931
Z^*_{Ti}	7.761	7.623
$Z^*_{O,ax}$	-6.128	-6.283
$Z^*_{O,rad}$	-2.186	-2.635

this calculation, and Born Effective Charges are a result of the phonon perturbations. However the author has not extended these results to the polarisation state, instead deferring to Berry phase methods by Vanderbilt and Kingsmith[109, 110]. While a Berry phase calculation is the more accepted method for calculation, its specialised, mathematical nature makes it conceptually and technically difficult to integrate into an existing research group. We believe that an approach based on charges and structure using tools that are standard and widely available is much more suitable to enhance the current research output of existing groups.

Functionally, the work by Lebedev is consistent, but has several factors that should be called into question. Firstly is the choice of functional. We have described how we selected the WC functional for use in these calculations, and that the LDA functional is not suitable for this type of material. A GGA based functional is far more suitable, and should always be used as a minimum for future perovskite calculations.

Secondly is the convergence of the calculations, which has not been made clear as to what method was chosen in order to select the convergence criteria.

The same convergence parameters were used across all structures, while we will argue in chapter 5 that separate convergence is more suitable in these comparative calculations. The convergence parameters are an energy cut-off of $30Ha$ ($816eV$) and a Monkhorst-Pack grid of 8^3, which are low compared to our convergence study in chapter 5, and a self-consistent energy convergence of $10^{-10}Ha$ ($2.72 \times 10^{-9}eV$). In CASTEP, a phonon calculation is recommended to have a self-consistent energy convergence of $10^{-10}eV$ at maximum in order to give a suitable convergence for phononic properties.

Thirdly, it is unclear as to whether the calculation was based on norm-conserving or ultrasoft pseudopotentials. While OPIUM[111] is used, as we would always recommend for creating pseudopotentials, it is important to ensure that the type of pseudopotential is clear.

Finally, there is inconsistency in the use of units, mixing Hartrees and Rydbergs for energy. It is important for clarity that units are kept as consistent as possible, and when reporting on external values that use different units the conversion is given. We ensure that this research consistently uses standard SI, except for lengths given in angstroms (1Å=$10^{-10}m$) and energy given in electron volts ($1eV = 1.609 \times 10^{19}J$), which are very commonly used in atomistic research. For other units we have used metric prefixes for reading clarity[112, Ch. 3].

Ultimately the research of Lebedev is the most comprehensive comparative study on perovskites using DFT to date, and while there are issues listed above that can be improved on, it ultimately provides an excellent framework that can be drawn on in terms of essential quantities, order of calculations, and throughput for a comparative study of perovskites.

3.3.2 Potassium Niobate (KNO)

Potassium niobate has similar phase transitions to barium titanate. A high temperature paraelectric phase, then tetragonal, orthorhombic, and finally rhombohedral ferroelectric phases with decreasing temperature. However these phase transitions occur at a much higher temperature. Due to this, the room temperature state of potassium niobate is orthorhombic, with the phase transition to a tetragonal unit cell at around 500K[113].

It is because of this fact that most of the characterisation of this material is based on the orthorhombic form. While the methodology we present is likely to be useful in evaluation of the orthorhombic phase piezoelectric properties in much the same way as it is applied to a rhombohedral structure in chapter 7. However several high temperature characterisations have been performed to give the lattice structure of the tetragonal phase.

In one such study by Hewat[114], the concept of aristotype ionic positions and the fixing of an atom to give relative displacements, although in this study it was the Nb B-site that is fixed rather than the A-site K ion. These concepts are the basis of our method described in section 5.3.2, with the aristotype positions being referred to as totally symmetric coordinates. This is further supported by Hewat in previous work[115], in which the relationship between displacement, effective charge, and polarisation is discussed. However the method of calculating the effective charge from the permittivity assumes a cubic structure. While it is reasonable to assume these are largely identical for the tetragonal phase of potassium niobate, which is highly pseudocubic, this is less likely to apply to a material like lead titanate with considerably greater anisotropy, as well as lower symmetry states where the non-diagonal terms of the effective charge tensor are significant.

TABLE 3.6: The unit cell parameters, tetragonality, and volume of the three pure tetragonal potassium niobate perovskite structures on ICSD, along with the temperature the experiment was performed at and the year it was published. We see that despite there being far less structural data than for barium titanate in this phase, there is good consensus on the lattice parameters over 40 years.

	1[116]	2[114]	3[115]
a (Å)	3.997	3.996	3.997
c (Å)	4.063	4.063	4.063
c/a	1.017	1.017	1.017
Vol (Å^3)	64.911	64.878	64.975
T (K)	550	543	543
Year	2013	1973	1973

Table 3.6 shows the unit cell data for potassium niobate from three published papers. These three give the only data on ICSD for $KNbO_3$, which is likely due to the requirements of specialist equipment in order to perform the synchrotron and neutron diffraction experiments at elevated temperature. Despite this we see that the differences between the three sets of structural parameters are very small, and therefore we consider the structure to be well defined. Although these temperatures are considerably higher, we will discuss alongside our own calculated results in section 5.2.4 that the thermal coefficients for our sample structures are so low that even this relatively high temperature does not cause a significant expansion of the lattice parameters.

3.3.2.1 First Principles Calculations of Potassium Niobate

As noted by Shigemi and Wada[117], interest in potassium niobate is recent due to efforts to reduce the use of lead in technology. As a result, many of the simulation studies are relatively recent and advanced, compared to basic studies on structure that are present for many other materials. With more advanced studies comes the use of better pseudopotentials and functionals, so the lack

TABLE 3.7: Lattice parameters, tetragonality, and volume calculated by prior simulation studies, the energy cut-off, Monkhorst-Pack grid, exchange-correlation functional of the simulations, and the year published. We see that only [118] has used both a GGA functional and norm-conserving pseudopotentials. This study has calculated many properties of interest for potassium niobate, however they have compared the same material between phases, whereas we are interested in the single phase between different materials. *) Due to the particulars of this study they have only reported on their supercell, this is the effective grid size to give that spacing in a single unit cell. **) This value is simply not possible. It is likely that the author means 35Ha (952eV).

	1[117]	2[118]	3[119]
a (Å)	3.986	3.992	3.950
c (Å)	4.142	4.128	3.983
c/a	1.039	1.034	1.008
V (Å^3)	65.809	65.784	62.145
$E_{cut}(eV)$	600	1700	35**
MP Grid	8^{3*}	8^3	8^3
Functional	PBE	PBE-WC	LDA
Pseudopotential	Ultrasoft	Norm-Conserving	Norm-Conserving
Year	2005	2012	2007

of studies when compared to systems such as barium titanate and strontium titanate is balanced by a higher average quality of the results. Additionally we see that Wan, et al.[118] also discuss the challenges of experimentally studying these crystals, and indicate that a first-principles method is suitable in overcoming these limitations in order to study the macroscale properties of the material by their relation to the atomic scale properties.

Table 3.7 shows selected results and computational details from first-principles studies on the tetragonal phase of potassium niobate. We see a common Monkhorst-Pack grid of 8^3, indicating that this is a sufficient grid for other authors. However it is always important to define a figure of merit and converge the system manually, especially when authors have not stated their convergence criteria. We see that number 1 has used a low cut-off that is indicative

of their choice of ultrasoft pseudopotentials, which is suitable for the structural characteristics they are studying and especially beneficial for the larger supercell they used, however makes this incompatible with our methodology. Number 3 is fundamentally incompatible with our method due to the use of the local-density approximation. We have already discussed how this is not suitable, and they give no reason for using it when a variety of other options were available. Additionally, the nonsensical cut-off energy makes it very difficult to comment on.

Study number 2 in the table by Wan, et al.[118] is very closely linked to our own research. They have calculated a wide variety of material, electronic, and piezoelectric properties of all phases of potassium niobate. While this is a good indication that others have considered similar methods to the one we will present in this thesis, they do not give the details of their calculations. They note that despite good agreement with experiment in their structural and elastic properties, their piezoelectric coefficient differs by 50%. Though these authors question if there is an inherent flaw in the method that would make it fundamentally unsuitable, it is important to remember that a factor of 2 error between vastly different approaches to calculate a value is actually very impressive. We may find that this is an error in their procedure, or a weakness of the method itself, though that will be difficult to confirm as this paper contains no details of how it was calculated.

We see the overall trends in their study that we can look for, such as the much greater difference they report between classic and effective charges than in the other two materials, for which it is likely that its I-V composition in the classic charges of K and Nb ions is responsible. They also report a spontaneous polarisation of $0.36 C/m^2$, which after thermal effects are taken into account is in good agreement with accepted experimental values[1]. Overall while this

study lacks detail on their calculation method and is only concerned with potassium niobate, it is an excellent source to draw from in our own research.

3.3.3 Lead Zirconate Titanate (PZT)

Lead zirconate titanate is likely the most important piezoelectric material. Unlike the other materials we are studying, this binary perovskite is a combination of lead titanate, which is described above as having fantastic piezoelectric properties, and the non-piezoelectric perovskite lead zirconate. The mix of these two materials has produced a widely used and well studied material with a massive amount of published literature behind it.

It is not possible to cover the entire breadth of literature on lead zirconate titanate, and much of the published material is not relevant to our studies. There are however, many reviews available to cover and compare the published literature on the material. For instance, a review from Panda and Sahoo in 2015[120] that covers the history of the material, fabrication of devices, and candidates to replace it due to its high lead content and subsequent environmental danger.

Primarily, we are only focused on the equal mixing of the zirconate and titanate aspects, whereas published material covers the whole spectrum of compositions. Most importantly is the 52% zirconate, 48% titanate mix that is extensively used and therefore most studied. Figure 3.4 shows the phase of PZT under different temperatures and compositions[1, p. 136]. It is by studying this that we can see why this particular composition is so important.

The morphotropic phase boundary at 52% zirconate that does not vary significantly with temperature is the key to the success of lead zirconate titanate. Mixes at this boundary see greatly increased piezoelectric properties due to the phase mixing that occurs, that persist across a wide temperature range,

FIGURE 3.4: The temperature-composition phase diagram of lead zirconate titanate taken from Jaffe[1, p. 136]. We see that between the tetragonal (F_T) and rhombohedral (F_R) is a near-vertical line at 52% zirconate. This is the morphotropic phase boundary, where the material properties are unusual due to the phase mixing, and as a result the piezoelectric properties are greatly increased. The steep gradient means that this feature is stable across a wide temperature range.

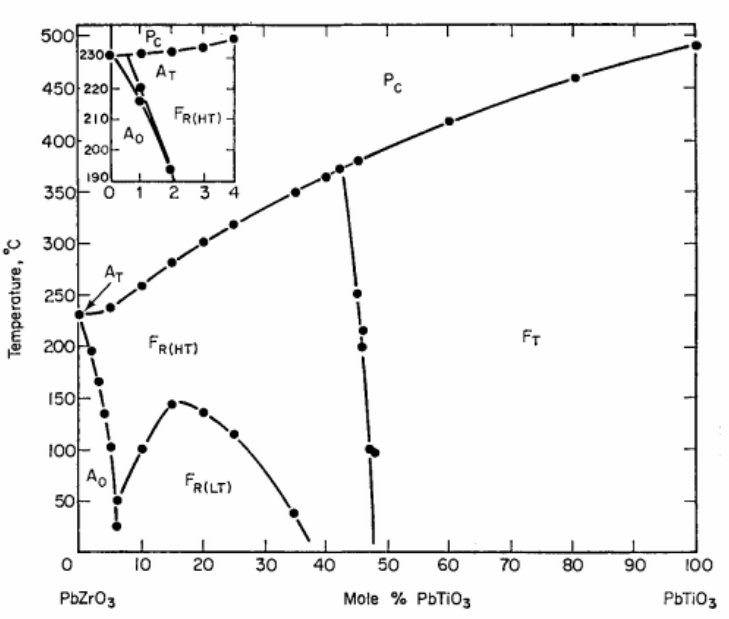

allowing for the creation of reliable and efficient devices. We select our chosen composition to be slightly to the right of this boundary in the tetragonal zone, for reasons that we will discuss shortly.

We consider the structures on ICSD for the composition we are studying, for which the lattice parameters, tetragonality, unit cell volume, and year are given in table 3.8. This represents the high quality data for the composition we are interested in marked as tetragonal. This is reduced from the large variety of compositions and dopant structures also available. These experiments were all performed under room temperature and pressure. We see that the studies have reported the lattice parameters for a basic perovskite unit of 5 atoms. Further investigation into the posted structures shows that these crystal structures are

TABLE 3.8: Lattice parameters from experiments obtained from ICSD for PZT with an equal mix of zirconate and titanate elements. We see that these results are more varied than the other materials in this chapter. In reality this is to do with the macroscopic mixing parameters of the experimental sample. While a sample may be on average a 50% mix of the two components, it is likely that this is not evenly distributed through the material, leading to random Ti and Zr-rich zones. Distribution and concentration of these zones are generally random, and therefore different samples will naturally give slightly varying results when it comes to characterisation. Additionally, though this is a binary perovskite, these have been reported by the original authors as if it were a basic, 5 atom unit cell.

	1[121]	2[121]	3[122]
a (Å)	4.042	4.049	4.030
c (Å)	4.128	4.113	4.145
c/a	1.021	1.016	1.029
V (Å^3)	67.442	67.430	67.319
Year	2006	2006	2000

reported based on a multiple occupancy B-site.

A multiple occupancy site is used where a crystal structure that seems to follow a simple pattern is in fact disordered. In this example, the characteristic 5 atom unit cell is present, however there are a massive number of degenerate and distinct energetic arrangements for the zirconate and titanate elements to take. We can approximate a unit cell, for instance by saying that the nearest neighbour to each basic perovskite cell will be the opposing atom. So for instance if we have a zirconium ion on a B-site, then the repeating cell is set up in such a way that the next B-site in either direction of the a-, b-, or c-axes will be a titanium ion. This is called a perfect mixing approximation and makes for a computationally feasible, approximate crystal structure. In diffraction experiments, the results give an average over the sample. We know instinctively that titanium and zirconium bond differently, despite sharing the same classical valance of 4+, and therefore have different bonding properties. We can guess, due to their different ionic radii and the fact that the unit

cells of zirconia and titania are significantly different, that the oxygen bonding properties of each type of basic cell will be slightly different to the other. In diffraction however, the result is averaged between the two, with no way to separate the differences on an atomic level, so the structure is reported as the 5-unit perovskite cell with a multiple occupancy B-site ion, that is a mixed pseudoion of the titanium and zirconium ions, with the ionic position given by the average position obtained by the experiment. In doing so we lose a lot of fidelity on the atomistic details of the binary perovskite, such as the difference in bonding for the Ti-O and Zr-O bonds causing the oxygen ions to be laterally displaced.

As a result of these macroscale factors, it is unclear on how relevant the experimental data available is to our first-principles study. While there is definite interest in DFT simulations of PZT, the addition of the macroscale effect of disordered arrangement in addition to the other approximations that we must make will likely make it difficult to compare our simulation to experimental data.

3.3.3.1 First Principles Calculations of Lead Zirconate Titanate

Above we have discussed the concept of multiple occupancy sites, and it is possible to replicate such ideas in a DFT methodology through the use of a Virtual Crystal Approximation (VCA). The opposing method is the use of a supercell, where a unit cell is created from a basic unit that has been explicitly repeated, and atoms modified. For instance, we might create a supercell composed of a lead titanate cell that is repeated in each direction once, for a total of 8 basic unit cells, which would be referred to as a $2 \times 2 \times 2$ supercell. We can then change some of the titanium ions to zirconium in order to create a PZT unit cell. This can preserve the local detail of the material, but is fundamentally

always ordered, and computationally very expensive due to the cubic scaling of DFT.

Overall the literature is split on the topic of the VCA in DFT, with papers such as Bellaiche and Vanderbilt describing it as "adequate" and "efficient"[123], and Ramer and Rappe commenting "This approach permits more complicated structures to be studied while maintaining tractability"[124]. However in this paper they note that the different methods for creating the pseudoion show different results, so how to select the mixing scheme is brought into question. Marton and Elsasser[125] comment that the VCA underestimates the tetragonality of their PZT system, which in our research would likely have a large effect on our polarisation calculations. Boykin, et al.[126] state that the VCA "shows shortcomings" in aspects of their calculations when compared to the supercell approach, but their work is based on semiconductors and as a result these findings may not be applicable to the systems we are studying.

Marton and Elsasser[125] demonstrate in their work that the supercell method they have used found a local structural effect shown in figure 3.5 that is not present in the virtual crystal approximation. This shows that the oxygen ions bond more closely to the titanium ions than the zirconium ions, creating an interesting displacement from the symmetric positions, despite the overall supercell maintaining a tetragonal lattice. As non-symmetric displacements of ions form the basis of this research, this is a clear indication that the type of local detail we are interested in is not present in the VCA, and as a result the supercell approach is the best option for use to use.

Beyond considerations of the supercell or VCA approach, computational research in PZT is focused on the simulation of different compositions, and comparisons of the rhombohedral and tetragonal states. While these are important topics, we are not aware of any research related to our project that concerns

FIGURE 3.5: The oxygen ion displacement observed by Marton and Elsasser[125] in their ordered supercell calculations that is not replicated in the virtual crystal approximation. As we are interested in local non-symmetric displacements, this is a clear indication that a supercell approach is more suitable for our work.

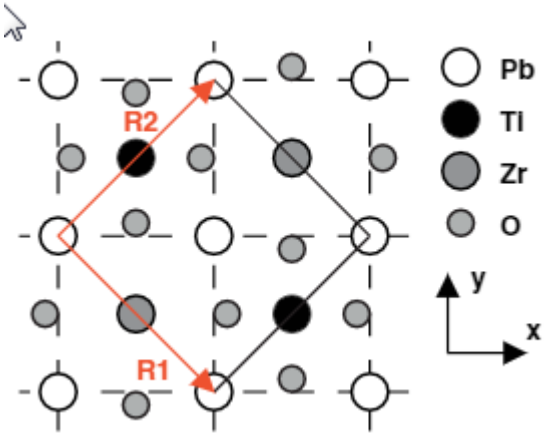

a comparison between the fundamental differences in the piezoelectric effect in PZT in comparison to the unary perovskites we study in chapter 5, and as a result while we will not have literature to compare with. This identifies a gap in current knowledge, allowing us to calculate novel properties for this important material.

3.3.4 Bismuth Ferrite (BFO)

The last of the sample materials we have chosen is the most difficult and most physically interesting. While the materials we have reviewed so far are interesting for their ferroelectric and piezoelectric properties, bismuth ferrite has magnetic and conductive properties in addition to these. Materials showing both ferroelectric and ferromagnetic character are known as multiferroics. The perovskite form of this material belongs to the R3m space group, which makes this structure most suitable for our research, however various forms of

the structure have been published, most commonly a rhombohedral-hexagonal state.

Interest in bismuth ferrite has come from the search for lead free materials to replace PZT. Unlike other candidates, the spontaneous polarisation and piezoelectric coefficient is comparable to that of the materials it must replace. Lebeugle, et al.[127] were able to produce a high quality single crystal in order to first measure the bulk polarisation, $0.60 C/m^2$, and observed piezoelectric behaviour in samples. The thin film behaviour is also excellent, these are easier to make than bulk single crystals yet are measured to have good polarisation properties. As the technology moves to smaller and more integrated devices, a material able to perform similarly well in bulk and thin film is very useful. A good, comprehensive review of the physics and applications of bismuth ferrite is given by Catalan and Scott[128].

Table 3.9 shows the lattice parameters and volume of perovskite bismuth ferrite and the year of its characterisation. All were performed at room temperature and pressure. We see that there is some discrepancy between the third study and the other two, but overall good consensus on this. While we could use the well published rhombohedral-hexagonal form, there are two issues. Firstly, as this research project is specifically focused on properties of the perovskite structure, it would be disingenuous to use a different structure for one material. Secondly, and more practically, bismuth ferrite is considerably more computationally difficult to perform calculations on than any of the other unary perovskites, as we will see in chapter 7. As a result, the increased number of atoms would only make the simulations even more costly, and would ultimately make this type of research untenable. While the hexagonal state is theoretically reducible to a 5-atom unit cell on a structural basis, it is the pairs

TABLE 3.9: Example structures of the rhombohedral perovskite form of bismuth ferrite listed on ICSD. We see that the structure is generally well agreed upon, and as a result we have a good starting point for our calculations. All experiments were performed at room temperature and pressure.

	1[129]	2[130]	3[131]
a (Å)	3.962	3.962	3.952
α (°)	89.40	89.52	89.60
V (Å^3)	62.18	62.19	61.72
Year	1967	1963	1960

of unit cells that allow for spin cancellation, so in practice we would still have non-zero spin and would not gain anything from this reduction.

In terms of its magnetic properties, rhombohedral bismuth ferrite has been found to be G-type antiferromagnetic[132]. In analogy to our PZT having perfect mixing as discussed earlier, G-type antiferromagnetism can be considered to be perfectly mixed in terms of spin polarisation. The iron ion is the cause of the spin polarisation in the bismuth ferrite unit cell, so for G-type behaviour every nearest neighbour has the opposite spin. So if we consider in a real material a single unit cell with a positive spin on the B-site, then the 6 surrounding unit cell B-sites will have negative spin. Really, this behaviour is analogous to the antiferroelectric effect, however we have not covered any antiferroelectric materials in this research.

In addition to this behaviour, there are other factors to be aware of. For instance, under certain conditions the material is known to show metallic properties. While it generally requires very high temperature and pressure to cause this transition, the corrections required to account for magnetic behaviour may inadvertently also bring to light this behaviour. A predicted phase diagram is shown in figure 3.6 given by Catalan and Scott[128]. Though some boundaries are speculative, it shows roughly the experimental phases and their ordering with temperature and pressure.

FIGURE 3.6: A phase diagram proposed by Catalan and Scott for the solid phases of bismuth ferrite across temperature and pressure[128]. Although they state that the lines are only a guide, it gives some insight into the antiferromagnetic to paramagnetic phase transitions, and the insulator to metallic transition.

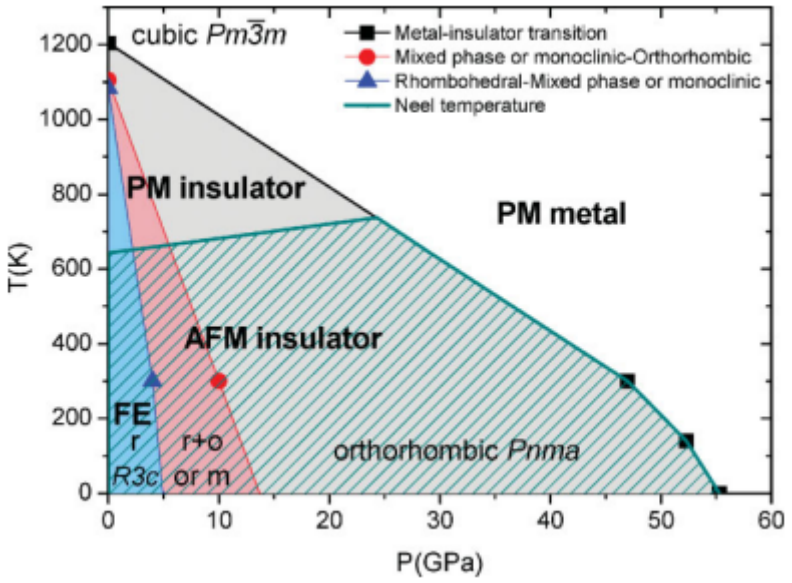

Despite the fact that bismuth ferrite is relatively new to the field of piezoelectrics due to its unusual properties and the difficulties inherent in creating pure crystal samples, it has received a huge amount of attention as a material that could be the basis of a lead-free future. While this will likely be a challenge to study, it will also be of great interest and use to the larger community.

3.3.4.1 First Principles Calculations of Bismuth Ferrite

As will be discussed in chapter 7 in more detail, the magnetic character of the spin polarised unit cell adds complications to the calculations that are not a factor in the the similar structures in chapter 5. As a result the computational complexity makes this material less favourable for ab-initio calculations. Further to this, composites such as lead palladium titanate[133] and bismuth

TABLE 3.10: The energy cutoff and Monkhorst-Pack Grid used for three selected DFT studies of bismuth ferrite. We also show the number of atoms in the unit cell, functional and pseudopotential used, and the year published. Two of the calculations used PAW pseudopotentials, which allows them to use a lower energy cutoff, as these are very similar to ultrasoft potentials. All simulations are performed on several perovskite unit cells, which is possible due to approximations made. Additionally, two have used a Hubbard potential (U) to modify their functional. *) Effective grid for the same spacing on a single perovskite cell. **) The paper does not explicitly discuss the pseudopotential, but based on the details this is assumed.

	1[136]	2[137]	3[138]
Energy Cutoff (eV)	1360	600	550
MP Grid	12^3*	14^3*	$10 \times 10 \times 8$*
Number of Atoms	40	40	120
Functional	LSDA	GGA+U	LSDA+U
Pseudopotential	Norm-Conserving**	PAW	PAW
Year	2007	2016	2009

ferrite lead titanate[134, 135] become extremely difficult due to the the magnetic features compounding with the difficulties in the composite binary lead titanate discussed above.

Table 3.10 shows the computational details of several first principles studies on bismuth ferrite. We see that in two of these studies, projector-augmented wave pseudopotentials are used, due to the author's use of the VASP code. Additionally, these are all performed on unit cells greater than our five-atom unit cell, despite the difficulty of calculation. This is enabled by the use of a frozen band approximation that we will discuss.

The functional used in each of the cases is either a local spin density approximation, or involves a Hubbard potential. We have discussed the L(S)DA and why we do not use it. The Hubbard potential is rarely used for inorganic crystals, as it covers extra energetic terms not included in the exchange-correlation energy. It is therefore usually seen in simulations of organic molecules in order

to account for Van-Der-Waal forces or hydrogen bonding. It is generally calculated by comparing a structure to experimental data for varying Hubbard parameters, a method which we find to be too reliant on empirical data to be truly considered ab-initio. In this case it appears to be making a correction for the antiferromagnetic coupling present in the structures, which may be required due to the frozen bands approximation.

In DFT an unconstrained, non-zero spin causes significant challenges to the calculation. This is because in a non-spin system the electron bands can be considered to have two energetically degenerate electrons of opposite spins. As the electron energy is the main feature of these calculations, the presence of pairs of electrons of equal energy creates a simpler problem as the band energy only needs to be calculated once. However in a spin-polarised system the same assumption cannot be made, increasing the complexity of the calculation. Additionally, the electrons have an extra degree of freedom in minimisation which needs to be addressed by the opening of empty bands above the valance level.

To combat this, calculations featuring spin often use what is known as a frozen-band approximation. This is based on the concept of frozen gaussians[139], where a dynamic quantum mechanical parameter such as electronic spin is replaced by a static, classical probability function. In DFT this is used and is well supported in many cases, such as in a bulk homogeneous system such as iron, where spin states in each atom are generally fixed. This approximation may be what allows the use of a linear response type perturbation theory to calculate phonon modes in these papers, though it seems unlikely that phonon modes are invariant of dynamic spin in the material. Also, by using even numbers of perovskite cells, the antiferromagnetic properties are used, allowing

for the total spin of the system to be zero due to the spin cancellation of pairs of cells.

However in the bismuth ferrite system there is evidence of magneto-electric coupling[132], which suggests that the magnetic and electric properties are not separate phenomena but interdependent. Then in a material with a spin polarized centre, we may expect an induced spin to be created on the other ions, despite not being classically ferromagnetic themselves. This coupling makes the magnetic properties inseparable from the electrical properties we wish to study, and as a result we do not believe this approximation is suitable for our research.

It is important to consider that the frozen band approximation allows the computational complexity to be significantly reduced, which makes the large unit cells in these calculations viable. However, as the computers available become more powerful, and the software becomes more robust and efficient, we hope to see the ability to calculate fully implemented spin on a supercell showing an ordered G-type antiferromagnetism, which would be a great step forward to understanding the fundamentals of multiferroics through first principles methods.

3.4 Summary

While properties of piezoelectric materials are calculated and readily available through literature, the manipulation of these properties to produce industrially relevant properties such as the piezoelectric coupling coefficient or charge constant is not performed. DFT is widely used and published in the study of these types of materials, making it an excellent choice to use as a trusted and reliable method. However while computational data is published it is not in a

format that is readily comparable to experimentalists, in particular those who wish to develop piezoelectrics for industrial purposes. While domain effects can be used to modify the piezoelectric effect in the material, a more fundamental understanding of these intrinsic effects in an effective single-crystal, single-domain simulated system will provide a new perspective and may be used with domain engineering to generate novel materials that may be used as lead free alternatives.

3.5 Research Aims

We wish to create a simple framework to understand piezoelectric properties in perovskite structures using properties that can be ascertained reliably through easily available DFT methods. Using this framework, we hope to expand it to a larger, binary system to identify how similar this is to the most basic unit, as well as identify and understand differences introduced by the added complexity. Finally, we will consider the multiferroic bismuth ferrite, to ascertain how much information our method is able to obtain with the added complication of ferromagnetic characteristics, which is known to cause issues in DFT. Our thesis questions are:

- Can intrinsic piezoelectric properties be predicted by creating a framework from readily available DFT tools?
- Can this framework identify overall similarities and differences in a more complicated binary material?
- How does the inclusion of ferromagnetism affect the capability of the framework to predict properties?

Chapter 4

Computational Equipment and Techniques

4.1 The CASTEP Code

4.1.1 Local Implementation

Multiple software packages are used locally to prepare and analyse results. Creation of input files is performed manually using Notepad++ with a user defined language containing all of the syntax and keywords. VESTA3 is used for visualisation of the 3D unit-cell structures and electron density shifts. MobaXTerm is used for a Unix-like environment for scripting and shell components.

The local computer is a Dell Precision T1700 Workstation with the following specifications:

- Intel Xeon CPU E3-1240 v3 @ 3,40GHz (8 cores)
- 16.0GB RAM

- Nvidia Quadro K2000 graphics card with 4095MB card memory.
- Windows 7 Enterprise Sevice Pack 1 64-Bit

Additionally, a personal laptop running GalliumOS[140] was used for portable shell access to resources.

4.1.2 HPC Implementation

CASTEP was compiled after discussions with Dr. P. Hasnip to use optimised compilers and libraries. Compilations are kept consistent through each chapter, and updated to a newer version upon a new project. The specifics of each compilation system are given below, however as a rule of thumb Intel was used to match the Intel x86_64 hardware.

Submission is handled using bash scripts that submit an mpirun request to the system job queue to be executed on the requested number of compute nodes based on a priority allocation system. Priority is allocated based on the user's use, along with the number of nodes and time requested up to a maximum 48 hours. Multiple job requests with similar parameters such as convergence testing is submitted as a single job containing multiple mpirun requests through standard shell 'IF' looping.

4.2 ARC HPC Facilities

The ARC facilities are a group of HPC systems located at the University of Leeds and are made centrally available to staff and students across the university, with access to on site support. Researchers can log in via ssh using

FIGURE 4.1: A submission script to execute an MPI-parallel version of the castep.mpi program on the files BTOTet.cell and BTOTet.param. The job parameters are to execute this calculation in the current working directory and with the current environment variables at the time of submission, to use the basic shell to issue the commands, request two nodes and execute eight MPI processes on each node (implicitly requesting each process use two physical cores on a 16 core per node system), run for a maximum of ten hours, and email the user at the beginning and end of the calculation.

```
#$ -cwd -V
#$ -S /bin/sh
#$ -l nodes=2,ppn=8
#$ -l h_rt=10:00:00
#$ -m be

mpirun castep.mpi BTOTet
```

freely available software and submit jobs to the intelligent queueing system through two login nodes by specifying the amount of time and compute nodes required. Jobs are executed on compute nodes when the queue system dictates, these nodes are not generally accessible by the user so the program commands must be able to run in a standalone manner. As we are based on a linux system, there is native command support for all types of scripting or job automation using bash, python, ruby, or other suitable scripting systems. This is largely personal preference, although there are limitations in all automation languages.

Tasks are submitted to the queue using a submission system based on shell scripts. This requests the system resources for the user and executes jobs on the nodes. An example script is shown in figure fig:subscr.

This script informs the queue that the user wishes to execute the castep.mpi program in the current directory on seed BTOTet (with corresponding BTOTet.cell and .param) on 2 nodes, executing 8 castep processes on each node for 10 hours. It will inform the user when the job starts and finishes by email. Nodes have 2GB per core, however this memory limit can be exceeded by tasking the node

to only execute a certain number of processes. In this example it is also possible by using Symmetric Multiprocessing (SMP) parallelisation integrated into the CASTEP program for each process to be executed across 2 cores, meaning that there are no idle cores in the node. As a user's priority is based on how many cores have been requested and not how many cores are active, it is most efficient priority-wise to use as much of a node's resources as possible. However, depending on system specifics it may be more efficient to leave a few cores idle to exploit inherent parallelism in the system than attempting to use a brute force method with as many cores as possible. In general, it is not recommended that more than 128 processes are used in a single CASTEP calculation as communication between the cores becomes prohibitively large and parallel efficiency is decreased. Combining both MPI and SMP is known as hybrid parallelism and can be used to efficiently increase calculation speeds on suitable hardware. Without a radical change in either computing hardware, such as a movement to a viable quantum processing method, or an analytical solution to arbitrarily large quantum systems, all that can be achieved is a minimisation of the "big iron" required. As a result of this, numerical methods will always be limited by the computational resources available, and the speed at which a large system is able to communicate between its individual components.

4.2.1 ARC1

ARC1 was the first large scale centralised HPC system at the University of Leeds. While it required many bugfixes, patches, and various home grown solutions to issues, it was a well used and user friendly machine. Chapter 5 was largely performed on ARC1 as we had access to private blades. This did not use a node syntax, instead nodes were allocated by a number of cores and

memory per core. While conceptually simple, it placed a heavy burden on the queuing system to efficiently allocate resources. This system should not be used on the more modern systems, and older scripts will likely be in need of updates.

The hardware specifications were as follows[141]:

- CentOS 5 based operating system
- 118 Sun X6725 Blade Server Compute Nodes with 2 servers per blade
  - 2× Quad-Core Intel X5560 2.8 GHz per server, 1888 cores total
  - 12 GB DDR3 Memory per server, 2.8TB total
- 4 AMD SMP Server Compute Nodes
  - 4× Quad-Core AMD 8384 2.7 GHz per server, 64 cores total
  - 128 GB DDR2 Memory per server, 512 GB total
  - 780 GB scratch RAID hard disk
- 8 HP Blade Server compute nodes with 2 servers per blade
  - 2× hex-core Intel 2.66 GHz per server, 192 cores total
  - 24 GB DDR3 memory per server, 384 GB total
  - 120 GB hard disk per server, 1.9 TB total
- 100 TB Lustre file system
- M2-72 IB Infiniband network connecting blades and file system

CASTEP-16.11 was compiled using the Intel 13.1.3.192 ifort compiler with IntelMPI 4.1.3 for parallel executable. MKL 10.3.2 and FFTW 3.3.3 were used as external math libraries. All were precompiled on the computer and linked to the CASTEP executable.

4.2.2 ARC2

ARC2 is the second and currently oldest running HPC system at the University of Leeds. It is far more standardised than its predecessor due in part to experience, and also being similar in design to the tier-2 system N8 Polaris. This is the first machine to allow for entire nodes to be allocated and controlled, giving a more versatile and flexible system that could be used in pure SMP, MPI, or hybrid modes for incremental improvements to computational efficiency.

The system statistics for ARC2 are as follows[142]:

- CentOS 6 based operating system
- 190 Blade server compute nodes.
- 2× 8-core Intel Sandy Bridge E5-2670 2.6GHz processors per node (3040 total).
- 32GB DDR3 1600MHz RAM per node (6TB Total)
- 170TB scratch memory storage
- InfiniBand high speed network between nodes

CASTEP-18.0 was compiled using Intel 16.0.2 ifort compiler with IntelMPI 5.1.0 for parallel execution. External libraries used were MKL 11.3u2 and FFTW 3.3.4, which were precompiled and linked as usual. Due to technical issues, at time of writing the ifort16 compiler in even numbered updates is highly recommended above newer versions.

4.2.3 ARC3

ARC3 is the newest and most versatile of the Leeds based HPC systems. While its core computing capability is a significant improvement over ARC2, it also contains a host of new hardware features for different types of computation. Most notable are the high power graphics processing units, which are optimised for physics and rendering, though generally less favourable for numeric computation than a CPU. There are also two nodes of Intel Xeon-Phi MCA processors, addressed in section 4.2.4. For the main work presented here however, it was the standard CPU power that was utilised for computation.

The hardware in the ARC3 system is shown below[143]:

- CentOS 7 based operating system
- 2× Intel Xeon E5-2650v4 2.2 GHz/1.8 GHz AVX on all except the Xeon Phi nodes
  - 252 nodes of 24 cores, 128 GB DDR4 memory, 100 GB SSD storage
  - 4 nodes of 24 cores, 768 GB DDR4 memory, 800 GB storage
  - 2 nodes of 24 cores, 128 GB DDR4 memory, 2 nVidia K80 GPUs, 800 GB storage
  - 6 nodes of 24 cores, 256 GB DDR4 memory, 4 nVidia P100 GPUs, 800 GB storage
  - 2 nodes of a Xeon Phi 7230 64 core CPU, 96 GB DDR4 memory, 16 GB high speed MCDRAM, 800 GB storage
- 836 TB storage in a Lustre file system
- High-speed Infiniband network at 56 GBit/s

FIGURE 4.2: A simple schematic of a NUMA system showing how memory and cache blocks are allocated on a multi-CPU system, and shared through a NUMA bridge.

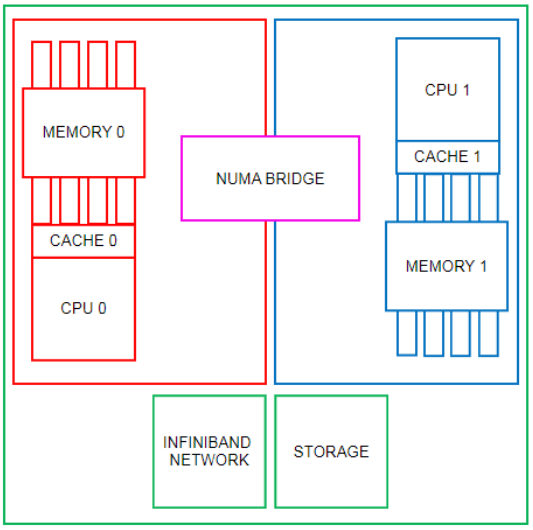

4.2.4 Hybrid Parallelism, Many Core Architecture, and Effective Utilisation of New Technology

Over the lifetime of this project, some interesting technologies have come to the forefront of computing. While simple ideals such as Moore's law discussed in chapter 2 provide a simple view of the increase in capability, the inevitable breakdown due to the simple limitations of size manufacturing requires that alternative methods are necessary to maintain progression.

The first that is important to note is hybrid parallelism, which has been mentioned previously as a way to reduce idling, but has come to the forefront in recent years as an important tool in its own right. First it is important to understand how a multiprocessor node is laid out. Figure 4.2 shows a simple schematic of how components are connected.

The only major difference from a familiar computer is the NUMA bridge, a proprietary technology that allows two regular CPUs and their individual memory allocations to communicate over a high-speed bus. Each CPU has its own cache and a number of cores, such as in ARC3 and ARCHER where each CPU is 12-core, giving a total of 24 cores per blade. Each blade is then connected through the Infiniband networking, another proprietary technology that allows high speed and high bandwidth but is ultimately a more powerful version of wired connections over ethernet. Understanding parallelism mechanisms is then about understanding how each shares its resources.

In order to facilitate the high speeds of modern processors with the limitations of the memory, there is an intermediate called the cache. This small, high speed memory acts as a buffer for the CPU and is shared by all cores. Information is moved between cache and memory by the processor automatically to have the most relevant data for the CPU ready for the current process.

In MPI we have processes, this is composed of a self contained block of memory containing all the information needed for a CPU core to calculate its designated share of the problem. In OpenMP we have threads, where multiple CPU cores are connected to the same block of memory and work together on the single problem. Thus the issues are clear. In MPI there is a lot of redundancy in the data, with RAM potentially containing many copies of the same information that must be regularly checked for errors among all processes in the standard "majority rules" method, and can cause issues in the cache due to each core requiring data that may be redundant.

The issue with OpenMP is the collaboration of CPU cores. While removing the redundancy of information as each core is working on the same memory set, and allowing cache to be used a lot more effectively, any delays in one core immediately affects the others, meaning that slower methods of access to

data can cause massive communication halts that the MPI redundancy eliminates. For instance, an OpenMP system can make very effective use of its own memory allocation and efficient cache management. However having to cross a communication bridge slower than the inter-core connections on the CPU and the cache, introduces large idle times, so even over a relatively fast connection such as the NUMA bridge if CPU0 has to access data in MEMORY1 for instance, the CPU will spend large gaps of time waiting. For a single CPU and memory allocation, MPI processes need to store some information in as many copies as there are processes, reducing the effective amount of memory per process that is available as well as the bandwidth of the cache per process. However, the communication between each process occurs infrequently, in many cases only at the beginning and end of calculations, reducing waiting time in the instances that there is a delay in access.

Recently, processor manufacturers have significantly improved the parallel handling of tasks, allowing sensible configurations to be handled automatically by the processor with little overhead, simplifying the process to a few simple rules. Most obviously, OpenMP threading should never be used beyond a single CPU and it's associated resources, so should always be a factor of the total core count. For instance, on a 24 core NUMA node containing two 12-core CPUs each process should use 2, 3, 4, 6, or 12 cores. 8-cores should not be used, as that would require sharing across the NUMA bridge.

The number of MPI processes should then match a parallelism scheme to allow each process to work as independently as possible, so for instance a system of 12 kpoints could have should have up to 12 processes, or a factor of this, e.g. 4 or 6. While the exact configuration can depend on many factors down to manufacturing of the individual CPU, it is often not practical to benchmark simple systems for each possible configuration. Therefore a good rule of thumb

for the current technology in ARC2 and ARC3, and by extension Polaris and ARCHER, is to use OpenMP and MPI in such a manner that each MPI process is threaded 4-ways through OpenMP. So if an example task on ARC3 were to have 24 k-points, then we could guess a good configuration would use 4 nodes, each with 6 MPI processes, using 4 threads per process. This would be requested in the submission script with the following line with the processes per node (ppn) and threads per process (tpp) flags.

```
#$ -l nodes=4,ppn=6,tpp=4
```

It is possible to use a wide variety of configurations that are likely to be very efficient, and also likely will take longer to benchmark than would be saved, however this represents a good rule of thumb.

Many-Core architecture is an extreme form of parallelism that is the conclusion of trends in the processor market for some time. In 2005, Intel changed the world when it brought the dual core processor to the market[144]. A single CPU that carried two discrete processor cores allowed for simultaneous code execution. In current technology Intel, AMD, and ARM microprocessors are built into virtually all devices, with common devices such as mobile phones carrying 6 or 8-core CPUs. In many systems, especially in devices that suffer from thermal throttling, the power of the cores are not as important as the efficiency at which software can be loaded evenly across a CPU. Another massively important technology was developed by Intel, that of hyperthreading. While developed decades ago, it became a staple of home computing in 2008. This allowed for simultaneous execution through the same processor core by executing other tasks while the CPU idled, for instance while waiting for information to be accessed in memory. This allows a single physical core to act as two virtual cores, with only a small overhead. These technologies changed the

way that personal computing operated, allowing for improvements across the board for work or personal use. In 2007 no matter the clock speed of the CPU, it was limited by the single core architecture, however now it is not unusual to see PCs with 8 virtual cores allowing for previously unimaginable productivity and multitasking on desktop computers.

Fuelled by the massive changes brought about by the introduction of multicore developments, Intel experimented with several ideas of how core increases could be used to streamline numerical simulations, linear algebra, and large scale matrix manipulation. In 2016 these efforts culminated in the Intel Xeon Phi Processor, a powerhouse of processing sporting 64 physical cores on chip, with 4-way hyperthreading for a total of 256 virtual cores per CPU. The tradeoff for such a high count is in the clock speeds, with a base of 1.30GHz compared to the 2.20GHz on the CPUs that make up the bulk of ARC3.

Benchmarking was performed based on the linear response calculation of barium titanate in chapter 5. Using parallel CASTEP-17.2 with ifort16, IMPI-2017, MKL 2017, and FFTW-3.3.6, identical linear response tasks were performed on a NUMA based Intel Xeon CPU E5-2650 v4 x2[145] node and an Intel Xeon Phi CPU 7230[146] with identical compile options with the exception of host optimisation for Xeon, and "-xMIC-AVX512" cross compilation for Xeon Phi for enhanced vectorisation. A transparent cache configuration is used, where a super-high speed MCDRAM bridge between the regular system memory and the onboard CPU cache is used as a high capacity cache to enable many MPI processes to continually move information from and to system memory without interference. Depending on the memory profile and requirements, this is entirely flexible between cache and system memory.

Figure 4.3 shows the individual perturbation cycling times for the phonon calculation on the Xeon Phi, the Xeon E5, and the doubled time for the E5.

FIGURE 4.3: Cycle times per perturbation for Xeon Phi, NUMA Xeon and hypothetical single Xeon (2*Xeon) CPUs. For this benchmark we used a linear response calculation for tetragonal barium titanate, with identical parameters used to the same calculation in chapter 5.

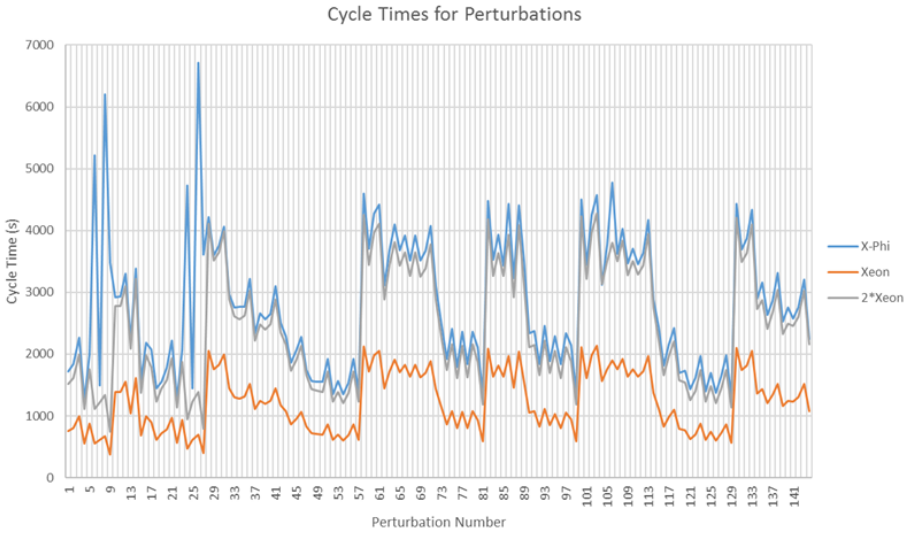

The reason for this is that the Xeon E5 NUMA configuration is a high speed connection between two processors. Thus assuming an ideal world, halving the CPUs to work out the single CPU performance doubles the time taken. This is obviously not true, but gives an ideal value.

Looking at these timings, we see that our hypothetical single CPU Xeon is almost identical to the Xeon Phi, although there are a few notable spikes. This could be due to mismatching seeds, or how the CASTEP code implements the Gamma-point calculation, and starting the path at a different place could have altered the timings. The pattern settles to an almost identical profile for the rest of the calculation. So we can say that given the price point and availability of the Xeon E5 there is no reason to be using the Xeon Phi. This is certainly true in the present, however it is definitely something to keep an eye on. While we expect that the enhanced vectorisation of the Xeon Phi is built into modern MKL and IMPI subroutines, it is unlikely to have been fully adopted in CASTEP or other dependant libraries. As these many-core

architectures become more refined and commonplace then development may shift to full integration of the features.

This leads to the second point, which is that the Xeon E5 second generation is a venerable beast of high performance computing, with the UK national HPC ARCHER and two of the top 10 world supercomputers (Piz Daint, Switzerland and Tianhe-2A, China[147] as of June 2018) being built on some variation of the platform. This means that testing, bug fixing, and improvements are likely to have been made on this specific platform, if not on the same model number. In contrast, the Xeon Phi represents the first in what could become a long dynasty of many-core processors, with each generation making incremental upgrades. Finally, our test is a classic case of CPU bound numerics, whereas many other applications have different hardware requirements.

Thus our results being equivalent shows the potential of this technology for its disruptive capability. The Xeon-Phi performing equivalently to its immediate rival in a test that overwhelmingly favours the Xeon E5 platform shows that for tasks where distribution is more important than CPU power this is already likely to perform better, along with programs which are optimised specifically for the new and powerful feature set. Not only that, but as this technology develops we will likely see larger incremental improvement from the newcomer than the long standing and well refined CPU. While it will not completely supplant the need for the traditional Xeon platform, there is likely to be a branching of the two technologies, where each evolves to fill a particular niche in the computing ecology. Thus it is essential that those in the high performance computing space are knowledgeable and prepared to ensure that the facilities and programs we use are tailored to take full advantage of the most suitable branch.

4.3 Methods and Algorithms Used in CASTEP Calculations

4.3.1 General Methods

At the core of every CASTEP calculation is the single point energy calculation. This is the self-consistent field (SCF) minimization to find the ground state by altering the electron density and solving for the energy. When the change of energy is within a set convergence value for consecutive minimizations the energy is determined to be converged to the ground state. As a general assumption, 100 cycles of this calculation were used as this number is usually sufficient for convergence, with more indicating issues with the calculation. Flags were set to treat the system as a non-metallic, non-spin polarised material in order to reduce the complexity of the calculation and save time.

During the SCF cycles the electron density undergoes a process called density mixing, where the new electron density requires a portion of the previous density to be mixed in order to create a stable calculation. The recommended scheme of Pulay density mixing was used for these calculations, which is a fast and generally suitable to most systems. For unusual systems with unstable electronic structures such as molecular ribbon monolayers, density mixing is unsuitable and instead the slower Ensemble DFT (EDFT) scheme must be employed. Initially, as we are dealing with a bulk insulator, this would simply increase the compute time considerably. For the same reason we have neglected to add empty bands into the structure and fixed the band occupancy in our initial work, as this is only required for unusual systems or specific calculations where the minimization benefits from being able to move electrons into higher

bands. For calculations involving bismuth ferrite however, extra bands and partial occupancy had to be employed for the calculations to work.

CASTEP's inbuilt speed optimisation was selected for the calculations. RAM is the fastest form of memory available to developers, as the system can read and write to it much faster than hard disk or flash memory, yet it is made directly available to a program. In order to increase the speed of a calculation CASTEP can be instructed to perform the entire calculation in RAM, only stopping to back up calculation data at set times. CASTEP can also be instructed to reduce the amount of RAM required by only storing SCF data in memory and read/writing all other steps to hard disk. This slows the calculation significantly, however can significantly reduce memory requirements.

In order to reduce the calculation time, the inbuilt symmetry finder for CASTEP was activated via the .cell parameter 'SYMMETRY_GENERATE'. At the cost of containing the system to a set symmetry, the Brillouin zone can be reduced to an irreducible form, significantly cutting down the number of k-points required as only k-points in the irreducible part are required for the calculations. The calculation is then mirrored to symmetrically identical parts of the Brillouin zone, with k-points weighted by the number of mirrored points.

4.3.2 Geometry Optimisation Methods

For geometry optimisation the recommended scheme is the low memory implementation of the BFGS algorithm (LBFGS). This method is identical to the BFGS method in chapter 3.2.1, however requires less RAM in its calculation. This method is recommended due to its lower system requirements, however for unusual systems there are many other schemes that can be used if LBFGS is found to be unsuitable for unusual systems.

The default bulk modulus estimation of 500GPa was used for all structures as they are 'hard' material. This can be optimised slightly by inputting a more accurate value for the bulk modulus; however this improvement is small as the algorithm automatically updates the bulk modulus used in the Hessian matrix with its own estimate as the optimisation is performed.

As the size and dimensions of the unit cell change, the finite plane-wave basis is altered. In order to account for this, CASTEP performs a stress calculation at the beginning of the optimisation in order to calculate the finite basis set correction. The default setting of 3 SCF calculations with different plane wave cut off energies was used to determine the dependence of the total energy on the logarithm of the cut off energy, i.e. $\frac{dE_{tot}}{dlog(E_{cut})}$. Using this quantity the finite basis correction can be made during the optimisation.

4.3.3 Phonon Methods

The phonon calculations were performed using CASTEP DFTP linear response[148] in chapters 5 and 6. Due to the requirement for a much more precise SCF cycle convergence the electron energy tolerance was lowered to $1 \times 10^{-10} eV$. This method is based on minimisation of second derivatives of energy by band calculation in reciprocal space. This is a fast and well implemented method in many popular DFT codes, however different implementations have different restrictions. In CASTEP, it is limited to finite band insulators with fixed electronic occupancy, and requires norm-conserving pseudopotentials.

For other materials, such as the bismuth ferrite in chapter 7 which has antiferromagnetic properties, the calculation requires empty bands and a variable occupancy unsuitable for the linear response calculation. For this, a more physical implementation is required for the calculation of phonon frequencies.

This is the finite displacement method of phonon calculation, based on real space ionic perturbations that make up the basis of phononic interactions. While this does not give electronic properties like the linear response calculation, including our effective ionic charges, it calculates the energy differentials through a robust method with very few limitations, however due to differences in how DFT handles unit cell boundaries and interatomic forces then a supercell approach is required to explicitly factor longer range cross-cell forces. This supercell can be created automatically in CASTEP by adding the 'SUPERCELL_MATRIX' block to the cell file to copy the unit cell in each direction a given number of times.

It is essential that different phonon methods are understood to ensure the best is used for a given system. Forethought into the calculations beforehand and studying the different mechanisms and outputs can ensure that these calculations, which are intensive and time consuming, allows the efficient allocation of resources.

Using these methods, which are basic functions in widely available DFT programs such as CASTEP, VASP, Ab-Init, or Quantum Espresso, we will build a framework to understand piezoelectrics on an atomistic scale.

Chapter 5

Piezoelectric Properties of Unary Perovskites

5.1 Introduction to Research on Unary Perovskites

In order to develop and test a methodology that will be applicable to all piezoelectric perovskite structures, it is important to select simple cases that cover a variety of the different formations of the material. To that end, three structures were selected.

The first, barium titanate ($BaTiO_3$), is a historic material in the field. First characterised by Megaw in 1945[35], the ferroelectric phase changes and easily recognisable structure has become emblematic of the field. Though it is generally not used in electronic applications due to its mediocre properties as a piezoelectric in comparison to its lead based counterparts, the long history of

the material has led to a wealth of information being available from countless studies.

The second, lead titanate ($PbTiO_3$), is an essential component of industrial piezoelectrics. The majority of piezoelectric materials used today are lead zirconate titanate (PZT), with more modern materials being fusions of this initial material with another piezoelectric, such as bismuth ferrite ($BiFeO_3$). The other component of PZT, lead zirconate ($PbZrO_3$), is a perovskite, however does not show piezoelectric or ferroelectric behaviour in its pure form, so is unsuitable for this study.

The third and final structure is potassium niobate ($KNbO_3$). Unlike the other structures which follow the II-IV valence model for perovskites, this material is based on I-V valances, where the A-site carries a charge of +1 and the B-site a charge of +5 in the classical model. It will be shown that while this is not the case, the effective ionic charges and overall electronic distribution are markedly different from the case of the II-IV materials. Though these materials are comparatively new in comparison to the other structures, they have gained in popularity due to their favourability over traditional lead based materials.

Notably absent from this list is the multiferroic material bismuth ferrite ($BiFeO_3$). While being able to model and compare the fundamental mechanisms behind its piezoelectric nature would be favourable, the methodology being used is not suitable for materials with the ferromagnetic characteristics present. While understanding this material can, and should, be explored, it is not feasible in the methodology presented in this chapter. It is instead studied as a separate system in chapter 7.

The compute configuration used is the ARC1 system setup detailed in section 4.2.1.

5.2 Performing the Calculations

5.2.1 Ground State Calculations

Two of the structures we are using can be thought of as non-ground state materials. That is, both barium titanate and lead titanate are not tetragonal at low temperatures, undergoing a phase transition to orthorhombic and finally rhombohedral as they approach absolute zero. Then under DFT it can be argued that the tetragonal structure is not the ground state, and therefore calculations involving them are invalid.

Realistically, DFT would not have become so widely used if it were only valid for true ground states at 0K temperature. Instead what we need to think of is the stability of of positions on a potential energy surface (PES), or as it is sometimes referred, free energy landscape. The potential energy surface is formed by calculating the continuous energy function across a set of structural, thermal, or conformational variables. Once we have a defined energy function it is possible to find the minima of the functions, and across the entire free energy landscape there will be a single minimum point with a lower energy than all others. This is the global minimum, or what we might consider the true ground-state.

Normally it is the Gibbs free energy considered in this type of system. The Gibbs free energy is given by equation 5.1[149, p. 70], with H being enthalpy, S being entropy, and T being temperature.

$$\Delta G = \Delta H - \Delta TS \tag{5.1}$$

The Gibbs free energy drives phase changes as it is a representation of the how the enthalpy, the thermodynamic property concerned with the energy of structure, is affected by thermal effects and entropy, two of the most important quantities in the physics of dynamical systems. As we do not take into account the thermal effects this can be reduced to the Gibbs free energy being equivalent to the enthalpy. Further, at zero pressure the enthalpy and free energy is reduced to the internal energy of the structure, which represents the total energy of the combined ionic and electronic energy. Then the minimum free energy defines the ground state across pressure and temperature, as well as many other possible phase parameters, defining the most energetically favourable state.

Figure 5.1 shows a simplified free energy function along a thermodynamic pathway X with two minima corresponding to phase 1 and 2. For illustrative purposes, we leave the pathway ambiguous. This is because this method is incredibly broad, as it is directly derived from the principle of least action. The thermodynamic pathway is a linear simplification of the multi-variate energy function. The Gibbs free energy is used in biophysics determining the free energy landscape from the arrangement of atoms in large molecules, and a reduced pathway may represent an average interatomic distance in order to determine the lowest energy arrangement of a folded protein. Similarly in magnetic or superconductive systems the free energy landscape may be based on spin ordering or coupling, and the pathway could be chosen to be a series of states of interest. It is even used in chemical reactions, to determine the activation energy and overall energetic favourability of the reaction.

So far so simple, but the difference in free energy between two structures is not the only factor in determining the phase. Consider carbon, which can be seen under normal conditions in the form of graphite, graphene, diamond,

FIGURE 5.1: A simple free energy curve for a two state system 1 and 2 along a thermodynamic path X, with a Gibbs free energy difference of ΔG_P and energy barrier of ΔG_B.

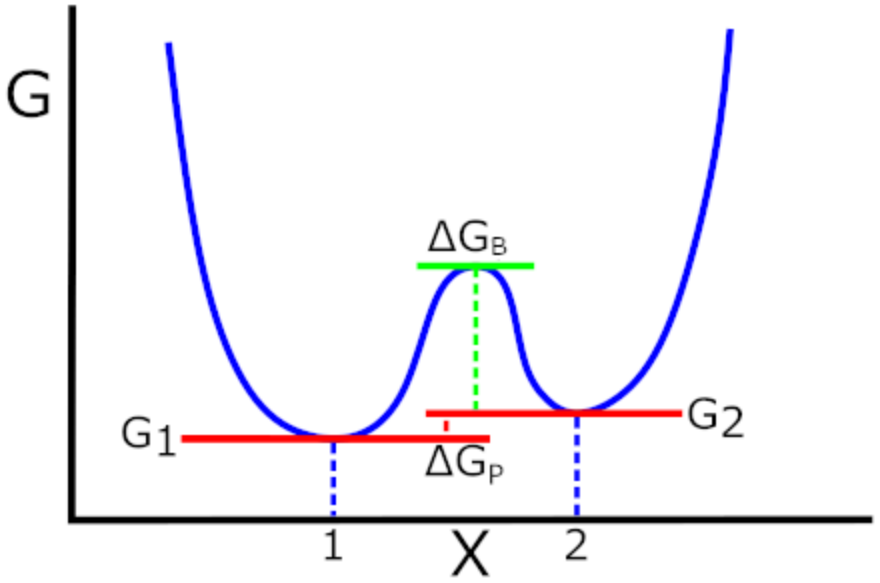

nanotubes, and fullerenes. Note that none of these are compounds, each is a structurally distinct form of pure carbon. If the only consideration was the minimum free energy then the only form of carbon would be graphite, and once the other forms were taken out of the pressure and thermal conditions that created them, they would instantly transform into graphite. Instead, we have a second quantity to consider, the free energy barrier. This is the energetic barrier to overcome in a phase transition and determines the rate of transition, or in other systems the rate of reaction by the relation shown in equation 5.2[150].

$$k = Ae^{-S\Delta G_B} \tag{5.2}$$

In our carbon example we know that graphite is the true ground state, or

stable state. Each of the others is a meta-stable state, and does undergo the transition to graphite, as the change in free energy is negative, therefore energetically favourable. However, given the large barrier for the transition, it may take millions of years for a regular piece of jewellery to fully convert.[151]

This is broadly applicable to any physical system, however now we must consider our specific system. The actual phase transition in multi-phase ferroelectrics such as barium titanate is based on the phonon properties, when the ferroelectric mode frequency drops to zero there is a spontaneous transition to a new state that becomes more energetically favourable. This is largely equivalent to expressing the phase change through a temperature dependant free energy pathway. However, each phase still exists across the free energy surface, especially when we remove the electric field and phonon behaviour and focus purely on the structural pathway. In DFT we consider a static snapshot of the system we are studying, with a defined free energy landscape for the material. Although there is one global ground state in the system, our method of geometry optimisation finds the nearest energy minimum for the structure. All states exist, and while it is important to consider the relative energy of each structure and the parameters of the minimisation algorithm, we know from the history of DFT that we are exploring the isolated energy well. This is the advantage to using the data collected from other studies as a starting point. We know that the structure will already be located in the region of the energy landscape that is associated with that particular state, and we are able to optimise to find the local ground state, which we are able to concentrate our studies on.

Applying DFT to a global landscape, rather than the local state that exists within a subspace of the landscape, is famously a weakness of DFT, as it is impossible to explore the continuous energy surface. While this is advantageous

for the study of a specific state, the AIRSS methodology attempts to populate a much larger space within the global landscape, and optimises to find all stable local minima. Though in practice it would take an infinite number of random structures to completely populate the energy landscape, this method has had great success in identifying interesting ground states, and the relative energy difference between them[152].

While the local ground state method does cause some problems, as we will see in subsection 5.2.6 due to the destabilisation of phonon modes associated with the changing phase, the use of the geometry optimisation method to find the local optimised structure is a core part of DFT studies, and we understand that despite some shortcomings in material properties, this is a well accepted and understood limitation.

5.2.2 Sample Structures

Crystallographic Information Files (CIF) were downloaded for the sample systems from ICSD[153]. After investigating potential structures, and viewing the structure through the visualisation program VESTA[154], a starting structure was chosen for barium titanate[34], lead titanate[101], and potassium niobate[116].

Some details of these database entries are as follows. BTO characterisation was performed at 290K, and the structure has the collection code 73643. PTO characterisation was performed at 293K, and the structure has the collection code 90693. KNO characterisation was performed at 550K, and the structure has the collection code 190921.

FIGURE 5.2: Sample structures for $BaTiO_3$ (left)[34] ICSD: 73643, $PbTiO_3$ (middle)[101] ICSD: 90693, and $KNbO_3$ (right)[116] ICSD: 190921, visualised using VESTA. Green – Ba, Blue – Ti, Red – O, Black – Pb, Purple – K, Sea Green – Nb.

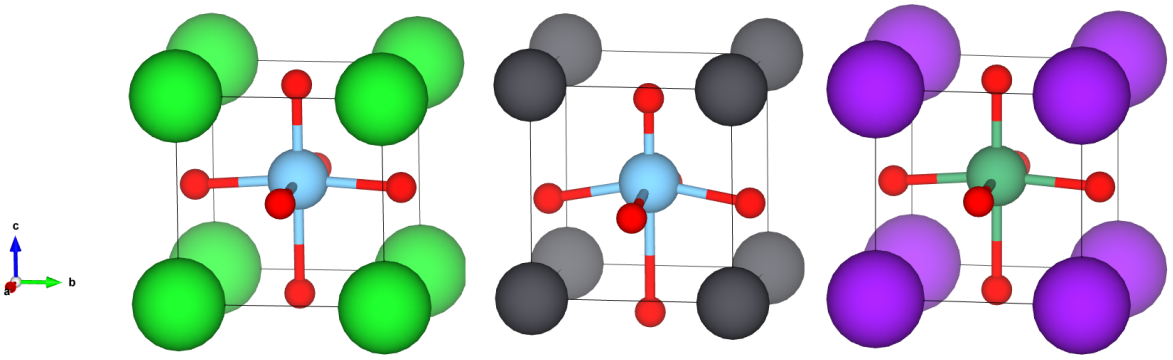

The visualisation of the three unit cells is shown in figure 5.2. Note that in the original file for lead titanate, the c-axis direction was anti-parallel to the direction of polarisation. This was reversed for consistency.

It is obvious that these materials are very similar in structure. Each one exhibits the classic perovskite structure of ABO_3. Each is a tetragonal structure with a space group of P4mm. This allows reduction of the polarisation to a single lattice axis giving a single element to focus on, as well as significantly reducing the number of piezoelectric coefficient elements. For lattices such as rhombohedral, different directional components will form matrix elements for lattice displacements, polarisation, and other properties.

5.2.3 Convergence Parameters

As with many numerical methods, there is a balance to be found between the precision of the calculation, and the amount of computing time and resources required. This is to do with the iterative nature of solving equations with no analytic solution. When we iterate, providing we are converging on a stable

solution, each iteration takes us closer to what we may consider as the "actual answer", however each iteration generally provides diminishing returns as the distance between successive iterative solutions lessens with each step. Convergence simply defines the level at which point the distance between each step, and therefore the distance to the solution, becomes insignificant to the task, and the iteration is complete.

In Density Functional Theory (DFT) calculations, this is almost universally reduced to two quantities, the kinetic energy cut off (E_{cut}), and the Monkhorst-Pack (MP) grid. There are no strict rules for the selection of convergence parameters, however it is important that it is both conclusive and sensible. Well-converged calculations can give new and unique insights into a system, while poorly converged calculations can give answers that lack any relation to physical behaviour.

The ferroelectric displacement of the material is highly sensitive to the forces applied on the atoms. As a result, it would be pertinent to select the forces calculated on the atoms as a figure of merit. This is calculated directly from the electron density as part of the self-consistent field (SCF) calculation, the most basic type of calculation available. This allows for convergence testing to be performed rapidly and reliably using automated scripting methods.

As later calculations would be based on the differences between the material at rest and under strain, this provided a basis for convergence testing, the difference in force calculations in the c-axis of the axial oxygen atom between a relaxed and strained structure. A rough calculation showed that the difference in force between the relaxed and expanded structure would be in the magnitude of $0.01 - 0.1 eV/\text{Å}$, so the calculation should be converged to less.

It was decided that the convergence parameters would be consistent across strain patterns, as these were the structures being directly compared, but not

across different chemical compositions. The structure and chemical composition defines the MP grid and cut off, respectively, therefore different materials should be converged separately and only indirectly compared.

5.2.3.1 Kinetic Energy Cut-Off

Every pseudopotential used was an OPIUM[111] generated, GGA, norm-conserving pseudopotential rated for a 'FINE' cut off of 680eV. Norm-conservation was required due using the linear response type phonon calculation later, therefore a higher energy cut-off than used in studies with ultrasoft potentials was expected. Single-point energy calculations were performed on a 4^3 MP grid for each material in a relaxed and strained state. The cut off energy was raised incrementally by 50eV every cycle from 400eV. The force on the target atom was extracted, and the change between successive cut off energies was calculated, known as the energy delta (Δ). The difference between these quantities for the two structures was calculated, which we name the diff, this was plotted against cut off energy. This is shown in figure 5.3. For readability, some extraneous points are omitted.

To ensure there are no convergence issues, and to ensure we are able to precisely optimise the geometry, we will define a kinetic energy cut off as converged when three successive points are $< 10^{-4} eV/\text{Å}$. We believe that this methodology, which we refer to a del-diff or Δ–diff, takes into account the successive changes in plane waves from the computational aspect, and the changes in the physical system we are considering, is suitable for this project.

From figure 5.3, the cut off is selected as $900eV$ for BTO, $850eV$ for PTO, and $1000eV$ for KNO. These figures are higher than the 'FINE' value given, which is expected, and well within the sensible capability of modern computation.

FIGURE 5.3: Plane wave convergence for the unary structures, showing how the force Δ-diff varies with increasing plane wave cut off for barium titanate (BTO), lead titanate (PTO), and potassium niobate (KNO).

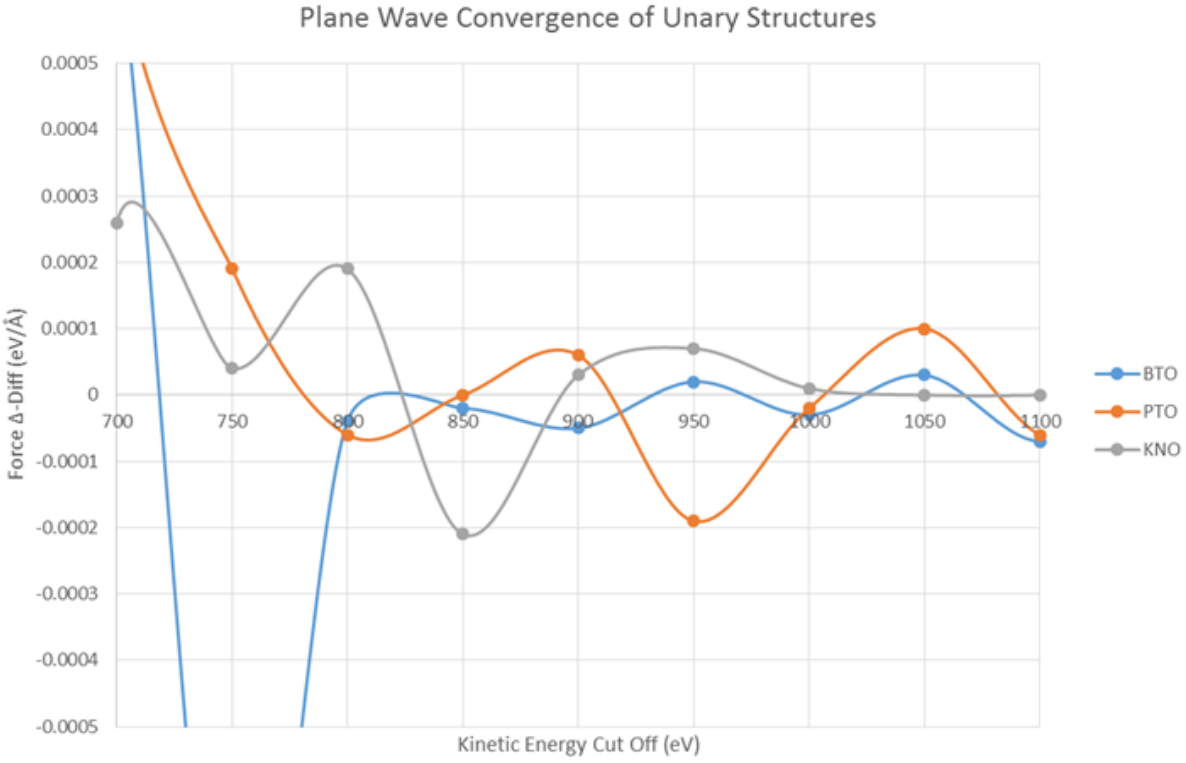

5.2.3.2 MP-Grid

It is essential that the Monkhorst-Pack is suitably converged. In compuatational terms, this acts as the sampling of grid elements in the reciprocal lattice, with a higher number meaning a greater density of grid points on which to calculate the electronic behaviour. As this must be an integer value, there is less freedom in terms of the values this can take. The number of points rises quickly in a three dimensional grid, leading to issues with the computing power available around 20^3. Additionally, there is the issue of diminishing returns as the grid becomes more dense. Consider the reciprocal lattice vector $c^* = \frac{2\pi}{c}$, which for barium titanate would be 1.54Å^{-1}. Then 4 k-ponts in this axis give a

spacing of 0.39Å^{-1}, and 10 k-points gives a spacing of 0.15Å^{-1}. However, if we consider the difference in spacing, or how much tighter our spacing becomes if we increase it by 1, then from 4 to 5 points decreases the spacing by 0.08Å^{-1}, whereas from 10 to 11 points only gives 0.01Å^{-1}. Thus while we are increasing the resources required polynomially, the amount by which we are tightening the spacing is decreasing exponentially.

In table 3.2 we see that previous studies have used a variety of grid densities, however we expect to see convergence at around the same 12^3 grid used by Evarestov.

If we were only considering the d_{33} element, we could apply a time saving measure by assuming that all electronic activity is occuring in the 3-direction, thus we could only converge the c-axis k-points. However, this would be an approximation, as we expect to see interesting behaviour in the 1,2-directions. Additionally, precision in these directions is necessary for studying the d_{31} piezoelectric coefficient. As such, all three axes are converged simultaneously and linearly with each other. This allows us to be agnostic to the features of the particular lattice symmetry, which is essential if we wish to observe, say, the piezoelectricity of a rhombohedral structure. We will, however, appeal to symmetry within CASTEP in order to find the irreducible Brillouin zone of the tetragonal structure, as this can drastically reduce the number of k-points actually required.

Ultimately, it may not be possible to see the same smooth, low tolerance convergence present in the plane waves. The same $\Delta - diff$ method is used, however in this case we simply seek a two-point plateau region in the plot. As the two convergences are independent of each other, we simply require both convergences to be "good", rather than equal. It is arguable that the convergence of both quantities is only as good as the weakest, however in

FIGURE 5.4: Force Δ-diff variation with Monkhorst-Pack grid for the unary structures seperated by odd and even values of the grid density for barium titanate (BTO), lead titanate (PTO), and potassium niobate(KNO).

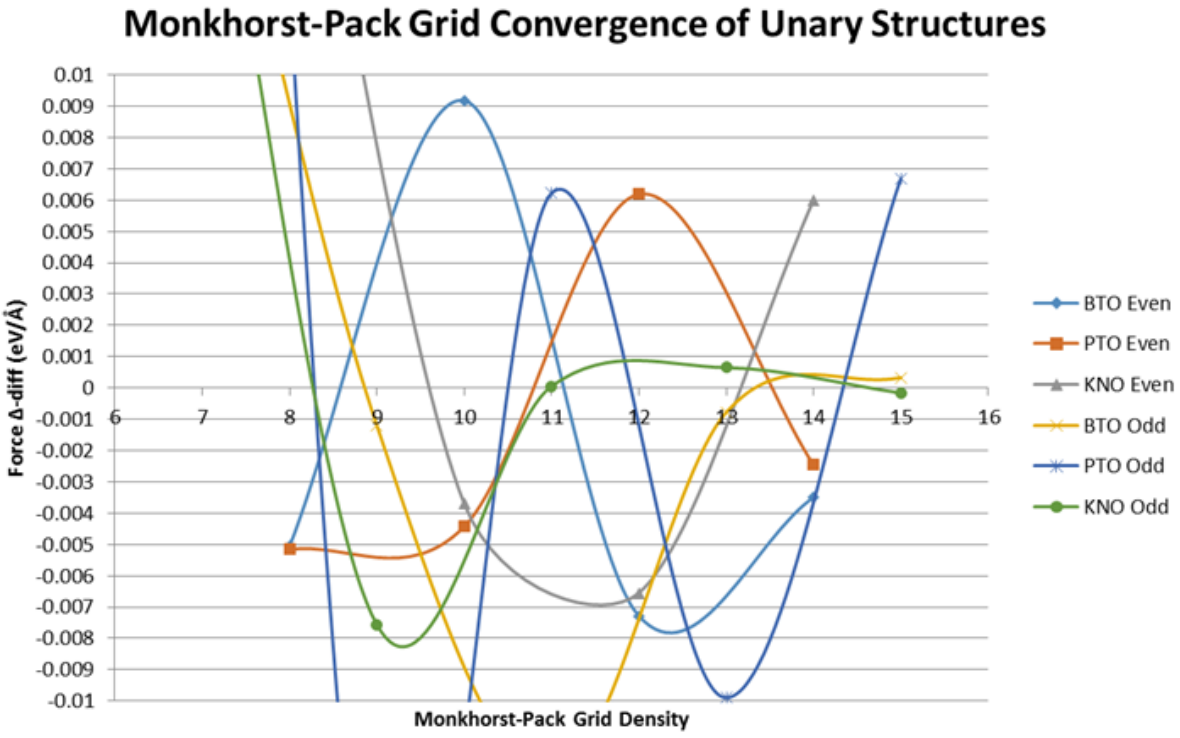

cases of truly independent quantities, it can also be argued that a hypothetical "total convergence" is some linear product. In this case, it would mean that the tight convergence of the plane waves makes up for a weaker Monkhorst-Pack convergence. Realistically, the different arguments are not clear cut, while there is merit to slightly different convergence levels, returns quickly become greatly diminished with larger differences between the two tolerances. On the advice of Dr. Hasnip, the number of k-points in the grid is sorted into odd and even values and these are treated independently. Figure 5.4 shows the odd and even Monkhorst-Pack grid using the $\Delta - diff$ method.

We see immediately that convergence is less obvious for the materials. However there are some plateaus occuring that we can select for our convergence. For

TABLE 5.1: Convergence criteria for future calculations.

	BTO	PTO	KNO
Energy Cut-off (eV)	900	850	1000
k-point Grid	15^3	10^3	13^3
k-point Spacing (Å^{-1})	0.0167	0.0256	0.0193

BTO this occurs at 13-15, for PTO 8-10, and for KNO at 11-13. Thus we will use grids of 15^3, 10^3, and 13^3 for BTO, PTO, and KNO respectively. These are reasonable for our calculation. While it may appear that these convergences are significantly less tight, it is important to remember that there are 3 axes each contributing to the precision. Converging each axis seperately would likely show that each one gives a precision equatable to our plane wave convergence, however performing such calculations are generally seen to be wasting resources due to the greatly increased number of calculations required, and the time taken to process them.

We have selected the convergence parameters for our system, as shown in table 5.1, and are now comfortable that future calculations will be physically relevant and computationally efficient.

5.2.4 Structural Optimisation

Once the convergence criteria have been met, it is essential to perform a geometry optimisation of the atomic structures to obtain the correct ground state in relation to our calculation parameters. From perturbation theory we know this will be above the true ground state of the actual system. We know that the actual ground state is far too complicated to solve, and the properly converged system is a "close enough" approximation for our purposes. Therefore, any further mention of the ground state will be in reference to our approximate ground state. Future computer systems may be able to calculate the actual

ground state, however such technology is firmly in the realm of science fiction at time of writing, as far as we know.

The calculation used the LBFGS scheme built into CASTEP. This is a low memory implementation of the BFGS algorithm, which is widely used for structural optimisation. Cell parameters and atomic positions were allowed to vary within the tetragonal coordinate system, reducing the MP-Grid to an irreducible symmetric zone, and reducing the number of free dimensions for the algorithm to search. This is a normal and widely used optimisation for this type of calculation.

As the research will be mainly focused on variance with stress, we will allow this property to freely vary during the optimisation of this and future structures, and the optimisation will use the force, energy, and displacement tolerances. This can be achieved by effectively setting the flag 'geom_stress_tol' to a value that is arbitrarily large, such that the calculation will always be within this value. These tolerances were set to an energy tolerance of $2 \times 10^{-8} eV$, force tolerance of $1 \times 10^{-4} eV/\text{Å}$, and displacement tolerance of 5×10^{-6}Å. These are tight tolerances, in order to fully capture the positional and force dependences of the ferroelectric displacement. The number of cycles required was higher than usual due to this tight tolerance, but was easily remedied by increasing this number from 100 to 300. The non-symmetric lattice parameters and atomic positions are given in table 5.2.

These values agree with our experimental data, with slight deviations which is expected from both the approximations inherent to numerical methods, and the well-known under-binding of the GGA functionals.

Additionally, the temperature effects can be discussed in order to explain some deviation, especially in the case of the high value of the c-parameter in PTO.

TABLE 5.2: Lattice parameters, tetragonality, volume, and fractional positions of the original .cif files and the optimised structures. We list the temperature of the experimental data and collection code from ICSD. Experimental data is based on the following references. BTO - [34], PTO - [101], KNO - [116].

	BTO		PTO		KNO	
	Expt.	Calc.	Expt.	Calc.	Expt.	Calc.
a (Å)	3.9925	3.9940	3.9039	3.8934	3.9979	3.9929
c (Å)	4.0365	4.0738	4.1348	4.3060	4.0645	4.1187
c/a	1.0110	1.0200	1.0591	1.1060	1.0167	1.0315
Vol ($Å^3$)	64.342	64.984	63.016	65.273	64.963	65.666
Pos_B	0.5215	0.5143	0.4719	0.4584	0.5171	0.5147
Pos_{Oaxial}	0.9747	0.9721	0.8661	0.8723	0.9740	0.9665
$Pos_{Oradial}$	0.4895	0.4808	0.3870	0.3664	0.4791	0.4691
ICSD Code	-	73643	-	90693	-	190921
Temp. (K)	0	290	0	293	0	550

DFT is well known to be strongly temperature-agnostic, and as such the optimised structure is referred to as 'extrapolated to 0K'. That is, even if the material does not exist at absolute zero due to phase changes, the results are interpreted as if a snapshot of the material was cooled until no heat energy remained. What this is actually based on is that the ions are static. On an atomic level, heat is considered to be representative of a magnitude of vibration. Low vibrational energy means the ions require less space, higher vibrations force ions to move more, which creates familiar effects on the macroscale such as thermal expansion of most metals. Although we see that there is a significant difference between the experimental temperature and our absolute zero state, thermal coefficients are numerically small and therefore we accept this as a noticeable but unavoidable weakness in our method.

For an approximate idea of the total thermal expansion effect, we can make some calculations. The thermal expansion coefficient of barium titanate at room temperature is in the order of $\alpha = 10^{-5}K^{-1}$[155]. We know that for a material, the change in length due to temperature is given by $\Delta L = L\alpha_L\Delta T$,

where L is the initial length, α_L is the coefficient of expansion in that direction, and ΔT is the change in temperature, then the change in length over a 300K difference is $\Delta L \approx 1.2 \times 10^{-2}$Å, or 1.2pm. In reality the thermal expansion coefficient tends to decrease with decreasing temperature, so the actual value is likely to be less. Then accounting for thermal expansion would give an increase of ¡1% of our lattice parameters, which we consider to be a small procedural error of the methodology which we are aware of, but can consider to be unimportant.

In these tetragonal structures, it behaves slightly differently due to the imbalance in the c-axis and the a,b-axis. This can be seen in figure 5.5, where the c-axis increases greatly in PTO, while the a-axis, and consequently b-axis, contract with decreasing temperature.

While this is most prominent in lead titanate, it happens to a lesser degree in the other two materials. Though the gradient becomes shallower approaching zero Celsius, the lattice parameter theoretically should continue increasing as we extrapolate down to 0K, accounting for larger c-parameter values and higher tetragonality. The tetragonal symmetry of the system is preserved so symmetric coordinates are omitted.

5.2.5 Linear Response Phonon Calculation

Linear response calculations were performed to calculate the Born effective charges, or effective ionic charges. This is easily performed by using the CASTEP task 'Phonon+Efield' which enables the DFPT package[148]. Though these tasks can be performed separately, the amount of crossover between the "big iron" computations involved makes it extremely efficient to perform both,

FIGURE 5.5: Thermal effect on lattice parameters for lead titanate (PTO)[1, p. 116].

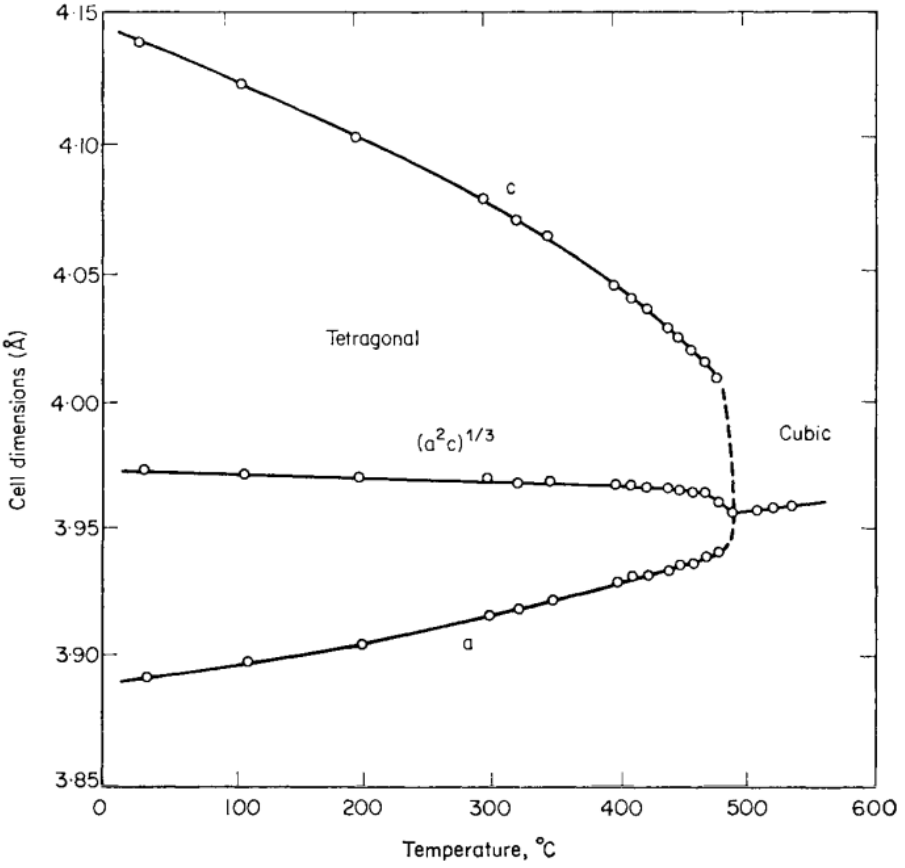

rather than running one and having to perform the other later. This is followed directly from the geometry optimisation step using the 'reuse' flag in the param file, which automatically imports the relaxed structure to machine precision, as well as data on forces, stress, and the full electron density.

We discovered that the effective charge matrices are invariant across the Brillouin zone, therefore for optimisation we only consider the Γ–Point. Only considering one point significantly reduces the number of perturbations that must be calculated. In addition, the phonon frequencies are all real at the gamma point, whereas imaginary frequencies may occur elsewhere. CASTEP cleverly contains a subroutine that makes all frequencies numerically real if

only the Γ–Point is specified. Since Fortran handles complex numbers as two real numbers with the imaginary constant $i = \sqrt{-1}$ (the famous $z = x + iy$ representation of complex numbers), this significantly reduces memory and compute time by only calculating the real portion, safe in the knowledge that the computed imaginary part would yield zero.

The Born effective charge tensor is a symmetric, 3×3, rank-2 tensor. However, in this symmetry all elements of the tensor such that for $i \neq j$, the elements are equal to zero. As such we can represent the charge matrix as a vector of the diagonal elements without loss of information. These charge vectors are shown in table 5.3.

We see that the charges are wildly different from the classical valance model, both in value and the fact they are not spherical, but instead produce elliptical geometry. The A and B site atoms act as electron donors to the oxygen atoms. We see in the case of the Pb and Nb ions, that the difference between the classical valance (+2 and +5 respectively) and the actual effective charge is significant. This justifies our rejection of the LDA functional, as it does not take into account gradients of the electron density function, which appear significant.

5.2.6 Dielectric Permittivity

The dielectric permittivity tensor is calculated as part of our electric field perturbation, with the results shown in table 5.4. This is generally calculated by the software, however in the case of barium titanate and potassium niobate, there is an ionic instability that causes a failure. This is due to the fact that these structures do not exist at 0K, both undergo phase transformations to the orthorhombic state, with a rhombohedral state at low temperature. This

TABLE 5.3: The calculated non-zero components of the Born effective charge tensor in units of electron charge for barium titanate (BTO), lead titanate (PTO), and potassium niobate (KNO).

	BTO			PTO			KNO		
	xx	yy	zz	xx	yy	zz	xx	yy	zz
$A(e)$	2.716	2.716	2.813	3.755	3.755	3.381	1.138	1.138	1.204
$B(e)$	7.397	7.397	5.976	6.157	6.157	5.121	9.461	9.461	6.743
$O_{axial}(e)$	-2.031	-2.031	-4.868	-2.029	-2.029	-4.327	-1.509	-1.509	-5.205
$O_{radial-1}(e)$	-2.158	-5.923	-1.961	-2.679	-5.204	-2.088	-1.780	-7.310	-1.371
$O_{radial-2}(e)$	-5.923	-2.158	-1.961	-5.204	-2.679	-2.088	-7.310	-1.780	-1.371

TABLE 5.4: Incorrectly calculated dielectric permittivity tensor (Perm.) elements and ferroelectric mode frequencies for the sample materials. This shows the unstable phonon mode extrapolated to negative frequencies in the BTO and KNO and resulting incorrect anisotropy in the permittivity tensor. For reference, PTO does not undergo this phase change and shows the expected behaviour of a larger permittivity perpendicular to the direction of polarisation than parallel to it. This occurs because the ferroelectric mode is responsible for the overall permittivity behaviour in ferroelectric materials, however the calculation of the dielectric tensor forces negative modes to be suppressed, removing them from the calculation.

	BTO		PTO		KNO	
	11	33	11	33	11	33
$Perm., \epsilon$	9.892	23.213	44.917	13.627	11.170	16.956
$Perm., \epsilon\epsilon_0 (\times 10^{-10} F/m)$	0.876	2.055	3.977	1.207	0.989	1.501
$FEMode, (cm^{-1})$	-116.157		91.895		-134.906	

is circumvented by effectively ignoring unstable modes. Normally the first 3 modes would be ignored, however in these cases the first 5 have been removed.

As temperature decreases, the ferroelectric mode frequency tends to zero. This drives the phase change to the orthorhombic state. However, in our calculations we have retained the tetragonal state to absolute zero, extrapolating this mode to negative wavelengths. In lead titanate, which does not undergo a phase change, this mode remains positive.

The necessity to ignore this ferroelectric mode in order to make the calculation means that the primary electrical behaviour of the ferroelectric is discarded. Therefore these results are given only for completeness, and this should act only as a cautionary tale that simply because a calculation can produce a result, it should be considered with a critical view and not implicitly trusted.

5.2.7 Elastic Constants

The elastic constants matrix was calculated using Andrew Walker's elastic constants scripts packaged with CASTEP and with updated versions on GitHub[156]. This analysis tool takes an optimised structure, generates a series of strain patterns, calculates the stress formed by these strains, and analyses them in order to generate the 6×6, rank-2 elastics tensor. This follows the usual material tensor form, indices 1-3 are based on directional stresses, and 4-6 are rotations around the 1-3 axes. Through symmetry, many of the matrix elements of the tetragonal structure are either equal, or zero. Two strain patterns are necessary for our systems, and 6 steps of 0.25% maximum strain were selected, for consistency with our own strained calculations. One of the full elastic tensors is shown in matrix 5.3.

$$\begin{bmatrix} 0.00441 & -0.00108 & -0.00171 & 0.00000 & 0.00000 & 0.00000 \\ -0.00108 & 0.00441 & -0.00171 & 0.00000 & 0.00000 & 0.00000 \\ -0.00171 & -0.00171 & 0.00715 & 0.00000 & 0.00000 & 0.00000 \\ 0.00000 & 0.00000 & 0.00000 & 0.01055 & 0.00000 & 0.00000 \\ 0.00000 & 0.00000 & 0.00000 & 0.00000 & 0.01055 & 0.00000 \\ 0.00000 & 0.00000 & 0.00000 & 0.00000 & 0.00000 & 0.00857 \end{bmatrix} \tag{5.3}$$

Given the size of the tensor, it is helpful to reduce it to its unique components. These are the diagonal components; $s_{11} = s_{22}$, s_{33}, $s_{44} = s_{55}$, and s_{66}, and the off diagonal components; $s_{12} = s_{21}$, and $s_{31} = s_{32} = s_{13} = s_{23}$. Table 5.5 gives the unique elements of the elastic tensors for the unary perovskite structures, with the units changed to inverse terapascals rather than gigapascals for readability. Table 5.5 also includes the calculated Young's modulus in the 1 and 3 (a- and c-axis) for reference.

Table 5.5: Calculated unique elastic constants and Young's modulus for BTO, PTO, and KNO.

	BTO	PTO	KNO
$s_{11}(TPa^{-1})$	4.410	8.504	3.883
$s_{33}(TPa^{-1})$	7.146	54.036	6.854
$s_{44}(TPa^{-1})$	10.554	19.953	15.033
$s_{66}(TPa^{-1})$	8.568	10.945	11.599
$s_{12}(TPa^{-1})$	-1.083	0.213	-0.929
$s_{13}(TPa^{-1})$	-1.711	-12.347	-1.321
$Y_1(GPa)$	226.76	117.59	257.54
$Y_3(GPa)$	139.94	18.51	145.91

We see that mechanically, barium titanate and potassium niobate are very similar. Despite their vastly different ionic composition, the bulk elastic constants are numerically close in all axes. Lead titanate by comparison, is hugely different in the 3-axis, the direction of polarisation. When it comes to the changes in polarisation due to mechanical strain, we would expect this elasticity to contribute to a significantly larger piezoelectric constant.

5.2.8 Strain Behaviour

In order to examine the strain behaviour, we select two strain patterns with two strains each. Other effects may require many more data points, but piezoelectricity being a linear effect, this should be sufficient. We select a 0.25% expansive and -0.25% compressive strain uniaxially in the 3-axis and biaxially in the 1,2-axis in order to study the change in polarisation in the 3-axis, allowing us to calculate the d_{33} and d_{31} elements of the piezoelectric tensor.

We take the lattice parameters from the optimised structure and write four new cell files, two for the 3-axis expansion and compression, and two for the 1,2-axis expansion and compression. This is easy to do manually; simply have the geometry optimisation output a cell file, manually calculate the strained

lattice parameters, and add constraints to the relevant axis. This allows a geometry optimisation to be performed on the atomic positions and other lattice parameters. It is important to add the constraints, as otherwise the minimisation of force, stress, and energy will simply return to the optimised, relaxed structure. Unfortunately, the current linux shells are incapable of maths with floating point numbers, so automating this would require a more advanced language, such as python or ruby.

Optimising these cells give us new lattice parameters and ionic positions that represent how the material relaxes under mechanical stress, an interesting viewpoint for the study of piezoelectric materials. This approach does assume that the composite ions (and electrons) in a material have sufficient time to relax under stress, however as even the most punishing ultra-sonic frequencies have cycles in the order of $\approx 0.1\mu s$, this is a reasonable assumption.

Table 5.6 gives lattice parameters and z-components of fractional positions for the relaxed cell and the strained cell, along with the z-component of the symmetrised stress tensor. We include for a more complete picture the lengths of the axial bonds between oxygen and the B-site ion separated into Bond-S (B-S) for the short length and Bond-L (B-L) for the longer length. The axial asymmetry is a distinguishing feature of this type of material, and we will need to consider the ratio of the bond lengths at a later time. Additionally, for comparison, we give a percentage difference from the relaxed structure for the lattice parameters and ionic positions.

We see that under strain, we do not see a linear repositioning as we might expect from a regular material. That is, the movements of ions are not linearly proportionate to the strain applied, with relatively large shifts observed particularly in the positions of radial oxygen ions. This, at its heart, may be the driving force behind the piezoelectric effect. In lead titanate the movement of

TABLE 5.6: Structural parameters of the unary perovskites under strain. C represents compression and E expansion. 33 is a strain in the c-axis and 31 are strains in the a,b-axes. The percentage is the difference from the rest state. Down the table are the independent lattice parameters, tetragonality, volume, fractional ionic position, short and long bond lengths for the Ti-O bonds, and the stress on the material in the direction of strain.

	BTO Strains								
	Rest	C33	%δ	E33	%δ	C31	%δ	E31	%δ
a (Å)	3.994	3.996	0.05	3.992	-0.05	3.984	-0.25	4.004	0.25
c (Å)	4.074	4.064	-0.25	4.084	0.25	4.086	0.30	4.062	-0.29
c/a	1.020	1.017	-0.30	1.023	0.30	1.026	0.56	1.015	-0.54
Vol (Å^3)	64.98	64.89	-0.14	65.08	0.14	64.86	-0.20	65.12	0.21
Frac Ti	0.514	0.514	-0.07	0.515	0.06	0.515	0.08	0.514	-0.09
Frac O_{ax}	0.972	0.974	0.15	0.971	-0.15	0.971	-0.15	0.974	0.14
Frac O_{rad}	0.481	0.482	0.18	0.480	-0.18	0.480	-0.22	0.482	0.21
B-S (Å)	1.865	1.868	0.14	1.863	-0.13	1.863	-0.11	1.867	0.11
B-L (Å)	2.209	2.196	-0.58	2.221	0.57	2.223	0.65	2.195	-0.63
T (GPa)	0.000	-0.279	-	0.266	-	-0.748	-	0.740	-
	PTO Strains								
a (Å)	3.893	3.896	0.05	3.891	-0.06	3.884	-0.25	3.903	0.25
c (Å)	4.306	4.295	-0.25	4.317	0.25	4.341	0.81	4.273	-0.78
c/a	1.106	1.103	-0.30	1.109	0.31	1.118	1.06	1.095	-1.02
Vol (Å^3)	65.27	65.18	-0.14	65.36	0.14	65.47	0.30	65.09	-0.28
Frac Ti	0.458	0.459	0.05	0.458	-0.05	0.458	-0.05	0.459	0.04
Frac O_{ax}	0.872	0.874	0.17	0.871	-0.16	0.868	-0.46	0.876	0.45
Frac O_{rad}	0.366	0.368	0.28	0.365	-0.28	0.364	-0.78	0.369	0.77
B-S (Å)	1.782	1.783	0.05	1.782	-0.04	1.780	-0.11	1.784	0.12
B-L (Å)	2.524	2.512	-0.46	2.535	0.46	2.560	1.45	2.488	-1.41
T (GPa)	0.000	-0.034	-	0.037	-	-0.245	-	0.270	-
	KNO Strains								
a (Å)	3.993	3.995	0.04	3.991	-0.04	3.983	-0.25	4.003	0.25
c (Å)	4.119	4.108	-0.25	4.129	0.25	4.130	0.28	4.108	-0.26
c/a	1.032	1.029	-0.29	1.035	0.29	1.037	0.53	1.026	-0.51
Vol (Å^3)	65.67	65.56	-0.16	65.77	0.16	65.52	-0.22	65.82	0.24
Frac Ti	0.515	0.515	-0.04	0.515	0.03	0.515	0.07	0.514	-0.08
Frac O_{ax}	0.967	0.968	0.15	0.965	-0.15	0.965	-0.15	0.968	0.14
Frac O_{rad}	0.469	0.470	0.21	0.468	-0.20	0.468	-0.34	0.471	0.32
B-S (Å)	1.861	1.863	0.10	1.859	-0.10	1.858	-0.12	1.863	0.12
B-L (Å)	2.258	2.246	-0.54	2.270	0.54	2.272	0.62	2.245	-0.58
T (GPa)	0.000	-0.291	-	0.270	-	-0.863	-	0.869	-

the radial oxygen ions is significant in comparison to the other materials. This calls into question some of the simplified models, in which the central chain of O-B-O is considered to contain the piezoelectric behaviour. The non-linearity is also present in the changes in bond length, with the longer of the bonds undergoing a far greater change than the shorter. We must consider how, if any, this structural feature is related to the overall properties of the material.

We know that in amorphous structures of lead titanate the non-linearity of the Ti-O bonds is scientifically interesting, as it is responsible for the photoluminescent effect in this material at room temperature[157]. This would be an interesting system to study, however DFT is highly unsuitable for macroscale amorphous materials due to the infinitely repeating unit cell discussed in section 2.2.3.2.

Under DFT, we know that an ionic movement is simply part of an electronic movement, where changing patterns of electron density encapsulate both electronic and ionic movement. It may be interpreted in molecular methods as the ionic movement driving electronic movement, the two are undeniably intertwined. However, there seems to be a distinct splitting in this between the ions affected most drastically by the electronic charge component of the Born effective charge, and the movement caused by mechanical strain. Alternatively, it could signal the opposite, as if the massive electronic charge acts as a mechanical stabiliser, and the radial oxygen movement is due to much of the electronic structure having been brought into the central O-B-O chain.

5.3 Analysis of Results

Once the calculations have been performed, we must consider the results of our simulations in a larger context. The quantities that we find most interesting

are the polarisation, and the piezoelectric coefficient, so we must consider how our results can give us access to these. We must also consider convention, to ensure our results can be fairly used and compared.

5.3.1 A note on the calculation of d_{31}

It was decided that the for the d_{31} component, the symmetry would be retained through the biaxial straining in the symmetric axis. While efficient, this raises the question of what our results will represent. As in a tetragonal structure we know that $d_{31} = d_{32}$, do we interpret the two stresses independently such that $d_{total} = d_{31} + d_{32} = 2d_{31}$, or that the strains occur as a result of pressure applied through the [110] direction, such that $d_{total} = \sqrt{d_{31}^2 + d_{32}^2} = \sqrt{2d_{31}^2} = \sqrt{2}d_{31}$. Ultimately, we decided that as our method was based on the combination of two uniaxial strains, it should be considered as such, thus we use the first approach. The factor of $\sqrt{2}$ between the two approaches is not significant for our aims, however does indicate that our bidirectional strain does not translate directly to a strain of the same quantity in a single direction, and changing from a clean 0.25% value to an irrational factor is undesirable.

5.3.2 Derivation of an Equation for the Calculation of Electric Polarisation

The polarisation and effective charges are strongly linked, however it is important to ensure that this is well defined for our method. That way, we can be transparent and unambiguous in our methodology. We begin with the equation for the Born Effective Charge[158].

$$Z^*_{k,ij} = \frac{\Omega}{|e|}\frac{\partial P^i}{\partial r^k_j} \tag{5.4}$$

First we must define our model. We will use a structural polarisation, fixed-ion approximation; that is, the polarisation is purely a result of ionic positions in the static structure. This can be expressed as $\vec{P} = \vec{P}(\vec{r})$.

Then we can replace the partial differential with a total differential, as $\frac{\partial \vec{P}}{\partial \vec{r}} = \frac{d\vec{P}}{d\vec{r}}$.

$$Z^*_{k,ij} = \frac{\Omega}{|e|}\frac{dP^i}{dr^k_j} \tag{5.5}$$

We can then rearrange the equation and create an integral problem to be solved.

$$\int dP^i = Z^*_{k,ij}\frac{|e|}{\Omega}\int dr^k_j \tag{5.6}$$

We must define a boundary condition in order to properly evaluate the indefinite integrals. We define a zero polarisation state $\vec{P}_0 = 0$ by appealing to the symmetry breaking of the system. In the paraelectric cubic system, there is no polarisation as ions are at totally symmetric coordinates in the structure. If we define a constant $\vec{r}_{symm}$ to be the absolute displacement of the ion at the totally symmetric fractional position, then we can define a displacement from the zero polarisation $\vec{r'} = \vec{r} - \vec{r}_{symm}$. Thus we have the condition that at $\vec{P}_0$, $\vec{r'} = 0$. It is trivial to perform a change of integration variable as $d\vec{r} = d\vec{r'}$. This gives us the following.

$$\int dP^i = Z^*_{k,ij}\frac{|e|}{\Omega}\int dr'^k_j \tag{5.7}$$

$$P^i - P_0^i = Z^*_{k,ij}\frac{|e|}{\Omega}(r'^k_j - r'^k_{j,0}) \tag{5.8}$$

Then by our boundary condition we know that $\vec{P}_0, \vec{r'}_0 = 0$. So we see the following.

$$P_i^k = \frac{Z^*_{k,ij} r_j^k |e|}{\Omega} \tag{5.9}$$

Then, by applying our knowledge of the tetragonal symmetry that i=1,2 are symmetric, so polarisation only occurs in the i=3 direction, and that the total polarisation is the sum of the ionic polarisations, we find the following.

$$P_{Tot} = \sum_k \frac{Z^*_{33} r'_3 |e|}{\Omega} \tag{5.10}$$

This gives us our equation for the polarisation, based on the effective charge and position of the ions.

5.3.3 Spontaneous Polarisations of Sample Structures

The spontaneous polarisation is a defining feature of ferroelectric materials, and such we must be able to calculate this value. Table 5.7 shows our calculated values using equation 5.10 in comparison to literature values from Jaffe, 1971[1].

Again, we see a general agreement with experimental results. We know that due to the increase in c-axis and decrease in a-axis with decreasing temperature, the spontaneous polarisation is increased. We see that our values are consistently overestimating, which is in line with this increase, and further

TABLE 5.7: Calculated spontaneous polarisation of barium titanate (BTO), lead titanate (PTO), and potassium niobate (KNO) alongside experimental values from Jaffe[1]. Taking into account thermal effects, where the spontaneous polarisation is reduced under increasing temperature, these values show excellent agreement with the experimental values. Also of interesting note is that our calculated value for KNO is identical to the one calculated by Wan, et al[118], indicating that we may have used similar methods to calculate the polarisations.

	BTO		PTO		KNO	
	Calc.	Expt.	Calc.	Expt.	Calc.	Expt.
$P_S(C/m^2)$	0.30	0.26	0.95	0.81	0.36	0.30

semi-empirical models could potentially take this value and make adjustments based on thermal behaviour if such steps were needed.

5.3.4 Piezoelectric Coefficients of Sample Structures

The piezoelectric coefficient (d_{ij}) is arguably the single most important measure of a piezoelectric material, as it is the measure of the amount of current released by a piezoelectric upon deformation, or alternatively the magnitude of deformation that may be achieved under an electric field. This is the cornerstone of many piezoelectric applications.

In order to calculate these components, we take the strain geometry from section 5.2.8 and use equation 5.10 to calculate the new polarisation of the structure. For the Born effective charge, we have a choice on whether to recalculate the Born effective charges for the new structure or continue to use the values previously calculated.

It was chosen that these new polarisations would be calculated using the previous effective charges for two reasons. Firstly, we look at the definition given by Gonze and Lee[158], "The proportionality coefficient relating, at linear order,

the polarization per unit cell, created along the direction β, and the displacement along the direction α of the atoms belonging to the sublattice κ, under the condition of a zero electric field". We can take that the Born effective charge is effectively the gradient of a linear function, and as such should remain constant under atomic displacements, whereas using new values would give a non-linear (or closely linear) curve which goes against such definitions.

Secondly, the phonon calculation is a computationally intensive task which, for the changes in geometry we observe, gives very little change to effective charges. As such we would question the necessity of using resources in such a manner. However, we accept that some may make equally valid arguments for recalculation.

The d_{ij} component is a the change in polarisation in direction i due to a stress in direction j, so we can simply plot the calculated polarisation in the c-axis due to the strain in the c-axis for d_{33} and a,b-axes for d_{31}, and apply a linear fit of $y = mx + c$. The piezoelectric coefficient is the gradient m, and the y-axis intercept c is our spontaneous polarisation. As we have previously calculated the intercept, we can subtract this in order to show a direct comparison between the three materials. Figure 5.6 shows this comparison.

Table 5.8 gives the calculated piezoelectric coefficients for the structures.

We see that while our predictions of polarisation were well in line with the experimental data available, there is a significant difference in our predictions and the measured quantities for the piezoelectric coefficient. In the publication by Wan, et al.[118] that we have discussed in chapter 3, they also reported an error of roughly factor 2. While this is disheartening, given the comparisons of the spontaneous polarisation, it does confirm that the fundamental issue is with the DFT method used to study it, and as a result there may be a clear procedural reason if we were to break down the DFT codes to their

FIGURE 5.6: Changes in polarisation against stress for BTO, PTO, and KNO with linear fittings and linear equation.

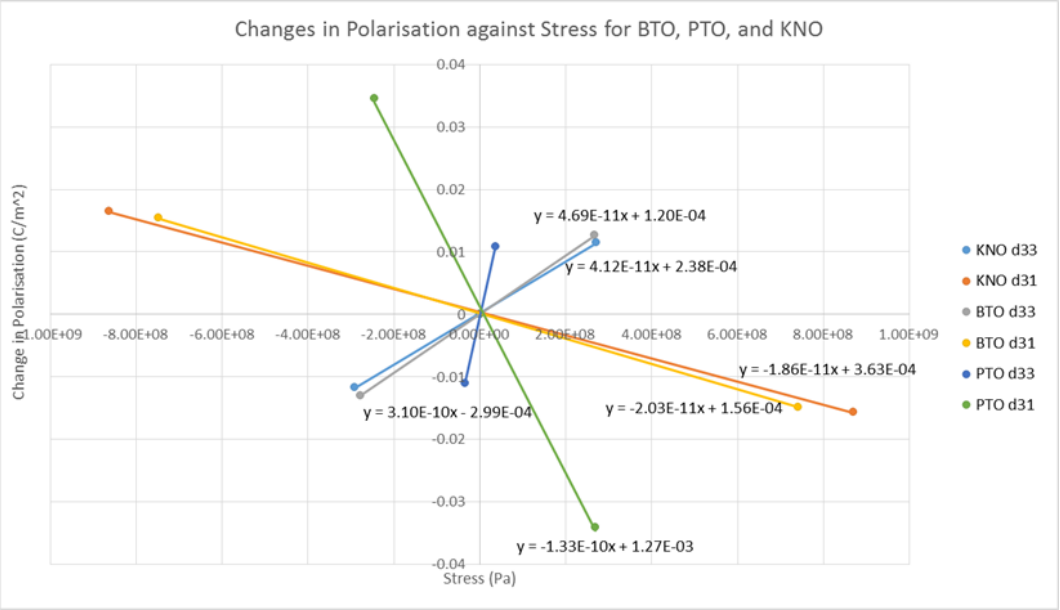

TABLE 5.8: The calculated piezoelectric coefficients of barium titanate (BTO), lead titanate (PTO), and potassium niobate (KNO), with experimental values for comparison. We see that despite the positive results for the spontaneous polarisation, there are large numerical differences between our calculated piezoelectric coefficients and the experimentally reported ones, similar to the differences found by Wan, et al.[118]. However, the values for KNO are in good agreement with their calculated results, indicating they also used a similar method to us to calculate these values. While the numerical values are considerably different, the overall trends have been preserved, so it seems that our simulations are still representative of the patterns in the real system, just not to a precise degree.

	BTO		PTO		KNO	
	Calc.	Expt.[31]	Calc.	Expt.[159]	Calc.	Expt.[160]
$d_{33}, pC/N$	47	86	310	193	41	30
$d_{31}, pC/N$	-20	-35	-133	-25	-19	-22

bare essentials. Ultimately though this is a fairly large error numerically, it does demonstrate the trends present in experimental comparisons of these two piezoelectric modes, which indicates that the computational system is still representative of the real system, though it would be ideal if this was more precise.

5.3.5 Electron Density Mapping

DFT is inherently based on the energy functional mapping the electron density field to the scalar value of energy. Therefore a natural part of the any task is the calculation of this electron density field. This is fundamentally a representation of electronic probability, much like the radial probability densities that can be found using traditional quantum mechanics of atomic electronic states by calculating solutions to Legendre polynomials. The full derivation of this is available in any good undergraduate textbook, such as Dunningham and Vedral[161], but the end result is the familiar electronic structure notation, e.g. $C = 1s^2 2s^2 2p^2$. While this approach is exactly solvable for hydrogen, larger atoms and even simple diatomic molecules rapidly require extraordinary computational power to calculate a numerical solution. As we have already discussed, this is where the strength of DFT lies, by mapping this large interacting problem to a simpler non-interacting model. In fact, a great advantage of DFT is that while there is a clear connection between the real electron density field and the non-physical wavefunction, we can discard this level of unnecessary abstraction in favour of a more real quantity, that of the static charge distribution.

Philosophical considerations aside, in reality quantum probability and static distribution are two sides of the same coin. It should be understood that the classical interpretation of the electron density field, i.e. where electrons

TABLE 5.9: Core and valance electron structures for each element, based on information within the norm conserving pseduopotential.

Ion	Core	Valance
Ba	$1s^2 2s^2 2p^6 3s^2 3p^6 3d^{10} 4s^2 4p^6 4d^{10}$	$5s^2 5p^6 6s^2$
Pb	$1s^2 2s^2 2p^6 3s^2 3p^6 3d^{10} 4s^2 4p^6 4d^{10} 4f^{14} 5s^2 5p^6$	$5d^{10} 6s^2 6p^2$
K	$1s^2 2s^2 2p^6$	$3s^2 3p^6 4s^1$
Ti	$1s^2 2s^2 2p^6$	$3s^2 3p^6 3d^2 4s^2$
Nb	$1s^2 2s^2 2p^6 3s^2 3p^6 3d^{10}$	$4s^2 4p^6 4d^4 5s^1$
O	$1s^2$	$2s^2 2p^4$

are, is equivalent to the quantum interpretation, i.e. the probability of a wavefunction collapsing to a certain outcome on measurement based on its probability density.

First we generate the charge density file for the rest and strained structures, either at runtime for the geometry optimisation task, or using the method outlined in section 5.3.5.1. Figure 5.7 shows the visualisation of the total static charge density for each structure at rest.

For consistency we have selected a saturation of 150 units, with a binding iso-surface of 15 units. This allows for a clearer image as it discards the high density of core electrons within pseudopotentials, as well as removing the insignificant regions of low electron density that are hard to discern due to colouration.

We see immediately that the electron density is highly localised around each ion. We know that a certain number of the electrons are bound in core states within the pseudopotential, and should be considered immobile. Table 5.9 shows the core (pseudo) and valance (explicit) electrons for each ion.

As expected, many of the total number of electrons are in the core region and therefore are locked in the pseudopotential. This is a great boon in terms of the efficiency of the calculation. If we assume, as is common, that only the

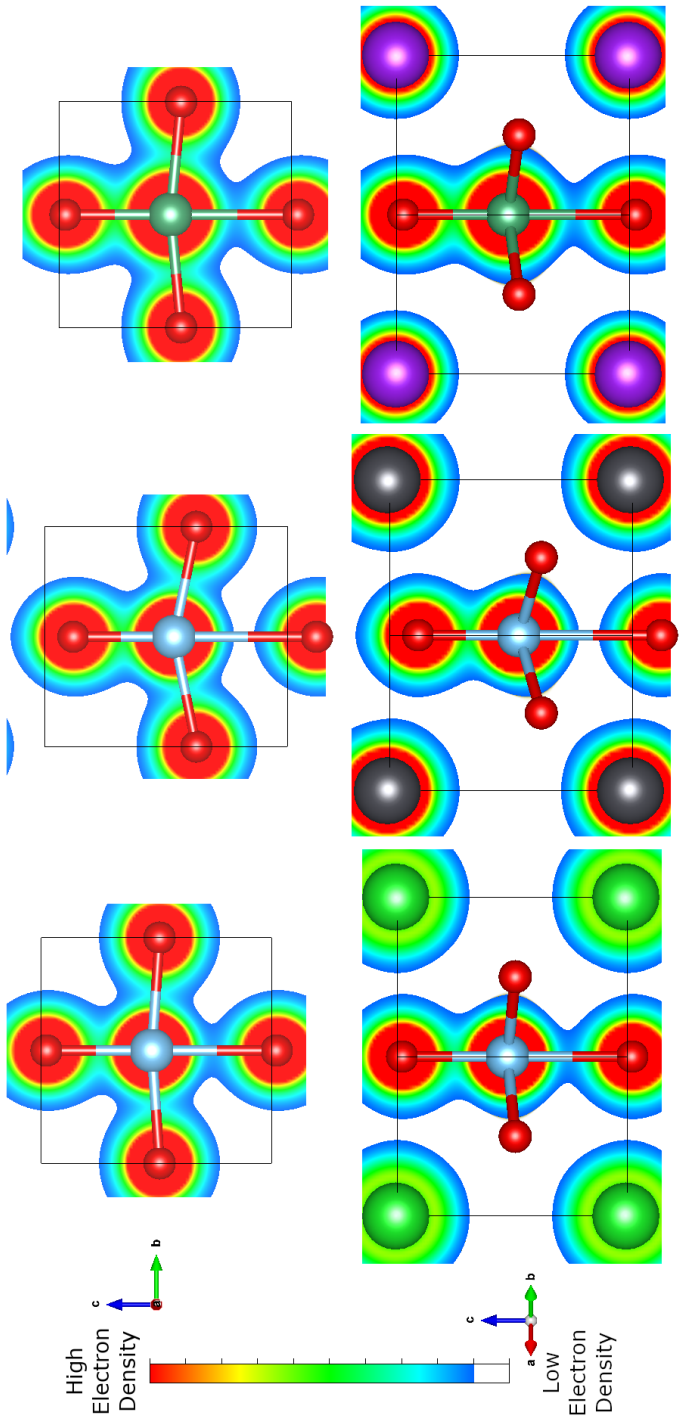

FIGURE 5.7: Cross sections of static charge density of BTO (Left), PTO (Middle), and KNO (Right) in the (100) plane at 0.5d from the origin (Top) and (110) plane at 1d from the origin (Bottom), where d is the inter-planar spacing for those planes.

valance states are involved in the material structure, then we are saving a huge amount of computation time in comparison to an all-electron code like Wien2k. Though the downside is that if core electrons are involved, this detail is lost.

5.3.5.1 A Note on Software Compatibility

The electron density field is automatically calculated and stored in a binary file as a natural part of any CASTEP calculation. However, to visualise this takes a few extra steps. Firstly, the .param file for the CASTEP task must have the flag 'WRITE_FORMATTED_DENSITY' set to TRUE. This outputs a highly verbose .den_fmt file. If the calculation has already been performed, this file can be generated at negligible cost from the binary output by using the REUSE flag on the binary file with the same .param, with the addition of the above flag. CASTEP will load the results of the previous calculation, and output a new set of output files with virtually no new calculation necessary.

The file contains a header and 4 columns. The first three are positions on the FFT grid the calculation used, and the fourth is the "charge", a positive number (despite electronic charge being negative by convention) that gives the number of electrons at the listed grid point, multiplied by the total number of grid points. There are two modifications that must be made for compatibility with VESTA. Firstly, the extension must be changed from .den_fmt to .charg_frm in order for VESTA to recognise the file. Second, the header must be deleted and replaced with a single string of the form `X Y Z ‘‘a b c charge’’` where X, Y, and Z are the dimensions of the FFT grid. This is given in the original header, in the .castep output file, or by looking at the last line of the density/charge file to see how the final point is labelled. Note the double quotes in the string.

This file contains only data on the charge distribution. If you want to overlay this information on a crystallographic model, a .cell file must be present in the same directory as the .charg_frm with the same name, e.g. barium-titanate.cell and barium-titanate.charg_frm in the same directory.

5.3.6 Electron Density Shift

In order to calculate the movement of electrons under strain, we subtract the static charge distribution at rest from that under strain. This effectively gives us the numeric difference at any point in the structure, with a positive number indicating electrons moving into a region, and a negative number indicating a movement away from a region. As should be expected, the number of electrons is conserved between the two calculations, so all increases should be balanced by decreases over the whole grid.

As FFT grids are necessarily dense, it is inadvisable to attempt this manually, and virtually any language should be able to automate the process of calculating the difference at each point. To keep it simple, we accept a slight change in the volume of each grid element to retain the same number of elements, so there is a one-to-one mapping between grid elements and a simple subtraction is all that is required, albiet some half-million times.

A prototype command using bash/awk to obtain the change in static charge for the expansion-33 (E33) strain pattern for suitably named barium titanate charge files would be the following:

```
join BTO_E33.charg_frm BTO_Rest.charg_frm |
awk '{ print $1,$2,$3,$4-$7 }' >
BTO_E33_Difference.charg_frm
```

This adds the columns of the rest file to the right of the columns in the strained file, then deducts the charge at each grid point and outputs the charge difference at each point to a new file. It is important to ensure the line numbers for each point match before performing this command, so it can be worth removing the header entirely and creating a new one after this process.

The electron density maps for each strain pattern are shown across the (100) and (110) plane in figures 5.8, 5.9, 5.10, and 5.11.

This forms the crux of the new research in this thesis. The view of the piezoelectric effect purely as an intrinsic property, on the atomic level. A novel way of understanding the fundamentals of the piezoelectric effect from the smallest scale possible is important to our overall view of the phenomenon. Understanding the electronic response of the ions is key to designs of future materials, as if we know the interaction of that atom explicitly, it is easier to replace.

Beginning with what might be considered the primary piezoelectric mode, the figures 5.8 and 5.9 show the static charge difference of the d_{33} piezoelectric coefficient in action. We see that each lobe of electron movement is localised to an individual atom. It is possible to identify a zone in which the vast majority of the charge movement is unambiguously tied to a single atom in the structure.

In terms of fundamental understanding, this is highly advantageous for an interest in the effects of different elements in the similar structures. In section 5.3.7 we discuss the idea of a partial piezoelectric coefficient, in which we consider the polarisation components by individual atom, and how the contribution is broken down.

Most obvious between expansive and compressive modes is the fact that they mirror each other completely. This confirms the linearity of the piezoelectric

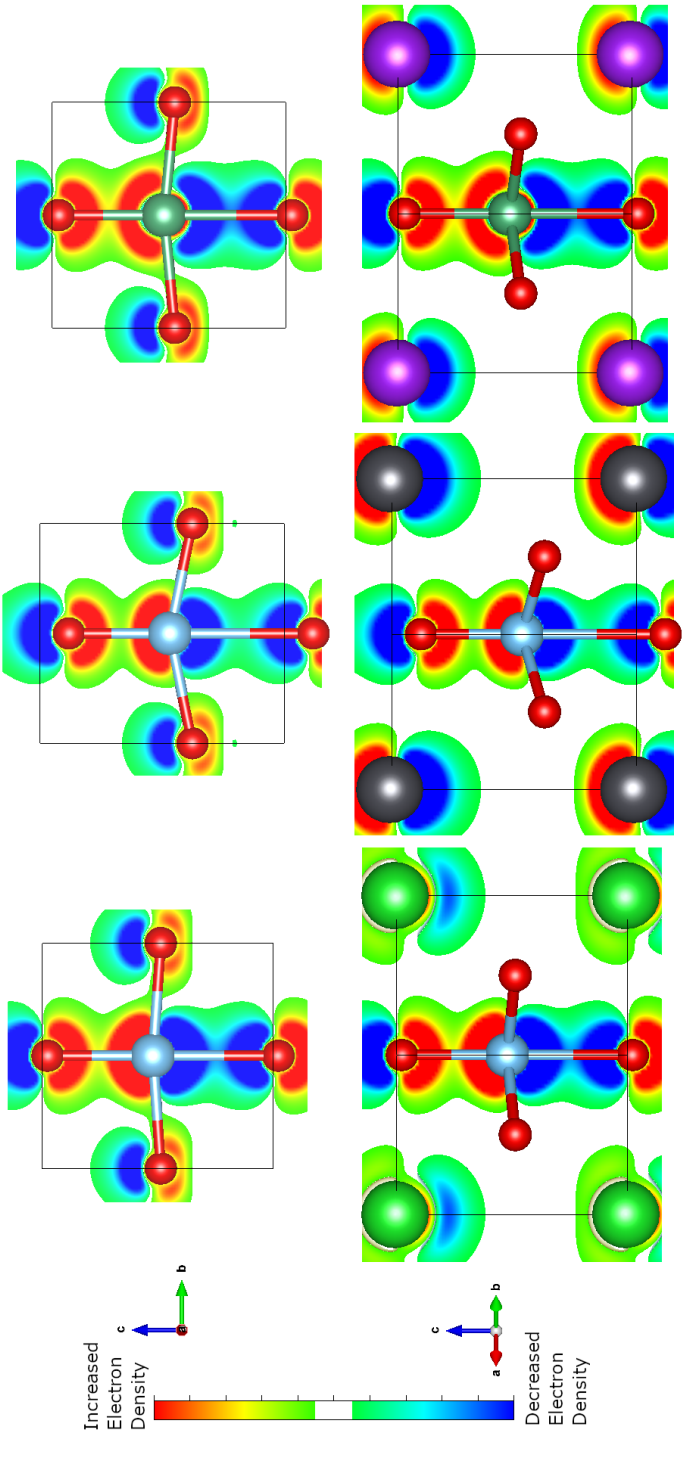

FIGURE 5.8: A cross section of the electron density shift of BTO (Left), PTO (Middle), and KNO (Right) in the (100) plane (Top) and (110) plane (Bottom) due to expansive strain in the c-axis.

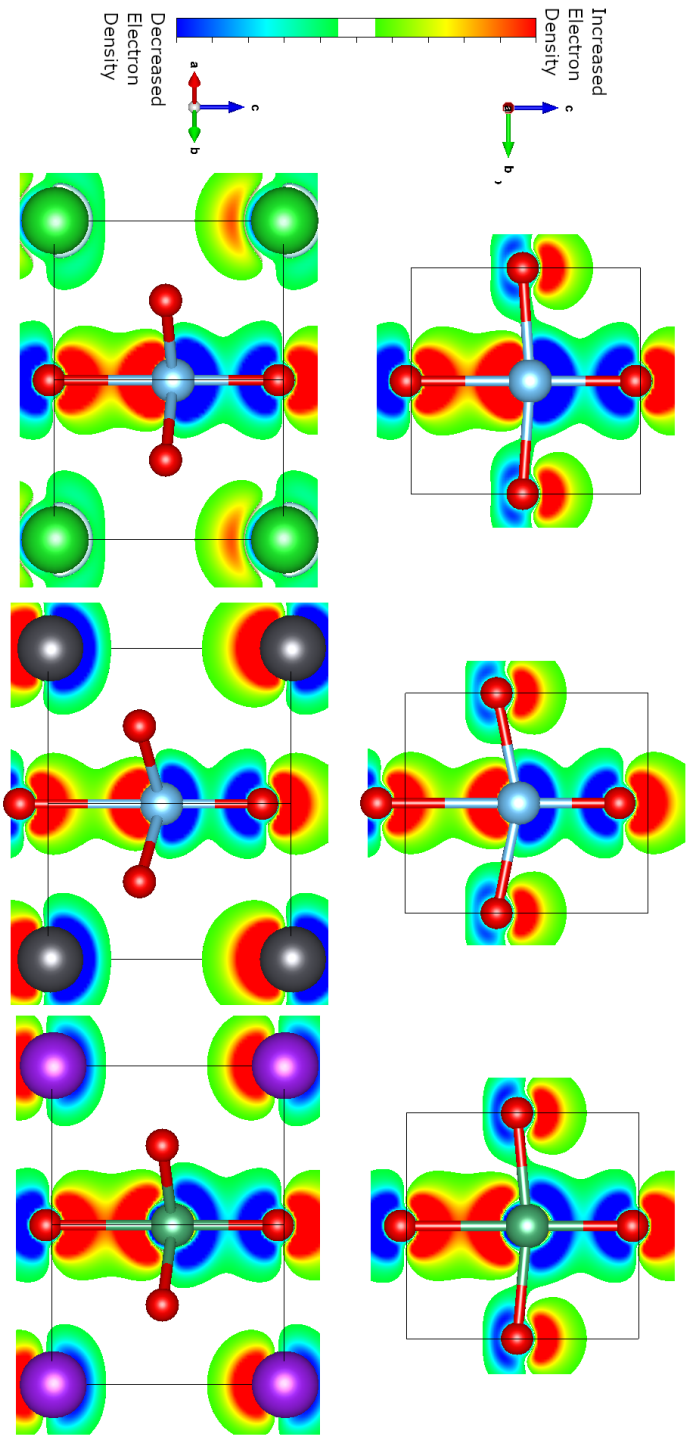

FIGURE 5.9: A cross section of the electron density shift of BTO (Left), PTO (Middle), and KNO (Right) in the (100) plane (Top) and (110) plane (Bottom) due to compressive strain in the c-axis.

effect with strains and thus stresses on the material. This is indicative of the macroscale effect where an alternating current causes oscillations in mechanical perturbation, or the converse equivalent, by a reverse of the electron movement happening depending on the direction of the oscillation.

It is also important to consider the shape of the charge differences. In this d_{33} component we see that there is a high degree of directionality. This is to be expected, as the the polarisation change and stress are parallel in the c-axis. This leads the lobes of the charge movement to be mainly focused in that direction. Most notable is the central O-B-O chain, in which there is a recurring pattern of short and long bonds along an alternating pattern of closely connected lobes of density movements. We recall from table 5.6 that the longer of these bonds changes significantly more than the shorter. In these density maps we see that both appear to have equal, although opposite, changes in charge density.

Comparing the different species of atoms within the structure, there is little to see between the initial d_{33} figures. In the O-B-O chain, the density lobes are more localised in the PTO structure, whereas in other structures the electron movements are more dispersed among the length of the bonds. In regards to the A-site, there is much greater involvement in the PTO and KNO structures, whereas the barium ion does not appear to induce much of a charge difference in BTO. These effects may suggest that the O-B-O chain largely defines the piezoelectric behaviour, and while we know that the A-site atom modifies behaviour this may not be direct, but an indirect effect on the electron sharing in the central chain. This would explain similarities in BTO and KNO, with differences in PTO, based on the figures we have created.

Turning to figures 5.10 and 5.11, the change in static charge density occurs across much more of the unit cell volume. While still localised, the overlap is

FIGURE 5.10: A cross section of the electron density shift of BTO (Left), PTO (Middle), and KNO (Right) in the (100) plane (Top) and (110) plane (Bottom) due to expansive strain in the a- and b-axes.

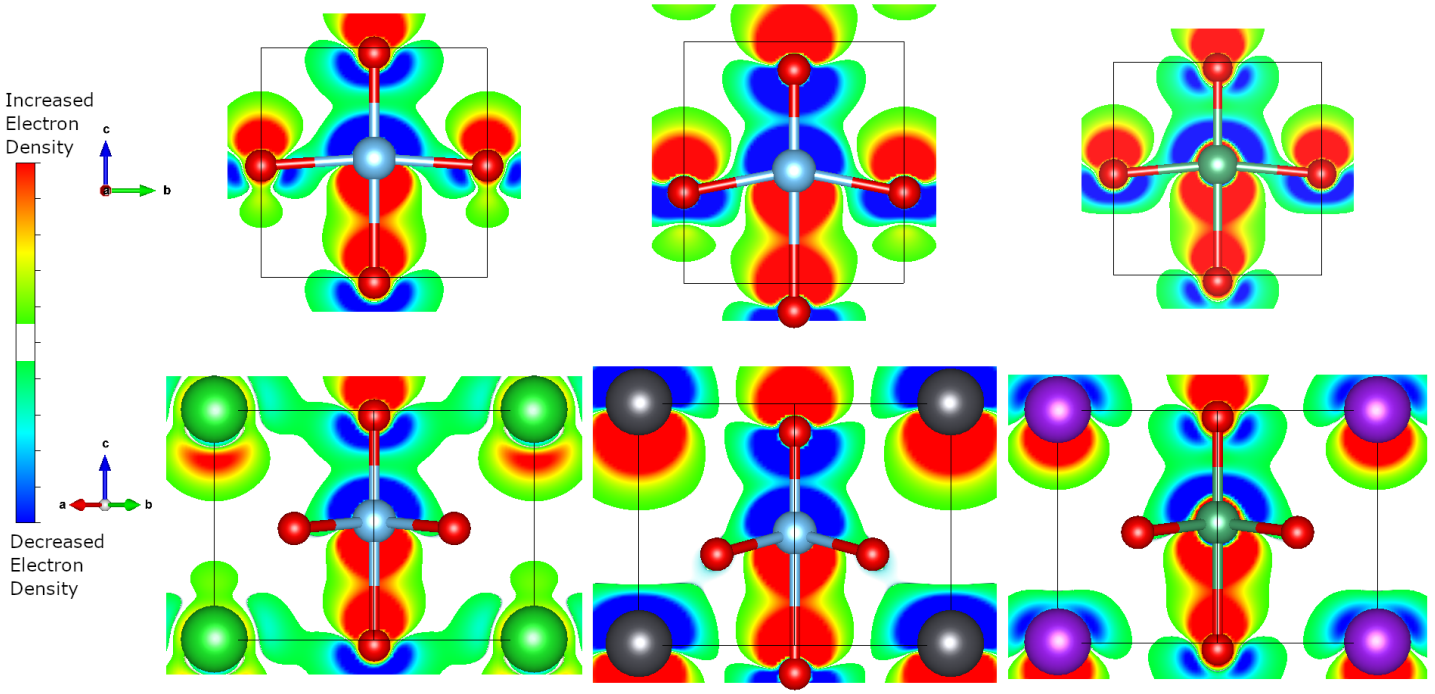

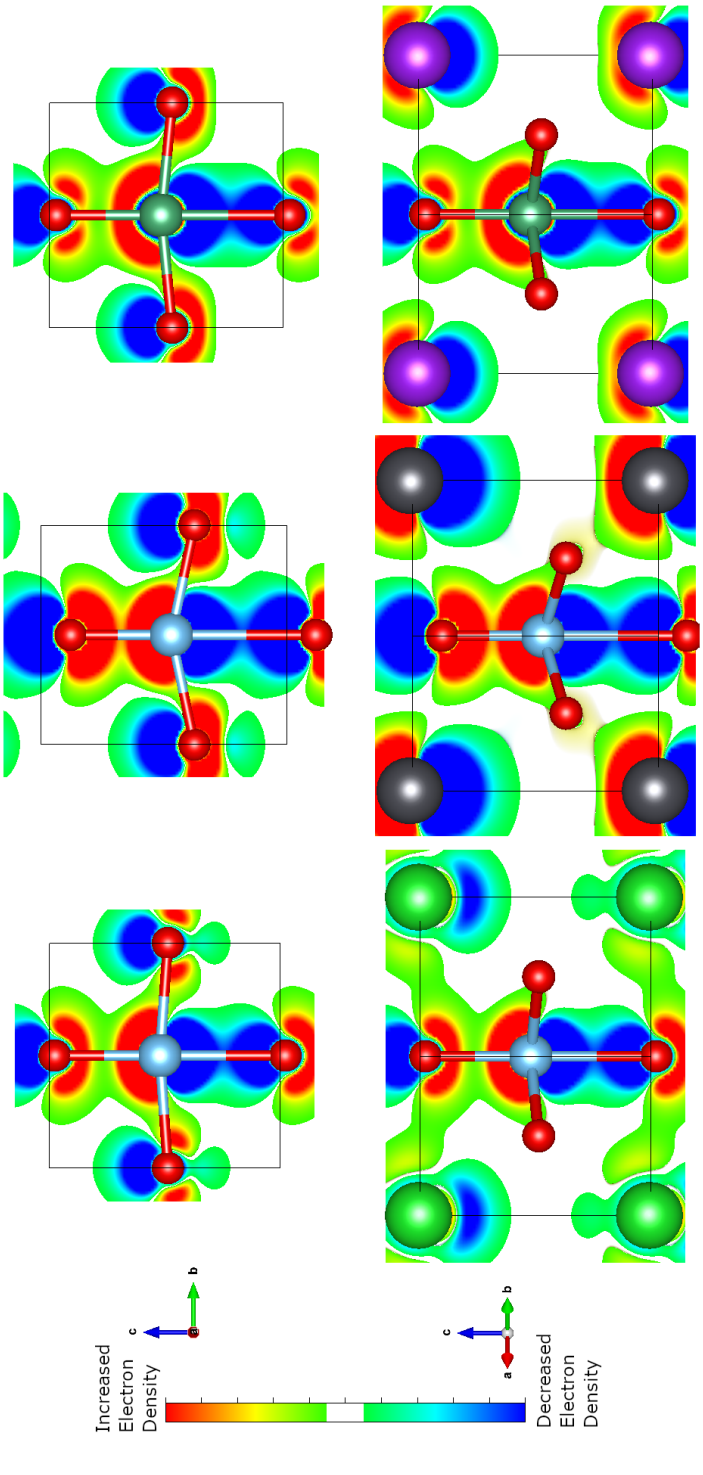

FIGURE 5.11: A cross section of the electron density shift of BTO (Left), PTO (Middle), and KNO (Right) in the (100) plane (Top) and (110) plane (Bottom) due to compressive strain in the a- and b-axes.

more prominent in the bonds, in particular in the PTO structure, where both bonds in the O-B-O chain show significant electron activity. All atoms show far greater effects in the density change lobes for PTO, whereas in BTO and KNO they seem equivalent. In KNO the radial oxygen ions are more involved, as are the density changes around the A-site in comparison to BTO. In BTO the axial oxygen atoms carry greater change, and although the A-site is less directly involved it can be seen in the (110) plane that there is a significant connection between the radial oxygen ion and the barium ion.

Again the compressive and expansive modes appear to be direct opposites, showing further the inherent linearity in properties relating to piezoelectricity, in addition to the piezoelectric effect itself. There is much greater lateral involvement, obviously as part of the a,b-axis components, and surrounding the radial oxygen ions particularly we see an interesting distribution. The lobes protruding anti-parallel to the polarisation appear broken and much more flat than the parallel lobes. These regions seem more symmetric in the a-axis than the prior figures that seemed symmetric around the ions in the c-axis. Figures showing the d_{33} component show symmetry in the direction perpendicular to polarisation and, excepting the ferroelectric deformation, symmetry in the parallel direction. However in the d_{31} figures the symmetry is restricted purely to the perpendicular direction, with a clear bias in the direction of polarisation. In the O-B-O chain, we see roughly the same behaviour, however it is in the A-site and radial oxygen ions differ.

This suggests that there are components to the different piezoelectric mode. A singular, identical mechanism in the central chain, and an independent component which distinguishes the separate modes. In order to further consider this core mechanism, we plot the charge difference along the c-axis through the centre of the B-site atom. This charge difference is plotted against the

FIGURE 5.12: Electron density shift along the central O-B-O column for expansive strain patterns for barium titanate (BTO), lead titanate (PTO), and potassium niobate (KNO). Positive numbers are an increase in electron density at that site, and negative numbers are a decrease in electron density at that site.

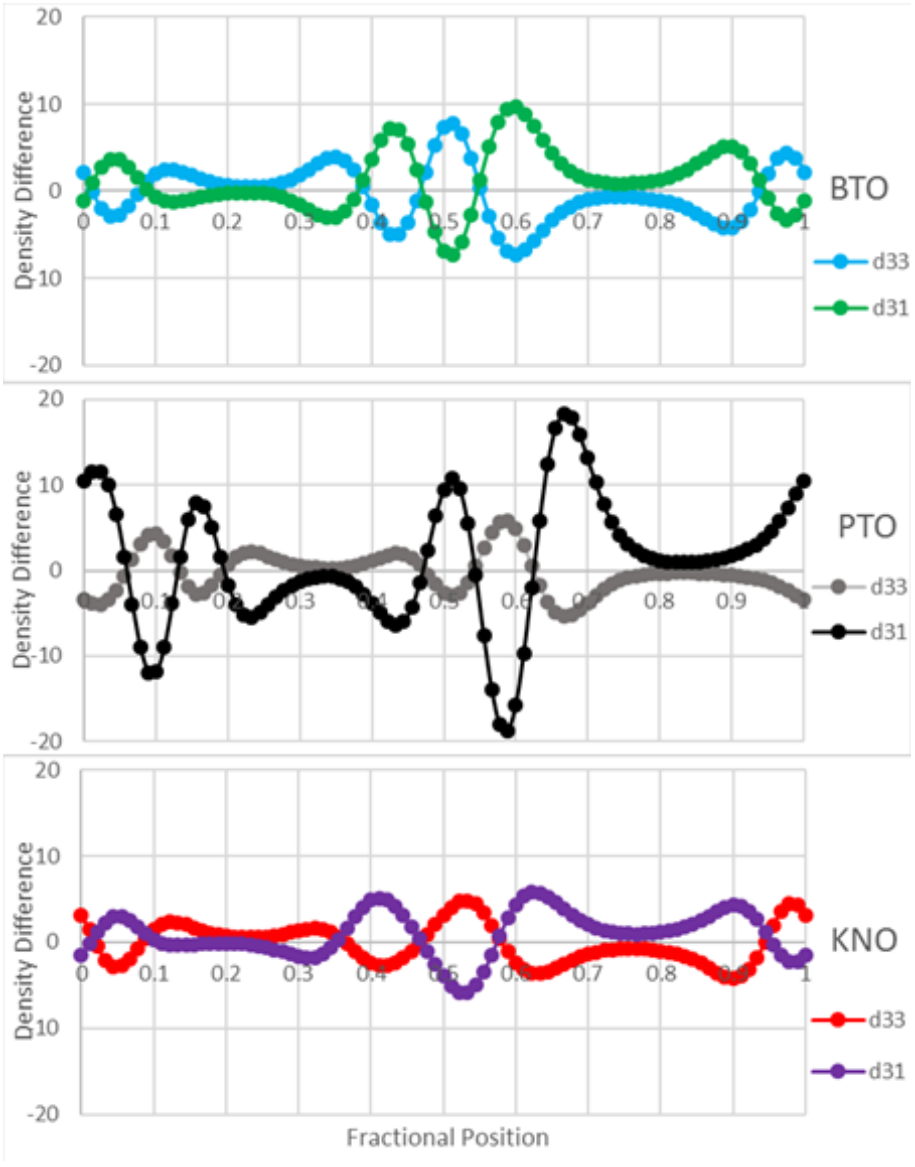

fractional coordinate, rather than the absolute coordinate, to allow for slightly different cell geometry. Figure 5.12 shows the charge difference for expansive modes. As we have seen, compressive modes are simply a change of sign, so removing them adds clarity.

There is a definite similarity in the behaviour of the oxygen ions in the BTO and KNO in figure 5.12, however it differs significantly in the central region where we expect to see the B-site ion. Therefore while the previous figures showed the two as similar, there are numerical differences arising from the different bonding of the B-site ions. This shows that while it may be insignificant to the overall, there are aspects of difference between the II-IV and I-V models.

We can see from figure 5.12 that the behaviour of both modes are very similar, in that the stationary points are at the same points but the sign is reversed. However the d_{31} mode shows a larger difference than the d_{33} mode. While this could be due to the way we forced a preservation of symmetry during the calculations, the proportional difference in the two modes is different for PTO against KNO and BTO. Numerically in PTO, the d_{31} mode is greater than twice the absolute value of the d_{33} mode for every point. For KNO and BTO however, the charge difference of the d_{31} mode is only slightly larger in absolute value.

This would suggest that the difference in these values is due to structural differences rather than chemical. BTO and KNO have similar elastic properties, whereas PTO has an elastic matrix that differs by 8-10 times. However, the ratio of the s_{33} to s_{31} is similar in all three structures, so the elastic asymmetry is not the cause. The effective charges of the ions are also not the root cause, as they would not account for the similar behaviour of the BTO and KNO structures. Instead of considering the total polarisation of each structure, we will consider it as a component system. Equation 5.10 gives independent components of the polarisation from the direction, but also contains a summation of the individual ions. Not only can we consider the individual polarisations, but also the change in polarisation under total stress, studying the piezoelectric effect on an atom-by-atom level.

FIGURE 5.13: Change in ionic polarisation for each ion in BTO compared to the unstrained rest state, against the axial stress on the unit cell in the direction of polarisation, with a linear fitting and the linear function shown. The gradient of the linear fit gives the partial piezoelectric coefficient of the ion.

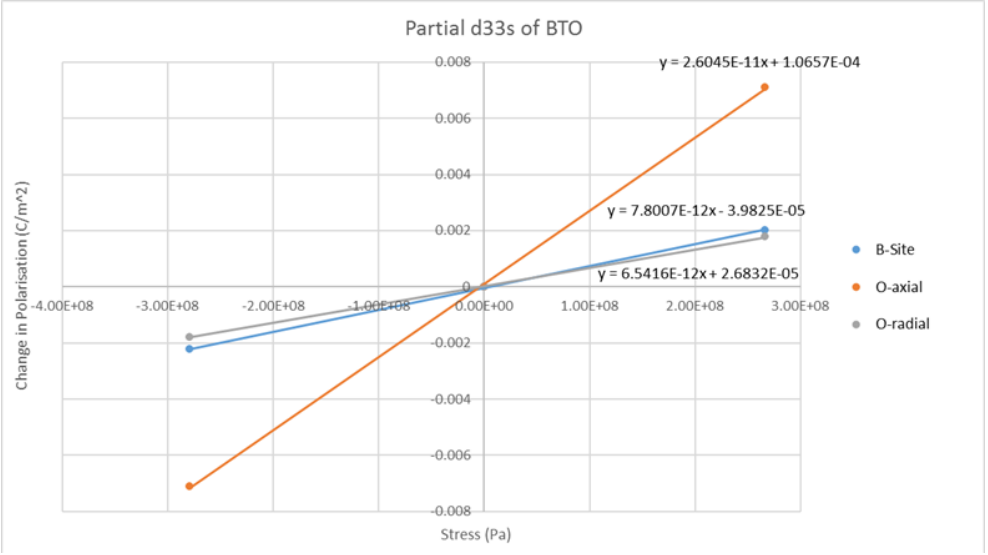

5.3.7 The Partial Piezoelectric Coefficient

We define the partial piezoelectric coefficient (δ_{ij}^{k}) as the change in polarisation in direction i of a single ion k due to mechanical stress applied across the cell in direction j. As polarisation of the k-th ion is naturally calculated as part of equation 5.10 then it is obvious how the change in polarisation per ion is found, which can then be plotted against the cell stress as in figure 5.13. This relation is linear as we may expect for a piezoelectric, giving the partial piezoelectric coefficient as the gradient.

We have defined this across a total stress per unit cell, as stress is effectively a force evenly distributed across an area. However we could attempt to define a pseudo-stress on the individual ions, assigning these properties would be difficult as there would need to be a system to split the cross section of a

material plane across a 3D space while remaining agnostic to specific physical properties of the material.

Table 5.10 shows the full table of the changes in polarisation and partial piezoelectric coefficient for each ion across the sample structures. Note that the value given for radial oxygen is per ion. As before, we have chosen to define the A-site as zero polarisation for all patterns. This is arbitrary and while it is necessary to define a zero point, depending on what is of interest any point can be selected.

Attempts to calculate polarisation are consistently plagued by the necessity for an arbitrary relativeness of the calculation. In this system we have defined a zero point and coordinate system for simplicity, but there is no reason beyond convenience for these choices. While this allows our system considerable freedom to generalise to many systems of interest with very different geometries and real-world implementations. Though this is an interesting aspect of the fundamental theory of polarisation, it may be that a more holistic approach is more enlightening. It may be beneficial to reconsider these as boundary conditions relevant to the physicality of the system, as in the wave and heat equations. However in the current context it is sufficient to understand this so that we understand the necessity of the selecting a system, and that our results will differ based on selection of a system, although conclusions we draw should be valid across all selections in order to be meaningful.

In all of the sample structures, the axial oxygen has the largest partial piezoelectric coefficient by a significant margin. This is curious in KNO, as it is proportionally larger than in BTO. We would expect the B-site, which in the case of Nb has a larger valance and effective charge, so it may be expected that it would represent the majority of the piezoelectric coefficient. However, this is not the case, and we can see that the electronic component of the effective

TABLE 5.10: Change in polarisation (ΔP_{nx}) and partial piezoelectric coefficient (δ_x^k) of ions in barium titanate (BTO), lead titanate (PTO), and potassium niobate (KNO). The subscript n corresponds to an expansive (E) or compressive (C) strain, x is the strain direction with 33 being a strain parallel to the direction of polarisation, and 31 being a strain perpendicular to the direction of polarisation, and k is the ion.

	BTO			PTO			KNO		
	B	O_{ax}	O_{rad}	B	O_{ax}	O_{rad}	B	O_{ax}	O_{rad}
$\Delta P_{C33}(mC/m^2)$	-2.23	-7.10	-1.78	1.50	-2.23	-2.60	-1.40	-7.52	-1.37
$\Delta P_{E33}(mC/m^2)$	2.02	7.09	1.78	-1.41	2.02	2.55	1.26	7.53	1.36
$\Delta P_{C31}(mC/m^2)$	2.98	7.89	2.27	-2.47	2.14	7.81	3.10	8.54	2.45
$\Delta P_{E31}(mC/m^2)$	3.06	-7.47	-2.13	2.15	-2.08	-7.69	-3.11	-7.90	-2.28
$\delta_{33}^k(pC/N)$	7.80	26.05	6.54	-41.30	205.03	73.08	4.73	26.79	4.85
$\delta_{31}^k(pC/N)$	-2.03	-5.15	-1.48	4.48	-40.96	-15.05	-1.80	-4.75	-1.37

charge follows the opposite trend, being larger for the oxygen in KNO, while larger for the B-site in BTO. Could it be then, that these electron movements are based on the electrons shared more than the valance of the components. Then manufacture would be based on increasing the amount of electron sharing and the bonding of this axial oxygen.

There is little difference between the d_{33} and d_{31} modes. The δ of the axial oxygen is a lower proportion of the total piezoelectric coefficient in the d_{31} mode, however it is still the majority in both modes across all structures.

What is most interesting, however, is the B-site Ti in PTO. Despite having the overall highest piezoelectric coefficients, the polarisation and δ is consistently of the opposite sign to the other structures. We understand why our polarisation calculation has the opposite sign, it is because unlike in BTO and KNO, the B-site is below the symmetric point in the axis of polarisation defined in subsection 5.3.2. However, the δ implies that this is not a result of our selection of symmetric points, but a fundamental difference in the piezoelectric effect, as the B-site is moving against the piezoelectric coefficient's primary effect. Looking at the differences between sample structures, this seems the most significant. Therefore when considering new materials on a fundamental level, it may not be a case of simply attempting to stack high δ coefficients of ions to create a highly piezoelectric material. Instead, perhaps we should seek to create these seemingly adversarial relationships in larger systems in order to maximize the overall piezoelectric coefficient.

5.4 Conclusions

In this chapter we have established a framework for calculating essential properties of the piezoelectric. Initially we have calculated structural properties,

phonon and electric field response, dielectric tensors, elastic matrices, and strain geometries using CASTEP. The results of these calculations have been discussed, differences between these results and previous values have been addressed, and with the exception of the dielectric tensors which has been addressed, these values have been deemed acceptable.

We have developed a new way to consider the intrinsic properties of simple piezoelectric materials using a DFT approach. Observing the electric changes of a material relaxed under stress has allowed us to calculate numerically and visually represent the properties of interest in these materials. By providing a fundamental tool set with clear, concise, instructions we have provided a novel way of considering atomic scale stress/strain behaviour of idealised materials in terms of electronic charge movement. Additionally, this metric of the partial piezoelectric coefficient has demonstrated that the simple chemical make-up of the structure seems to have little bearing on the overall piezoelectric property. Instead, the overall effect is caused by a combination of structural and electronic properties that we are able to determine.

Now that we have discussed the individual calculations and their methodology, we must move on in order to consider more realistic structures that may be larger and feature more complicated interactions behind the overall identical mechanics. For the first of these we will consider a binary structure of lead zirconate titanate in equal parts, with the chemical formula $PbTi_{0.5}Zr_{0.5}O_3$, and often referred to by the shortened form PZT.

Chapter 6

Piezoelectric Properties of Binary Perovskites: Lead Zirconate Titanate

6.1 Introduction to the Sample Material

When considering the binary structure to calculate properties for, the obvious choice is lead zirconate titanate (PZT), a binary solution of lead titanate that was studied in chapter 5, and the perovskite lead zirconate with the unit cell formula $PbZr_{1-x}Ti_xO_3$ with $0 \leq x \leq 1$. Initially discovered in 1952[162], it has been an essential material in core components of all electronics. As a binary solution, there are interesting properties of the phase diagram that are not present in the unary materials, arising from the composition. Figure 6.1 shows the compositional and temperature phase diagram[1, p. 136].

Most interesting about this is the sharp vertical line between rhombohedral and tetragonal occurring at $x \approx 0.48$. This morphotropic phase boundary (MPB)

FIGURE 6.1: Temperature and composition phase diagram for lead zirconate titanate. Composition is given by the mixing percentage of lead titanate, with 0% corresponding to pure lead zirconate, and 100% corresponding to pure lead titanate. The phases are labelled as paraelectric (P), ferroelectric (F), and antiferroelectric (A), with the subscript being the crystal category cubic (C), rhombohedral (R), tetragonal (T), and orthorhombic (O).

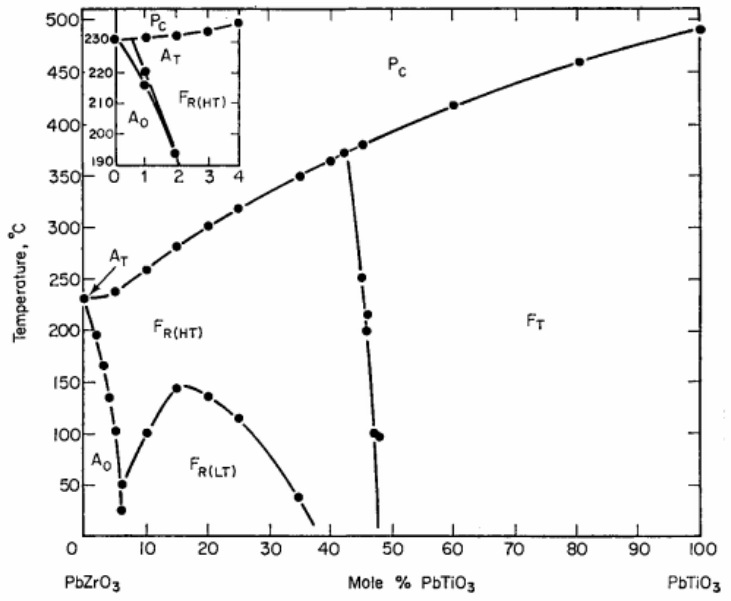

is often used in devices as there is an increase in the properties associated with piezo- and ferroelectricity that persists over a wide range of temperatures. These calculations are performed close to this mark on the tetragonal side, where $x = 0.5$. The sample structure is constructed using a supercell method with 8 perovskite cells in a 2^3 configuration, giving a compositional resolution of 12.5% . While calculations of this sort across the MPB would be interesting, the size of the supercell required to achieve the resolution of 4% necessary would be made up of 25 perovskite cells, and this can only be broken into a $5 \times 5 \times 1$, it is impossible to create a well mixed cell. Using 50 perovskite cells would mediate this issue, however this would give a unit cell of 250 atoms. Even if an interested researcher had the resources for such a task, there are undoubtedly better uses for them.

It is well known that using a virtual crystal approximation is unreliable for PZT, as while some compositions agree well with a supercell method, these are the exception more than the rule. However this is generally where a single perovskite cell is used to replicate much larger structures. Rather than putting the entire burden on a thoroughly disproved method, it may be that using a hybrid of these two ideas could produce a viable solution. For instance, an 8 perovskite cell in a $2 \times 2 \times 2$ configuration is well sized for fast calculations on reasonable HPC hardware, and can likely host dozens of non-degenerate conformations. In pure supercell as we have performed it, there is a compositional resolution of 12.5%, meaning that for our binary structure we could only use mixes of $x = 0.125, 0.25, 0.375,$ or 0.5. However if we assigned a single ion as the virtual ion, then theoretically we have a continuous spectrum of compositions that may be explored, without relying entirely on the virtual crystal that we know is unreliable.

While this method is not relevant to this work, it would be interesting to see how a virtual ion performs in a 2^3 or 3^3 supercell to calculate properties of a material for which creating the full structure would be unfeasible.

Once again this system is heavily idealised for the DFT methodology. Here, in addition to the previous assumptions of perfect single crystal, we assume perfect mixing of the B-site ions. That is, throughout the crystal for each B site (Ti, Zr) ion, the nearest B-site neighbour along the a-, b-, and c-axes are non-matching. This is not a realistic structure on a macroscale, as either due to the energetics of ion migration or simply limitations in fabrication, crystals of our 50-50 composition show Ti and Zr rich regions on scales too large to investigate using DFT. The distribution of these would be far more suited to a phase field method[163], especially due to the composition profile crossing

the phase boundary, causing the single crystal to show a tetragonal structure in the Ti rich regions and rhombohedral in the Zr rich regions.

That said, the atomistic calculations performed on an idealised structure are no different to the limitations of any other calculation or study. While it is important to acknowledge, these are not factors that invalidate our method.

These investigations were performed using the ARC2 configuration shown in section 4.2.2.

6.1.1 Building the Unit Cell

Rather than attempt to find a suitable unit cell on ICSD, a supercell was built based on the lead titanate cell used in the previous study for the base perovskite unit. This cell was doubled in all axes and populated with equivalent atoms for each unit. It is essential to keep track of which atoms are where in order to calculate their asymmetric displacement, so each group of five atoms were grouped into a unit, and units were distinguished by 0 or 1 in each direction, giving each cell a designation of the form (000). So the cell containing the origin was 000, surrounded in a, b, and c by 100, 010, 001 respectively. While it is possible to become confused between this and planar notation, it was ultimately simple and versatile. While the method by which you determine the positions of atoms in the supercell does not matter, it is highly recommended that a clear nomenclature is used. Each atom was given an approximate ferroelectric fractional coordinate displacement of 0.01, in line with the structure of a deformed perovskite. Fundamentally it is only important to build as far as it being visibly recognisable, as a geometry optimisation to minimise the energy will be required to settle the final cell to something more representative of the real structure.

Figure 6.2 shows the constructed unit cell. While missing various minor features relevant to the crystal structure that are discussed later in the chapter, this represents a viable perovskite initial structure that can be used as a starting point for a calculation. Practically any unit cell that is physically possible can be used for calculations, so there is no need to wait for experimental data and any hypothetical scenario can be created, such as an ultra-high pressure phase. Any unit cell where atoms do not overlap can be input into a calculation, but there are other factors as to if the state is one observed in reality. This is why it is common to use experimental data as a starting point, or to use a visualiser and personal knowledge of how a similar cell might behave in order to build a system representative of the real life case.

In order to keep parity with the previous calculations, the pseudopotentials for lead titanate were reused, with the addition of the zircoium pseudopotential from the same library.

6.2 Performing the Calculations

6.2.1 Convergence

Convergence is the first consideration of any project, which in the space of pseudopotential based DFT is the kinetic energy cut-off and the Monkhorst-Pack grid. The cut-off is based entirely on the pseudopotentials used. The Monkhorst-Pack grid is based more on the relative positions of pseudopotentials, particularly the interatomic distance. Therefore, rather than convergence of the full unit cell, we instead can perform calculations on lead zirconate and take the established convergence parameters of lead titanate from chapter 5. Then we simply take the largest cut-off energy and the smallest k-point spacing

FIGURE 6.2: A VESTA visualisation of the initial PZT cell we have constructed. Black - Pb, Blue - Ti, Green - Zr, Red - O.

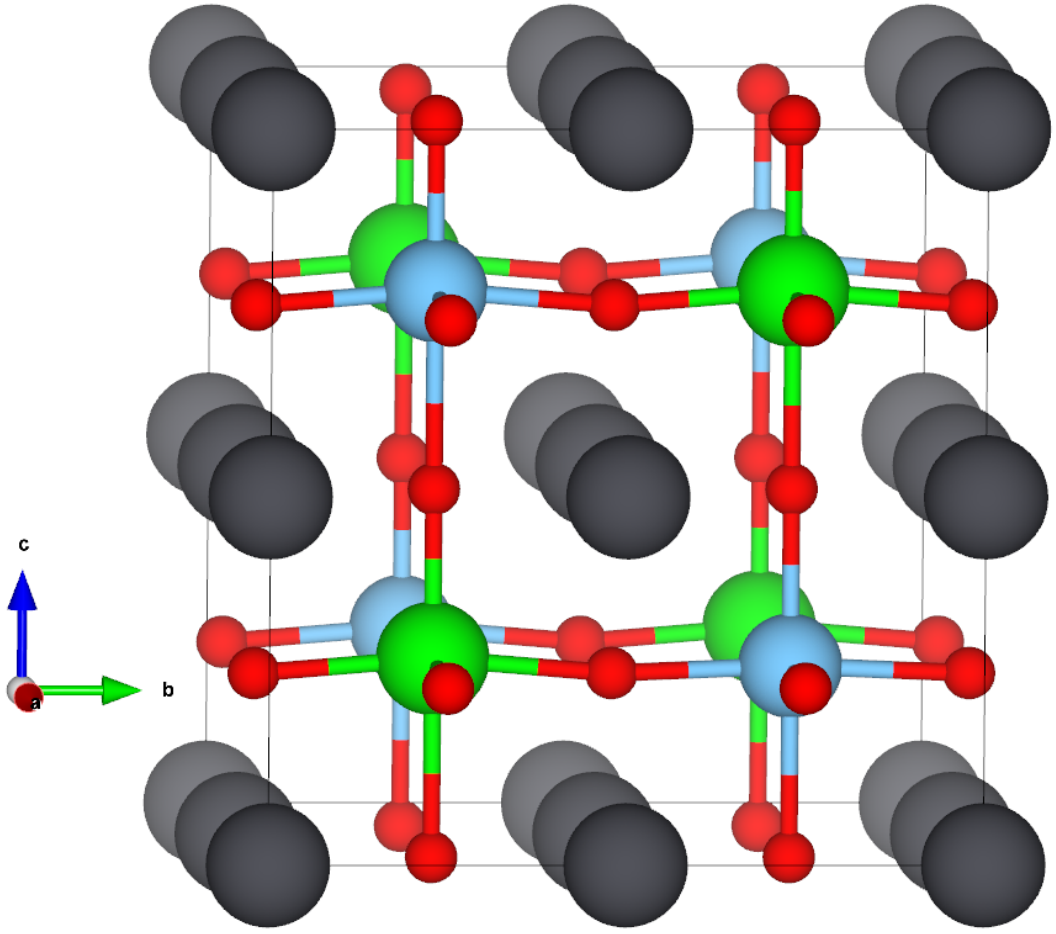

for converged values. This method is well known and particularly for larger cells can be an excellent cost cutting measure for the initial convergence.

The same method as in section 5.2.3 is used, with a del-diff method with three successive points within $10^{-4}eV/\text{Å}$ for energy cut off and a two point plateau for the Monkhorst-Pack grid. These were practically identical to the results for lead titanate, which is not surprising. Both titanium and zirconium are simple transition metal elements, so do not require particularly strenuous calculations. However lead and oxygen pseudopotentials are well known to be particularly hard, requiring significant convergence parameters. Thus it is expected that

the identical pseudopotentials would be the deciding factor in the numerical convergence.

Overall, the calculations were found to be converged to a sufficient force resolution with a cut-off energy of $850eV$ and an MP grid of 5^3. As the axes are made up of 2 basic cell lengths, the reciprocal lattice vector is halved, therefore half as many k-points are needed along each axis for the same density.

6.2.2 Unit Cell Geometry

We employ the full unit cell for the initial geometry optimisation. This is of course necessary for the resting state to compare the electron density of perturbed structures to, and is essential as a precursor the the linear response calculation. It can also show interesting features of the geometry, as seen before where lead titanate was found to have a a B-site ion with negative partial polarisation.

This geometry calculation was set to the same parameters of an energy tolerance of $2 \times 10^8 eV$, force tolerance of $1 \times 10^4 eV/\text{Å}$, and displacement tolerance of $5 \times 10^6 \text{Å}$. However, by the non-symmetric structure with significantly more atoms, the calculation took longer than the unary optimisations combined. It is important to remember that supercell type constructions rarely fall into a point group due to the large cells and arrangements of atoms compared to their simpler counterparts. While individual ionic constraints and cell constraints can be applied as a time saving measure, it can be much more interesting to simply leave symmetry out of the calculation and observe how the superstructure differs in geometry from the individual cells it is made up of. Therefore the initial geometry optimisation, and the subsequent perturbed optimisations are left with P1 symmetry and no constraints other than the perturbed strain.

TABLE 6.1: Lattice parameters, tetragonality, and unit cell volume of the PZT full cell and reduced perovskite unit, with lead titanate (PTO) and lead zirconate (PZO) values for comparison.

	PZT	Single Unit	PTO	PZO
a (Å)	8.050	4.025	3.893	4.160
c (Å)	8.425	4.212	4.306	4.160
c/a	1.047	1.047	1.106	1.000
Vol. (Å^3)	545.995	68.249	65.273	72.007

The results of the lattice parameters for an unperturbed geometry are shown in table 6.1. The single unit is half of each lattice parameter, giving a 5 atom cell with an eighth the volume of the full cell. The values for tetragonal PTO from chapter 5 and a geometry optimisation of cubic PZO are also given for comparison.

Without any forced geometry the unit cell was found to optimise to a semi-tetragonal structure. While the internal ionic coordinates do not fit the basic P4mm perovskite symmetry, due to the way symmetry is defined, the lattice parameters are found to fit the basic conditions of $a = b \neq c$ and $\alpha = \beta = \gamma = 90°$ to approximately five decimal places, which we can consider a numerical error. There may be some merit to creating lattice constraints around this fact as a time saving measure, but gains are likely to be small and the reduction of minimisation directions may actually lead to longer geometry calculations.

Overall the PZT appears to fit between the two extremes, an average between the large physical strain of the lead titanate and the simple symmetry of the cubic material lead zirconate. In terms of its piezoelectric potential, while there are other factors to consider in a real use case, the lower tetragonality may inhibit the piezoelectric properties but in doing so allow the material to be reliably created without defects and cracking as is common in PTO due to the high ferroelectric strain.

TABLE 6.2: Real space displacement from symmetric positions of ions in PZT in the direction parallel and perpendicular to the axis of polarisation, which aligns with the c-axis in our cell.

	Displacement	
Ion	Parallel	Perp.
Pb (Å)	0.0000	0.0000
Ti (Å)	-0.2311	0.0000
Zr (Å)	-0.2104	0.0000
$O_ax(Ti)$(Å)	-0.5065	0.0000
$O_ax(Zr)$(Å)	-0.3757	0.0000
$O_rad(Ti)$(Å)	-0.5524	0.0535
$O_rad(Zr)$(Å)	-0.5523	-0.0534

As part of the overall calculation we consider the displacement from a hypothetical set of symmetric fractional positions. On a single perovskite unit level, these are identical to the previous positions, however these have been expanded to the further set by first defining the origin unit with $0 \leq x, y, z \leq 0.5$ fractional positions, then adding 0.5 for each of the relevant expansion units. This gives a total set of the necessary zero polarisation symmetry that we can calculate a polarisation from. Important to note is that these are again corrected to the origin Pb ion, so this site has a displacement and polarisation of zero by convention. Table 6.2 shows the displacement of ions parallel and perpendicular to the direction of polarisation along the c-axis.

We must consider how in the previous structures, it was important to have a cubic-like set of fractional coordinates to act as symmetric points to calculate relative displacements. In the binary structure, these are expanded by a factor of two, as there are two simple perovskite cells in the axis of polarisation. Then the fractional symmetric coordinates are expanded to (0.25, 0.75) for B-site ions, and (0.0, 0.5) for the oxygen ions. We can calculate our polarisation as a relative real-space displacement of ions from these positions.

In order to make classification of the oxygen ions easier, in addition to our previous axial and radial ions we now consider them to be owned by a perovskite cell identified by the B-site ion. There is no distinction to be made further as oxygen ions in an axial and radial configuration linked to the same B-site ion are identical. From the previous notation, in each axis the first oxygen ions belong to the 0 unit, and the second to the 1. There is no difference in the c-axis displacement of radial oxygen ions, which is unsurprising given the weak interaction to the overall piezoelectric movement seen in chapter 5. The displacement of Ti and Zr are very similar, though Ti does displace slightly more. However there is a disproportionate displacement of axial oxygen ions to the titanium B-site. This suggests that while the ionic properties of the two B-sites are superficially similar, there is asymmetry in the B-axial oxygen bonding. Our example of a perfectly mixed cell distributes this difference evenly, but altering the arrangement or composition to a non-degenerate state to observe how this coupling reacts may be of interest in further studies. All c-axis displacements of the B-site ions are below the symmetric point relative to the A-site, which may correspond to an adversarial element of the piezoelectric coefficient. It is unclear what causes this effect, though the lead ion is certainly a factor. Whether it be its sheer size or electronic coupling, it is definitely worth looking into similar geometries if a replacement is to be found for lead based materials.

Most noticeable in these results however is the lateral movement of radial oxygen ions. The coupling above remains present as the ions are drawn toward the titanium site and away from the zirconium. Though under classical models the valance charge of these two ions is the same, it is likely that we see a more positive effective charge of the Ti, giving an overall greater attraction to the negative oxygen ions and allowing them to bond more closely against the weaker electrostatic attraction of the Zr ion.

FIGURE 6.3: A VESTA visualisation of the PZT cell rest-state, following the calculation of optimised ionic positions and lattice parameters.

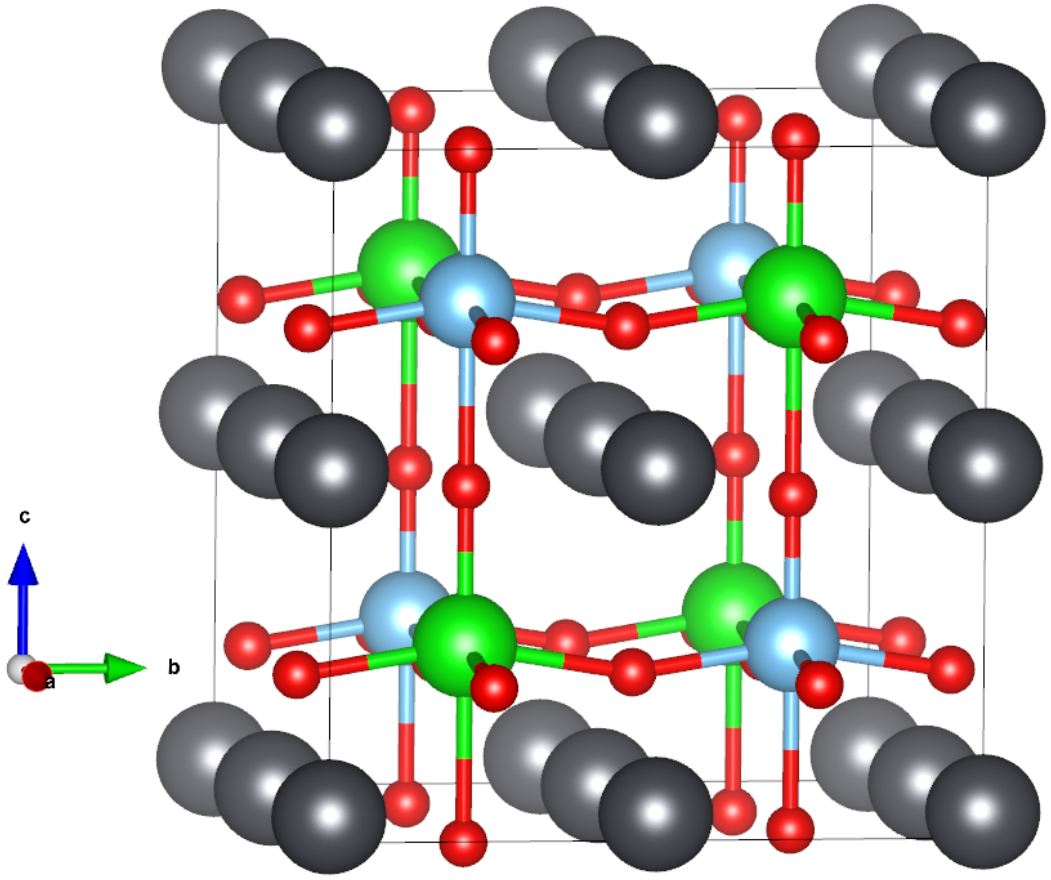

Given our perfect mixing this feature can be seen as either a sawtooth configuration of atoms, or a rotational mode that is cancelled over large volumes. It is hard to tell what to expect the result of this, or how it would change under different proportions and arrangements. However simple spring models may suggest that under pressure a scissoring action may occur, which could account for a more elastic material than those in rigidly ordered lines. Alternatively, it may give more compliance to rotational modes, or perhaps a combination of the two effects to create a more durable material than its unary counterparts.

Figure 6.4 shows the sawtooth pattern arising from the asymmetry between oxygen ions and their bonded B-site. The view is down the polarisation axis,

with the oxygen saw pattern running in the a-axis. VESTA calculated the angle formed by three neighbouring oxygen ions to be 177.0°, translating to a skew angle of 1.5°. While this does not seem to be a large difference in itself, this demonstrates a quantitative difference in the Zr and Ti B-site. In section 6.2.5 we will consider the angle of displacement and examine how it differs under stress.

6.2.3 Linear Response

Calculations were performed using the DFPT Linear Response package for CASTEP[148] in the same way as in chapter 5. All parameters were the same, with a task of "Phonon+Efield", electron energy tolerance of $1 \times 10^{-10} eV$, phonon and electric field tolerences of $1 \times 10^{-5} eV/\text{Å}^2$ and Å^3 respectively, and max cycles increased to 200. The phonon calculation is limited to the gamma point once again in order to reduce the amount of computation that must be performed.

Once again the dielectric tensor is not able to be calculated due to the projected negative phonon mode in the tetragonal state. This could indicate that when real PZT in this composition is cooled, it undergoes a phase transition to a pseudo-rhombohedral state. Referring back to figure 6.1, we see that despite the often touted thermal stability of the MPB, there is still a gradient. It is possible that somewhere between the lowest point of this graph at $0°C$ and the projection to absolute zero that the line crosses the 50% composition, which would explain why the ferroelectric mode has become unstable in this calculation.

Effective charge tensors have been calculated for each ion. Unlike the prior unary perovskite cells, there are off-diagonal components of these tensors.

FIGURE 6.4: Distance from the unit cell boundary and the skew angle, the angle formed between the ionic plane parallel to the unit cell boundary that passes through the centre of the oxygen ion, and the centre of the neighbouring oxygen ion. This shows an oxygen ion on the edge of the a-axis bound to a Ti B-site ion. The neighbouring oxygen ion bound to the Zr site has an equal skew angle and distance, but is on the opposite side of the unit cell boundary to represet the longer bond between the oxygen and zirconium ions.

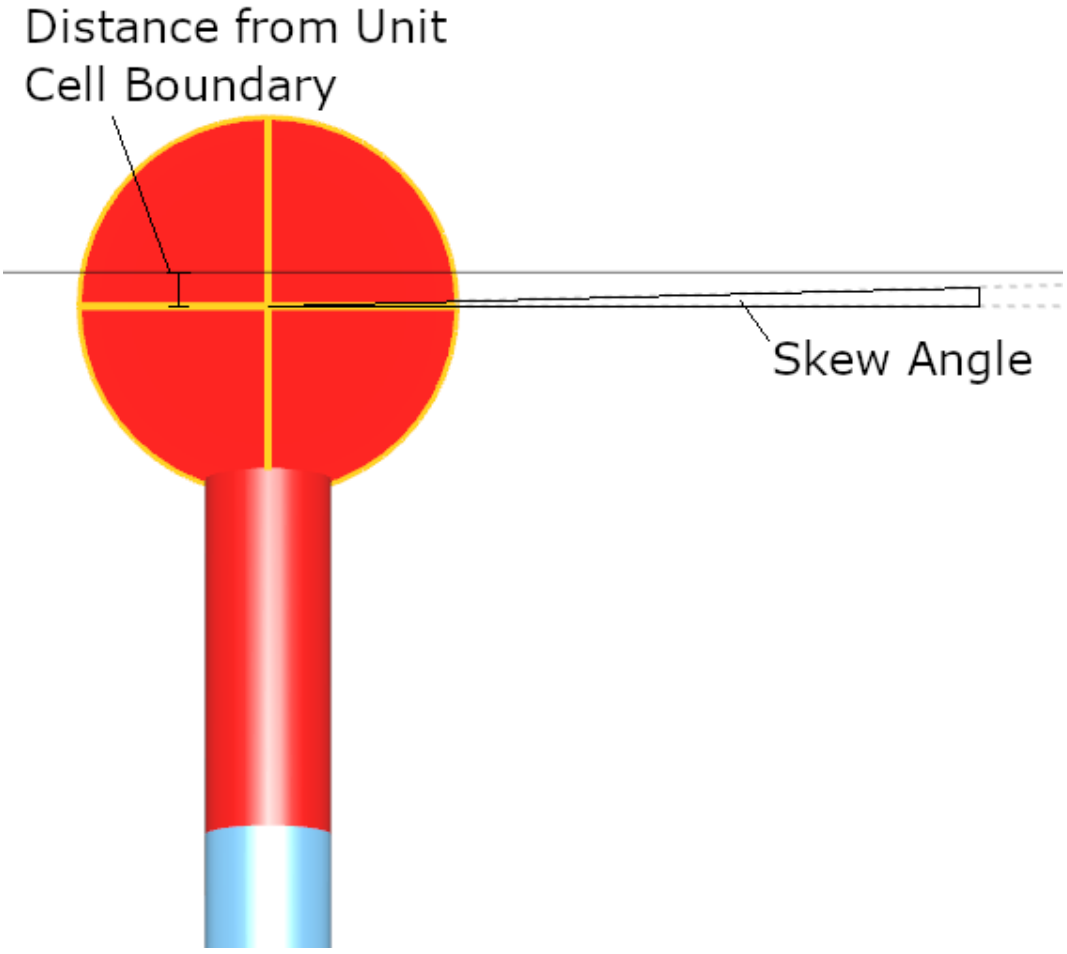

Given the unusual perpendicular offset, it should be expected that there is more freedom of directionality when ions are perturbed, leading to changes in polarisation in other directions. These elements demonstrate that, unlike in the unary systems, there is explicit coupling between the change in polarisation and ionic movements in a different axis. Secondly it is not symmetric around the diagonal as we expect from other matrices such as stress tensors, as $Z_{yz} \neq Z_{zy}$, or even the full rank 3 piezoelectric tensor. So despite the linear properties of the piezoelectric effect that allow its total reversibility, the properties behind it are not symmetric. It is possible to classify the effective charges of each ion by the B-site ion within the single perovskite cell, as cells with differing B-sites are distinct from each other, while cells with the same B-site have identical charge tensors. As in any case, the lack of applied symmetry introduces slight numeric errors, however these are only evident from the 5th decimal place. Tables 6.3 and 6.4 show the full effective charge tensors of each ion in a Ti based unit and a Zr based unit respectively.

For our sawtooth effect, we see that our initial belief that this was due to the charge of the B-site ion was wrong, with Zr having a higher charge across all diagonal elements. Instead, the radial oxygen ions themselves carry equal off-diagonal charges in the direction that they are shifted in. In the zirconium based cell they carry a positive charge, which will repel against the positive charge of the Zr ion and extend the bond distance. In titanium however, they carry a negative charge which should cause attraction to the central ion and shorten the distance. This fits with the observation, though it cannot be said for certain what the root cause of this is. Though it is evident that the off-diagonal elements of the effective charge will not make a large difference over the much stronger bonding forces, the small 3.0° shift, or effectively 1.5° for each atom from the cell border is significant in terms of understanding the binary structure.

TABLE 6.3: The effective charge tensors of ions in a Ti centred cell calculated using linear response. These show the change of polarisation in direction Y caused by ionic displacement in direction X.

Ion	Effective Charge XY (e)		
Pb	3.876	0.221	0.000
	0.221	3.876	0.000
	0.000	0.000	3.150
Ti	6.009	0.000	0.000
	0.000	6.009	0.000
	0.000	0.000	5.609
O_{axial}	-2.090	0.000	0.000
	0.000	-2.090	0.000
	0.000	0.000	-4.928
$O_{radial,1}$	-2.711	0.000	0.000
	0.000	-5.024	-0.045
	0.000	-0.055	-2.107
$O_{radial,2}$	-5.024	0.000	-0.045
	0.000	-2.711	0.000
	-0.055	0.000	-2.107

TABLE 6.4: The effective charge tensors of ions in a Zr centred cell calculated using linear response. These show the change of polarisation in direction Y caused by ionic displacement in direction X.

Ion	Effective Charge XY (e)		
Pb	3.876	-0.221	0.000
	-0.221	3.876	0.000
	0.000	0.000	3.150
Zr	6.150	0.000	0.000
	0.000	6.150	0.000
	0.000	0.000	6.016
O_{axial}	-2.352	0.000	0.000
	0.000	-2.352	0.000
	0.000	0.000	-4.569
$O_{radial,1}$	-2.711	0.000	0.000
	0.000	-5.024	0.045
	0.000	0.055	-2.107
$O_{radial,2}$	-5.024	0.000	0.045
	0.000	-2.711	0.000
	0.055	0.000	-2.107

Diagonal elements once again show a large movement of charge from the A- and B-site ion to the oxygen ions, and a high degree of charge asymmetry in different axes. We expect that this will again lead to the oxygen ions bearing the largest partial piezoelectric coefficient.

6.2.4 Elastic Constants

Due to the size of the unit cell and lack of symmetry, it was decided that the elastic compliance tensor is far too expensive to compute given the time and resources available. It requires six completely unsymmetrised patterns which are calculated over six steps by default, leading to a total of 36 geometry optimisations, each being a significant task in itself. As a result this was determined to be an inefficient use of the shared resources.

6.2.5 Piezoelectric Perturbations

We continue the same strain patterns of the uniaxial ±0.25% in the c-axis for the d_{33} mode, and the biaxial ±0.25% in the a- and b-axes. This is kept for consistency, although in this case is not necessary to preserve any symmetry. Geometry optimisations are performed using the same parameters in section 6.2.2 for consistency. Table 6.5 shows the unit cell parameters and relevant stress tensor components for each of the 4 strain patterns. Once again E and C refer to expansion and compression strain patterns, with 33 indicating a strain in the c-axis and 31 indicating a- and b-axis strain. As the rest structure ideally has no stress due to the full structural optimisation, the percentage difference is not a meaningful quantity and is left out.

TABLE 6.5: Unit cell parameters, tetragonality, volume, and axial stresses under strain, and percentage difference from rest structure. Strain patterns are labelled by compressive (C) and expansive (E), 33 is strain in the axis of polarisation, and 31 is strain in the direction perpendicular to the axis of polarisation.

Parameter	C33	δ%	E33	δ%	C31	δ%	E31	δ%
a (Å)	8.056	0.07%	8.045	-0.06%	8.030	-0.25%	8.0704	0.25%
c (Å)	8.404	-0.25%	8.446	0.25%	8.460	0.41%	8.3937	-0.37%
c/a	1.043	-0.32%	1.050	0.31%	1.053	0.66%	1.040	-0.62%
Vol. ($Å^3$)	545.348	-0.12%	546.685	0.13%	545.500	-0.09%	546.692	0.13%
$Stress_c(GPa)$	-0.171	-	0.153	-	0.000	-	0.000	-
$Stress_a(GPa)$	0.000	-	0.000	-	-0.487	-	0.501	-

In comparison to table 5.6 not a great deal has changed, with the percentage changes in parameters being largely similar to the PTO results previously. The percentage increase is slightly larger, but it is expected that the more noticeable differences will be in the ionic movement, especially given the lateral movement of ions in addition to the overall change in polarisation.

Comparing these two quantities is not immediately simple. In the previous chapter the comparison between the three structures with different lattice parameters it made sense to consider the fractional positions, whereas in this case the binary system is more natural to consider the real space displacement between the two components, as the lattice parameter is identical and with very similar ionic charges it allows a more direct consideration of the change in polarisation being a result of ionic movement. The largest difference is simply that these results automatically take account of the change in unit cell size, as we know the change is uniform across PZT, whereas in the unary samples the axial length changes were not equal, therefore adding an extra variable to be considered when comparing. Therefore we may address general trends, but not directly compare the numerics.

Table 6.6 shows displacements of the ions in the strained structures, and the percentage difference of their displacement from the unstrained structure.

In dealing with the real space displacement and changes in this quantity, it makes considerations of the partial polarisation and piezoelectric coefficient easy to predict. Pb ions do not play a part in either, despite only the origin ion being fixed. This is likely a result of the mixing of the cell, which gives a diagonalised symmetry that would mean each ion is held symmetrically by equal forces applied along diagonal lines through the cell. Choosing a non-degenerate conformation would likely cause an imbalance that creates movements in the

TABLE 6.6: Ionic displacements for each ion in the PZT unit cell caused by expansive (E) and compressive (C) strains in the axis of polarisation (33) and perpendicular to the axis of polarisation (31), and the percentage difference from the rest geometry, categorised by Ti and Zr centred units.

	C33		E33		C31		E31	
Ti Cell	Disp.	δ%	Disp.	δ%	Disp.	δ%	Disp.	δ%
Pb (Å)	0.000	0.00%	0.000	0.00%	0.000	0.00%	0.000	0.00%
Ti (Å)	-0.231	-0.22%	-0.232	0.26%	-0.227	-1.55%	-0.236	2.12%
O_{ax} (Å)	-0.500	-1.36%	-0.513	1.38%	-0.513	1.24%	-0.504	-0.57%
$O_{rad1}(c)$ (Å)	-0.546	-1.08%	-0.558	1.08%	-0.559	1.21%	-0.549	-0.63%
$O_{rad1}(b)$ (Å)	0.054	0.11%	0.053	-0.12%	0.054	0.11%	0.053	-0.43%
$O_{rad2}(c)$ (Å)	-0.546	-1.08%	-0.558	1.08%	-0.559	1.20%	-0.549	-0.63%
$O_{rad2}(a)$ (Å)	0.054	0.08%	0.053	-0.13%	0.054	0.10%	0.053	-0.46%
Zr Cell	Disp.	δ%	Disp.	δ%	Disp.	δ%	Disp.	δ%
Pb (Å)	0.000	0.00%	0.000	0.00%	0.000	0.00%	0.000	0.00%
Zr (Å)	-0.211	0.11%	-0.210	-0.03%	-0.206	-2.10%	-0.216	2.66%
O_{ax} (Å)	-0.370	-1.63%	-0.382	1.68%	-0.381	1.53%	-0.373	-0.79%
$O_{rad1}(c)$ (Å)	-0.546	-1.08%	-0.558	1.08%	-0.559	1.21%	-0.549	-0.62%
$O_{rad1}(b)$ (Å)	-0.053	0.11%	-0.053	-0.10%	-0.053	0.11%	-0.053	-0.43%
$O_{rad2}(c)$ (Å)	-0.546	-1.08%	-0.558	1.08%	-0.559	1.21%	-0.549	-0.62%
$O_{rad2}(a)$ (Å)	-0.053	0.13%	-0.053	-0.09%	-0.053	0.14%	-0.053	-0.42%

non-origin Pb ions, which could represent an elementally rich or poorly mixed region.

B-site ions show little movement, as seen previously, however this is made up in a small part by a high effective charge. Displacements of Zr and Ti appear to be opposing signs however, which likely means that while the partial polarisations will be negative, they will have opposing signs in the partial piezoelectric coefficient. This indicates that the addition of the lead zirconate does create a stabilisation effect for the lead titanate, sacrificing some piezoelectric performance for a system that is easier to fabricate and integrate into systems. Axial oxygen ions show the largest percentage change in displacement across both units, with radial oxygen ions showing a large movement in the c-axis, but much smaller effects in their lateral movements in the a- and b-axes. This fits to the identified non-diagonal charge contribution in the effective charge tensor that was previously seen. Though it was an unusual feature to be present, it is very small numerically compared to the main axis quantities, and as such any effects as a result of these elements are likely to be very small in comparison.

We consider the sawtooth angle for the oxygen ions as a function of the strain in the perpendicular and parallel direction. These are considered by two angles, the splay angle is directly measurable from within the visualisation software by calculating the angle formed by three consecutive ions, and the skew angle, which is the angle formed by the splay against an even flat line parallel to the unit cell axis but through the centre of the central ion which we will refer to as the ionic plane, representing the angle off the plane towards the next ion in the chain. This is shown figuratively in figure 6.5.

The splay and skew angles for radial (R) and axial (A) oxygen ions are shown in table 6.7. While the skew angles themselves are significant, it seems that the magnitude is an emergent property of the composition and mixing of the unit

FIGURE 6.5: Geometric demonstration of the splay and skew angles in PZT as in figure 6.4, but showing a larger cross section of the material with three oxygen ions. There is less clarity of the angles involved due to their small values, however the angles and positions are identical to the previous figure.

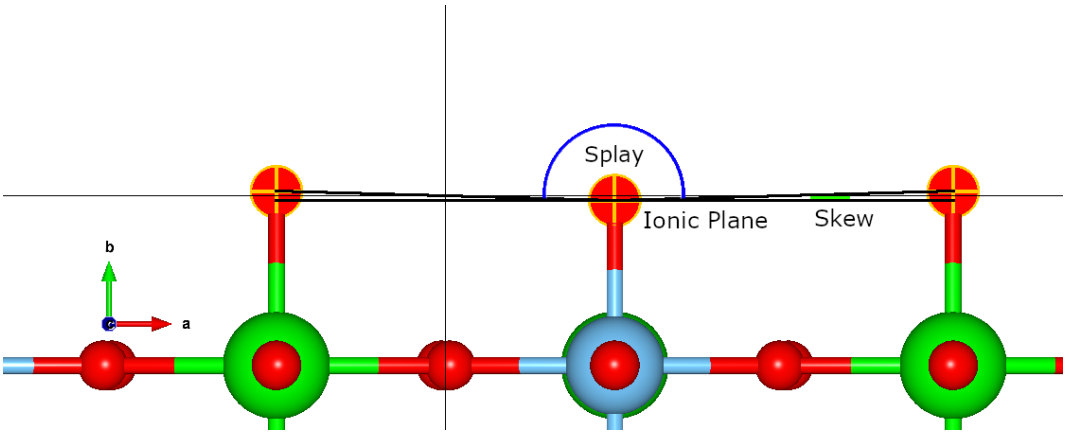

TABLE 6.7: The splay and skew angles for radial (R) and axial (A) oxygen ions in each strain pattern.

	Rest	C33	E33	C31	E31
$R - Splay(^\circ)$	176.9582	176.9565	176.9595	176.9468	176.9712
$R - Skew(^\circ)$	1.5209	1.5218	1.5203	1.5266	1.5144
$A - Splay(^\circ)$	176.2796	176.3034	176.2570	176.2545	176.3000
$A - Skew(^\circ)$	1.8602	1.8483	1.8715	1.8728	1.8500

cell. Even under our relatively large material strain the skew only varies in the hundredth of a degree for the axial oxygen, and as small as the thousandth of a degree in the radial ions. In older notation, this means that the change in axial skew is less than one minute at its highest, and for the radial ion less than half of that. So while comparing skews in different compositions and using different elements would be a valid measure, the differences over strain pattern are negligible at best and likely to be clouded by numerical convergence precision.

6.3 Analysis of Results

Once all the calculations are complete, the results as a whole can be analysed to calculate the desired properties. Using the same methods as in chapter 5 on a larger scale, we can calculate the total polarisation and piezoelectric coefficients, as well as their partial variants, and the electron density shifts.

6.3.1 Polarisation

6.3.1.1 Partial Ionic Polarisation

The polarisation is calculated using the equation 5.9, which is the generalised version of the prior equation. It is repeated below as equation 6.1 for reference.

$$P_i^k = \frac{Z^*_{k,ij} r_j^k |e|}{\Omega} \tag{6.1}$$

Unlike in chapter 5, the influence of the lateral elements in the displacement vector and the off-diagonal components of the Born effective charge tensor means that, for at least some of the ions, this is no longer a simple product but a matrix operation. For a given ion k, we see that index analysis over i,j is consistent with a matrix-vector multiplication, with implicit summation over the j index. We will consider a generic matrix multiplication explicitly, to demonstrate. We use the partial polarisation for a single ion $p_{x,y,z}C/m^2$ with a given charge matrix $Z_{xx,xy,...,zz}$ at a displacement from symmetric positions of $r'_{x,y,z}m$. V represents a conversion factor of $|e|/\Omega$. Where e is the electron charge in coulombs, and Ω is the unit cell volume in m^3. If the calculation is performed in angstroms and cubic angstroms, there is a 10^{-20} factor included in the denominator for the conversion. This is usually most convenient given

the form of the normal output files of electronic structure codes. As the volume is different for each unit cell, this should be recalculated for each strain pattern.

$$\begin{bmatrix} p_x \\ p_y \\ p_z \end{bmatrix} = V \begin{bmatrix} Z_{xx} & Z_{xy} & Z_{xz} \\ Z_{yx} & Z_{yy} & Z_{yz} \\ Z_{zx} & Z_{zy} & Z_{zz} \end{bmatrix} \begin{bmatrix} r'_x \\ r'_y \\ r'_z \end{bmatrix} \tag{6.2}$$

Then the matrix multiplication is the set of linear equations shown in equation 6.3.

$$\begin{aligned} p_x &= Z_{xx}r'_x + Z_{xy}r'_y + Z_{xz}r'_z \\ p_y &= Z_{yx}r'_x + Z_{yy}r'_y + Z_{yz}r'_z \\ p_z &= Z_{zx}r'_x + Z_{zy}r'_y + Z_{zz}r'_z \end{aligned} \tag{6.3}$$

We can take the first radial oxygen ion in a Ti cell in the rest structure, for which we have a calculated Born effective charge tensor and displacement vector. Then we can simply fill in the linear equations above.

$$\begin{aligned} p_x &= V \times [(-2.711 * 0.0000) + (0.000 * 0.0535) + (0.000 * -0.5524)] \\ p_y &= V \times [(0.000 * 0.0000) + (-5.024 * 0.0535) + (-0.045 * -0.5524)] \\ p_z &= V \times [(0.000 * 0.0000) + (-0.055 * 0.0535) + (-2.107 * -0.5524)] \end{aligned} \tag{6.4}$$

We can calculate V for the unit cell from the volume and basic constants to have a value of $0.0293 C/m^2$. Therefore our final polarisation vector is given in equation 6.5.

$$p_{\vec{r}} = \begin{bmatrix} 0.0000 \\ -0.0072 \\ 0.0341 \end{bmatrix} C/m^2 \tag{6.5}$$

This calculation was initially repeated for each ion, however it was found that, like the geometry, these can be classified as Ti-centred and Zr-centred units, substantially reducing the number of calculations that need to be performed. Table 6.8 shows the partial polarisations of each ion for the two standard units. Radial oxygen ions are unique in that they have a non-zero lateral component, with our convention set such that "radial 1" (rad1) has a b-axis component, and "radial 2" (rad2) has an a-axis component. This is just a result of how the CASTEP code output the results, which is presumably determined by how the initial cell was constructed. Most important is to ensure that the nomenclature remains consistent over multiple calculations, providing that is true the convention is not important.

If we consider that the the polarisation is a measure of the dipole moment per unit volume, then considering the partial polarisation can be thought of as a comparison of relative dipole moments. Of course, we could simply consider it as a charge*distance, but this would not account for differences or changes in volume.

Overall we see that the partial polarisation in the lateral direction cancels out, allowing for a small rounding error, in all structures. The other ions have zero partial polarisation in perpendicular directions, so we see that although there are laterally polarised ions, this is cancelled in the macrostructure. This shows that not only does the unit cell retain a tetragonal-like axis system, but also that the elongated access is parallel to the overall direction of polarisation. So

TABLE 6.8: Partial ionic polarisation of each ion, sorted by Ti and Zr centred units. Subscripts a, b, and c are the lattice direction of the partial ionic polarisation. Oxygen and B-site values that equal zero are omitted. Lead ions are included to demonstrate that all A-site ions have zero polarisation despite only one of the ions being fixed.

Ti Cell	Rest	C33	E33	C31	E31
$Pb_c(C/m^2)$	0.0000	0.0000	0.0000	0.0000	0.0000
$Ti_c(C/m^2)$	-0.0380	-0.0380	-0.0381	-0.0375	-0.0386
$O_{ax,c}(C/m^2)$	0.0732	0.0723	0.0742	0.0742	0.0725
$O_{rad1,c}(C/m^2)$	0.0341	0.0337	0.0344	0.0345	0.0337
$O_{rad1,b}(C/m^2)$	-0.0072	-0.0072	-0.0071	-0.0072	-0.0071
$O_{rad2,c}(C/m^2)$	0.0341	0.0337	0.0344	0.0345	0.0337
$O_{rad2,a}(C/m^2)$	-0.0072	-0.0072	-0.0071	-0.0072	-0.0071
Zr Cell	Rest	C33	E33	C31	E31
$Pb_c(C/m^2)$	0.0000	0.0000	0.0000	0.0000	0.0000
$Zr_c(C/m^2)$	-0.0371	-0.0372	-0.0371	-0.0364	-0.0379
$O_{ax,c}(C/m^2)$	0.0504	0.0496	0.0511	0.0512	0.0497
$O_{rad1,c}(C/m^2)$	0.0341	0.0337	0.0344	0.0345	0.0337
$O_{rad1,b}(C/m^2)$	0.0071	0.0072	0.0071	0.0072	0.0071
$O_{rad2,c}(C/m^2)$	0.0341	0.0337	0.0344	0.0345	0.0337
$O_{rad2,a}(C/m^2)$	0.0071	0.0072	0.0071	0.0072	0.0071

while the PZT structure is visually very different from the unary perovskites of the previous chapter, the key piezoelectric features are identical.

The negative B-site partial polarisation also shows as a feature of the structure as in lead titanate, however this feature is also apparent in the lead zirconate based units despite not being a feature of the pure material. So we expect to see this feature in the electron density shift between both the Ti sites and the Zr sites. This could be due to the equalisation of the unit cells, as we have discussed the stabilisation effect that the zirconate unit has against the pure lead titanate, however obviously the features of the titanate cell have been introduced to the larger PZT units. This is common in composite systems, though it is not guaranteed behaviour. This type of composite relies on the ability to create a system averaging between its composite parts, allowing a particular

poor quality to be mediated at the expense of reducing desirable properties. Of course, many composite crystals and alloys are utilised due unexpected behaviour, such as in BTO doped with strontium to give an unexpectedly high dielectric constant.

The axial oxygen ions once again have the highest polarisation, however the radial ions are much more involved, with the two accounting for approximately as much of the polarisation as the axial oxygen ion. The z-axis charges are lower, which could be a result of greater lateral charge elements. In the previous study the homogeneous perovskite composition symmetrically suppresses lateral considerations, whereas the lateral elements in this material seem to carry significant charge. This may be due to the composition scheme used, where all neighbouring cells are opposing. Then it may be that in this system, made up of two dissimilar base materials, effectively requires a large electronic charge component (recalling that this is the effective charge minus the classical valance charge) to create the previously discussed equalisation effect.

If that is the case, then of interest would be the lateral partial polarisations in multiple composite materials for different degrees of mismatch, a measure that could be broken down to how well matched structural or piezoelectric properties are. Of particular interest would be the mixture of the multiferroic bismuth ferrite, and our lead titanate sample. Both show high piezoelectric properties and very large tetragonality, and how they equalise between individual units to form the larger pseudotetragonal structure.

In this system however, we see that the greatest difference between the two flavours of perovskite unit is in the difference in the polarisation of the axial oxygen, with the titanium centred cell showing 50% greater polarisation for this ion than the zirconate counterpart. Neither the effective charge nor the displacement differences are this large, indicating that this is a combination

effect. This would indicate stronger hybridisation in the short bond between the B-site and oxygen. While this effect is seen in the sawtoothing discussed above, this axial effect seems much larger. Then looking at the geometry we consider the effect of the relative positioning of the lead ions. In the basic perovskite unit's cubic form there is no distinction in the axial and radial ions, this is only clear in the tetragonal form. While we broadly define it in terms of the axis of polarisation and B-site it is also important to recognise that, especially in lead titanate, we must consider the position relative to the A-site. While this is not as significant in the unary samples, with lead it is visually much further displaced. Then what we see is a result of a blocking effect, or electronic shielding as a longer range effect of the lead ion, allowing much greater differences in the axis of polarisation between our two flavours of units.

As discussed earlier, the binary system allows the stabilisation of lead titanate to something more industrially useful, however this shielding may be responsible for allowing the Ti-O system that was identified as important in chapter 5 to maintain strong piezoelectric properties, allowing PZT to be used as successfully as it has.

6.3.1.2 Total Material Polarisation

The total polarisation is calculated by the sum of the partial polarisations. The definition of partial polarisation we have given includes the volume of the unit cell in its calculation, so this is consistent with the standard unit of measurement. In the unary systems we can consider the partial (ionic) polarisation, a volume normalised dipole moment of each ion, and the total cell polarisation, and there was no reason to consider a middle ground. However, as this cell is made up of a number of perovskite units, it is possible to look at the polarisation of these component pieces in comparison to the overall structure.

Not only that, we can consider a hypothetical material made up entirely of these individual units, and how this compares to a known base structure. For instance, we can compare the lead titanate and lead zirconate composites to real lead titanate and zirconate polarisations.

There are many different ways to arrive at this quantity, which we will refer to as the theoretical sublattice polarisation (TSP). As polarisation is simply the dipole moment per unit volume, we could define a subset of ions within a given volume, such as the single perovskite unit, and calculate the partial polarisations with the new volume correction factor V. These can be summed across all the dipoles contained in the selected volume, although it is obviously possible to arbitrarily define a volume element such that the resulting polarisation is zero, or infinite, or anything between, so it is important to state the selected volume element and the reason why it is selected. The most obvious is to select a single perovskite unit of 5 atoms centred on one of the B-site ions, then calculate the TSP of the perovskite unit volume.

Of course, since we know that the volume of one of these units is one-eighth of the total volume, we can add our partial polarisation and divide by the volume fraction (effectively multiplying by 8). This is the simplest method for taking sublattices of the total cell, but lacks versatility for more complicated shapes, such as if there was a need to consider a lagrangian surface.

Table 6.9 shows the total spontaneous polarisation of the PZT structure, the TSP of the lead zirconate and lead titanate units, and the calculated spontaneous polarisation of lead titanate from chapter 5 for comparison.

Overall, we see that the pure PTO has the highest polarisation, followed by the PTO-TSP within the PZT. Obviously this is due to the equalisation between the two subcells lowering the effective properties of the PTO. PZT is averaged between the TSP of PTO and that of PZO, which sits at the bottom. Pure

TABLE 6.9: Total Polarisation of lead zirconate titanate (PZT) and lead titanate (PTO), and Theoretical Sublattice Polarisation (TSP) of lead zirconate (PZO) and and lead titanate (PTO). This is the polarisation of a single Zr or Ti centred perovskite unit in the PZT unit. Pure lead zirconate is not shown as it does not have spontaneous polarisation and is not ferroelectric or piezoelectric.

	Polarisation
PZT (C/m^2)	0.739
PZO-TSP (C/m^2)	0.651
PTO-TSP (C/m^2)	0.827
PTO (C/m^2)	0.948

PZO is not shown due to its symmetric structure causing no spontaneous polarisation.

The total polarisation is not split evenly between the two sublattices, with 56% being contributed by the PTO, and 44% coming from PZO. This is likely due to the lead shielding in the c-axis allowing the $Ti - O_{ax}$ region to support a much larger polarisation without interference from the neighbouring Zr B-site.

There are considerations to be made when comparing to real values. While the extrapolation to absolute zero is always an issue for temperature dependent effects, the proximity to a finite gradient morphotropic phase boundary raises questions as to the validity of considering the composition of real materials. There are also considerations of how a crystal is formed, with the usual factors of purity and domain structure being added to by mixing and local concentration. All in all it is possible to find many literature results across many values. For instance, Jaffe et al. gives a value of $\approx 0.27 C/m^2$ for 50% PZO-PTO[1, p. 147], well below our calculated value, whereas the MPB composition of a thin film sample given by Damjanovic gives a spontaneous polarisation of $\approx 0.60 C/m^2$[164, p. 351], which accounting for the usual DFT effects is much more representative of the calculated value. As a result, we believe the $0.74 C/m^2$ is representative of the system presented, with a wealth of literature

FIGURE 6.6: The change in polarisation against axial stress in PZT for strains in the c-axis (d_{33}) and a- and b-axes (d_{31}), and linear fit. The piezoelectric coefficient is given by the gradient of the linear equation.

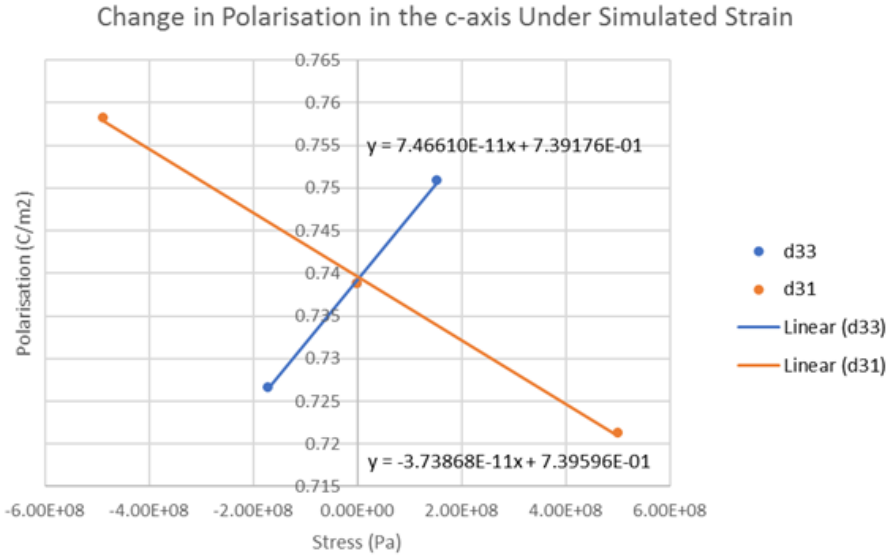

values that can reasonably given to support or argue against the accuracy to real values.

6.3.2 Piezoelectric Coefficient

The piezoelectric coefficient of the structure is calculated as the linear gradient of the polarisation as a function of material stress as calculated by the perturbed geometry optimisation in section 6.2.5. This is shown in figure 6.6, where the d_{33} mode is due to strain in the c-axis, and d_{31} is due to strain in the a- and b-axes. Note that as this is a biaxial strain, so this gradient actually represents $d_{31} + d_{32}$, which are identical and therefore is $2 \times d_{31}$.

We see that the piezoelectric coefficients are $d_{33} = 74.66pC/N$ and $2 \times d_{31} = -37.39pC/N$, therefore $d_{31} = -18.69pC/N$. Again there are a wide range of values to compare to due to material considerations, and it is not possible to

know exactly where we are at absolute zero with regards to the phase boundary. Many reported quantities are altered by the studies in mixing ratios and dopants, however if we compare to a literature value of $d_{33} = 125pC/N$ and $d_{31} = -60pC/N$ reported by Park et al.[165]. This value was chosen for our reference as the strain loading experimental method most closely matches our strain simulation method.

There is approximately a factor-two numeric error as in our other results, however this has been discussed previously. A similar numeric error in such a different system may lend further evidence to the idea of a systematic issue, the polarisation values are well matched, but a factor two error in the implementation of the material stress seems responsible. It may be worth looking into the physicality of stress implementation in calculations in the code, or performing a full elastic constants calculation with many steps and a high precision in order to compare the stress from the geometry optimisation against other methods of calculation. However, given these are based on the CASTEP geometry optimisation, they may also carry this inaccuracy. We also see that the basic relations between the coefficients remain, continuing our belief that this methodology is suitable for comparative considerations. To further understand the binary nature of the material, we must now break down these values into the ionic contributions.

6.3.3 Partial Piezoelectric Coefficient

The partial piezoelectric coefficients for every ion are calculated by taking the gradient of the ionic polarisation against the cell stress. This is the same method used prior, however in order to reduce the number of points that need to be plotted, which would be 40 series of 3 points for a total 120 points on a very crowded graph, an average gradient method is used. This is a standard

TABLE 6.10: Partial piezoelectric coefficients (δ_{ij}) of the ions in lead zirconate titanate in the two primary piezoelectric modes (d_{33} and d_{31}), separated by Ti and Zr centred perovskite unit.

	δ_{33}		δ_{31}	
	Ti-Unit	Zr-Unit	Ti-Unit	Zr-Unit
$A-site(pC/N)$	0.00	0.00	0.00	0.00
$B-site(pC/N)$	-0.28	0.44	-1.18	-1.57
$O_{axial}(pC/N)$	5.67	4.78	-1.78	-1.48
$O_{radial}(pC/N)$	2.02	2.02	-0.84	-0.84

method for creating linear fits in software, where the gradient of every pair of points is calculated using $m = \Delta y/\Delta x$, and the arithmetic mean is taken of the gradients. While there are more advanced algorithms, these provide little to no improvement on a data set of this type, and are better suited to more points per series, and systems that undergo a transition from linear to some other function. Table 6.10 shows the partial piezoelectric coefficients of the constituent ions of the unit cell. This has been separated by Ti and Zr centred units again, as these are found to match to a rounding error in the third decimal place. This does not seem physically relevant, and is carried through from the precision of effective charges and ionic positions. Reporting to $10fC/N$ is more than sufficient.

Additionally we have calculated $\delta_{11} = 0.02pC/N$ and $\delta_{13} = 0.16pC/N$, and $\delta_{11} = -0.02pC/N$ and $\delta_{13} = -0.16pC/N$ for the lateral oxygen atoms in the Ti and Zr based unit respectively. These have not been included in the above table as it is difficult to consider how they should be included. These elements do not exist in the overall piezoelectric coefficient. However it is not simply a case of our model, these elements cannot exist in any of tetragonal classes, so we know that they always cancel out. Therefore, there are considerations to be made for the physicality of these values.

Are local charges generated on local scales only to be immediately cancelled?

Or does the necessity of material strain taking time mean that the charges can equilibrate adiabatically, thus the charge is never generated? If that is so then what would happen under a strain at relativistic speeds, and how does the piezoelectric effect alter under relativistic conditions? If charges are generated, is this measurable with a sufficiently precise timescale in measurements of dielectric properties? We cite the tetragonal structure of the cell, but it is only tetragonal in lattice parameters, not in ionic positions. But then, literature would suggest that no piezoelectric is truly anything other than monoclinic. To an arbitrary position no material fits a crystal class. Ultimately, the question of "Do crystals exist?" is beyond the scope of this project, and likely beyond any project.

It is essential to consider all of these values, not just the ones that seem non-physical, as the result of a model that is based on assumptions, and equations that are derived from that model. So as a result these are calculated and reported as the result of our established equations, though it is up to a reader to decide if these are relevant to their research in a broader scope.

We have not considered the SMP in these systems, as the selection of a sublattice and the unit cell stress is unclear. In the direction of applied stress it does not change, as the stress is per unit area, meaning that a smaller area of the sublattice is subjected to the same amount of stress. Other directions may apply a similar rule, or it may be dependant on symmetric properties.

In the 31-component, the zirconate unit B-site ion has a slightly larger contribution. In the 33-component the Zr ion is seen to behave as seen in barium titanate and potassium niobate, with a positive partial piezoelectric coefficient. This is despite the negative partial polarisation, which is shared by the Ti ion, though the Ti retains its negative partial piezoelectric coefficient. This means that under a positive stress, the polarisation decreases in the Ti ion and

increases in the the Zr ion. This difference, rather than both in average, is because of the lead shielding between units. In seeking lead-free alternatives it is essential to ensure the physical displacement and shielding effect is accounted for, in addition to chemical effects. Of course, the effective ionic radius of lead is not abnormal compared to equivalent A-site ions such as bismuth or barium. So there must be an underlying electronic cause of the physical difference, and understanding how to recreate it in other materials is essential.

In all other units the axial oxygen ion is the primary contributor, as seen in the unary structures. So despite the properties discussed we still see many of the previous features of the unary perovskite. Clearly the fundamental effect is the same, as we would expect, but there are many smaller features which can be characterised to give the complete effect.

In the 33-mode, the oxygen ions take almost the entirety of the burden for the piezoelectric effect, with the zirconium and titanium ions taking almost no part in the overall effect. This is more evenly split in the 31-mode, in addition to being entirely like the barium titanate, in that all contribute to the overall effect, unlike the countering effect of the titanium in lead titanate and the 33-mode.

Numerically we expect the contributions in the 31-mode to be much lower as the overall piezoelectric coefficient is smaller, however the change in the ionic components is surprising, as while the overall coefficient is lower for the 31-mode, the B-site ions actually give a higher partial coefficient. It may be expected that, as a linear effect, the components would show a linear relation, where the ratio of partial coefficients is always the same and is simply multiplied to scale. This is not the case, as previously seen in the unary structures. However the distribution is very different from previous results. This may be as a result of the equalisation effect on the lateral unit borders, which is not

present in the axial polarisation direction due to the A-site shielding. What may be of interest is the boundary, without such a large physical displacement from the A-site. For instance, how does the solid solution of potassium niobate and barium titanate behave. While being more physically similar, there is no electronic shielding effect, leading to a more hydrostatic equalisation effect.

If we consider the overall unit, contributions to the overall piezoelectric coefficients are much more balanced than the polarisation, which seems likely due to the adversarial nature of the titanate ion causing a negative partial coefficient in the 33-mode and a reduced coefficient in the 31-mode. In the 33-mode the Ti and Zr units contribute 50.6% and 49.4% respectively to the total piezoelectric coefficient, whereas in the 31 mode these proportions are reversed. The equal proportions may be significant, though could equally be a coincidental quirk of precision and numerical errors around an equal splitting. Of more interest is if this behaviour is prevalent across other solid solutions. Confirming if this is a general effect of solutions would be an interesting study in itself, as the result of different independent components evenly contributing to the piezoelectric effect in solution is an unusual and interesting result in itself.

In order to further understand the electronic effects we can consider the electron density shift. While the partial piezoelectric coefficient is a powerful tool to understand how the piezoelectric effect acts, this gives a more visual interpretation of the system.

6.3.4 Electron Density Shift

We calculate the electron density shift by using the same method as in section 5.3.6, where the formatted electron density file for the rest structure is subtracted from the perturbed ones, with this superimposed over the unit cell.

Since CASTEP does not directly allow the user to choose an FFT grid to use, there are issues with geometry optimisations of a certain size, as the basis correction it performs may alter the dimensions of the grid based on the energy derivative for a changing cell. This means that for sufficiently large volume changes, the number of grid elements can change and make the simple method of evaluating the change significantly harder. It can be done with some experience in NumPy or MATLAB to plot a continuous three-dimensional function that is defined at all points, meaning that the difference is also defined at all points regardless of the initial grid. In our system, the grid changed for the modes that included a compressed c-axis, which would be the C33 and E31 mode. Fortunately we know that these are mirrored forms of the E33 and C31 mode from the previous chapter, and therefore these can be presented alone without the need for complicated manipulation.

Figure 6.7 shows the electron density in the E33 perturbation in the 100 plane at a distance of $0.25 \times d$ (2.01Å) from the origin. The saturation and scaling has been set identically to the previous details, though it is important to remember that the units used are arbitrary so this is for consistency and clarity rather than necessity.

To discuss rendering, this structure is far more demanding than the previous structures. While not at the level where the images need to be pre-rendered, though this would be an option given the GPU capacity of ARC3, this size of cell and number of charge points is a strain on certain types of hardware and can cause significant heating, stalling, and memory issues on less powerful devices such as the average laptop. It is advisable for usability that a desktop machine is used with some dedicated physics or render device. For unit cells of this size any dedicated GPU is likely to provide a good experience, though as systems get larger then the issue of visualisation may become an issue in

FIGURE 6.7: A cross section of the electron density shift of PZT caused by an expansive strain in the c-axis of 0.25%, in the 100 plane at 0.25d from the origin.

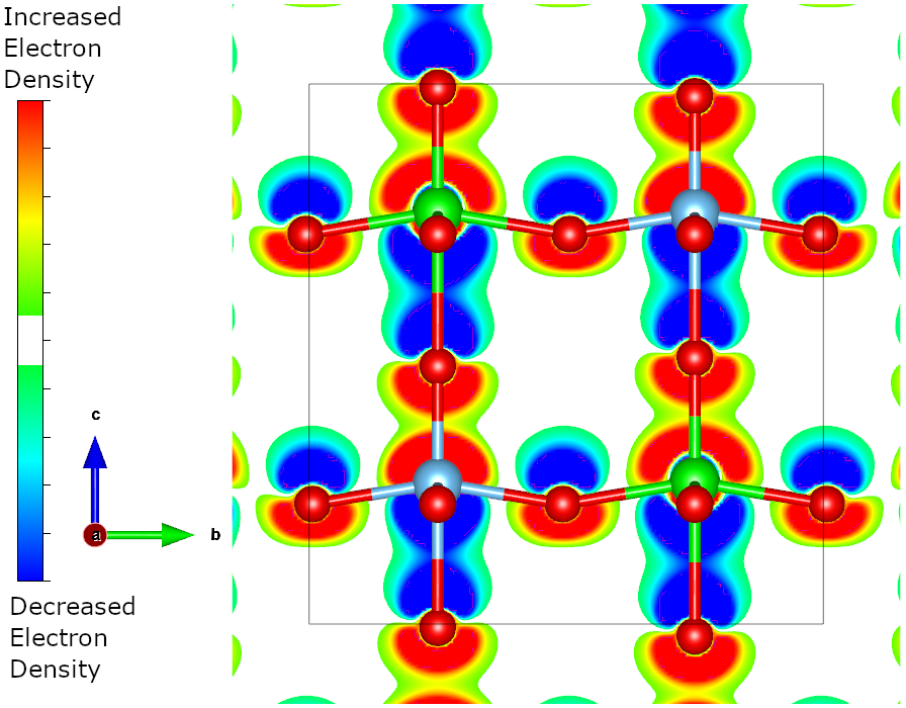

itself. Fortunately, the technology is already in place in the form of high-end render units, and for more numeric tasks such as the grid manipulation to obtain the difference, the many core architecture system discussed in chapter 4 can be used to break up the many simple problems into an embarrassingly parallel problem that can scale linearly to the number of cores available. For a structure of this size, a consumer grade GTX 970 was used, which is not a specialist piece of hardware and is relatively common.

Considering the figure, the most obvious feature is that while we are in the 33 mode the density shift lobes appear to have a greater lateral element than the unary structures, especially around the radial oxygen ions. This demonstrates the effect we have discussed throughout this chapter about the equalisation effect. There is a lower overall piezoelectric capacity due to electron density

being held up to equalise the two independent systems into a viable single material. This causes the lateral boundaries to hold electron density, which is then perturbed as an electron density shift under the strain. We can investigate this further in the next figures.

Also important is to see that the patterns between A-site and axial oxygen ion seem more KNO- or BTO-like than PTO-like. This is evidenced by a far less clear delineation in the "long bond" lobes which have a reasonable crossover, whereas these were visually separate in the unary PTO. Then the idea that the equalisation with a non-piezoelectric causes a stabilisation effect may be evidenced here, where the mixing of PZO allows a more stable material along the lines of its counterparts than pure PTO, that is known for breaking due to its own strain in crystal fabrication.

We see the sawtoothing effect in the oxygen ions with the slight misalignment, but our assertion that these do not change significantly under piezoelectric behaviour is shown by the fact that their density shift appears identical to the oxygen ions in the other perovskite units, and to those in the unary structures.

Figure 6.8 shows the same perturbation with a distance of 0.5d from the origin, crossing the A-site and lateral oxygen ions.

These are included for completeness but largely do not show anything particularly interesting. The lead ions do seem to be mirroring the oxygen ions, with a large, flat increase in electron density and a more rounded decrease. The opposing direction is consistent with the positive effective charge of the lead ion as opposed to the negative effective charge of the oxygen ions. This demonstrates that, while our choice of using the A-site as a boundary condition of the method, there would be much to be gained by reconsidering the same method but analysing lead shifts. However as we were initially interested in

FIGURE 6.8: A cross section of the electron density shift of PZT caused by an expansive strain in the c-axis of 0.25%, in the 100 plane at 0.5d from the origin.

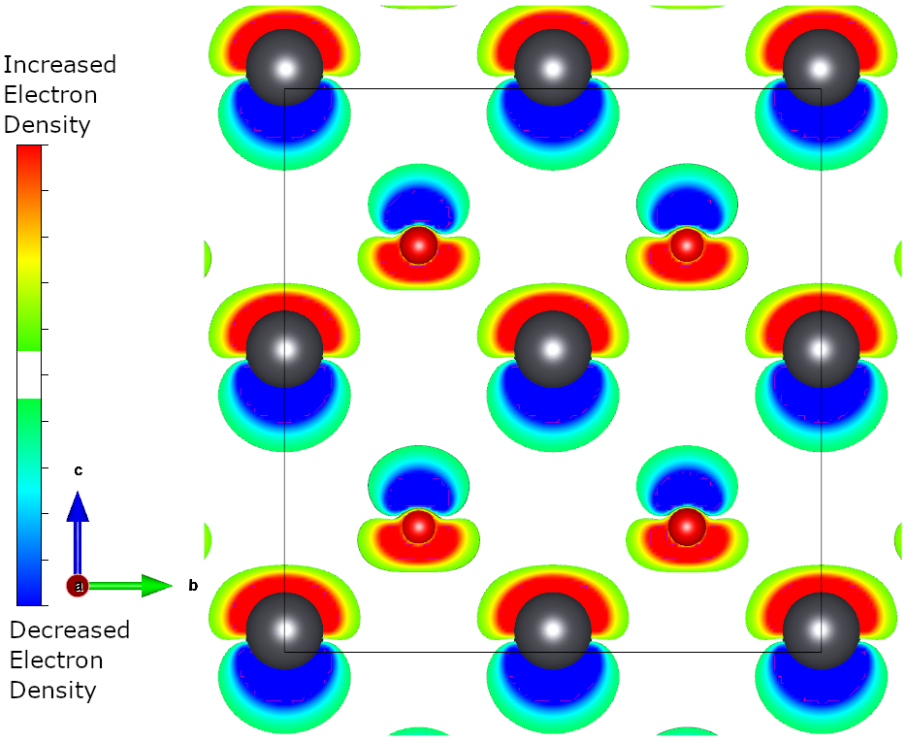

the B-site and oxygen effects then our choice to use the A-site as a reference point was still a valid choice.

Figure 6.9 shows the 110 plane at $1 \times d$ (5.75Å) from the origin.

While this observation is interesting, it does preclude features we may have expected from this view. With this being a lead based material, we may have hoped to see extra covalent effects coupling the lead ions to B-site and axial oxygen ions. The A-site ions are noticeably more active than the A-sites of BTO and KNO in the previous chapter, though the central axial column retains the features most similar to the KNO structure. This may well be a result of the zirconate contribution, as the stabilisation takes effect by altering the initial lead titanate to be more like its weaker counterparts. Then it may be that if

FIGURE 6.9: A cross section of the electron density shift of PZT caused by an expansive strain in the c-axis of 0.25%, in the 110 plane at 1d from the origin.

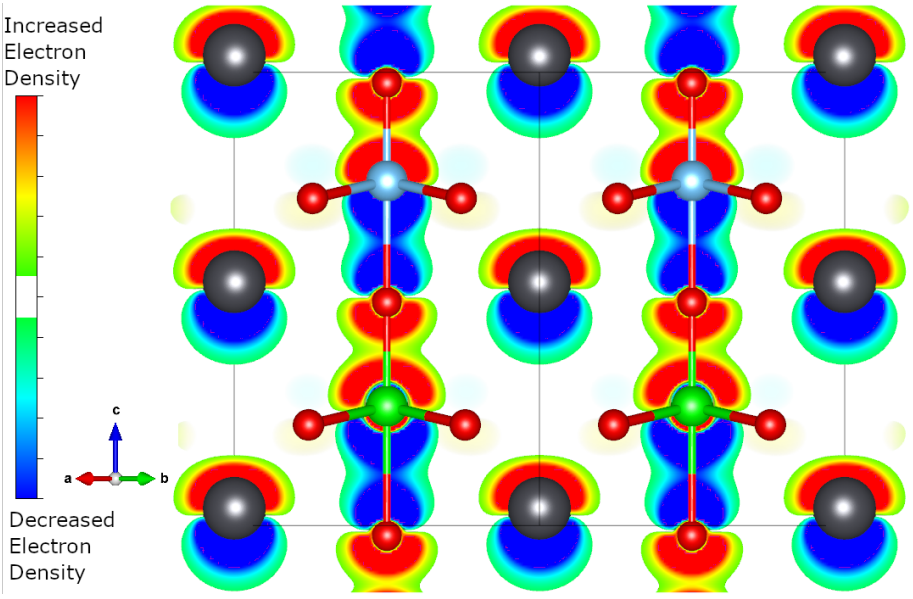

we were to observe the effects of mixing with another powerful piezoelectric, we would see a different picture. We may expect to see much more localised lobes along bonds, or an electronic coupling occurring spatially between the A-site and other ions, though it is unclear if these two seemingly opposing effects would cancel out using this method of visualisation.

We will now consider the C31 perturbation electron density shift. There will be a focus on how this compares to the unary system and significant changes between the E33 and C31 modes, however we expect it to share many features above which need not be repeated. Figure 6.10 shows the electron density shift in the 100 plane at a distance of 0.25d from the origin.

This shows the same behaviour change as in the unary structures, with the similar behaviour in the direction of polarisation, but extended perpendicularly along the cell. In this form it is most similar to the PTO shift, where the electron density shift lobes largely retain their directionality and do not

FIGURE 6.10: A cross section of the electron density shift of PZT caused by a compressive strain in the a,b-axes of 0.25%, in the 100 plane at 0.25d from the origin.

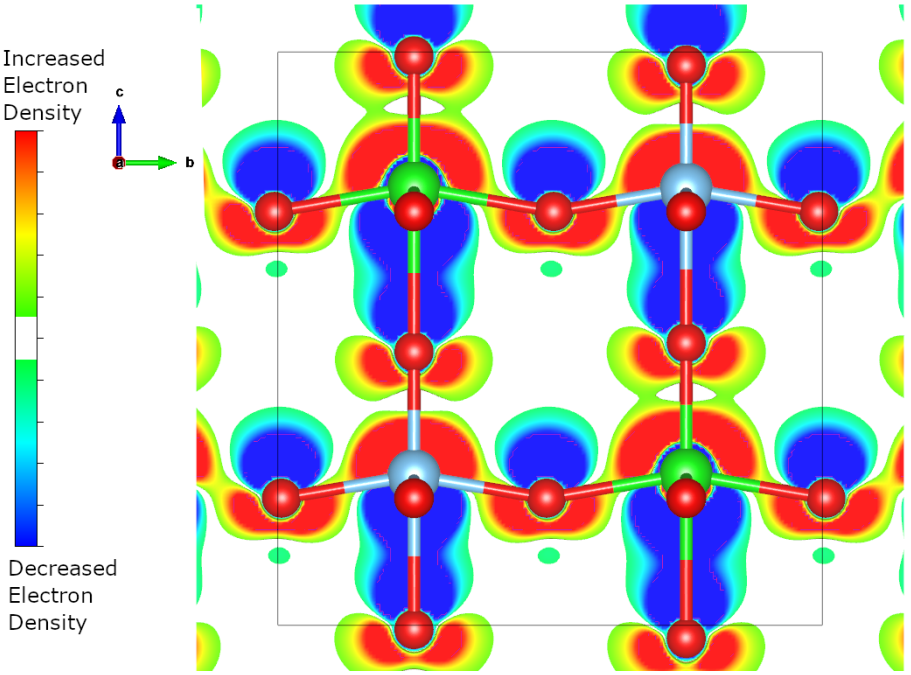

split entirely as in the other structures we performed calculations for. With the exception of a slightly more diffuse axial bond in the zirconate based cell causing the lobes to join, there is no marked difference between the different flavours of unit.

The whole system retains a marked degree of directionality in this electronic density movement, and although there is some notable interaction between radial oxygen ions and the B-site, ultimately this seems more coincidental to the strain direction, whereas the direction of polarisation is showing the most relevant shifts. That said, there is a slight imbalance in the positive lobes of the radial oxygen ions, showing a clear preference towards the titanium ions. This demonstrates at its heart the fundamental meaning behind the piezoelectric coefficient and the piezoelectric effect itself as a movement of charge. These are the movements of charge as calculated in our values for δ_{11}^{O-rad} and δ_{13}^{O-rad}

FIGURE 6.11: A cross section of the electron density shift of PZT caused by a compressive strain in the a,b-axes of 0.25%, in the 100 plane at 0.5d from the origin.

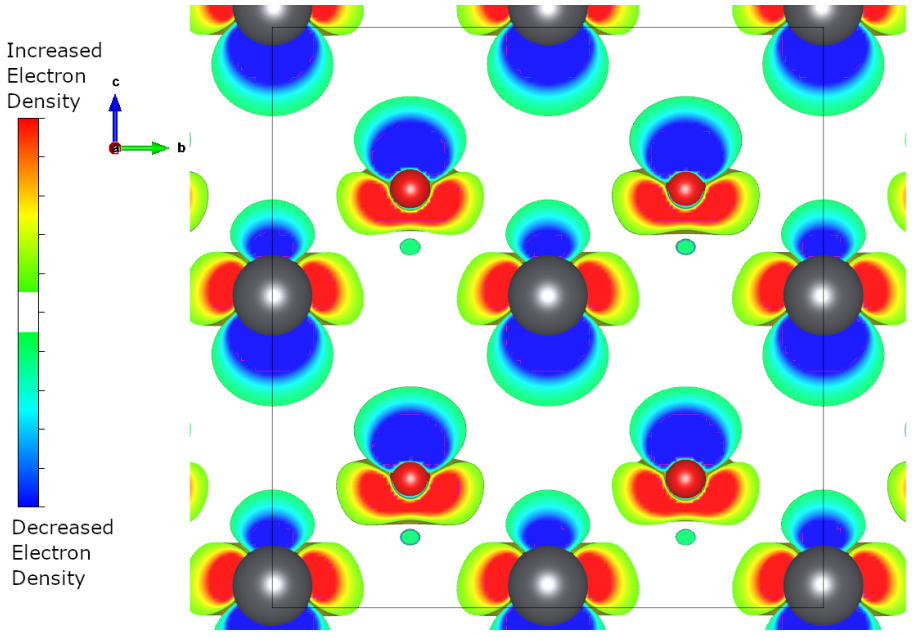

elements, which can be seen to cancel over the cell. Likewise, the much larger shifts show a clear preference in direction, corresponding to a charge differential and overall generation of current.

Considering the same mode, figure 6.11 shows the 100 plane at a distance of 0.5d from the origin.

It is in this mode that the most interesting and surprising feature appears, the split lobes of the lead ion is a feature not apparent in the unary structures. The lead ions do carry an off-diagonal charge in the Born Effective Charge elements which appear to oppose the radial oxygen ions, which is part of the overall unit equalisation theory. The wide lobes in both modes cover a large volume around the A-site, which may result in the shielding we have seen in the axis of polarisation.

FIGURE 6.12: A cross section of the electron density shift of PZT caused by a compressive strain in the a,b-axes of 0.25%, in the 110 plane at 1d from the origin.

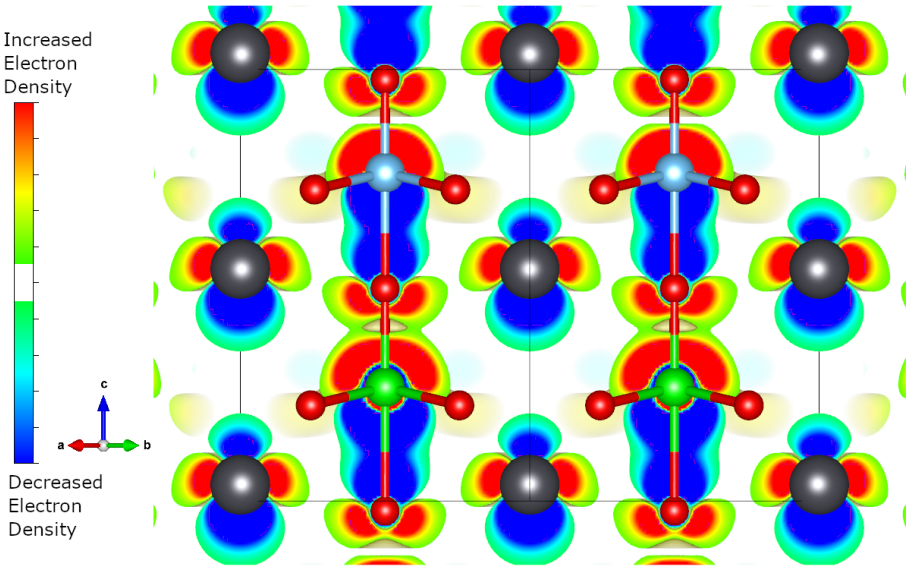

Figure 6.12 shows the C31 perturbation in the 110 plane at a distance of 1d from the origin.

We can definitely see that in this plane there is no imbalance laterally in the axial oxygen ion between B-sites, as in this plane the lateral B-sites are identical. This geometry may mean that if the density shift of those ions were rotated then the overall shape would be more elliptic, with the longer axis running between the Ti centres. However as these are the axial oxygen ions, this effect may simply be due to the proximity to the lead A-sites.

There is no visible coupling in this mode between the A-site and the polyhedron, however the distance between the A-site and axial oxygen lobes are short, which may indicate that on a lower density shift level these zones are connected. We are confident that there is a coupling between these two ions causing what we have referred to as a shielding effect, which leads to an asymmetry between the two flavours of unit along the axis of polarisation. Additionally the lobe

FIGURE 6.13: A cross section of the total electron density of the unstrained PZT structure in the 110 plane at a distance of 1d from the origin.

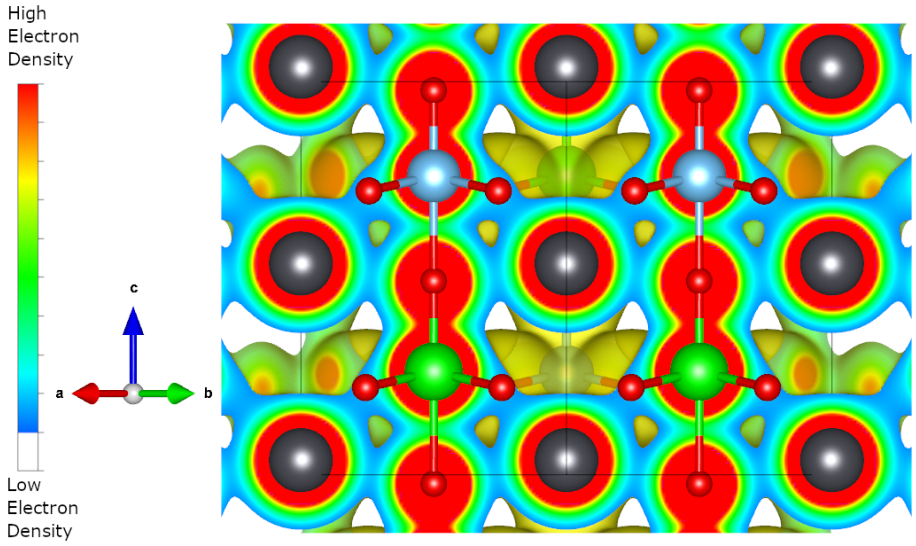

anti-parallel to the polarisation is much more disperse than the others. This may be responsible for the huge shift of the central polyhedra when compared with the displacement in other piezoelectric structures. It is important to remember that this is not an absolute charge, but a relative charge difference, therefore it is not a case of repulsion or attraction. In fact, it can be tied back to the Born-Oppenheimer approximation that is so fundamental to our method. Due to the massive size of the ions and their slow speeds, their movement is a perturbation based on the movement of electrons, which is represented as a change in density. Then the changes in the ionic displacement are incidental to the perturbation of the overall electron density, which is the driving factor behind this physical mechanism.

If we consider figure 6.13, which shows the total electron density of the unstrained structure we can see the large scale density function at work in a low level coupling between the A-site lead and both the B-site and axial oxygen.

The total electron density is hard to interpret due to the arbitrary units used

and the large maximum densities within the pseudopotential conflating the issue, however for comparison the lowest total electron density between these is ≈ 80 arbitrary units. The shorter B-site to axial oxygen bond has a lowest density of ≈ 500 units, and the longer has a lowest density of ≈ 175 units.

Overall then this area of electron density has a far weaker bonding effect than the polyhedral bonds, but is definitely a physically meaningful feature that could explain the large displacement of the B-site and axial ions. Comparing other supercells to consider the magnitude of these bonds and their comparative ratios may be a good project, however if this is considered the covalency of the A-polyhedron system, then we would need to consider how the ionic contribution plays a part. While the Born Effective Charge might be a good indicator, the total is a measure of the ionic-like behaviour, which is not necessarily separate from the covalent system. However the same linear response methodology, with a k-point path to take the geometry into account, would be an important project for determining the covalent-ionic behaviour of the system.

6.4 Conclusions and Further Work

Using our method from the previous chapter, we have ascertained that the workflow can be used on more complicated and larger structures. We have performed calculations for geometry, linear response, and strain perturbation of a PZT cell, and we have processed these calculations to calculate the polarisation, piezoelectric coefficient, set of partial piezoelectric coefficients, and generated visually interesting and informative electron density shifts.

Throughout this chapter we have confirmed that this methodology retains the same accuracy and issues regardless of size and number of dimensions.

We have also brought attention to interesting features of the structure, such as the oxygen sawtoothing, equalisation density, and the relation between the polarisation and piezoelectric coefficient for the full unit and, more importantly, for subcells of this unit.

We have also proposed the lead shielding effect, dampening the axial equalisation, and discussed the ways in which the electron density shift and total electron density can be used to identify the essential features and mechanisms of the interactions that are responsible for the physical features of the PZT system and perovskite piezoelectrics in general.

While this research has shown interesting results as a proof of concept, the computational time necessary to push through the full project has meant that the results are too shallow to draw broader trends from. Further work in this project would be based on performing similar calculations on PZT systems with different mixing and composition, as well as looking at other binary systems such as $Na_xK_{1-x}NbO_3$ which we already have basic concepts from due to our KNO calculations in chapter 5. By determining and comparing our derived properties we can build a clearer picture of how multicomponent crystals act, by finding similarities and differences it will be possible to see how mixing, doping, and proportions work in the material on an atomic scale, giving greater insight into designing and optimising new piezoelectric materials for real applications.

Chapter 7

Multiferroic Materials

7.1 Introduction to Bismuth Ferrite

In this chapter we aim to evaluate the feasibility of the previous methods in chapters 5 and 6 on a material with esoteric properties. Multiferroics are defined as "materials that inherently exhibit both magnetic and electric polarizations" by Schirber[166]. Of the few materials that demonstrate this property we have selected bismuth ferrite, a rhombohedral (R3m) perovskite with the chemical formula $BiFeO_3$. In keeping with our previous system, we will use the shorthand BFO to refer to this material. This was initially characterised by Zaslavskii in 1960[131], however due to concerns with the structure listed on ICSD[153] we have instead opted to use data from a later characterisation by Tomashpolskii[129] as ICSD lists it as "high quality", though what designates high or low quality data is not made explicit. This unit cell is shown in figure 7.1, with $a = 3.962$Å and $\alpha = 89.40°$. The structure was characterised using x-ray diffraction at room temperature and pressure, and has ICSD collection code 28027.

FIGURE 7.1: VESTA visualisation of the rhombohedral bismuth ferrite cif structure. This unit cell was characterised by Tomashpolskii[129], using x-ray diffraction at room temperature and pressure. ICSD code: 28027. Purple - Bismuth, Rust - Iron, Red - Oxygen.

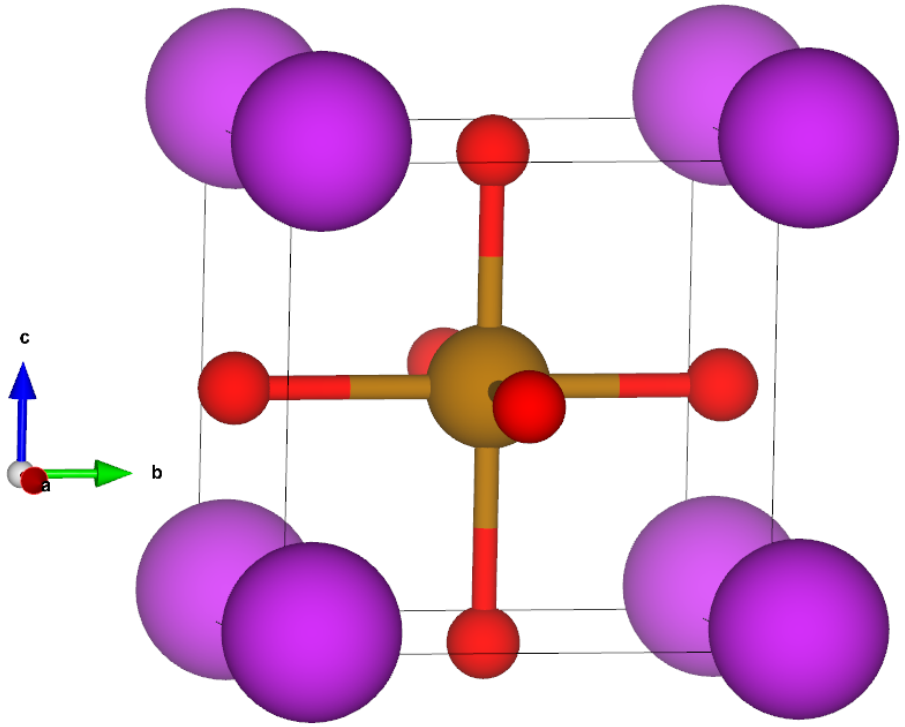

Initially the cell appears cubic, as with many perovskites. However in actuality this structure is slightly rhombohedral, fitting the the conditions $a = b = c$ and $\alpha = \beta = \gamma \neq 90°$. This can be viewed as a cubic structure that has been skewed in the (111) direction. This is a commonly seen ferroelectric phase, out of the four materials used in chapters 5 and 6 barium titanate and potassium niobate have a temperature dependant rhombohedral phase, and lead zirconate titanate has a compositional rhombohedral phase. This leads the material to have a polarisation in the [111] direction, giving eight polar directions in a regular multi-domain system. As we lack the resources to perform simulations on a multi-domain level, our sample is considered to be a single-domain, single-crystal polarised in the (111) direction.

The reason that bismuth ferrite is incompatible with our methodology is due to the magnetic characteristics emergent from the iron ion at the B-site. This is not an insurmountable issue for DFT methods, which have been used to characterise the G-type anti-ferromagnetic coupling[132]. This type of arrangement is based on an oppositional spin polarisation in the ferromagnetic electron structure. We are all familiar with the method by which spins align to create a ferromagnet, however in analogy to the anti-ferroelectric property an anti-ferromagnet is formed when neighbouring magnetic ions have an opposing spin polarisation that cancels out the magnetic effect on a very short scale. There are 3 main groups of anti-ferromagnetic ordering, in A and C-type there is magnetic ordering within a plane, say the [100] or [110] planes, which is cancelled by the neighbouring plane having an opposite spin polarisation. G-type can be considered to be fully mixed, as in our arrangement of the B-site ions in chapter 6, so for every B-site iron ion, the nearest neighbours along every axis have an opposing spin polarisation[167]. This is separate from the electronic polarisation, which is parallel in unit cells along the (111) axis. We can think of these two phenomenon as a polarisation of different properties of electrons. Ferromagnetism is a polarisation of spin, whereas ferroelectricity is polarisation of charge.

Under DFT, the electric polarisation is simply represented as a non-centrosymmetric centre of charge in the electron density function. The spin however is an explicit property that must be taken into account in the electronic minimisation. There are several factors that cause issues that will be explained as they become relevant in section 7.2. Briefly however, they are largely represented by the following list.

- The explicit spin polarisation
- The inclusion of empty bands

- Density cycle method
- A suitable pseudopotential
- The phonon implementation
- Structural effects of magnetic properties

7.2 Performing the Calculations, and Evaluating Which are Feasible

7.2.1 Convergence

Calculations were performed on ARC3, the hardware configuration of which can be found in section 4.2.3. Due to our requirements, the standard 24-core compute was used.

First it is essential to select the pseudopotentials and converge the Monkhorst-Pack grid and kinetic energy cut-off as previously. There are several different suitable methods to select pseudopotentials, as we are able to use ultrasoft pseudopotentials due to the lack of linear response in the phonon calculation. We considered ultrasoft potentials, modified electron string potentials, and norm-conserving potentials using the newly implemented norm-conserving pseudopotential generator in CASTEP, NCP18.

Some basic test cases using the bismuth ferrite structure showed that we needed to enable special flags in the CASTEP calculations. Firstly, the 'spin_polarized' flag was set true, as expected, and 'nextra_bands' was set to 17 to add 17 extra bands into the band structure. This increases the computational complexity

but allows for spin, and the extra bands give the minimiser more freedom in electronic states.

Though the advantages to ultrasoft potentials should be faster calculations due to a lower cut-off energy, in practice it was found that they were far too unstable for reliable calculations. Under the density mixing scheme for metals_method the SCF minimisation failed to converge often, sticking in false minima until the calculation timed out. By contrast, the norm-conserving potentials were found to be much more reliable under density mixing. This is likely due to the tendency for NCPs to contain more valance electrons and relying less on a pseudoion, as well as generally creating a smaller pseudoion. While we could have altered the electronic strings in the ultrasoft pseudopotentials, there is very little information on how to modify these strings, which could have required a significant time investment with no guaranteed reward.

Instead of density mixing, we could change the metals_method to EDFT. This technique is much more robust and reliable at the cost of much greater CPU requirements, virtually guaranteeing SCF convergence. This is usually required for materials with very unusual conductivity properties, such as the edges of nano-ribbons. Given that the use of this method will require much greater computational resources, it was instead decided that the norm-conserving pseudopotentials would be more worthwhile to use despite the likelihood of greater kinetic energy cut off.

For our convergence technique, we use the initial del-diff methodology from section 5.2.3 to calculate the force differences, and plot the changes in these differences over increasing convergence parameters. The Monkhorst-Pack grid size was kept equal along all three axes and increased by one each cycle, and the kinetic energy cut-off was calculated between 400 and 1500eV in increments of 50eV. Figures 7.2 and 7.3 show the plotted convergence data.

FIGURE 7.2: Force difference changes on the axial oxygen ion in bismuth ferrite using the δ-diff method from chapter 5, against single axis Monkhorst-Pack grid size.

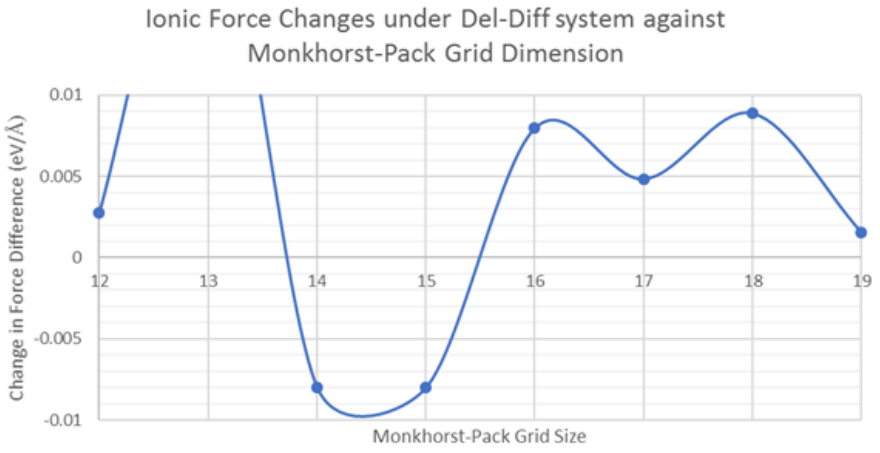

FIGURE 7.3: Force difference changes on the axial oxygen ion in bismuth ferrite using the δ-diff method from chapter 5, against the kinetic energy cut-off.

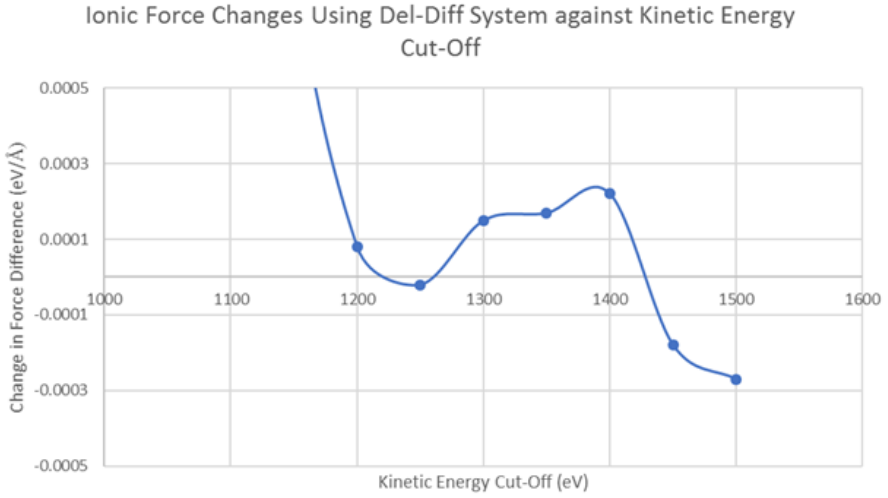

Figure 7.2 shows that in the Monkhorst-Pack grid we see that the force difference is almost identical between 14^3 and 15^3, therefore we select a value of 15^3 as the converged grid. This corresponds to a spacing of 0.017Å^{-1} in the initial cell along each axis. As for the cut-off energy, the set of 3 points from 1300 to 1400eV shows almost no variation, so the value of $1400eV$ is selected. If we read the headers of the pseudopotential files in a text editor we see that the highest projected cut-off is in the iron ion, with a fine rating of $1170eV$ and an extreme rating of $1872eV$. As we require precise ionic positions, then this level of precision is reasonable. For consistency we use an SCF energy tolerance of $1 \times 10^{-10}eV$.

The requirement of a high cut off energy is likely due to the magnetic properties of iron. Comparing to a titanium pseudopotential from the same library, the listed extreme cut-off is 827eV. This is despite the pseudoion having the same core electron structure. The third energy level is considered valance in both cases and is explicitly calculated, along with the $4s^2$ orbital. We know that the 3d electron orbital is what creates the overall magnetic moment, and by reading the pseudopotential report we see that the Ti pseudoion with the extra 3 and 4 levels converges to around -1576eV, whereas the Fe pseudoion converges to a total energy of -3336eV. Ordinarily we would not expect to see such a drastic difference between such similar ions with only 4 valence electrons difference, demonstrating how this extra spin is a costly inclusion.

The structure has been successfully converged, and we already see how the differences begin to stack making the task more computationally expensive. The activation of the 'spin_polarization' flag immediately doubles the calculation time, as the spin pair electrons that are normally degenerate must now be independently calculated. While we have avoided having to use the EDFT method, the high cut-off energy does significantly increase time, as time scales

by the square of the cut off energy. So if we take the barium titanate example, the plane wave cut-off used was 900eV, with the 1400eV for bismuth ferrite, then we are using $\approx 156\%$ of the energy cut-off, which means that the time taken is $1.56^2 \approx 2.4$ times the amount of time of the equivalent BTO calculation purely from the increased energy cut off. In addition, the extra bands added for the calculation give a total of 37 non-pseudoised bands, whereas the BTO calculation contained 20. Though we do not know the behaviour of CASTEP under increasing bands, the most optimistic prediction would be another factor of two. The Monkhorst-Pack grid has the same number of points pre-symmetry, however we recall that the grid for BTO was significantly more dense than the other materials. There are also considerations as to the symmetry, the rhombohedral structure has six symmetry operations compared to the eight for tetragonal, increasing the proportion of the reciprocal cell that is irreducible. That said this is a consideration of the structure, not the properties of the ions, and as such this would be the case with any rhombohedral structure, such as the low temperature states of barium titanate and potassium niobate.

Overall then, while there is some randomisation involved in the code implementation, we expect that despite its similar perovskite structure, the single unit of BFO could take computation times an order of magnitude higher than the unary perovskites in chapter 5. While this is not a problem in itself, given the newer and more powerful hardware available to us to mitigate this, it demonstrates that not all of these systems are equal in this type of simulation, and this extra time would need to be factored in to consider the bismuth ferrite-lead titanate binary, for instance.

A key method to counteract this is to optimise the calculation for speed using the parameter flag 'opt_strategy : Speed'. By containing the entire calculation in RAM, this speeds up the overall calculation by drastically reducing

the amount of time wasted reading and writing to a slower storage medium. On modern hardware, the memory per core and capacity for hybrid-parallel calculations makes this feasible for all but the most memory intensive tasks.

Now we are aware of how our simulations already differ from those we saw beforehand, these parameters can be used in calculations to determine physical properties of the structure.

7.2.2 Geometry Optimisation

The geometry optimisation is performed with the same tolerances as in previous chapters as shown below.

- Energy change per ion of $2 \times 10^{-8} eV$
- Maximum ionic force of $1 \times 10^{-4} eV/\text{Å}$
- Maximum ionic displacement of 5×10^{-6} Å

Stress is left as a free parameter by setting it to $0.1 GPa$, well above what would we expect to be a binding tolerance, so as to not interfere with the calculation. The LBFGS algorithm is used as before as it is efficient and fast, and requires no extra configuration for the multiferroic system beyond those that have already been addressed.

Table 7.1 shows the geometry optimisation results, both directly from the calculation (abs.) and relative (rel.) to the A-site bismuth being positioned at (0,0,0) in the cell, as it is usually defined. Experimental comparison is taken from the original .cif file used above[129].

TABLE 7.1: Optimised lattice parameters, volume, and fractional coordinates of bismuth ferrite with experimental comparison. Absolute (Abs.) are the values directly from the output file and .cif file. Relative (Rel.) values are the fractional coordinates relative to the A-site bismuth ion being set at the origin of the unit cell. Major and minor oxygen coordinates are the displacement parallel and perpendicular respectively to the face of the unit cell.

	Calc.		Expt.[129]	
	Abs.	Rel.	Abs.	Rel
a (Å)	3.903	-	3.962	-
$\alpha(^\circ)$	88.61	-	89.40	-
Vol. (Å^3)	59.39	-	62.18	-
Frac-Bi	-0.066	0.000	0.050	0.000
Frac-Fe	0.498	0.564	0.500	0.450
Frac-O_{maj}	0.520	0.586	0.500	0.450
Frac-O_{min}	0.006	0.072	-0.021	-0.071

We see that the lattice parameters are in good agreement with the experimental data for a rhombohedral structure extrapolated to absolute zero. We know that in the hexagonal-rhombohedral form the a- and c-lattice parameters decrease with decreasing temperature[168], which we can interpret in the primitive cell as a reduction in a and α.

The atomic positions are unusual. The cell initially uses a centred Fe ion as the reference point, but we have converted to a Bi relative cell as with our own simulation results. What is most interesting is the relative positions of the iron and oxygen ions with regards to a central symmetry point. We would generally say that for a positive polarisation the positively charged ions need a positive displacement to generate a positive dipole moment, and the negatively charged ions must be negatively displaced. While we have seen in lead titanate that this is not necessarily the case, the fact that our calculation seems to be in an opposing symmetry is unusual.

In reality there are many considerations, the first is that there is simply a temperature effect causing the switch somewhere between the room temperature result and absolute zero. The next is the possibility that these are different states. A known weakness of the BFGS algorithm is that it struggles with energetically degenerate or metastable states with a small free energy barrier. Depending on the parameters of the minimisation and the free energy landscape of the system, it is possible for the minimisation step to pass through a weak barrier and form another state. This is not a great concern as these low barriers of activation typically cause these states to appear unstable as thermal perturbations can push the real material into a different state, so such materials can only exist in the state for a short time. The other is to do with our understanding of the material. We have used a perovskite view of BFO, but it could be that this geometry is more consistent with the R3c hexagonal type group, which many BFO structures are listed as. Due to the size of the cell and its non-perovskite nature, we have not considered it, but despite it hosting the same equivalent positions and lattice symmetry, this may be the more technically correct structure.

The final option, of course, is that we are simply not viewing the symmetry in the correct way. The direction of polarisation is non-axial, so it may not be relevant to compare the axial values and instead we should consider the symmetry in the direction of polarisation. It may be the case that symmetric positions defined in this system are different to how they were considered previously, and that these lattice vectors and fractional positions are misleading.

We note that while this type of calculation can take variable amounts of time due to the unpredictable number of LBFGS steps, this calculation took 4-5 times as long as the equivalent optimisations in chapter 5. While this is not

as slow as we predicted, we are using much more powerful hardware than previously, which would offset the extra calculation complexity.

7.2.2.1 Symmetry of the Rhombohedral Cell

We will discuss the rhombohedral symmetry, to understand how our symmetric reduction works. If we think of the unit cell as a pseudocubic shape with faces and corners then the A-site and B-site, which in this case is Bi and Fe but is applicable to all such structures, lie on the corners and in the centre, respectively. These ions are free to move in the (111) direction following the polarisation, meaning that the positions can be represented as $Frac_{Bi} = (0.0 + \Delta_{Bi}, 0.0 + \Delta_{Bi}, 0.0 + \Delta_{Bi})$ and $Frac_{Fe} = (0.5 + \Delta_{Fe}, 0.5 + \Delta_{Fe}, 0.5 + \Delta Fe)$ where each Δ_k is equal across axes.

In our relative positions above, we have defined $\Delta_{Bi} = 0$. The three oxygen ions occupy the faces, so we have defined a major displacement in the plane of the face and a minor displacement perpendicular to the face. Then the positions for the oxygen ions can be represented as $Frac_O = (0.5 + \Delta_{O-maj}, 0.5 + \Delta_{O-maj}, 0.0 + \Delta_{O-min})$ for the first, with linear rotations of elements for the other two positions. As the Bi and Fe positions are all equal, we have only listed one of the 3 elements, and in the oxygen ion positions we give one of the two major coordinates and the minor. Of course, it would be equally valid to only list the Δ_k values as a fractional displacement, as these are equivalent. Thus through symmetry the whole structural parameter set can be uniquely identified in this manner.

7.2.2.2 Cartesian Vectors

The first thing to note about fractional positions in this type of material as a whole is that they are in terms of the lattice vectors, not cartesian vectors. In the tetragonal structures previously, these were equivalent and it was implicit that the lattice vectors were trivially mapped to an (x, y, z) axis base as the (a, b, c) set was orthogonal and easily normalised. This, along with the fact that the axis of polarisation was parallel to a lattice vector meant that coordinate selection was obvious. The rhombohedral vectors however, do not form an orthonormal basis set, and the axis of polarisation is not along any single vector, then being aware of this mismatch is essential.

For an approximation, we could simply assume that the axes are cubic, which would allow the same method to be used as before. This is the most basic method, which is less accurate but easiest to apply. While we still have to consider a 3-dimensional problem, so many displacements are identical.

We can solve differences in the structures by performing the calculations on structures relative to each other. This is convenient when performing d_{ij} calculations, as it can be considered simply using the difference in distance from the fixed A-site, or even from the hypothetical maximum symmetry state of zero polarisation. This method is easy to perform on small scales, but can become cumbersome if it must be repeatedly applied.

The next method is to create a transformation matrix. Effectively a mapping between the (a, b, c) vector and the (x, y, z) by means of simple matrix multiplication. The difficulty in this approach comes from forming the transformation matrices, as the operations themselves are simple enough. While these should be generic, finding suitable transformations to match the specific orientation of the given problem, and forming them manually is not as trivial

as it initially sounds. Such prototype transformations have been calculated elsewhere[169], but applying them without instruction can be difficult.

In order to calculate a transformation matrix using the given equations[169], we used values of $a = 3.902$Å, $\alpha = 88.602^\circ = 1.547rad$. Equation 7.1 shows the transform matrix formed by indexing horizontally across the 3-vector notation. Though it is not clear entirely what basis this forms, multiplication with the fractional coordinates have successfully measured the interatomic distances as measured by VESTA[154] to a rounding error. This demonstrates that this method is reliable, though can give confusing results indicating an unexpected change of basis. All elements are multiplied by the lattice parameter, so we have given both the real space transform and the coordinate transform. The determinate of the coordinate transform matrix is ≈ 1 which can be attributed to rounding error, so is easily invertible and does not affect the length of vectors it multiplies.

$$T = \begin{bmatrix} 2.793 & 2.793 & 0.132 \\ -2.726 & 2.726 & 0.000 \\ 0.000 & 0.000 & 3.900 \end{bmatrix} = a \times \begin{bmatrix} 0.716 & -0.698 & 0.000 \\ 0.716 & 0.698 & 0.000 \\ 0.034 & 0.000 & 0.999 \end{bmatrix} \tag{7.1}$$

Then we can calculate the absolute cartesian displacements from fractional positions using the basic matrix operation $x_i = T_{ij}a_j^*$ where a_j^* is the fractional position vector relative to (a, b, c).

The final and most general method would be to simply do away with the lattice vectors and define the cartesian axes in relation to the polarisation. As axis positioning is arbitrary, eliminating the polarisation states from two of the axes greatly simplifies the problem, though it is complicated slightly by locating the symmetric positions and geometrically calculating the displacements.

Issues also arise due to the necessity to convert all properties with directional components to the new axes.

Each approach is justifiable, however it should be made clear which is being used, and the same method should be applied consistently. We will be applying the matrix transform method, due to a personal preference of solving matrix equations.

7.2.3 Phonon Calculation

The phonon calculation is where our method has the most issues, and is the main break-point in what we are capable of calculating for bismuth ferrite. We must run the SCF minimisation as a spin polarised calculation, which means that the electronic structure must be calculated with variable electronic states. This type of calculation, referred to by CASTEP as a "partial occupancy" calculation or a "metallic" system. While in other calculation types this just extends the calculation, it makes it incompatible with the linear response phonon calculation.

Many avenues of the electric field calculation become impossible due to this issue, in our calculations the Born Effective Charge, LO/TO splitting, and electric field response are disabled. Not only are these not possible in CASTEP, but from discussions with the developers we find that these quantities simply do not exist for materials that are spin polarised. In recent work, these quantities are reported in by using a supercell method in other codes, that allows them to fix the spins to cancel out, creating an overall non-spin polarised structure[137]. However, this approach is disingenuous, as the electronic states of the material are not likely to alter the electronic states sufficiently to make these techniques relevant. In our own output files we can see that while the spin of the iron

ion is the largest, the other ions in the system gain an induced spin, which the minimisation method is able to account for in our calculations due to the extra bands.

We also recognise the unusual conduction properties that have been observed experimentally in BFO[170]. Freezing bands is a good method in insulators as it simplifies calculations significantly, but in conductors and semi-conductors it can remove band interactions that are crucial to understand the electronic structure and properties of the material.

This raises the issue touched on about the dielectric permittivity in chapter 5, that simply because a value can be generated from a simulation, it does not mean it is physically relevant. Other research papers, such as Wei, et al.[137], all use VASP as their DFT code, so it may be that a different implementation of the phonon calculation is used that does allow for electric field calculations of structures without fixed occupation. On the other hand it may be that VASP does not have as many warnings for unrealistic calculations as CASTEP does. It is worth noting that VASP supports different types of pseudopotential and has a slightly different set of tasks it is able to perform, which may give it an advantage in this rare type of case. However it does not have an implementation of linear response, so finite displacement methods must always be used, requiring a supercell to be built. Overall it is definitely worth investigating which of the available codes best suits a particular project.

7.2.4 Elastic Compliance

The elastic compliance tensor was calculated using the elastic constants framework by Andrew Walker[156]. This calculation was performed as before, using two strains patterns, each with six strains between -0.25% and 0.25%. The first

strain was along the x-axis, while the second was a non-linear strain represented by the strain tensor (ϵ_{ij}) in equation 7.2, where x is a number corresponding to our overall magnitude of strain.

$$\epsilon_{ij} = \begin{bmatrix} 0.0 & 0.0 & 0.0 \\ 0.0 & 0.0 & x \\ 0.0 & x & 2x \end{bmatrix} \tag{7.2}$$

These are the minimal set of independent perturbations on the lattice, which are needed to calculate the elastic compliance tensor. Once completed, we were able to generate the entire elastic compliance tensor, which shows the following symmetry in non-zero elements shown in equation 7.3.

$$\begin{aligned} s_{11} &= s_{22} \\ s_{12} &= s_{21} \\ s_{13} = s_{23} &= s_{31} = s_{32} \\ 2 \times s_{14} = -2 \times s_{24} = 2 \times s_{41} &= -2 \times s_{42} = s_{56} = s_{65} \\ s_{44} &= s_{55} \end{aligned} \tag{7.3}$$

Additionally the s_{33} and s_{66} elements are unique, non-zero elements. This is consistent with the tables shown in Nye[22]. Table 7.2 shows the unique elastic compliance elements.

We see a high compliance in the diagonal elements, with low negative compliance in off diagonal elements. This suggests that the material is highly elastic, generating large strains in the direction of the relatively small stresses applied and leading to large piezoelectric coefficients due to high linear displacements for ionic charges. However, it is resistant to stress in the perpendicular directions. For mechanical applications this is ideal. In comparison to table 5.5,

TABLE 7.2: The unique elastic tensor elements (s_{ij}) of bismuth ferrite calculated using the elastic compliance calculation method.

Compliance	BFO
$s_{11}(TPa^{-1})$	14.96
$s_{12}(TPa^{-1})$	-5.14
$s_{13}(TPa^{-1})$	-5.37
$s_{14}(TPa^{-1})$	-1.79
$s_{33}(TPa^{-1})$	15.44
$s_{44}(TPa^{-1})$	26.43
$s_{56}(TPa^{-1})$	-3.59
$s_{66}(TPa^{-1})$	40.19

we see that this behaviour is similar to the direction of polarisation for lead titanate. This leads us to believe that we would have piezoelectric coefficients around the magnitude of PTO. Of interest is that the largest elements are the rotational elements, rather than the axial ones. If so then the material may be more suited to rotational type mechanisms for its piezoelectric properties.

Elastic constant calculations were more difficult to perform than the basic geometry optimisation. Whether due to the rhombohedral symmetry or the free movement of the spin polarisation axis, minimiser errors occurred and the LBFGS algorithm would regularly fall into false energy minima. While this can easily be fixed automatically in software by reverting to a previous state and allowing the minimisation algorithm to undergo different random steps, it does raise questions as to the reliability of these calculations implemented in an automated system.

If we consider the goal of creating an automated pipeline to perform calculations, this would be simple to perform on the unary, and most tasks would apply trivially to the binary systems, although time limits imposed by servers would need to be considered to ensure calculations were actually complete before moving to the next step.

In a multiferroic however, it is clear that manual intervention on calculations may be necessary regularly. Therefore, if we were to attempt to classify large groups of piezoelectric materials using the framework we have described, then any multiferroic materials either previously known or discovered due to warnings in the calculation should be removed from the data set and kept separate, in order to not hold up the less computationally difficult materials and to be given the special attention necessary to ensure smooth running.

7.2.5 Strain Perturbations

In order to improve our efficiency given the long calculation times of the material, we did not perform perturbations on the material. Instead, we reused strained structures from the elastic constants calculation which fit our criteria. We wanted one strain from each pattern with an FFT grid that matched that of our initial geometry optimisation. Grid information is printed in the CASTEP output file at a higher verbosity level, which required setting "iprint : 2" in the .param file. The final structure of each of the strains after the optimisation step was taken using the 'castep2cell' post-processing tool installed with CASTEP, and each was dryrun to calculate the grid. It was found that the 96^3 grid we required was used in the 4th step in both strain patterns.

In order to generate the electron density without repeating the calculation, the "CONTINUATION" flag in the .param file was set to the binary .check file, the task was set to perform a single point energy calculation, and the "WRITE_FORMATTED_DENSITY" flag was set true. This allowed CASTEP to read the binary file, extract the previously calculated electron energy minimisation data, and output the final electron density as a formatted, readable file. These are used to generate electron density shifts shown in section 7.3.3.

FIGURE 7.4: VESTA visualisation of the electron density of bismuth ferrite in a cross section of the (100) plane at 0.5d from the origin.

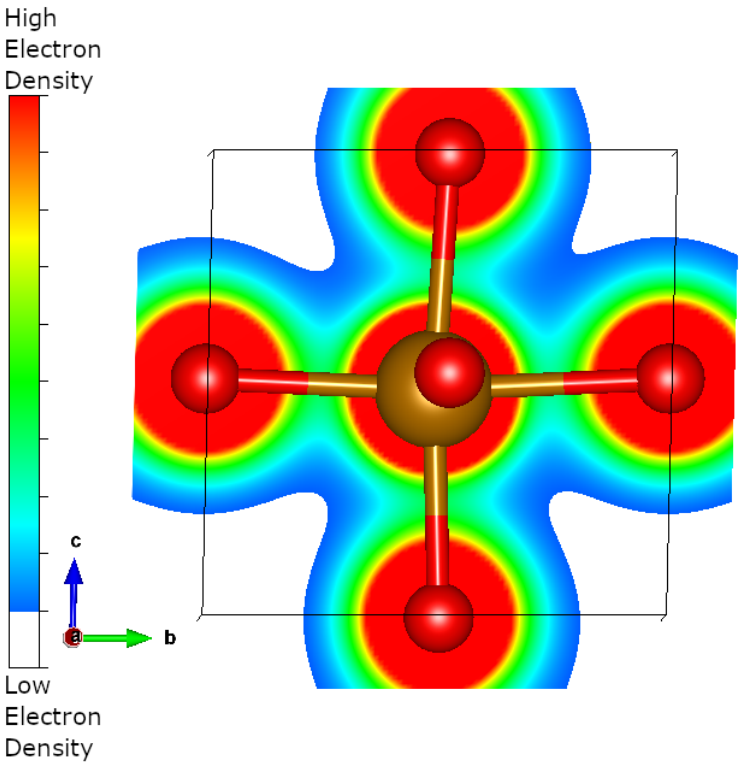

7.3 Analysis

7.3.1 Total Electron Density Map

The total electron density map is created by taking the .den_fmt file from the geometry optimisation and converting it to a VESTA compatible .charg_frm. It can then be superimposed over the output .cell file and displayed as 3D volumetric data or 2D cross sections.

Figures 7.4 and 7.5 show the total electron density in the BTO cell in the (100) plane at 0.5d from the origin, and the $(\bar{1}10)$ through the origin.

FIGURE 7.5: VESTA visualisation of the electron density of bismuth ferrite in a cross section of the $(\bar{1}10)$ plane through the origin. The direction of the polarisation vector in this view passes from the bottom right bismuth ion to the top left.

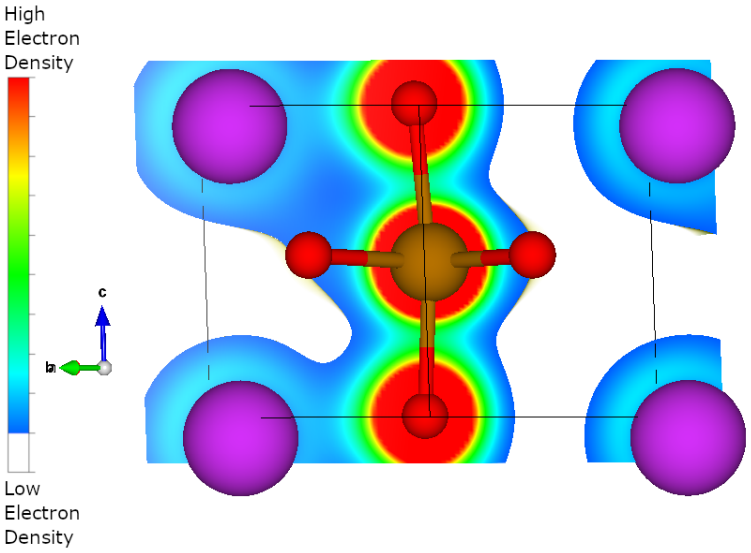

Both figures have been standardised to the settings used for PTO in figure 5.7 as it is the most suitable direct comparison. In the (100) plane the overall form is similar, though slightly more diffuse than the the previous structures. Bonds are formed in the oxygen polyhedron to the central B-ion, and electron density is mostly clustered around the ions.

The interesting behaviour occurs in the $(\bar{1}10)$ plane. At first glance this may seem an esoteric choice, however if we consider the direction of polarisation in the rhombohedral structure, the (111) vector passes from the bottom right to top left of the figure from the perspective shown. We see that the ions are displaced in that direction, with electronic coupling between oxygen ions and the nearest A-site bismuth ion. This demonstrates the polarisation of the rhombohedral phase. In the tetragonal structure, we would expect to see this type of coupling in the c-axis, though it is much weaker in the previous, non-magnetic materials and as a result does not show in their density maps.

We have established two planes of interest and observed the ferroelectric displacement, however the difference between this material and the previous is more likely to be in the density shift rather than the total. First however, we must consider the greatest difference.

7.3.2 Total Electron Spin Density Map

The electron spin density is similar to the electron density, however this tracks the spin at each point of the FFT grid rather than the charge. In the previous structures spin was cancelled within orbitals by degenerate electrons, however the free spin in bismuth ferrite leads to the magnetic behaviour.

Figures 7.6 and 7.7 show the spin density in the (100) plane at 0.5d from the origin and $(\bar{1}10)$ at the origin. We have an isosurface of 0.25, with a saturation of -50 to 2.

The first thing to notice is that, as in this system the spin is negative, the colours are reversed, as red represents a more positive (but magnitudally lower) spin and blue more negative (but with a higher magnitude). Then the highest concentration of negative spin is in the blue area around the iron ion. This is unsurprising as it is the core magnetic component of the system. If we were to place a second cell neighbouring the first, we would expect to see a positive spin due to the G-type antiferromagnetism.

More interesting is the small but significant induced spin around the oxygen ions evident in both planes. This demonstrates that, while iron is the key magnetic component in the multiferroic material, the spin causing this effect is induced around the bonding ions and shared through the structure. Reading the Mulliken analysis performed by CASTEP, we see that while the iron is the main contributor with a spin of $-3.26\hbar/2$, the oxygen ions develop a spin of

FIGURE 7.6: VESTA visualisation of the spin density of bismuth ferrite on a cross section of the (100) plane at 0.5d from the origin. The central iron ion shows a high negative spin at that site, with lower spin values induced in surrounding oxygen ions and bonds. The oxygen ions have a negative induced spin, and the bonds have a positive induced spin.

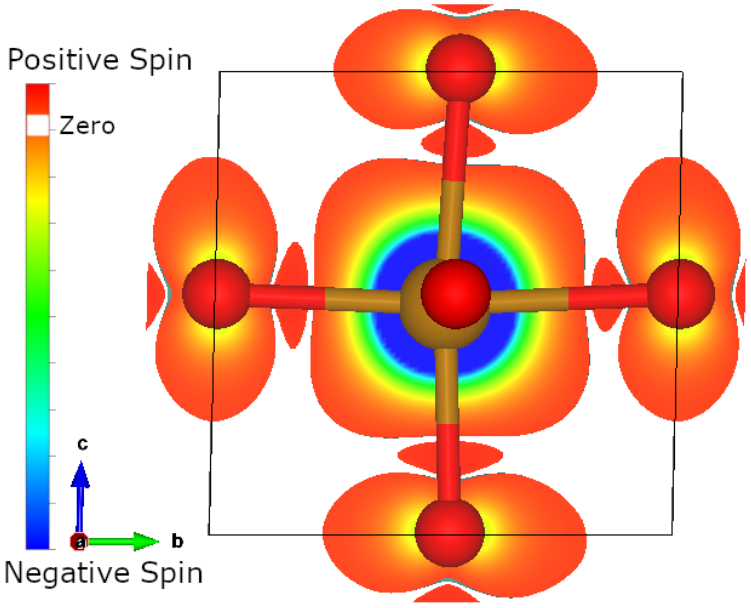

FIGURE 7.7: VESTA visualisation of the spin density of bismuth ferrite on a cross section of the $(\bar{1}10)$ plane through the origin.The central iron ion shows a high negative spin at that site, with lower spin values induced in surrounding oxygen ions and bonds. The oxygen ions have a negative induced spin, and the bonds have a positive induced spin.

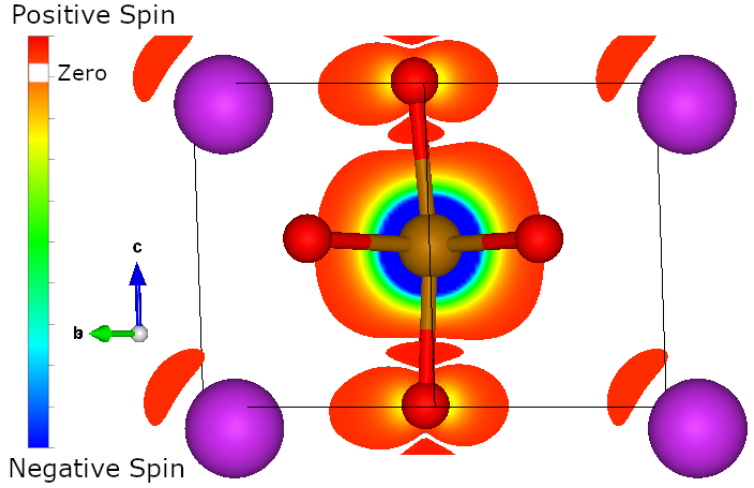

$-0.11\hbar/2$ each, and the bonds between the iron and oxygen ions carrys a spin of $0.10\hbar/2$. While for the most part we have a spin highly localised to the central ion, this induction and propogation may be enough to cause significant differences to the electric polarisation.

In the $(\bar{1}10)$ plane we see a distinct directionality in the spin pattern, evident in the lobes around the oxygen ions and the induced spin on the bismuth ion prominent in the direction of polarisation. While it is not definitive, it suggests that the magnetic and electric properties within the mutliferroic are coupled to some extent. If spin were entirely localised to the iron ion, it may suggest that the two effects are not intrinsically linked. Given that we have seen in previous materials that the oxygen ions are the main driving force behind the piezoelectric effect, it would not be unreasonable to assume that in the multiferroic the magnetic and electric properties were decoupled. This bias in the spin field, which is the driver for magnetic properties, in the direction of the electric polarisation as seen in the charge field, the driver of the piezo- and ferroelectric effects, suggests that these two properties are linked. That said, it remains beyond our capability to understand whether or not these two effects are complimentary or counter to each other.

7.3.3 Electron Density Shift

The electron density shifts were calculated by subtracting the charge of the formatted electron density of the unstrained structure from that of the strained structure at every point in the FFT grid. This can then be plotted over a cell file in VESTA show the electron density shift of the structure. Saturation and isosurface level are kept consistent with our other calculations.

FIGURE 7.8: VESTA visualisation cross section of the electron density shift of the first strain pattern for bismuth ferrite in the (100) plane at a distance of 0.5d from the origin.

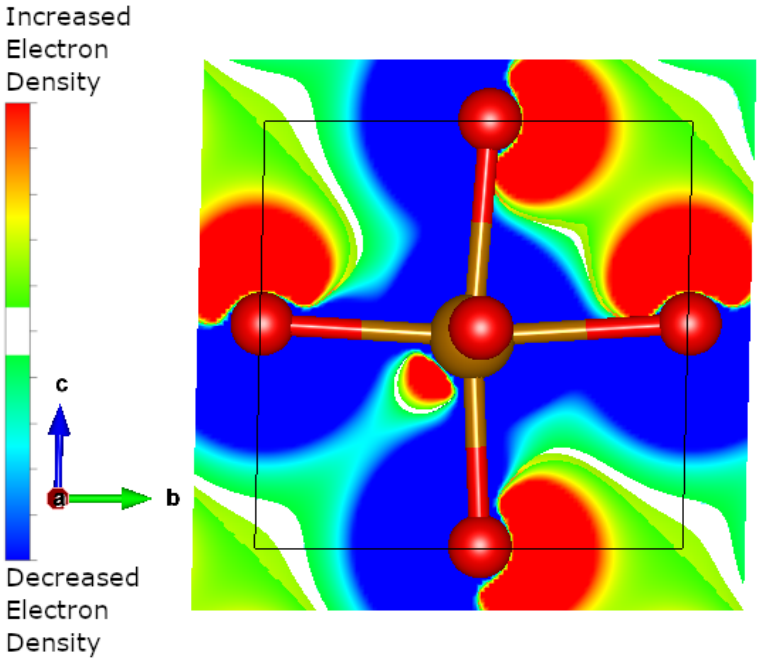

7.3.3.1 Strain Pattern 1

The first strain pattern is given by the matrix in equation 7.4 with the magnitude of strain $x = -0.167\%$.

$$\epsilon_{ij} = x \times \begin{bmatrix} 1 & 0 & 0 \\ 0 & 0 & 0 \\ 0 & 0 & 0 \end{bmatrix} \tag{7.4}$$

Figures 7.8, 7.9, and 7.10 show the electron density shift over three planes of interest, the (100), ($\bar{1}$10), and (211) respectively. Each is set to pass through the mid point of the cell, giving a distance from the origin of 0.5d, 0, and 2d respectively, where d is the interplanar spacing for each plane.

FIGURE 7.9: VESTA visualisation cross section of the electron density shift of the first strain pattern for bismuth ferrite in the $(\bar{1}10)$ plane through the origin.

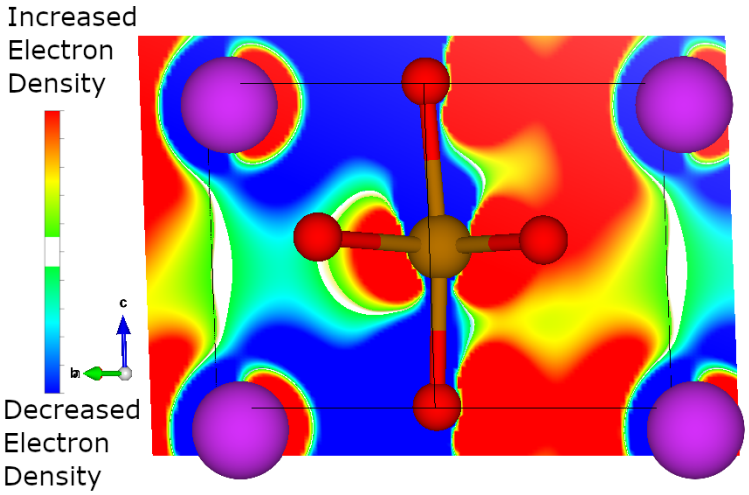

FIGURE 7.10: VESTA visualisation cross section of the electron density shift of the first strain pattern for bismuth ferrite in the (211) plane at a distance of 2d from the origin.

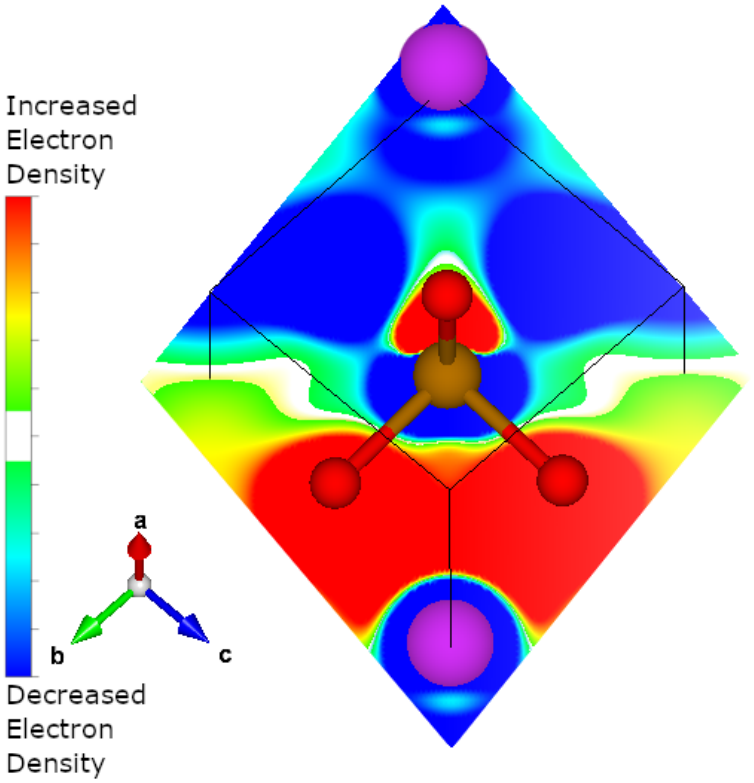

Immediately we see that the electron density shift in bismuth ferrite is considerably less localised than in the other materials. While those could be feasibly be divided into ionic properties that allowed us to construct our partial piezoelectric coefficient and discuss the partial polarisation, in the multiferroic material the density change is much more disperse. This emphasises the concept in section 7.2.3 that the partial occupancy is not simply representative of the the spin polarisation, and just because the overall spin is cancelled, it does not mean the occupancy can be fixed. We can see how the Born Effective Charge is not physically meaningful, as in previous calculations the movement of electrons could clearly be tied to the movement of ions with little ambiguity, whereas in these electron density shifts we see that the electronic movement is far more diffuse.

In the (211) plane we have the most clear indication of directionality as the strain appears to cause a shift along the lines between the furthest A-site ions, which we expect as the direction of polarisation. Thus the polarisation is changing in the known rhombohedral manner due to the material strain.

The other planes seem to show coherence, but it is not clear on how exactly the directionality is applied. For instance, in the (100) plane we see that there is definitely a symmetry in the distortied (111) diagonal, however much of the density shift is more lateral, though the lateral elements of the structure would cancel. Thus if we were to break this down into a set of partial piezoelectric coefficients, we would expect numerically large quantities that cancel out when considered from the axis of polarisation. If so, then we could strive towards a method through dopants or the application of electromagnetic forces to desymmetrise the system, allowing the crystal to present the full density changes on the macroscale.

The $(\bar{1}10)$ plane is the least obvious to interpret, as it appears to be entirely delocalised. In this view we see how it may be possible to divide some of the electronic charge and shift to individual ions. Bismuth and oxygen ions seem to demonstrate the behaviour seen previously with directional lobes, however unlike before where the isosurface level clears up much of the cross sectional area, this cross section is significantly active at every point. There may also be issues with the visualisation, as the circular area around the bismuth ions in this structure may be indicative of a very large pseudopotential core radius. If this is the case, then unlike the small and localised A-site shifts in the unary and binary materials so far, the electron density shift of bismuth is the most significant aspect of this bonding. In a classical valence model the Bi and Fe ions would both carry a +3 charge, so it could be that between the classical and electronic charge, the A-site is far more active in the piezoelectric system.

While this shift does seem to show a directionality, it does not appear to correlate strongly with the direction of polarisation in the material. However it is impossible to conclude if this is a stronger or weaker mode due to the wide spread of shift throughout the cell. It appears that there is a large amount of piezoelectric activity, but there is a lot of cancellation across different non-polar directions until only the directions associated with this mode remain. Again this implies that if there were a way to alter the directionality of the shift, or the piezoelectric system in general, then it may be possible to tune the material to a state where losses are minimised. However, it may also be that losses are consistent across different geometries and effects.

Meanwhile in the same plane, the iron seems to lack any direction. We have seen small lobes of directional density shift in the other planes so this may simply be a quirk of this particular plane. Or the coherence of vertical positive shift and horizontal negative could be indicative of an incompatibility in certain

axes between the electronic and spin polarisation systems. We would expect a coupling between the electric and magnetic dipole moment of the iron ion, and as such a proper 3D analysis may demonstrate directions in which the two moments enhance or oppose each other as in the previous chapters.

We must now consider the second strain pattern, to ascertain which of these features repeat in an example of the overall piezoelectric behaviour, and which are mode specific.

7.3.3.2 Strain Pattern 2

The second strain pattern is non-linear unlike all strain patterns so far. It is represented by the matrix shown in equation 7.5. The total magnitude of the strain is -0.167% as was previously the case, however the fact that we do not have a simple linear strain means that the coefficient x is a more complicated form. Overall it is only important that the magnitude of strain is the same.

$$\epsilon_{ij} = \frac{x}{2} \times \begin{bmatrix} 0 & 0 & 0 \\ 0 & 0 & 1 \\ 0 & 1 & 2 \end{bmatrix} \tag{7.5}$$

Immediately we expect problems with our method of viewing this. The non-linear strains likely mean a 3D analysis is more suitable, as the flat cross sections we take are not likely to show the skew strain taking place. However given a lack of alternatives, we will demonstrate what electron density shift features can be seen in the cross sections.

Figures 7.11, 7.12, and 7.13 show the electron density shift over three planes of interest, the (001), $(\bar{1}10)$, and (112) respectively. Each is set to pass through

FIGURE 7.11: VESTA visualisation cross section of the electron density shift of the second strain pattern for bismuth ferrite in the (001) plane at a distance of 0.5d from the origin.

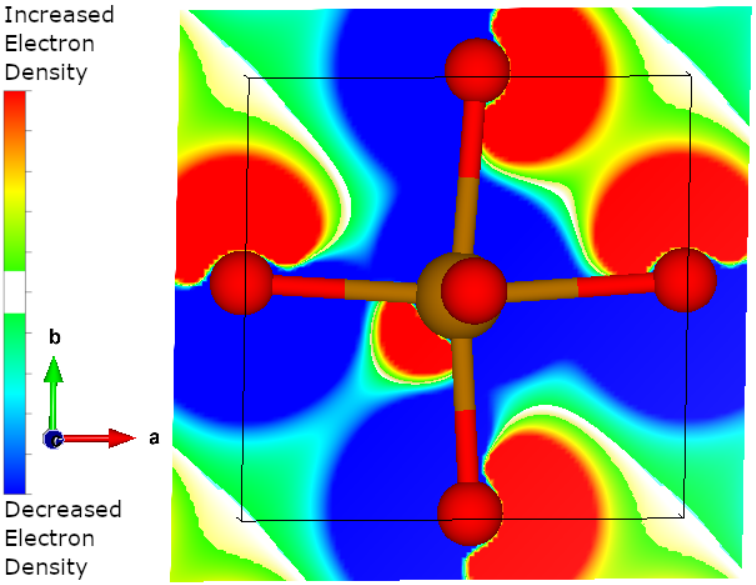

FIGURE 7.12: VESTA visualisation cross section of the electron density shift of the first strain pattern for bismuth ferrite in the $(\bar{1}10)$ plane through the origin.

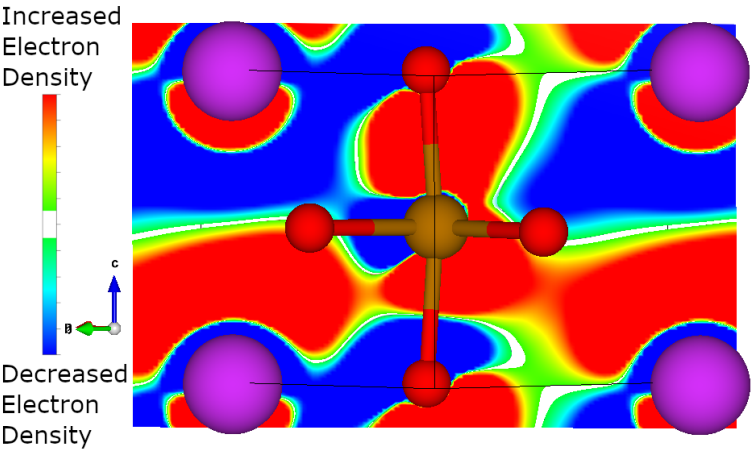

the mid point of the cell, giving a distance from the origin of 0.5d, 0, and 2d respectively, where d is the interplanar spacing for each plane.

The first thing to note about the overall structure is that the axial planes in the (100) and (001) directions in the different strains are highly similar. This

FIGURE 7.13: VESTA visualisation cross section of the electron density shift of the first strain pattern for bismuth ferrite in the (112) plane at 2d from the origin.

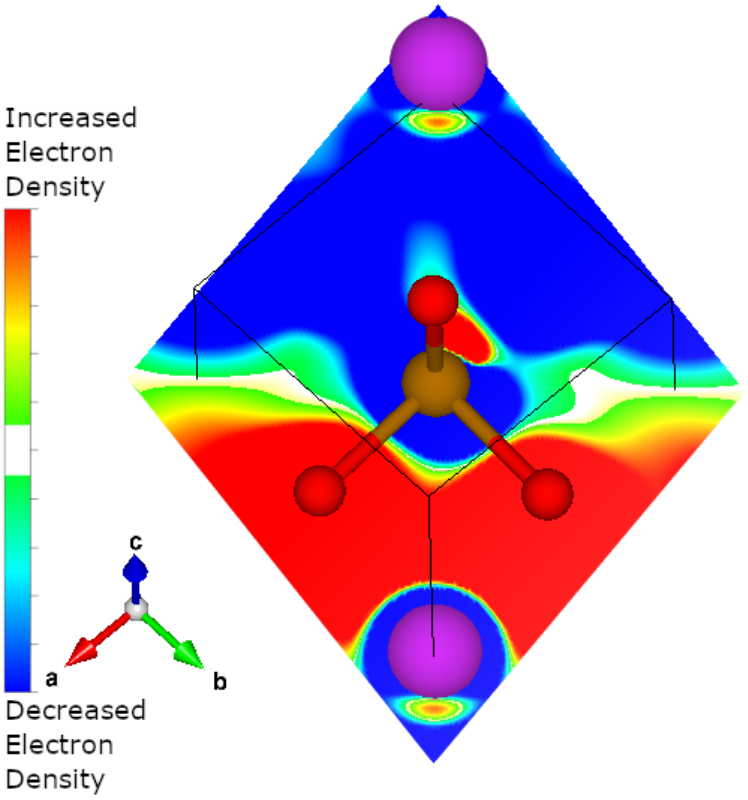

is likely due to this type of shift being generic to all piezoelectric modes. It shows the same symmetry and lateral shifting, which ideally would be altered to prevent inefficiencies due to dipole moment cancellation.

The other two planes are largely identical to the previous strain pattern, both show coherence and some directionality, and they are heavily delocalised. However we do see asymmetric characteristics. The reason for this is due to the off diagonal elements creating a rotation effect in the electronic density shift. This was seen in the elastic compliance tensor due to the rotation stress directions being large. This feature, while likely cancelling on the macroscale, will be an interesting feature of the partial piezoelectric coefficient matrix, and even further would be to perform this type of strain over many steps, and calculate

a rate of rotational shift. Though the utility of this quantity may not be immediately obvious, this and the indicated rotational compliance elements are essential to the development of rotary piezoelectric devices.

For the more general features of the density shift we can refer to section 7.3.3.1, as we expected many of the features are generic to the different modes. Therefore the electronic shift density has been fully evaluated as much as is possible in a 2D space.

7.4 Conclusions and Further Work

In this section we have performed calculations on the multiferroic structure bismuth ferrite in the rhombohedral form. We have presented optimised geometry for the structure, and calculated the elastic compliance tensor. Methods of mapping the rhombohedral axes to the cartesian polarisation have been discussed. The difficulties inherent in performing calculations on a multiferroic material have been addressed, and if it is still desirable the tweaks to the calculation parameters required to make it work. We have used the electron density shift to discuss how the delocalisation of the electron density movements under stress provide a fundamentally different picture of the piezoelectric effect in the system to that of the classical unary perovskites in chapter 5.

We have also identified features in the spin and charge density fields to indicate a coupling between the two prominent effects.

There are several avenues to continue in this line of work. Firstly, though it does not seem that the VASP calculations used by others are physically meaningful due to the static occupancy model used, discussions with the developers or obtaining a license to test the validity of the calculations would be sensible.

Due to the differing implementations of the methods, it may be that even if those particular results are found to be unphysical there are other interesting features made apparent by looking at the system differently.

Interest in the rotational strain patterns we discussed in section 7.3.3.2 may lead to the development of better methods to consider the off-diagonal strain elements. The use of curved cut-off planes or different methods of 3D rendering may make this line of enquiry easier to interpret, and the calculation of rotation angles due to stress and strain is important when considering applications.

As DFT codes develop, it may be that newer methods become available that allow us to overcome the limitations of the current systems, so keeping an eye on new methods available year on year will allow us to stay current on research into this class of materials.

In the future, we should consider binary supercells of bismuth ferrite with, for example, lead titanate. This mix, known as BFPT, shows excellent potential as an industrial piezoelectric, and as such it would be interesting to see how the two materials mix on an atomic scale. How will the two different perovskite units equalise? Will the inclusion of the PTO force the BFO units to become more localised, or given the magnetic character of the superstructure will the delocalisation spread throughout the cell. Also, how will the mixing of A- and B-sites affect the energetic states? Will Bi and Fe preferentially match in units, or will we actually see a quaternary BFO-PTO-BiTO-PFO system? BiTO is used to distinguish this unit from barium titanate.

Overall, multiferroics show great properties for piezoelectric applications, and despite the difficulties inherent in performing calculations it is still well worth the time and effort required to understand them.

Chapter 8

Conclusions and Further Work

8.1 Conclusions

Over this project we have performed many calculations and considered many physical and theoretical effects in relation to the overall piezoelectric properties of the material. First, we must revisit the initial questions from section 3.5 shown below.

- Can intrinsic piezoelectric properties be predicted by creating a framework from readily available DFT tools?
- Can we use this framework to identify overall similarities and differences in a more complicated binary material?
- How does the inclusion of ferromagnetism affect the capability of the framework to predict properties?

Beginning with the first question. In chapter 5 we demonstrated through the use of single point energy calculations, geometry optimisations, and linear response calculations that we can calculate the polarisation and change in polarisation under stress, i.e. the piezoelectric coefficient, to a reasonable numerical accuracy given the assumptions we have set out. These calculations were performed on barium titanate, lead titanate, and potassium niobate, which covers a variety of common types of piezoelectric pervoskite structures. Furthermore, we created a novel way to consider how these properties are broken down on an atomistic scale by defining and demonstrating the partial piezoelectric coefficient (δ_{ij}^{k}), a mathematical breakdown of how the piezoelectric coefficient is broken down to an individual ion scale. We also demonstrated a new method of visualising the piezoelectric effect through the Electron Density Shift (EDS) allowing us to use widely available free software for the visualisation of how the electron density moves under the type of stress that we associate with piezoelectricity.

For the second question we have performed the calculations on lead zirconate titanate in chapter 6. We have broken down the binary structure into its components using our derived calculation of the polarisation, and studied it through the use of our electron density shift and partial piezoelectric coefficient. This has allowed us to identify the way different materials combine into binary structures through an effective equalisation across the boundaries of simple units, the sawtooth effect produced due to slightly different bonding properties and consequently the partial piezoelectric constants that do not exist in the bulk material. Despite the differences in the polarisation contributions from different units, their partial piezoelectric contributions are equal. We have identified a region in the electron density of a weak coupling between the A- and B-sites and the axial oxygen ions which has allowed us to explain the radial/axial asymmetry through the idea of an effective shielding

caused by the A-site coupling. These are all of interest in themselves, and as a whole demonstrate a far bigger picture of the interactions of binary materials and how they mix, which is essential when designing new materials through combinations of previous materials of interest.

Finally, we have performed calculations on the multiferroic material bismuth ferrite in chapter 7, known for its G-type antiferromagentic and ferroelectric properties. We have determined what information we are able to ascertain using the previous methods, and what is beyond the reach of current software. The physical properties of the system inhibit our ability to use this framework to calculate the same properties, largely due to the fact that the software is unable to calculate the electric field response of the lattice. The program states that the Born Effective Charge and the LO/TO phonon splitting is not meaningful for a system with empty bands, so whether this is a weakness of the code or a fundamental block in the understanding of the material remains to be seen. However, we have outlined the changes that can be made to the calculations to incorporate the exotic properties and have been able to calculate a reduced set of parameters for this material of interest. We have also tacitly used this chapter to expand our understanding of the low symmetry states, by discussing general purpose issues with lattice alignment and pros and cons of different steps to overcome them.

Thus we conclude that we have successfully answered the three major questions laid out at the beginning of this project. While there is still much to be done in the field of computational piezoelectrics, we have introduced a series of tools that will widen the field by allowing researchers to perform computational tasks and interpret results supporting their experimental work. This can be done without having to spend time getting to grips with deeper theories of

electronic movement and polarisation, and is appealing as it can be done in the background in an safe and time-efficient manner.

8.2 Further Work

Though we have discussed what further work should occur in detail in the relevant chapters, we will now summarise the key points here.

From chapter 5, we identified the following further work for unary perovskites.

- The inclusion of dielectric tensors into the framework in order to calculate the crucial electric field coupling in ferroelectric materials.
- Evaluating where a potential factor 2 procedural error occurs in the piezoelectric coefficient calculations due to the application of stress in the simulations.

From chapter 6 we identified the following further work for binary perovskites.

- Calculations on different binary perovskites, to ascertain whether the properties such as equalisation and sawtoothing are unique to the bonding in PZT or general features of binary structures.
- How mixing and composition affect the intrinsic properties we have calculated for the binary PZT system.
- If the trends we have identified are present when applied to solid solutions of tertiary mixes and beyond.

From chapter 7 we identified the following further work for multiferroic materials.

- Can different codes with different implementations of DFT features give different insights into the piezoelectric properties of these traditionally difficult materials.

- Can we discover novel properties of the non-local electronic system and rhombohedral symmetry by considering linear steps in the perturbation modes.

- How does the multiferroic material behave in a binary system with other multiferroics and more traditional ferroelectrics?

Each of these points would be a valid step in developing a new understanding of the piezoelectric effect from an atomistic scale. Overall we have taken a fundamental step in novel ways of discussing piezoelectric materials, and this can now be built upon in further research across the field.

Bibliography

[1] B. Jaffe, W. R Cook Jr., and H. Jaffe. Piezoelectric ceramics. In J. P. Roberts and P. Popper, editors, *Non-Metallic Solids*. Academic Press London Ltd., 1971.

[2] M.G. Lippmann. Principe de la conservation de l'electricite. *Annales de Chimie et de Physique*, 24(1):145–178, 1881.

[3] J. Curie and P. Curie. Contractions et dilations produites par des tensions dans les cristaux hemiedres a faces inclinees. *Comptes Rendus Hebdomadaires des seances de L'Academie des Sciences*, 93(1):1137–1140, 1881.

[4] S. Katzir. Who knew piezoelectricity? rutherford and langevin on submarine detection and the invention of sonar. *Notes and Records of the Royal Society*, 2012.

[5] Morgan Advanced Materials. Piezo ceramic components. `http://www.morgantechnicalceramics.com/en-gb/`, September 2015. Accessed:25/9/18.

[6] Morgan Advanced Materials. Ultrasonic transducers. `http://www.morgantechnicalceramics.com/products/product-groups/ultrasonic-transducers`, September 2015. Accessed:25/9/18.

[7] J. Briscoe and S. Dunn. Piezoelectric nanogenerators – a review of nanostructured piezoelectric energy harvesters. *Nano Energy*, 14:15–29, 2015.

[8] IFLS. Teenager invents energy-generating shoe insoles. `http://www.iflscience.com/technology/teenager-invents-energy-generating-shoe-insoles`, June 2014. Accessed:25/9/18.

[9] Pavegen. Harvesting kinetic energy from every footstep. `http://www.pavegen.com/`, September 2015. Accessed:25/9/18.

[10] J. Frantti, J. Lappalainen, S. Eriksson, V. Lantto, S. Nishio, M. Kakihana, S. Ivanov, and H. Rundlof. Neutron diffraction studies of pb (zrx ti1-x) o3 ceramics. *Japanese Journal of Applied Physics*, 39:5697–5703, 2000.

[11] Gov.uk. Rohs: compliance and guidance. `https://www.gov.uk/guidance/rohs-compliance-and-guidance`, April 2014. Accessed:25/9/18.

[12] C. Curtis. Quarter of the world will be using smartphones in 2016. `http://www.telegraph.co.uk/technology/mobile-phones/11287659/Quarter-of-the-world-will-be-using-smartphones-in-2016.html`, December 2014. Accessed:25/9/18.

[13] G.E. Moore. Cramming more components onto integrated circuits. *Electronics*, 38:114–117, 1965.

[14] E. Roberts. Singularity. `http://cs.stanford.edu/people/eroberts/cs181/projects/2010-11/TechnologicalSingularity/pageviewa478.html?file=forfeasibility.html`, March 2011. Accessed:25/9/18.

[15] Oak Ridge National Laboratory. Introducing titan. `https://www.olcf.ornl.gov/titan/`, October 2012. Accessed: 25/9/18.

[16] C. J. Pickard and R. J. Needs. Highly compressed ammonia forms and ionic crystal. *Nature Materials*, 7:775–779, 2008.

[17] S. Ninet, F. Datchi, P. Dumas, M. Mezouar, G. Garbarino, A. Mafety, C. J. Pickard, R. J. Needs, and A. M. Saitta. Experimental and theoretical evidence for an ionic crystal of ammonia at high pressure. *Phys. Rev. B*, 89:174103, 2014.

[18] Georg Schusteritsch, Steven P. Hepplestone, and Chris J. Pickard. First-principles structure determination of interface materials: The ni$_x$InAs nickelides. *Phys. Rev. B*, 92:054105, 2015.

[19] Chris J. Pickard and Richard J. Needs. Structures and stability of calcium and magnesium carbonates at mantle pressures. *Phys. Rev. B*, 91: 104101, 2015.

[20] Nanomotion. The piezoelectric effect. `https://www.nanomotion.com/piezo-ceramic-motor-technology/piezoelectric-effect/`, July 2014. Accessed: 25/09/18.

[21] A.L. Kholkin, N.A. Pertsev, and A.V. Goltsev. Piezoelectricity and crystal symmetry. In A. Safari and E.K. Akdogan, editors, *Piezoelectric and Acoustic Materials for Transducer Applications*, pages 17–36. Springer US, 2008.

[22] J.F. Nye. *Physical Properties of Crystals*. Oxford University Press, 1957. Appendix E.

[23] R. Mirman. *Point Groups, Space Groups, Crystals, Molecules*, page 488. World Scientific Publishing, 1999.

[24] Z.L. Wang and J. Song. Piezoelectric nanogenerators based on zinc oxide nanowire arrays. *Science*, 312:242–246, 2006.

[25] GEL/15. Piezoelectric properties of ceramic materials and components. part 1: Terms and definitions. Standard, British Standards Institution, 2002.

[26] H. P. Rooksby. Compounds of the structural type of calcium titanate. *Nature*, 155(3938):484, 1945.

[27] APC International. Piezoelectric constants. `https://www.americanpiezo.com/knowledge-center/piezo-theory/piezoelectric-constants.html`, November 2015. Accessed: 25/9/18.

[28] Channel Industries. 600 barium titanate piezoelectric. `http://www.matweb.com/search/datasheet.aspx?matguid=b030bd8a82774bff8e485986efe77af5`, November 2015. Accessed: 25/9/18.

[29] Morgan Advanced Materials. Pzt400 series. `http://www.morgantechnicalceramics.com/sites/default/files/datasheets/pzt400_series.pdf`, November 2013.

[30] Mide Technology Company. Quickpack spec sheet and material properties. `http://www.mide.com/pdfs/quickpack_specs_piezo_properties.pdf`, November 2015. Accessed: 25/9/18.

[31] D. Berlincourt and H. Jaffe. Elastic and piezoelectric coefficients of single-crystal barium titanate. *Physical Review*, 111(1):143–148, 1958.

[32] A. Kip. *Fundamentals of Electricity and Magnetism*, chapter 5. McGraw-Hill Book Company, second edition, 1969.

[33] A. J. Bell. A classical mechanics model for the interpretation of piezoelectric property data. *Journal of Applied Physics*, 118(22):224103, 2015.

[34] G.H. Kwei, A.C. Lawson Jr., S.J.L. Billinge, and S.-W. Cheong. Structures of the ferroelectric phases of barium titanate. *Journal of Physical Chemistry*, 97(10):2368–2377, 1993.

[35] H. D. Megaw. Crystal structure of barium titanate. *Nature*, 155(3938): 484–485, 1945.

[36] J. W. Edwards, R. Speiser, and H. L. Johnston. Structure of barium titanate at elevated temperatures. *Journal of the American Chamical Society*, 73(6):2934–2935, 1951.

[37] R. Martin. *Electronic Structures*. Cambridge University Press, 2nd edition, 2010.

[38] C. F. Matta and R. J. Gillespie. Understanding and interpreting molecular electron density distributions. *Journal of Chemical Education*, 79 (9):1141, 2002.

[39] R. Prasad. *Electronic Structure of Materials*. CFC Press, 2013.

[40] K. Burke. The abc of dft. `http://dft.uci.edu/doc/g1.pdf`, April 2007.

[41] Z. Wu and R. E. Cohen. More accurate generalized gradient approximation for solids. *Physical Review B*, 73(23):235116, 2006.

[42] J. A. Hooper. Ab-initio modelling of barium titanate using density functional theory. Master's thesis, SCAPE, University of Leeds, 2014.

[43] K. Burke. Basics of dft. `http://elk.sourceforge.net/CECAM/Burke-DFT.pdf`, July 2011. Accessed: 25/9/18.

[44] T. Rowland. Functional. `http://mathworld.wolfram.com/Functional.html`, 2015. Created by Eric W. Weisstein.

[45] E. Fermi. A statistical method for determining some properties of the atoms and its application to the theory of the periodic table of elements. *ZEITSCHRIFT FUR PHYSIK*, 48(1-2):73–79, 1928.

[46] E. Teller. On stability of molecules in thomas-fermi theory. *Reviews of Modern Physics*, 34(4):627–631, 1962.

[47] N.H. March. The thomas-fermi approximation in quantum mechanics. *Advances in Physics*, 6(21):1–101, 1957.

[48] K. Hohenberg and W. Kohn. Inhomogenous electron gas. *Physical Review*, 136(3B):627–631, 1964.

[49] W. Kohn and L.J. Sham. Self-consistent equations including exchange and correlation effects. *Physical Review*, 140(4A):1133–1138, 1965.

[50] V. Fock. Approximation method for the solution of the quantum mechanical multibody problems. *ZEITSCHRIFT FUR PHYSIK*, 61(1-2): 126–148, 1930.

[51] P. Blaha, K. Schwarz, G.K.H. Madsen, D. Kvasnicka, J. Luitz, R. Laskowski, F. Tran, and L.D. Marks. Wien2k. `http://www.wien2k.at/index.html`, October 2014. TU Vienna.

[52] J.K. Dewhurst, S. Sharma, L. Nordstrom, F. Cricchio, O. Granas, and E.K.U. Gross. The elk fp-lapw code. `http://elk.sourceforge.net/`, July 2015. Accessed: 25/9/18.

[53] J. Hafner, G. Kresse, D. Vogtenhuber, and M. Marsman. Vasp. `https://www.vasp.at/`, November 2015. Accessed: 25/9/18.

[54] S. J. Clark, M. D. Segall, C. J. Pickard, P. J. Hasnip, M. J. Probert, K. Refson, and M. C. Payne. First principles methods using castep. *Zeitschrift fuer Kristallographie*, 220(5-6):567–570, 2005.

[55] P.J. Hasnip. Electronic structure, plane waves and pseudopotentials. In *CASTEP 2014 Training Workshop*, 2014. 18th-22nd August.

[56] C.K. Skylaris, P.D. Haynes, A.A. Mostofi, and M. C. Payne. Introducing onetep: Linear-scaling density functional simulations on parallel computers. *Journal of Chemical Physics*, 122(1):084119, 2005.

[57] S. J. Clark, M. D. Segall, C. J. Pickard, P. J. Hasnip, J. Yates, M. J. Probert, K. Refson, and M. C. Payne. Castep. `http://www.castep.org/`, November 2015. Accessed: 25/9/18.

[58] Clark S.J. The power of first principles simulations. In *CASTEP 2014 Training Workshop*, 2014. 18th-22nd August.

[59] F. Herman, J.P. Van Dyke, and I.B. Ortenburger. Improved statistical exchange approximation for inhomogeneous many-electron systems. *Physical Review Letters*, 22(16):807–811, 1969.

[60] J.P. Perdew, K. Burke, and M. Ernzerhof. Generalised gradient approximation made simple. *Physical Review Letters*, 77(18):3865–3868, 1996.

[61] V.N. et al. Staroverov. Comparative assessment of a new nonempirical density functional: Molecules and hydrogen-bonded complexes. *Journal of Chemical Physics*, 119(23):12129, 2003.

[62] J. C. Phillips and L. Kleinman. New method for calculating wave functions in crystals and molecules. *Physical Review*, 116(2):287–294, 1959.

[63] D. L. Geatches. *Clay Minerals and their Gallery Guests: An Ab Initio Investigation into their Interactions*. PhD thesis, Department of Physics, Durham University, 2011.

[64] Center for Molecular Modeling. Comparing solid state dft codes, basis sets and potentials. `https://molmod.ugent.be/deltacodesdft`, May 2014. Accessed: 25/9/18.

[65] D.R. Hamann, M. Schluter, and C. Chiang. Norm-conserving pseudopotentials. *Physical Review Letters*, 43(20):1494–1497, 1979.

[66] D. Vanderbilt. Soft self-consistent pseudopotentials in a generalized eigenvalue formalism. *Physical Review B Rapid Communications*, 41 (11):7892–7895, 1990.

[67] P. Blochl. Projector augmented-wave method. *Physical Review B*, 50 (24):17953, 1994.

[68] V. Cocular, C. J. Pickard, and E. A. Carter. Ultrasoft spin-dependent pseudopotentials. *Journal of Chemical Physics*, 123(21):214101, 2005.

[69] S.J. Clark. Semiconductor band structures. `http://cmt.dur.ac.uk/sjc/thesis_dbj/node75.html`, August 2012. Accessed: 25/9/18.

[70] H.J. Monkhorst and J.D. Pack. Special points for brillouin-zone integrations. *Physical Review B*, 13(12):5188–5192, 1976.

[71] I. Lawrie. *A Unified Grand Tour of Theoretical Physics*. Institute of Physics Publishing, 2nd edition, 2002.

[72] J. Patterson and B. Bailey. *Solid-State Physics: Introduction to the Theory*. Springer, 2nd edition, 2010.

[73] N.A. Spaldin. A beginner's guide to the modern theory of polarization. *Journal of Solid State Chemistry*, 195(1):2–10, 2012.

[74] K.W. Lee and W.E. Pickett. effective charges and infrared response of libc. *Physical Review B*, 68(8):085308, 2003.

[75] Z. Wu, R.E. Cohen, and D.J. Singh. Comparing the weighted density approximation with the lda and gga for ground-state properties of ferroelectric perovskites. *Physical Review B*, 70(10):104112, 2004.

[76] V.N. Staroverov, G.E. Scuseria, J. Tao, and J.P. Perdew. Tests of a ladder of density functionals for bulk solids and surfaces. *Physical Review B*, 69 (7):075102, 2004.

[77] P.P. Rushton. *Towards a Non-Local Density Functional Desription of Exchange and Correlation.* PhD thesis, Department of Chemistry, Durham University, 2002.

[78] A.W. Hewat. Structure of rhombohedral ferroelectric barium titanate. *Ferroelectrics*, 6(1):215–218, 1974.

[79] A. Mahmoud, A. Erba, Kh.E. El-Kelany, M. Rerat, and R. Orlando. Low-temperature phase of $batio_3$: Piezoelectric, dielectric, elastic, and photoelastic properties from ab initio simulations. *Physical Review B*, 89 (4):045103, 2014.

[80] A.V. Bandura and R.A. Evarestov. First-principles calculations on thermodynamic properties of $batio_3$ rhombohedral phase. *Journal of Computational Chemistry*, 33(18):1554–1563, 2012.

[81] B.G. Pfrommer, M. Cote, S.G. Louie, and M.L. Cohen. Relaxation of crystals with the quasi-newton method. *Journal of Computational Physics*, 131(1):233–240, 1997.

[82] D. Vanderbilt. First-principles based modelling of ferroelectrics. *Current Opinion in Solid State and Materials Science*, 2(1):701–705, 1997.

[83] S. Tinte, M.G. Stachiotti, C.O. Rodriguez, D.L. Novikov, and N.E. Christensen. Applications of the generalized gradient approximation to ferroelectric perovskites. *Physical Review B*, 58(18):11959–11963, 1998.

[84] X. Zhao, Y. Wang, M. Zhang, N. Zhao, S. Gong, and Q. Chen. First-principles calculations of the structural, electronic and optical properties of ba zrx ti1-x o3 (x = 0, 0.25, 0.5, 0.75). *Chinese Physical Letters*, 28 (6):067101, 2011.

[85] J. Long, L. Yang, and X. Wei. Lattice, elastic properties and debye temperatures of a ti o3 (a = ba, ca, pb, sr) from first - principles. *Journal of Alloys and Compounds*, 549(1):336–340, 2013.

[86] R.A. Evarestov and A.V. Bandura. First-principles calculations on the four phases of $batio_3$. *Journal of Computational Chemistry*, 33(11):1123–1130, 2012.

[87] S. Piskunov, E. Heifets, R.I. Eglitis, and G. Borstel. Bulk properties and electronic structure of $srtio_3$, $batio_3$, $pbtio_3$ perovskites: an ab initio hf/dft study. *Computational Materials Science*, 29(2):165–178, 2003.

[88] J.P. Perdew. Density functional theory and the band gap problem. *International Journal of Quantum Chemistry*, 28(S19):497–523, 1986.

[89] S.H. Wemple, M. Didomenico Jr., and I. Camlibel. Dielectric and optical properties of melt-grown $batio_3$. *Journal of Physics and Chemistry of Solids*, 29(10):1797–1803, 1968.

[90] D.J. Gardiner. Introduction to raman spectroscopy. In D.J. Gardiner and P.R. Graves, editors, *Practical Raman Spectroscopy*. Springer-Verlag, 1989.

[91] S. Baroni, S. Groncoli, A.D. Corso, and P. Giannozzi. Phonons and related crystal properties from density-functional perturbation theory. *Reviews of Modern Physics*, 73(2):515–563, 2001.

[92] Ph. Ghosez, E. Cockayne, U.V. Waghmare, and K.M. Rabe. Lattice dynamics of batio3, pbtio3 and pbzro3: A comparative first-principles study. *Physical Review B*, 60(2):836–843, 1999.

[93] K. Refson. Running phonon calculations. `http://www.tcm.phy.cam.ac.uk/castep/Phonons_Guide/Castep_Phononsch2.html#x7-80002`, June 2013. Phonon and Related Calculations Using CASTEP.

[94] E. Bousquet and P. Ghosez. First-principles study of barium titanate under hydrostatic pressure. *Physical Review B*, 74(18):180101, 2006.

[95] S. Tinte, M.G. Stachiotti, M. Sepliarsky, R.L. Migoni, and C.O. Rodriguez. Atomistic modelling of $batio_3$ based on first-principles calculations. *Journal of Physics: Condensed Matter*, 11(1):9679–9690, 1999.

[96] F. Barnardini, V. Fiorentini, and D. Vanderbilt. Spontaneous polarization and piezoelectric constants of iii-v nitrides. *Physical Review B: Rapid Communications*, 56(16):R10024, 1997.

[97] D. Vanderbilt. Berry-phase theory of proper piezoelectric response. *Journal of Physics and Chemistry of Solids*, 61(1):147–151, 2000.

[98] A. Zoroddu, F. Barnardini, P. Ruggerone, and V. Fiorentini. First-principles prediction of structure, energetics, formation enthalpy, elastic constants, polarization, and piezoelectric constants of aln, gan, and inn:

Comparison of local and gradient-corrected density-functional theory. *Physical Review B*, 64(4):045208, 2001.

[99] T. Furuta and K. Miura. First-principles study of ferroelectric and piezoelectric properties of tetragonal srtio3 and batio3 with in-plane compressive structures. *Solid State Communications*, 150(47-48):2350–2353, 2010.

[100] V.G. Bhide, M.S. Hegde, and K.G. Deshmukh. Ferroelectric properties of lead titanate. *Journal of the American Ceramic Society*, 51(10):565–569, 1968.

[101] J. Joseph, T.M. Vimala, V. Sivasubramanian, and V.R.K. Murthy. Structural investigations on pb (zrx ti1-x) o3 solid solutions using the x-ray rietveld method. *Journal of Materials Science*, 35(6):1571–1575, 2000.

[102] R.J. Nelmes and W.F. Kuhs. The crystal structure of tetragonal pb ti o3 at room temperature and at 700 k. *Solid State Communications*, 54 (8):721–723, 1985.

[103] Y. Kuroiwa, S. Aoyagi, A. Sawada, J. Harada, E. Nishibori, M. Takata, and M. Sakata. Evidence for pb-o covalency in tetragonal pb ti o3. *Physical Review Letters*, 87(21):217601, 2001.

[104] V.G. Bhide, K.G. Deshmukh, and M.S. Hegde. Ferroelectric properties of pbtio3. *Physica*, 28(9):871–876, 1962.

[105] C. Pavithra and W. Madhuri. Dielectric, piezo and ferroelectric properties of microwave sintered pbtio3 synthesized by sol–gel method. *Journal of Sol-Gel Science and Technology*, 85(2):437–445, 2018.

[106] A. Yamada, C. Maeda, T. Umemura, F. Uchikawa, K. Misu, S. Wadaka, and T. Ishikawa. Preparation and piezoelectric property of lead titanate

thin films for ghz-band resonators. *Japanese Journal of Applied Physics*, 36(9B):6073, 1997.

[107] A. Stashans, C. Zambrano, A. Sanchez, and L.M. Procel. Structural properties of pbtio3 and pbzrxti1xo3: A quantum-chemical study. *International Journal of Quantum Chemistry*, 87(3):145–151, 2002.

[108] A.I. Lebedev. Ab initio calculations of phonon spectra in atio3 perovskite crystals (a = ca, sr, ba, ra, cd, zn, mg, ge, sn, pb). *Physics of the Solid State*, 51(2):362–372, 2009.

[109] D. Vanderbilt and R.D. Kingsmith. Electric polarization as a bulk quantity and its relation to surface-charge. *Physical Review B*, 48(7):4442–4455, 1993.

[110] R.D. Kingsmith and D. Vanderbilt. Theory of polarization of crystalline solids. *Physical Review B*, 47(3):1651–1654, 1993.

[111] J. Yang. Opium - pseudopotential generation project. `http://opium.sourceforge.net/index.html`, April 2018. Accessed: 19/1/19.

[112] Bureau International des Poids et Mesures. *The International System of Units*. Bureau International des Poids et Mesures, 8th edition, 2006.

[113] S.L. Skjaervo, K. Hoydalsvik, A.B. Blichfeld, M.A. Einarsrub, and T. Grande. Thermal evolution of the crystal structure and phase transitions of knbo3. *Royal Society Open Science*, 5(6):180368, 2018.

[114] A.W. Hewat. Cubic-tetragonal-orthorhombic-rhombohedral ferroelectric transitions in perovskite potassium niobate: neutron powder profile refinement of the structures. *Journal of Physics C: Solid State Physics*, 6 (16):2559–2572, 1973.

[115] A.W. Hewat. Soft modes and the structure, spontaneous polarization and curie constants of perovskite ferroelectrics: tetragonal potassium niobate. *Journal of Physics C: Solid State Physics*, 6(6):1074–1084, 1973.

[116] S. Kawamura, E. Magome, Moriyoshi C., Y. Kuroiwa, N. Taniguchi, H. Tanaka, S. Maki, M. Takata, and S. Wada. Electronic polarization in k nb o3 visualized by synchrotron radiation powder diffraction. *Japanese Journal of Applied Physics*, 52(9):09KF04, 2013.

[117] A. Shigemi and T. Wada. Evaluations of phases and vacancy formation energies in knbo3 by first-principles calculation. *Japanese Journal of Applied Physics*, 44(11):8048–8054, 2005.

[118] L.F. Wan, T. Nishimatsu, and S.P. Beckman. The structural, dielectric, elastic, and piezoelectric properties of knbo3 from first-principles methods. *Journal of Applied Physics*, 111(10):104107, 2012.

[119] S. Cabuk. Electronic structure and optical properties of knbo3: First principles study. *Optoelectronics And Advanced Materials - Rapid Communications*, 1(3):100–107, 2007.

[120] P.K. Panda and B. Sahoo. Pzt to lead free piezo ceramics: A review. *Ferroelectrics*, 474(1):128–143, 2015.

[121] G.A. Rossetti jr., G. Popov, E. Zlotnikov, and N. Yao. Domain structures and nonlinear mechanical deformation of soft pb (zrx ti1-x) o3 (pzt) piezoelectric ceramic fibers. *Materials Science and Engineering: A*, 433 (1-2):124–132, 2006.

[122] J. Frantti, J. Lappalainen, S. Eriksson, V. Lantto, S. Nishio, M. Kakihana, S. Ivanov, and H. Rundlof. Neutron diffraction studies of pb (zrx ti1-x) o3 ceramics. *Japanese Journal of Applied Physics*, 39(9B):5697–5703, 2000.

[123] L. Belliache and D. Vanderbilt. Virtual crystal approximation revisited: Application to dielectric and piezoelectric properties of perovskites. *Physical Review B*, 61(12):7877–7882, 2000.

[124] N.J. Ramer and A.M. Rappe. Application of a new virtual crystal approach for the study of disordered perovskites. *Journal of Physics and Chemistry of Solids*, 61(2):315–320, 1999.

[125] P. Marton and C. Elsasser. First-principles study of structural and elastic properties of the tetragonal ferroelectric perovskite pb(zr0.50ti0.50)o3. *Physica Status Solidi B*, 248(10):2222–2228, 2011.

[126] T.B. Boykin, N. Kharche, G. Klimeck, and M. Korkusinski. Approximate bandstructures of semiconductor alloys from tight-binding supercell calculations. *Journal of Physics: Condensed Matter*, 19(3):036203, 2007.

[127] D. Lebeugle, D. Colson, A. Forget, M. Viret, P. Bonville, J. F. Marucco, and S. Fusil. Room-temperature coexistence of large electric polarization and magnetic order in bifeo3 single crystals. *Physical Review B*, 76(2), 2007.

[128] G. Catalan and J.F. Scott. Physics and applications of bismuth ferrite. *Advanced Materials*, 21(24), 2009.

[129] Yu.Ya. Tomashpolskii, Yu.N. Venevtsev, and G.S. Zhdanov. X-ray diffraction study of the atomic structure of ferromagnetic bi fe o3. *Kristallografiya*, 12(1):252–257, 1967.

[130] Yu.Ya. Tomashpolskii, Yu.N. Venevtsev, and G.S. Zhdanov. The electron diffraction study of the crystal structure of bi fe o3. *Doklady Akademii Nauk SSSR*, 153(1):1313–1314, 1963.

[131] A.I. Zaslavskii and A.G. Tutov. The structure of new antiferromagnetic bi fe o3. *Doklady Akademii Nauk SSSR*, 135(1):815–817, 1960.

[132] C. Ederer and N.A. Spaldin. Weak ferromagnetism and magnetoelectric coupling in bismuth ferrite. *Physical Review B*, 71(6):060401, 2005.

[133] E. Gradauskaite, J. Gardner, R.M. Smith, F.D. Morrison, S.L., R.S. Katiyar, and J.F. Scott. Lead palladium titanate: A room-temperature multiferroic. *Physical Review B*, 96(10):104104, 2014.

[134] T.P. Comyn, T. Stevenson, M. Al-Jawad, G. Andre, A.J. Bell, and R. Cywinski. Antiferromagnetic order in tetragonal bismuth ferrite-lead titanate. *Journal of Magnetism and Magnetic Materials*, 323(21):2533–2535, 2011.

[135] F. Esat, T.P. Comyn, and A.J. Bell. Microstructure development of bifeo3-pbtio3 films deposited by pulsed laser deposition on platinum substrates. *Acta Materialia*, 66(1):44–53, 2014.

[136] P. Hermet, M. Goffinet, J. Kriesel, and Ph. Ghosez. Raman and infrared spectra of multiferroic bismuth ferrite from first principles. *Physical Review B*, 75(22):220102, 2007.

[137] L. Wei, S. Fan, X.P. Wang, B. Liu, Y.Y. Zhang, X.S. Lv, Y.G. Yang, H.J. Zhang, and X. Zhao. Lattice dynamics of bismuth-deficient bifeo3 from first principles. *Computational Materials Science*, 111(1):374–379, 2016.

[138] A. Lubk, S. Gemming, and N.A. Spaldin. First-principles study of ferroelectric domain walls in multiferroic bismuth ferrite. *Physical Review B*, 80(10):104110, 2009.

[139] E.J. Heller. Frozen gaussians: A very simple semiclassical approximation. *Journal of Chemical Physics*, 75(6):2923–2931, 1981.

[140] The GalliumOS Project. Galliumos. `https://galliumos.org/`, sep 2018. A fast and lightweight Linux distro for ChromeOS devices.

[141] M. Callaghan. Arc1. `http://arc.leeds.ac.uk/systems/arc1/`, June 2017. Accessed: 25/9/18.

[142] M. Callaghan. Arc2. `http://arc.leeds.ac.uk/systems/arc2/`, June 2017. Accessed: 25/9/18.

[143] M. Callaghan. Arc3. `http://arc.leeds.ac.uk/systems/arc3/`, June 2017. Accessed: 25/9/18.

[144] Intel News Release. Dual core era begins, pc makers start selling intel-based pcs. `https://www.intel.com/pressroom/archive/releases/2005/20050418comp.htm`, April 2005. Accessed: 25/9/18.

[145] Intel ARK. Intel xeon processor e5-2650 v4. `https://ark.intel.com/products/91767/Intel-Xeon-Processor-E5-2650-v4-30M-Cache-2_20-GHz`, January 2016. Accessed: 25/9/18.

[146] Intel ARK. Intel xeon phi processor 7230. `https://ark.intel.com/products/94034/Intel-Xeon-Phi-Processor-7230-16GB-1_30-GHz-64-core`, April 2016. Accessed: 25/9/18.

[147] TOP500.org. Top 10 sites for june 2018. `https://www.top500.org/lists/2018/06/`, June 2018.

[148] K. Refson, S.J. Clark, and P.R. Tulip. Variational density functional perturbation theory for dielectrics and lattice dynamics. *Physical Review B*, 73(15):115114, 2006.

[149] P. Atkins. *The Laws of Thermodynamics: A Very Short Introduction*. OUP Oxford, 1st edition, 2010.

[150] P. Salamon, D. Wales, A. Segall, Y-A. Lai, J.C. Schon, K.H. Hoffmann, and B. Andresen. Rate constants, timescales, and free energy barriers. *Journal of Non-Equilibrium Thermodynamics*, 41(1):13–18, 2016.

[151] C.S. Baird. Why do diamonds last forever? `http://wtamu.edu/~cbaird/sq/2013/12/17/why-do-diamonds-last-forever/`, December 2013. Accessed: 2/12/18.

[152] Chris J. Pickard and Richard J. Needs. Topical review: Ab initio random structure searching. *Journal of Physics: Condensed Matter*, 23:053201, 2011.

[153] Hellenbrandt. The inorganic crystal structure database (icsd)—present and future. *Crystallography Reviews*, 10(1):17–22, 2004.

[154] K. Momma and F. Izumi. Vesta 3 for three-dimensional visualization of crystal, volumetric and morphology data. *Journal of Applied Crystallography*, 44(6):1272–1276, 2011.

[155] Y. He. Heat capacity, thermal conductivity, and thermal expansion of barium titanate-based ceramics. *Thermochimica Acta*, 419(1-2):135–141, 2004.

[156] A. Walker. Github - andreww/elastic-constants. `https://github.com/andreww/elastic-constants`, June 2016. Accessed: 25/9/18.

[157] E.R. Leite, E.C. Paris, F.M. Pontes, C.A. Paskocimas, E. Longo, F. Sensato, C.D. Pinheiro, J.A. Varela, P.S. Pizani, C.E.M. Campos, and F. Lanciotti Jr. The origin of photoluminescence in amorphous lead titanate. *Journal of Materials Science*, 38(6):1175–1178, 2003.

[158] X. Gonze and C. Lee. Dynamical matrices, born effective charges, dielectric permittivity tensors, and interatomic force constants from density-functional perturbation theory. *Physical Review B*, 55(16):10355–10368, 1997.

[159] M.J. Haun, E. Furman, S.J. Jang, H.A. McKinstry, and L.E. Cross. Thermodynamic theory of pbtio3. *Journal of Applied Physics*, 62(8): 3331–3338, 1987.

[160] S. Wada, K. Muraoka, H. Kakemoto, T. Tsurumi, and H. Kumagai. Enhanced piezoelectric properties of potassium niobate single crystals by domain engineering. *Japanese Journal of Applied Physics*, 43(9B): 6692–6700, 2004.

[161] J. Dunningham and V. Vedral. *Introductory Quantum Physics and Relativity*, chapter 5. Imperial College Press, 1st edition, 2011.

[162] G. Shirane, K. Suzuki, and A. Takeda. Phase transitions in solid solutions of pbzro3 and pbtio3 (ii) x-ray study. *Journal of the Physical Society of Japan*, 7(1):12–18, 1952.

[163] N. Provatas and K. Elder. *Phase Field Methods in Materials Science and Engineering*. Wiley VCH Verlag GmbH & Co. KGaA, October 2010.

[164] D. Damjanovic. Hysteresis in piezoelectric and ferroelectric materials. In Mayergoyz. I. and G Bertotti, editors, *The Science of Hysteresis Vol. 3*. Academic Press, 2005.

[165] G-T. Park, J-J. Choi, J. Ryu, H. Fan, and H-E. Kim. Measurement of piezoelectric coefficients of lead zirconate titanate thin films by strain-monitoring pneumatic loading method. *Applied Physics Letters*, 80(24): 4606–4608, 2002.

[166] M. Schirber. Synopsis: Multiferroic surprise. `https://physics.aps.org/synopsis-for/10.1103/PhysRevLett.115.087601`, August 2015. Accessed: 25/9/18.

[167] T.J. Stevenson. *Magnetic and electric properties of bismuth ferrite lead titanate ceramics*. PhD thesis, School of Process, Environmental, and Materials Engineering, University of Leeds, 2010.

[168] J.D. Bucci, B.K. Robertson, and W.J. James. The precision determination of the lattice parameters and the coefficients of thermal expansion of bifeo3. *Journal of Applied Crystallography*, 5(1):187–191, 1972.

[169] W. Setyawan and S. Curtarolo. High-throughput electronic band structure calculations: Challenges and tools. *Computational Materials Science*, 49(2):299–312, 2010.

[170] Z.X. Cheng, A.H. Li, X.L. Wang, S.X. Dou, K. Ozawa, H. Kimura, S.J. Zhang, and T.R. Shrout. Structure, ferroelectric properties, and magnetic properties of the la-doped bismuth ferrite. *Journal of Applied Physics*, 103(7):07E507, 2008.